Measurement of the W-boson Polarisation in Top-Quark Decays with the ATLAS Detector

Dissertation

zur Erlangung des mathematisch-naturwissenschaftlichen Doktorgrades
"Doctor rerum naturalium"
der Georg-August-Universität Göttingen

im Promotionsprogramm ProPhys
der Georg-August University School of Science (GAUSS)

vorgelegt von
Andrea Helen Knue
aus Meppen

Göttingen 2013

Betreuungsausschuss:

Prof. Dr. Arnulf Quadt, II. Physikalisches Institut, Universität Göttingen

Prof. Dr. Ariane Frey, II. Physikalisches Institut, Universität Göttingen

PD. Dr. Kevin Kröninger, II. Physikalisches Institut, Universität Göttingen

Mitglieder der Prüfungskommission:

Referent: Prof. Dr. Arnulf Quadt, II. Physikalisches Institut, Universität Göttingen

Korreferent: Prof. Dr. Wolfgang Wagner, Fachbereich C, Bergische Universität Wuppertal

Weitere Mitglieder der Prüfungskommission:

Prof. Dr. Ariane Frey, II. Physikalisches Institut, Universität Göttingen

Prof. Dr. Andreas Dillmann, Deutsches Institut für Luft- und Raumfahrt Göttingen

PD. Dr. Kevin Kröninger, II. Physikalisches Institut, Universität Göttingen

PD. Dr. Martin Rein, Deutsches Institut für Luft- und Raumfahrt Göttingen

Tag der mündlichen Prüfung: 12.03.2013

Measurement of the W-boson Polarisation in Top-Quark Decays with the ATLAS Detector

von

Andrea Helen Knue

A measurement of the W-boson polarisation in top-quark decays is presented. The top-antitop events were produced in proton-proton collisions at a centre-of-mass energy of $\sqrt{s} = 7$ TeV at the LHC. The data set corresponds to an integrated luminosity of $\int \mathcal{L}\, dt = 4.7$ fb^{-1} and was collected by the ATLAS experiment. The measurement was performed in the lepton+jets channel which is characterised by an isolated electron or muon, missing transverse energy and at least four jets. One of the jets has to be identified as a b-jet. The W-boson polarisation was studied using the angular distribution of the charged lepton in the rest frame of the W-boson. The event is fully reconstructed using a kinematic likelihood fit. The fractions of left-handed, right-handed and longitudinally polarised W-bosons were estimated from the data distribution using a binned likelihood fit. The W-helicity fractions obtained from the combined likelihood fit are:

$$\begin{aligned} F_0 &= 0.659 \pm 0.029\ \text{(stat.)} \pm 0.071\ \text{(syst.)} \quad , \\ F_L &= 0.317 \pm 0.014\ \text{(stat.)} \pm 0.026\ \text{(syst.)} \quad , \\ F_R &= 0.024 \pm 0.019\ \text{(stat.)} \pm 0.057\ \text{(syst.)} \quad . \end{aligned}$$

Limits on anomalous Wtb-couplings were set. All results are in good agreement with the Standard Model predictions.

Post address:
Friedrich-Hund-Platz 1
37077 Göttingen
Germany

II.Physik-UniGö-Diss-2013/01
II. Physikalisches Institut
Georg-August-Universität Göttingen
March 2013

Messung der W-Boson Polarisation in Top-Quark Zerfällen mit dem ATLAS-Detektor

von
Andrea Helen Knue

Eine Messung der W-Boson Polarisation in Topquark-Zerfällen wird vorgestellt. Es wurden Topquarks untersucht, welche in Proton-Proton Kollisionen bei einer Schwerpunktsenergie von $\sqrt{s} = 7$ TeV am LHC erzeugt wurden. Der Datensatz basiert auf einer integrierten Luminosität von $\int \mathcal{L}\, dt = 4.7$ fb^{-1} und wurde mit dem ATLAS-Detektor gesammelt. Die Messung wurde im Lepton+Jets Kanal durchgeführt, welcher durch ein isoliertes Elektron oder Myon, fehlende transversale Energie und mindestens vier Jets charakterisiert wird. Einer der Jets muss als b-Jet identifiziert sein. Zum Studium der W-Boson Polarisation wurde die Winkelverteilung des geladenen Leptons im Ruhesystem des W-Bosons verwendet. Das Ereignis wurde vollständig mit Hilfe eines kinematischen Likelihood-Fits rekonstruiert. Die Anteile der linkshändigen, rechtshändigen und longitudinal polarisierten W-Bosonen wurden durch einen gebinnten Likelihood-Fit an die Datenverteilung bestimmt. Ein kombinierter Likelihood-Fit wird durchgeführt, um die W-Helizitätsanteile für den Lepton+Jets Kanal zu bestimmen. Das Ergebnis ist wie folgt:

$$\begin{aligned} F_0 &= 0.659 \pm 0.029\ (\text{stat.}) \pm 0.071\ (\text{syst.}) \quad , \\ F_L &= 0.317 \pm 0.014\ (\text{stat.}) \pm 0.026\ (\text{syst.}) \quad , \\ F_R &= 0.024 \pm 0.019\ (\text{stat.}) \pm 0.057\ (\text{syst.}) \quad . \end{aligned}$$

Es wurden obere und untere Grenzen auf die Größe der anomalen Wtb-Kopplungen gesetzt. Alle Messungen sind in guter Übereinstimmung mit den Vorhersagen des Standardmodells.

"So once you know what the question actually is, you'll know what the answer means."

Douglas Adams, *The Hitchhiker's Guide to the Galaxy*

Contents

1. Introduction

The fundamental questions of mankind are: Where do we come from? Where are we going? What are we made of? Particle physics plays an important role to answer, in particular, the last question. The structure of the Universe and the forces between the elementary particles that build all surrounding matter has been the interest of mankind since the ancient greeks brought up the idea of fundamental particles as building blocks of all matter that they called "atomos". In the hunt for these particles, larger and larger experiments have been built, using the latest technology available. To investigate elementary particles and their interactions, large energies and fast and efficient particle detectors are neccessary. The LHC, which started its proton-proton collision programme in 2010, and its four main experiments ALICE, ATLAS, CMS and LHCb have broken record after record for the highest center-of-mass energy, luminosity and data aquisition rate. Thousands of physicists and engineers are working in these collaborations to contribute to the answers of open questions of mankind.

The Standard Model of Particle Physics (SM), which will be introduced in Chapter 2, is the most successful theory and its predictions are in good agreement with all measurements. With the data taken at the LHC, many measurements can be performed at a so far unprecedented precision which allows for detailed tests of the SM. The top quark, having a mass close to the scale of electroweak symmetry breaking, is a *standard candle* for many of these tests. The top quark has a large Yukawa coupling, leading to its high mass. With its corresponding short lifetime it decays before it can hadronise, therefore being the only *bare* quark that can be investigated. Its properties, like charge and spin, are directly transferred to the decay products. Measuring these decay products allows to answer fundamental questions about the structure of its vertices and the nature of its couplings. The top quark and its properties will be discussed in detail in Chapter 3.

The goal of this thesis is to test the Lorentz structure of the Wtb-vertex by studying the polarisation of W-bosons. Due to the small b-quark mass, the production of right-handed W-bosons is strongly suppressed. The expected W-helicity fractions have been calculated to next-to-next-to leading order precision. The measurement of a significant right-handed fraction would point to physics processes beyond the Standard Model. The angular distribution of the charged lepton in the rest frame of the W-boson is used as key observable in the analysis. A template fit is performed to the data distribution and the statistical and systematic uncertainties are evaluated. Limits are set on six-dimensional operators in effective Lagrange densities and on anomalous couplings that would affect the Wtb-vertex. Since the analysis on first LHC data in 2010, the measurement of the W-helicity fractions has been continuously improved. With increasing data and MC statistics, the statistical and systematic uncertainties were reduced. The results have been published in two conference notes for the Moriond and the Lepton/Photon conference 2011 [1, 2] based on a data set corresponding to 35 pb^{-1} and 0.7 fb^{-1}, respectively. Furthermore, a combination of four measurements (performed in the lepton+jets and the dilepton channels at ATLAS) has been published using 1.04 fb^{-1} of data [3], leading to the most precise result worldwide.

The measurement presented in this thesis has been performed using the full 2011 ATLAS data set of 4.7 fb^{-1}. With the increased understanding of the ATLAS detector and the larger data set, again the uncertainties can be reduced. The theoretical framework of the Standard Model and the top-quark itself are introduced in Chapters 2 and 3. The experimental setup is described in Chapter 4, discussing the accelerator chain as well as the ATLAS detector and its subcomponents. The objects that are used in the underlying analysis are presented in Chapter 5, followed by the description of the signal and background modelling using Monte Carlo simulation and data driven estimates. These are shown in Chapter 6. The data set and the event selection applied in the analysis are discussed in Chapter 7. The analysis strategy itself is introduced in Chapter 8. Most Standard Model measurements are limited by systematic uncertainties. The study and evaluation of these uncertainties will be the topic of Chapter 8 and 9. The final measurement with statistical and systematic uncertainties is discussed in Chapter 9. The results are summarised in Chapter 10.

2. The Standard Model of Particle Physics

The first part of this chapter deals with the principles of elementary particle physics, describing the particle content and the fundamental forces. In the second part the focus is placed on the Higgs mechanism that is responsible for the creation of particle masses as well as current measurements of a new Higgs-like boson at ATLAS and CMS. The Standard Model of Particle Physics is a successful theory that so far withstood all tests to disprove it. Nevertheless, it does not provide explanations for several observations and is believed to be only valid up to an energy of $\mathcal{O}$(TeV).

2.1. Elementary Particles

The Standard Model of Particle Physics (SM) [4, 5, 6, 7, 8, 9] describes the elementary particles[1] (fermions with spin $\frac{1}{2}$) and the fundamental forces mediated by gauge bosons (spin 1). It is based on a number of principles that are explained in the following. Up to now three generations of fermions were found (see Fig. 2.1). Since the number of generations is not predicted by the SM, more than three generations might exist.

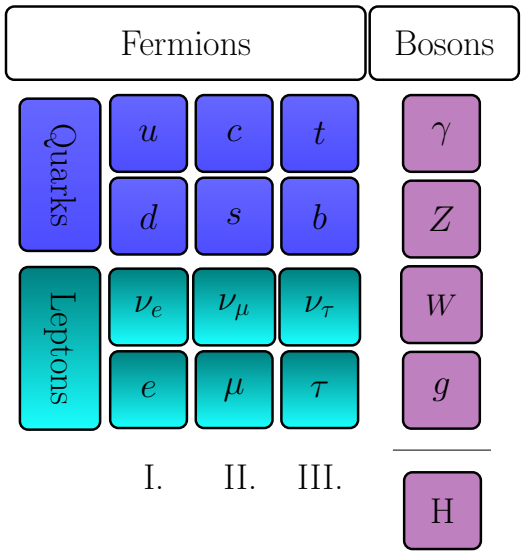

Figure 2.1.: Particle content in the SM. In total 24 fermions (six quarks and six leptons plus their corresponding antiparticles) are known. The forces are mediated by the gauge bosons γ, $W^{\pm}$, Z^0 and g. Recent measurements suggest that the new scalar boson found both by the ATLAS [10] and CMS [11] collaborations is consistent with the SM Higgs boson.

[1] The term *elementary particles* in this context describes point-like particles without any substructure.

The lifetime measurement of the Z^0-boson [12] shows that only three *light* neutrino generations are possible. In addition, the mass of the Z^0-boson sets a limit on the mass of a possible light 4th lepton generation ($m_{4\text{th gen.}} < \frac{m_Z}{2}$). The existence of a heavy fourth generation down-type (b') and up-type quark (t') has however been excluded at 95 % confidence level (C.L.) for masses of $m_{b'} < 670$ GeV [13] and $m_{t'} < 656$ GeV [14], respectively. As depicted in Fig. 2.1, each generation consists of two quarks (up-type and down-type) and two leptons (charged lepton and corresponding neutrino)[2]. The generations are ordered by the increasing mass of their constituents. Fermions of the same type (for example the charged leptons) but from different generations are only distinguished by their masses. These are free parameters of the SM. Their values can be found in Tab. 2.1 [3].

Particle	Charge [e]	I_3	Mass [MeV]	Source
e	-1	-1/2	0.511	[15]
μ	-1	-1/2	105.7	[15]
τ	-1	-1/2	1776.8	[15]
$\nu_{e,\mu,\tau}$	0	+1/2	< 2 eV	[15]
u	+2/3	+1/2	1.8-3.0	[15]
d	-1/3	-1/2	4.5-5.5	[15]
c	+2/3	+1/2	$1.275(25) \cdot 10^3$	[15]
s	-1/3	-1/2	95(5)	[15]
t	+2/3	+1/2	$173.18(94) \cdot 10^3$	[16]
b	-1/3	-1/2	$4.18(3) \cdot 10^3$	[15]

Table 2.1.: Measurements of the lepton masses. The charges of the particles are shown alongside the third component of the weak isospin, I_3.

2.2. The Fundamental Forces

The interactions between the particles are described by Quantum Field Theories (QFT). The Lagrange density has to be renormalisable and invariant under local gauge transformations. In these quantum field theories, particles are described as fields ψ that are solutions of the Euler-Lagrange equations. The interactions between those fields are mediated by gauge bosons. The Euler-Lagrange equation contains terms for the free particle fields (propagators) as well as for the interations (vertex factors): $\mathcal{L} = \mathcal{L}_{\text{free}} + \mathcal{L}_{\text{interaction}}$. The Feynman rules that can be deduced from the Langrange equations allow to calculate the transition probabilities between two quantum mechanical states using *Fermis Golden Rule*.
The strong theory and the electroweak theory are represented by the gauge groups $SU(3)_C$ and $SU(2)_L \times U(1)_Y$[4], respectively. Since this thesis focuses on the V-A structure of the weak interaction, a small overview of the strong interaction is given in Section 2.2.1, followed by a more detailed discussion of electroweak interactions in Section 2.2.2. Gravity is not included in the SM and will not be discussed in detail. Compared to the other forces, it is by far the weakest. The masses and other properties of the gauge bosons[5] are compared in Tab. 2.2.

[2] Each particle has a corresponding antiparticle with the same mass but opposite charge and hypercharge.
[3] For masses with a very small uncertainty, the uncertainty is not shown.
[4] Where C denotes the colour charge, L the isospin and Y the hypercharge Y = 2 (Q - I_3).
[5] The photon mass has only an upper limit. In the Standard Model, the photon has to be massless.

Force	Gauge boson	Mass [GeV]	Spin	Em. charge [e]	Colour charge
Strong	gluon g	0	1	0	yes
Electromagnetic	photon γ	$< 1{\cdot}10^{-18}$	1	0	no
Weak	Z^0-boson	91.1876(21)	1	0	no
	$W^{\pm}$-bosons	80.385(15)	1	$\pm$ 1	no
Gravity	Graviton G	$< 7{\cdot}10^{-32}$	2	0	no

Table 2.2.: The fundamental forces with their corresponding gauge bosons. The masses of the gauge bosons are taken from Ref. [15]. Gravity is not included in the SM. The Graviton is a hypothetical spin-2 particle and has not been found yet.

2.2.1. The Strong Interaction

The gauge group for the strong interaction is the non-abelian $SU(3)_C$ group. The corresponding Lagrange density[6] is:

$$\mathcal{L}_{SU(3)} = \sum_q \overline{\psi}_{q,a}(i\gamma^\mu \partial_\mu \delta_{a,b} - g_s \gamma^\mu t^C_{ab} A^C_\mu - m\delta_{ab})\psi_{q,b} - \frac{1}{4} F^A_{\mu\nu} F^{\mu\nu}_A \quad . \tag{2.1}$$

The quark spinors are denoted by ψ_q with q being the quark flavour. The gluon fields are identified by $\mathcal{A}_\mu$. The $SU(3)_C$ group has eight generators that are denoted here by $t^C_{ab} = 1/2\lambda^C_{ab}$, where the λ^C_{ab} are the three-dimensional Gell-Mann matrices. The latter part of formula 2.1 contains the field strength tensor of the gauge field:

$$F^{\mu\nu}_A = \partial_\mu A^A_\nu - \partial_\nu A^A_\mu - g_s f_{\mathrm{ABC}} A^B_\mu A^C_\nu \quad . \tag{2.2}$$

The last term in equation 2.2 contains the structure constants of QCD, described by f_{ABC} with:

$$[t^A, t^B] = i f_{\mathrm{ABC}} t^C \quad . \tag{2.3}$$

g_s is related to the strong coupling constant α_s via: $g_s = \sqrt{4\pi\alpha_s}$. The colour charge C is an additional quantum number of the quarks that has been introduced to avoid a violation of the Pauli-principle[7]. The colour charge can take three possible values: *red, green and blue* [8]. The generators of the $SU(3)_C$ gauge group can be identified with eight massless vector bosons, called *gluons*. Since the generators of the $SU(3)_C$ group do not commute, the gluons couple to themselves: In contrast to photons that are mediators of the electromagnetic force without carrying an electric charge themselves, gluons do carry colour charge and therefore couple to other gluons (self-coupling). The coupling constant of the strong interaction, α_s, depends on the energy scale Q^2 [17]:

$$\alpha_s(Q^2) = \frac{12\pi}{(33 - 2n_f)\ln(\frac{Q^2}{\Lambda^2_{\mathrm{QCD}}})} \tag{2.4}$$

where n_f is the number of quark flavours that can be produced at the energy Q^2 ($Q^2 \leq m_q^2$) and the scale Λ_{QCD} which is of $\mathcal{O}(200$ MeV). This formula shows that α_s is small for large energy

[6] Following the notation used in [15], Chapter 9: *Quantum Chromodynamics*, page 1.

[7] The observation of the Δ^{++} resonance (consisting of three up-quarks) would lead to the violation of the Pauli-principle. If the quarks can be distinguished by a different *colour*, the Pauli-principle remains valid.

[8] The antiquarks are then correspondingly antired, antigreen and antiblue.

scales Q^2 and therefore at small distances. This leads to the *confinement* of the quarks, the force between them increases with the distance. When being close to each other, quarks are *asymptotically free* [6].
Since coloured objects cannot be observed it can be assumed that quarks only exist in colour neutral groups of quark-antiquark (mesons) or three quarks (baryons). Only quarks and gluons carry colour charge, therefore the leptons are not taking part in the strong interaction. The strong coupling constant α_s as shown in formula 2.4 dependends on the energy scale Q^2. Usually, it is quoted at m_Z^2. At this energy scale, the number of possible quark flavours is five since all quarks but the top quark can be produced. The corresponding world average yields [15]:

$$\alpha_s(m_Z^2) = 0.1184 \pm 0.0007 \quad . \tag{2.5}$$

2.2.2. The Electroweak Interaction

The unification of the electromagnetic and the weak force was introduced by Glashow, Weinberg and Salam (GWS) [7, 8, 9]. The corresponding gauge group is the $SU(2)_L \times U(1)_Y$ group consisting of the non-Abelian SU(2) and the Abelian U(1) group. It has four generators that lead to four massless fields: W_1^μ,W_2^μ,W_3^μ generated by the weak isospin and B_μ^0 generated by the hypercharge Y. Y is related to the isospin and the electric charge by the Gell-Mann-Nishijima equation[9]:
$Q = I_3 + Y/2$. The bosons, manifesting themselves as physical particles, are a mixture of the massless bosons described above. This results in the following equation for the neutral currents:

$$\begin{pmatrix} Z^0 \\ \gamma \end{pmatrix} = \begin{pmatrix} \cos\theta_W & \sin\theta_W \\ -\sin\theta_W & \cos\theta_W \end{pmatrix} \begin{pmatrix} B^0 \\ W_3^\mu \end{pmatrix} \tag{2.6}$$

with θ_W being the weak mixing angle or *Weinberg angle* that can be expressed using g and g'[10]:

$$\sin\theta_W = \frac{g'}{\sqrt{g^2 + g'^2}} \quad . \tag{2.7}$$

The same holds for the bosons of the charged current interactions:

$$W^\pm = \frac{1}{\sqrt{2}}(W_1^\mu \mp i W_2^\mu) \quad . \tag{2.8}$$

In the electroweak theory, the gauge bosons are massless. Massive gauge bosons would lead to the violation of local gauge invariance. This is in contradiction to the measurements that are listed in Tab. 2.2 that do not only show that some bosons have a non-vanishing mass but that the $W^\pm$- and Z^0-bosons are very massive objects. The concept of mass generation by introducing spontaneous symmetry breaking is explained in the next section.

[9] See for example in [18], p 46.
[10] Here g is the coupling constant of the SU(2) and g' the coupling constant of the U(1) gauge group.

The Weak Interaction

For this thesis, the concepts of *chirality* and *helicity* are important. Chirality (often also called *handedness*) is defined as the eigenvalues of the chirality operator γ^5. A spinor ψ can be written as the sum of a left-handed and a right-handed part:

$$\psi = \psi_{\mathrm{L}} + \psi_{\mathrm{R}} \quad . \tag{2.9}$$

With the definition of the projection operators

$$P_L = \frac{1}{2}(1-\gamma_5) \quad \text{and} \quad P_R = \frac{1}{2}(1+\gamma_5) \quad , \tag{2.10}$$

the left-handed and right-handed parts can be projected out:

$$P_{\mathrm{L}}\psi = \psi_{\mathrm{L}} \quad , \quad P_{\mathrm{R}}\psi = \psi_{\mathrm{R}} \tag{2.11}$$

The eigenvalues of the chirality operator are -1 (left-handed) and +1 (right-handed). In contrast to chirality, helicity is a reference-frame dependent quantity and is defined as the projection of the spin[11] onto the direction of the momentum $\vec{p}$:

$$h = \frac{\vec{\Sigma} \cdot \vec{p}}{|\vec{p}|} \quad . \tag{2.12}$$

Helicity and chirality are only the same for massless particles. Although they are not the same for massive particles, the terms left/right-handed are used in general in helicity studies and will hence be used throughout this thesis. If the spin is parallel to the direction of the momentum, the helicity is positive (right-handed). For an anti-parallel configuration, the helicity is negative (left-handed). If the mass of the neutrinos is assumed to be negligible [12], neutrinos can only have negative helicity and antineutrinos only positive helicity.
In the weak interaction, parity[13] is not conserved. The fermion fields are left-handed isospin doublets or right-handed isospin singlets:

$$\begin{array}{ccc} \begin{pmatrix} \nu_e \\ e^- \end{pmatrix}_L & \begin{pmatrix} \nu_\mu \\ \mu^- \end{pmatrix}_L & \begin{pmatrix} \nu_\tau \\ \tau^- \end{pmatrix}_L \\ e^-_R & \mu^-_R & \tau^-_R \\ \begin{pmatrix} u \\ d' \end{pmatrix}_L & \begin{pmatrix} c \\ s' \end{pmatrix}_L & \begin{pmatrix} t \\ b' \end{pmatrix}_L \\ u_R, d_R & c_R, s_R & t_R, b_R \end{array}$$

The weak interaction only couples to the left-handed doublets (while the right-handed singlets couple also to the electromagnetic interaction). The electroweak eigenstates d', s' and b' are a mixture of the mass eigenstates d, s and b:

$$\begin{pmatrix} d' \\ s' \\ b' \end{pmatrix} = \begin{pmatrix} V_{ud} & V_{us} & V_{ub} \\ V_{cd} & V_{cs} & V_{cb} \\ V_{td} & V_{ts} & V_{tb} \end{pmatrix} \begin{pmatrix} d \\ s \\ b \end{pmatrix} \tag{2.13}$$

[11] $\vec{\Sigma}$ is the spin-operator.
[12] Measurements of the neutrino mass difference squared are summarised in [15] and have shown that the neutrinos do have masses. These masses, however, are very small (see Tab. 2.1) compared the the masses of the charged leptons and of the massive W-boson.
[13] Parity is the transformation that changes the sign of the three dimensional space coordinates.

The matrix shown here is the so-called *Cabibbo-Kobayashi-Maskawa-matrix* (CKM-matrix). The matrix elements of this unitary CKM-matrix have been determined experimentally and the diagonal entries were found being close to one.
For the exchange of a W-boson, the vertex factor can be written as:

$$-\frac{i\, g_{\mathrm{W}}}{\sqrt{2}}\,\gamma^{\mu}\, V_{\mathrm{CKM}}\,\frac{1}{2}(1-\gamma^{5}) \tag{2.14}$$

with the weak coupling constant $g_{\mathrm{W}} = \sqrt{\alpha_{\mathrm{ew}} 4\pi}$. The vertex has hence a V-A (vector - axial vector) structure:

$$\underbrace{\gamma^{\mu}}_{\text{vector coupling}} \quad - \quad \underbrace{\gamma^{\mu}\gamma^{5}}_{\text{axial vector coupling}} \tag{2.15}$$

The test of the (V-A)-structure of the top decay vertex (Wtb-vertex) will be the main topic of this thesis. The experimental realisation of such a test is explained in detail in Chapter 8.

2.2.3. The Higgs Mechanism

The issue of non-vanishing fermion and gauge boson masses is solved by introducing the *Higgs mechanism* which has been formulated by Brout, Englert, Guralnik, Hagen, Higgs and Kibble: [19, 20, 21, 22]. In this theory, a doublet of complex scalar fields ϕ is introduced:

$$\phi = \frac{1}{\sqrt{2}}\begin{pmatrix}\phi_{+}\\ \phi_{0}\end{pmatrix} = \frac{1}{\sqrt{2}}\begin{pmatrix}\phi_{1}+i\phi_{2}\\ \phi_{3}+i\phi_{4}\end{pmatrix} \quad . \tag{2.16}$$

The corresponding Higgs potential is of the form:

$$V(\phi) = \mu^{2}\phi^{\dagger}\phi + \lambda(\phi^{\dagger}\phi)^{2} \tag{2.17}$$

with $\mu^2 < 0$ and $\lambda > 0$, as shown in Fig. 2.2:

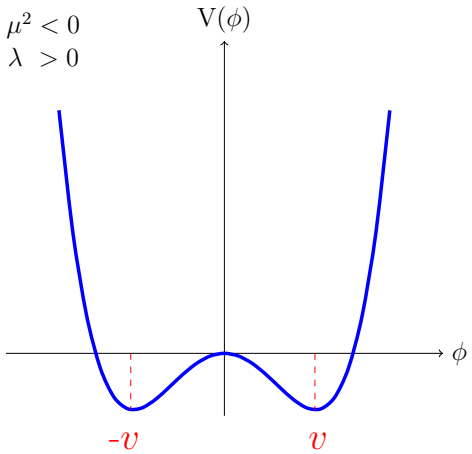

Figure 2.2.: Sketch of the Higgs potential with the parameters $\mu^2 < 0$ and $\lambda > 0$.

With this parameter choice, a non-vanishing vacuum expectation value v exists with $v = \sqrt{-\mu^2/\lambda}$. This leads to the spontaneous breaking of the electroweak symmetry. A new particle, called the *Higgs boson*, occurs with a mass of $m_H = \sqrt{2}\mu$. Furthermore, the $W^{\pm}$- and Z-bosons obtain mass:

$$m_Z = \frac{1}{2}vg \quad \text{and} \quad m_W = \frac{1}{2}v\sqrt{g^2 + g'^2} \quad . \tag{2.18}$$

The fermion masses are generated by the coupling of the fermions to the Higgs field (*Yukawa* coupling). The Yukawa coupling is denoted by λ_f and is related to the fermion masses by:

$$m_f = \frac{1}{\sqrt{2}}\lambda_f v \quad . \tag{2.19}$$

The Yukawa coupling is proportional to the particle mass. Therefore the coupling to the top quark is the largest one. With the vacuum-expectation value calculated from the Fermi coupling-constant G_F[14] taken from [15] and the current world average of the top-quark mass as listed in Tab. 2.1, the top-Higgs Yukawa coupling yields approximately 0.995.
The full Lagrangian of the $\mathrm{SU(2)_L \times U(1)_Y}$ symmetry group can be expressed as the sum of the gauge interactions (containing the gauge self-interaction terms), the fermion term (containing the gauge interaction with the fermion fields), the Higgs term and the Yukawa term of the Higgs-fermion interaction[15] explained above:

$$\mathcal{L}_{\mathrm{SU(2)_L \times U(1)_Y}} = \underbrace{-\frac{1}{4}W_{\mu\nu}W^{\mu\nu} - \frac{1}{4}B_{\mu\nu}B^{\mu\nu}}_{\mathcal{L}_{\mathrm{Gauge}}} + \underbrace{\bar{\psi_L}\gamma^\mu(iD^\mu)\psi_L + \bar{\psi_R}\gamma^\mu(i\partial_\mu - g'\frac{Y}{2}B_\mu)\psi_R}_{\psi\mathcal{L}_{\mathrm{Fermions}}} +$$

$$\underbrace{|(iD^\mu)\phi|^2 - V(\phi)}_{\mathcal{L}_{\mathrm{Higgs}}} - \underbrace{(\lambda_l\bar{\psi_L}\phi\psi_R + \lambda_q\bar{\psi_L}\phi\psi_R + h.c.)}_{\mathcal{L}_{\mathrm{Yukawa}}} \tag{2.20}$$

using the covariant derivative:

$$D^\mu = \partial^\mu + ig\frac{\vec{\tau}}{2}\vec{W}^\mu + ig'\frac{Y}{2}B^\mu \quad , \tag{2.21}$$

with $\vec{\tau}$ being the Pauli matrices. The introduction of spontaneous symmetry breaking therefore allows the fermions and bosons to have mass without violating gauge invariance. Although the Higgs mechanism has been formulated in the early 1960ies it took up to summer 2012 until the discovery of a Higgs-like boson could be announced. The searches at the LHC will be discussed in more detail in the following subchapter.

[14] $G_F = (\sqrt{2}v^2)^{-1}$
[15] The terms λ_l and λ_q describe the Yukawa couplings for leptons and quarks, respectively.

2.2.4. Higgs Searches at the LHC

Over the last decades, the search for the elusive Higgs boson has been continued with increasing effort and more and more stringent limits have been set on its mass. While an upper limit on the Higgs mass ($m_H < 158$ GeV at 95% C.L. was set from precision electroweak measurements [23]) and the results from LEP provided a lower limit ($m_H > 114.4$ GeV @ 95% C.L. [24]), the Tevatron collider provided additional limits [25]. Furthermore, the results from the Tevatron collider presented in Summer 2012 also showed an excess of events in the mass range of 115-135 GeV with a corresponding significance of 2.5σ [25]. In the production in association with a weak boson and in the decay into two b-quarks, the global significance amounts to 3.1σ [26].
In the mass regime accessible with the LHC, the Higgs boson decays predominantly into a $b\bar{b}$ or a WW-pair. In addition to these channels, searches have been perfomed in the $H \to \tau^+\tau^-$, $H \to ZZ$ and $H \to \gamma\gamma$ channels. The latter channel has a relatively small branching ratio but has, as the decay into two Z bosons, a very clean signal.
The ATLAS and CMS experiments both reported in July 2012 the observation of a new boson, consistent with the Standard Model Higgs boson [10, 11]. Both experiments combined the data collected at 7 and 8 TeV with an integrated luminosity of up to 5 and 6 fb^{-1}, respectively. The searches were conducted in several channels and updated with more data collected at 8 TeV recently (see Fig. 2.3 (left) and 2.4). The excess observed by ATLAS has a significance of 7.0σ [27].

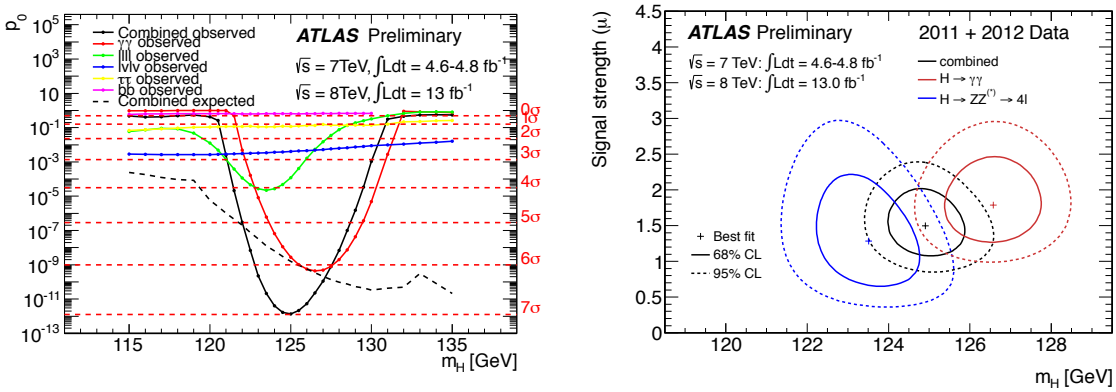

Figure 2.3.: Combination of the Higgs result for 7 and 8 TeV data performed at ATLAS. The significance of the separate channels as well as the combined significance is shown in the left plot. The right plot shows the masses extracted from the $H \to \gamma\gamma$ and $H \to ZZ$ channels as well as their combination. The mass difference shown has a significance of 2.7σ [27].

Having the best mass resolution, the Higgs mass is extracted from the H$\to \gamma\gamma$/ZZ channels both in ATLAS and CMS. The ATLAS results in these channels show a mass difference of about 3.0 GeV [27][16]. The separate results as well as the combination is shown in Fig. 2.3b. The combined mass is:

$$m_H = 125.2 \ \pm \ 0.3 \text{ (stat.)} \ \pm \ 0.6 \text{ (syst.) GeV} \tag{2.22}$$

[16] This result has a significance of 2.7 σ.

which is consistent with the result from CMS [28]:

$$m_{\mathrm{H}} = 125.8 \ \pm \ 0.4 \ (\mathrm{stat.}) \ \pm \ 0.4 \ (\mathrm{syst.}) \ \mathrm{GeV} \quad . \tag{2.23}$$

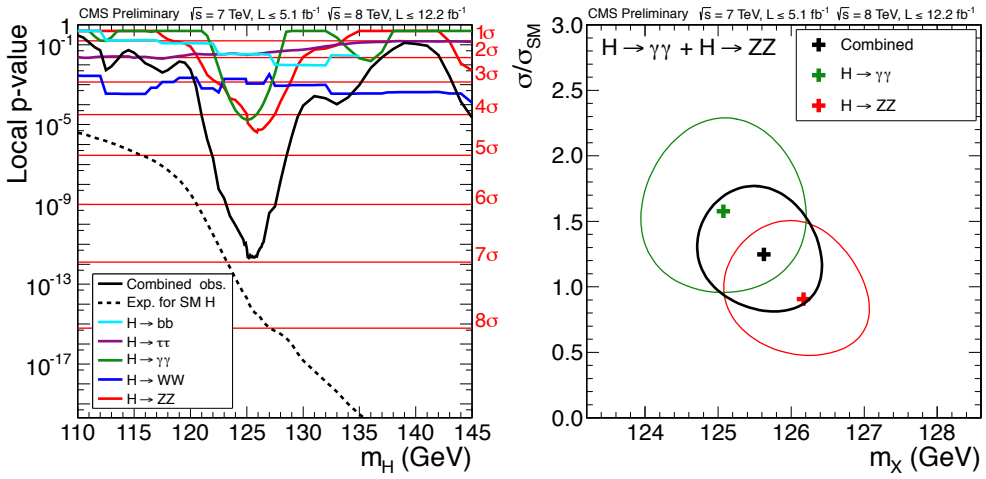

Figure 2.4.: Combination of the Higgs result for 7 and 8 TeV data performed at CMS. The significance of the separate channels as well as the combined significance is shown in the left plot. The right plot shows the different masses extracted from the $H \to \gamma\gamma$ and $H \to ZZ$ channels as well as their combination. The masses from the two channels are in good agreement [28].

Apart from the measured mass, further properties are studied. The decay of the Higgs boson into two photons excludes the spin-1 hypothesis (Landau-Yang theorem [29, 30]). Furthermore the Higgs is found to have positive parity and to favour the spin-0 over the spin-2 hypothesis [31] (although the spin-2 hypothesis has not been fully excluded yet). Furthermore, decaying into particles with the overall charge of zero, the Higgs-like boson is expected to have zero charge.

2.2.5. Open Questions in the Standard Model

Although the Standard Model has been proven to be a very successful theory, a multitude of open questions remain unanswered. First of all, the SM only describes $\mathcal{O}(5\ \%)$ of the energy density in the Universe. The dark matter could be explained by the existence of a weakly interacting massive particle. So far, the SM it does not provide such a candidate particle. Another weak point of the SM is the fact that there is no theory for a unification of the strong and the electroweak force. This problem could be solved by an extension of the SM with Supersymmetric Particles. In the Minimal Supersymmetric Standard Model (MSSM) [32], each fermion has a boson as supersymmetric partner and each boson is associated with a supersymmetric fermion. These additional particles would allow the unification of the electroweak and the strong interaction at a certain energy scale. In addition, the MSSM would provide a dark-matter candidate, called *neutralino*. Moreover, gravity has not been included in the SM so far. Further beyond SM processes will be discussed in the next Chapter in the context of the Wtb-vertex. Furthermore, model-independent extensions to the SM Lagrangian are introduced.

3. The Top Quark and Its Properties

The top-quark, predicted already in 1977 as the electroweak isospin partner of the b-quark, was discovered in 1995 by the CDF and DØ collaborations [33, 34] in 1.8 TeV proton-antiproton collisions at the Tevatron collider located at Fermilab, Illinois.
It is the heaviest known elementary particle to date with a current world average mass[1] of $m_{top} = 173.18 \pm 0.56$ (stat.) $\pm$ 0.75 (syst.) GeV [16]. Having a mass close to the scale of electroweak symmetry breaking ($v = 246$ GeV), its properties may be able to open a window to processes beyond the SM. Being by far the heaviest fermion, it has the strongest coupling to the SM Higgs field and consequently the largest Yukawa coupling as discussed in Chapter 2.2.3. Moreover, it has a very short lifetime that does not allow for the top-quark to form bound states with other particles (see Chapter 3.4). This unique feature allows to study the top-quark as a *bare* quark that transfers its properties directly to its decay products.

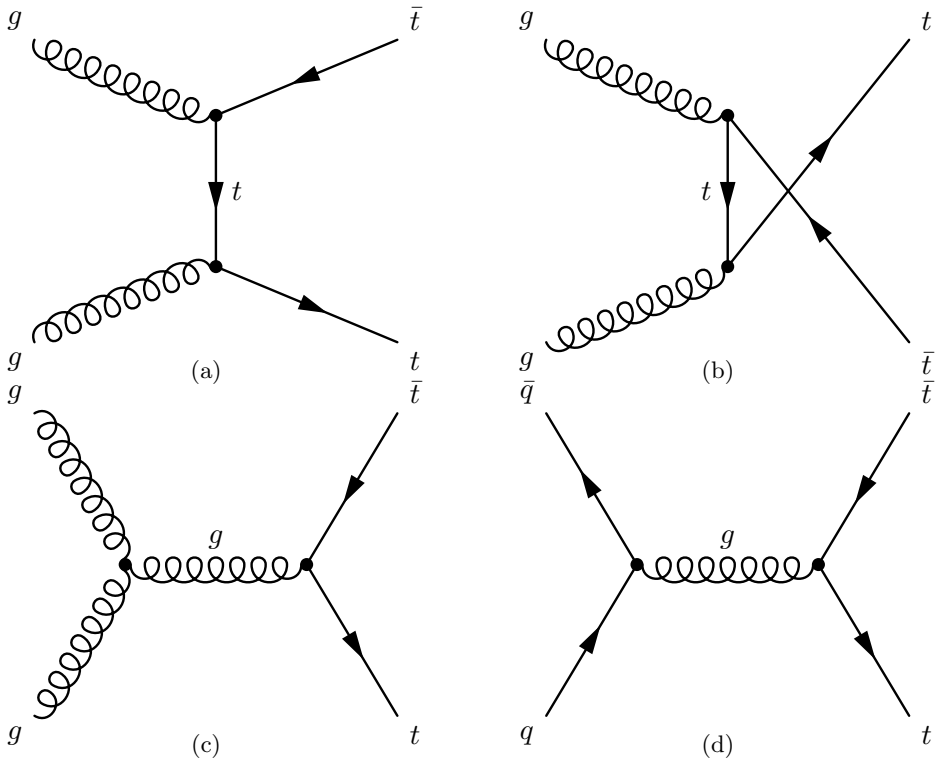

Figure 3.1.: Leading order Feynman diagrams for top-quark pair production in pp collisions. Fig. (a-c) show the top-quark pair production via gluon-gluon fusion, while Fig. (d) shows the production via quark-antiquark annihilation.

[1] This combination contains Tevatron results only.

In the first two sections, the production mechanisms of top-quark pairs as well as single top-quarks are presented, followed by a discussion of the corresponding decay channels. Finally, the unique properties of the top-quark are presented with a focus on the (V-A) nature of the Wtb-vertex structure.

3.1. Top-Quark Pair Production

At the LHC, the dominant production process of the top-quark is top-quark pair production via the strong interaction. As shown in the leading order (LO) Feynman diagrams in Fig. 3.1, top-quark pairs can be produced via gluon-gluon fusion (Fig. 3.1 a-c) or via quark-antiquark annihilation (Fig. 3.1 d). The cross section via quark-antiquark annihilation is low since the only source of antiquarks is the quark sea of the proton.
The production cross section can be written using the factorisation theorem as follows[2]:

$$\sigma^{pp\to X}(p_1,p_2) = \sum_{i,j} \int dx_1 dx_2 f_i(x_1,\mu_{\mathrm{F}}^2) f_j(x_2,\mu_{\mathrm{F}}^2) \hat{\sigma}_{i,j}(p_1,p_2,\alpha_s(\mu_{\mathrm{R}}^2),\mu_{\mathrm{R}}^2) \tag{3.1}$$

while taking the sum over all partons i,j with μ_{F} being the factorisation and μ_{R} the renormalisation scale, respectively. To cancel out ultraviolet divergencies at higher order, the theory has to be renormalised at a certain scale. In top-quark analyses, μ_F and μ_R are often set to the top-quark mass. The short distance cross section $\hat{\sigma}_{i,j}$ can be calculated using perturbation series in orders of α_s. Each quark or gluon inside the proton carries a certain fraction of the proton momentum. These momentum fractions are denoted by x_1 and x_2. The probability for a parton to carry a certain value x_i of the proton momentum has to be taken into account. This is described by the parton density functions (PDFs) f_i,f_j. These functions cannot be calculated analytically but have to be measured in data, for example in ep collisions (HERA), $p\bar{p}$ collisions (Tevatron) or in pp collisions at the LHC. The PDFs used for the analyses are provided by different collaborations, such as CTEQ [35], MSTW [36] or NNPDF [37]. Examples for PDFs at a certain scale Q are shown in Fig. 3.2.

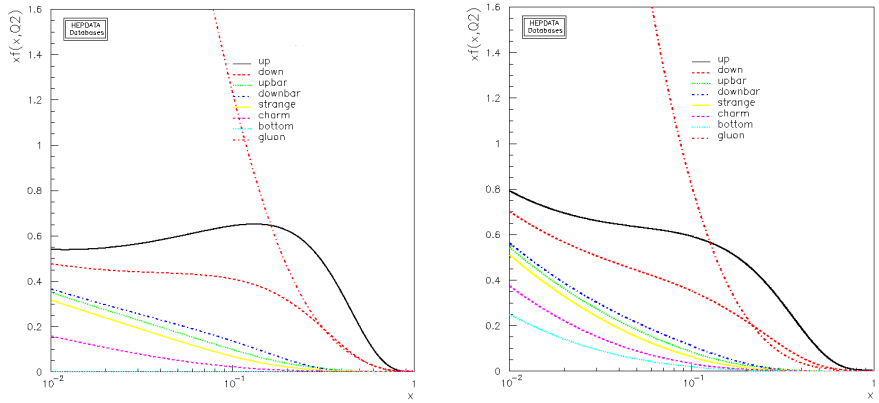

Figure 3.2.: Parton density functions for Q equals to the b-quark mass (left) and to the top-quark mass (right) obtained from the CT10 PDF set [35].

[2] See for example in [17], page 238.

The production cross section for top-quark pairs depends on the centre-of-mass energy $\sqrt{s}$ of the colliding protons. The interacting partons have a much smaller centre-of-mass energy:

$$\sqrt{s_{\text{eff}}} = \sqrt{x_1 x_2 s} \quad , \tag{3.2}$$

where x_1 and x_2 are the proton momentum fractions for parton 1,2 respectively. In order to produce a top-antitop pair, the centre-of-mass energy of the partons has to be at least as large as twice the top-quark mass. If the assumption $x_1 = x_2 = x$ is made, this leads to:

$$x \leq \frac{2m_{\text{top}}}{\sqrt{s}} \quad . \tag{3.3}$$

For the $t\bar{t}$-production at threshold, the proton momentum fraction at the LHC has to be at least $x = 0.05$ (Tevatron Run II: $x = 0.18$).
The top-quark pair cross section combination for $\sqrt{s} = 7$ TeV data using both ATLAS and CMS results reads [38]:

$$\sigma_{t\bar{t}} = 173.3 \ \pm \ 2.3 \ (\text{stat.}) \ \pm \ 9.8 \ (\text{syst.}) \ \text{pb}. \tag{3.4}$$

The ATLAS results from different channels are shown in Fig. 3.3. The measurements for the 7 and 8 TeV data are shown in Fig. 3.3 (right) as well as the results from CDF and DØ at 1.8 and 1.98 TeV. The comparison with the predicted values shows that the measurements are in agreement with the SM predictions. The theoretical production cross-section for $t\bar{t}$-events at $\sqrt{s} = 7$ TeV is calculated using HATHOR [39] at approximate NNLO precision[3] to $166.78^{+16.5}_{-17.8}$ pb.

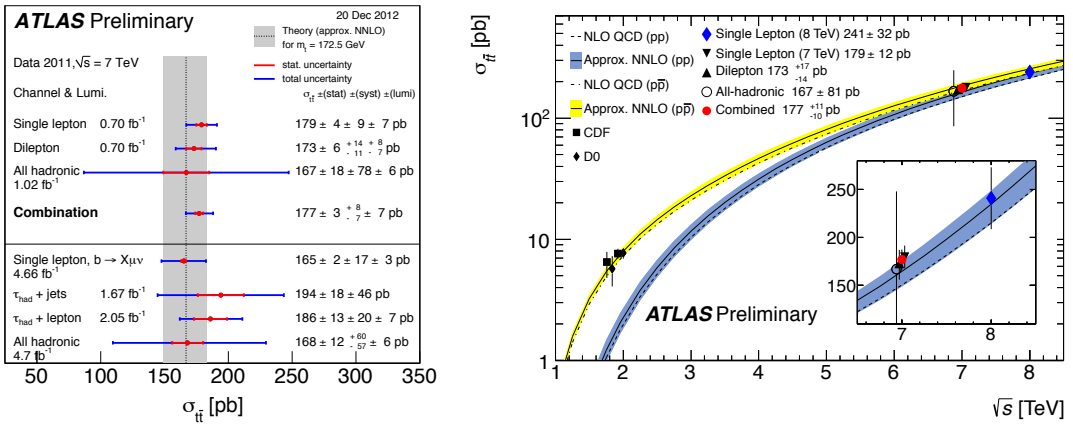

Figure 3.3.: Top-quark pair cross section measurements at ATLAS [40]. Left: Measurements at $\sqrt{s} = 7$ TeV in the lepton+jets, dilepton and all hadronic channels. Right: Cross section measurements from ATLAS at 7 and 8 TeV as well as the cross section measurements from CDF and DØ at 1.8 and 1.98 TeV.

[3] The top-quark mass is set to $m_{top} = 172.5$ GeV.

3.2. Single Top Quark Production

In addition to the production process shown in the previous section, top-quarks can also be produced as single top-quarks via the weak interaction. The production of single tops has been first observed in 2009 by the CDF and DØ collaborations [41, 42]. Three different production mechanisms exist and their corresponding Feynman diagrams are shown in Fig. 3.4: The t-channel production of a top-quark and a light quark, the s-channel production of a top and a bottom-quark as well as the associated production of a top-quark and an on-shell W-boson. Evidence for the associated production was found recently both at ATLAS [43] and CMS [44]. There are two main reasons for this late discovery of single top-quarks (14 years after the first top observation): The production rate is smaller than the one for $t\bar{t}$-production, albeit only a factor of two. Single top events have a lower jet-multiplicity and therefore suffer from large background rates. Predictions[4] for the cross sections are compared with the recent ATLAS results in Tab. 3.1. Due to the V-A structure of the Wtb-vertex, single top-quarks are produced fully polarised.

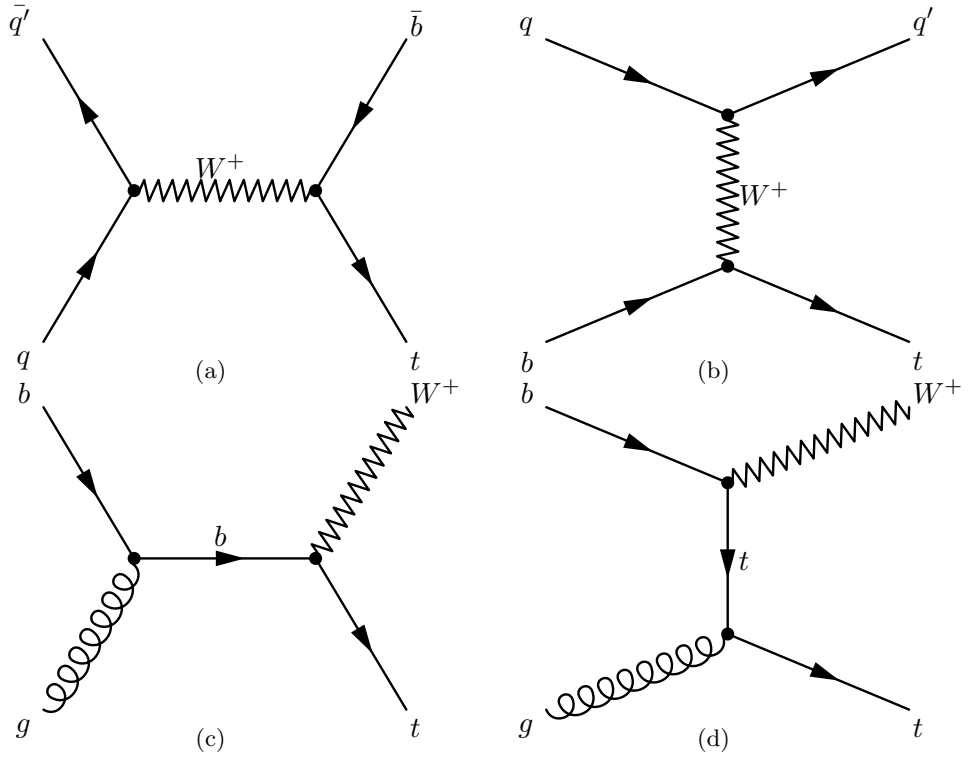

Figure 3.4.: Leading order Feynman diagrams for single top quark production in pp collisions. Figures (a) and (b) show the s- and t-channel production, respectively. Figures (c) and (d) show the production of a single top in association with a W-boson.

The measurement of the single top production rate also allows for a direct measurement of the CKM matrix element V_{tb}. It has been extracted from the t-channel and Wt-channel cross section by comparing the measured cross section to the theoretical value (see Tab. 3.1):

$$|V_{\mathrm{tb}}|^2 = \frac{\sigma_{\mathrm{meas.}}}{\sigma_{\mathrm{theory}}} \quad . \tag{3.5}$$

[4] Theoretical cross sections have been obtained using a top-quark mass of $\mathrm{m_{top}} = 172.5$ GeV.

Assuming the off-diagonal entries $|V_{td}|$ and $|V_{ts}|$ are small compared to $|V_{tb}|$, the coupling strength at the Wtb vertex yields [45]:

$$|V_{tb}| = 1.13^{+0.14}_{-0.13} \quad \text{(t-channel)} \tag{3.6}$$

and [43]:

$$|V_{tb}| = 1.03^{+0.16}_{-0.19} \quad \text{(Wt-channel)} \quad . \tag{3.7}$$

For the SM assumption of $|V_{tb}| \leq 1$, a lower limit is set using the t-channel result [45]:

$$|V_{tb}| > 0.75 \quad \text{at 95 \% C.L.} \tag{3.8}$$

Channel	$\int dt\mathcal{L}$ [fb^{-1}]	σ_{theory} [pb]	$\sigma_{\text{meas.}}$ [pb]
t-channel (t)	4.7	$41.9^{+1.8}_{-0.8}$ [46]	53.2 ± 10.8 [47]
t-channel ($\bar{t}$)	4.7	$22.7^{+0.9}_{-1.0}$ [46]	$29.5^{+7.4}_{-7.5}$ [47]
total t-channel	1.04	$64.6^{+2.7}_{-2.0}$ [46]	83 ± 20 [45]
Wt-channel	2.05	15.7 ± 1.1 [48]	16.8 ± 5.7 [43]
s-channel	0.7	4.6 ± 0.2 [49]	< 20.5 pb @ 95% C.L. [50]

Table 3.1.: Measurements of the single top-quark cross sections for the separate t-channels, the total t-channel, the s-channel and the associated production performed at ATLAS using 7 TeV data. The measured cross sections are compared to their predicted values which have been evaluated for a top-quark mass of 172.5 GeV.

3.3. Top-Quark Decay

As shown in the previous subchapter, the CKM matrix element $|V_{tb}|$ is close to unity, therefore the top-quark decays almost exclusively into a W-boson and a b-quark. The different decay channels are hence characterised by the decay channels of the W-boson (see Tab. 3.2), which decays either leptonically into a charged lepton and its corresponding neutrino or into two quarks $q\bar{q}'$.

Process	Branching ratio [%]
$W \to q\bar{q}'$	67.60 ± 0.27
$W \to e\bar{\nu}_e$	10.75 ± 0.13
$W \to \mu\bar{\nu}_\mu$	10.57 ± 0.15
$W \to \tau\bar{\nu}_\tau$	11.25 ± 0.20
$\tau \to e\bar{\nu}_e\nu_\tau$	17.83 ± 0.04
$\tau \to \mu\bar{\nu}_\mu\nu_\tau$	17.41 ± 0.04

Table 3.2.: Branching ratios of the W-boson, which decays either into two quarks or two leptons. Leptonically decaying τ-leptons are considered to be part of the lepton+jets channel. The values are taken from [15].

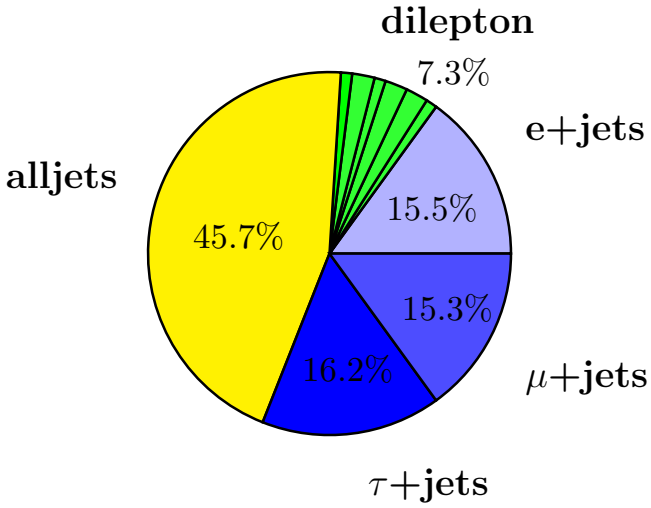

Figure 3.5.: The decay channels of $t\bar{t}$ events: the all jets (fully hadronic), the dilepton and the lepton+jets channel. The lepton+jets channel comprises the e+jets and μ+jets channel as well as τ+jets events with an electron or muon in the final state.

Therefore one can distinguish three different decay channels for the top-quark:

a) The channel with both W-bosons decaying hadronically is called the *all hadronic* or *all jets channel*. It has the largest branching ratio as shown in Fig. 3.5, but suffers from the large background contamination from QCD multijet production.

b) The channel with both W-bosons decaying leptonically is called the *dilepton channel*. It has the smallest branching ratio of all decay channels. Furthermore, the event reconstruction for the dilepton channel is more complex since the kinematics are underconstrained due to two undetectable neutrinos which contribute to the missing transverse energy.

c) In the *lepton+jets channel* one W-boson decays hadronically and the other decays leptonically. It is often called the *golden channel* due to its relatively high branching ratio and comparatively small background contamination. Although τ+jets events are shown as a part of the lepton+jets channel in Fig. 3.5, only leptonically decaying τ+jets events are considered for the analysis.

This analysis is performed in the lepton+jets channel. The signature in the detector is characterised by four high-p_{T} jets, one isolated high-p_{T} lepton and missing transverse energy due to the undetectable neutrino. Only events with an electron or muon in the final state are considered in the lepton+jets channel, therefore lepton+jets events with a hadronically decaying τ-lepton are not part of the signal.

3.4. Top-Quark Properties

As already mentioned in the introduction, the top quark is the heaviest particle known today. The current world average mass amounts to [16]:

$$m_{\text{top}} = 173.18 \pm 0.56 \text{ (stat.)} \pm 0.75 \text{ (syst.) GeV} \quad , \tag{3.9}$$

whereas the LHC combination in 7 TeV collision data yields [51]:

$$m_{\text{top}} = 173.3 \pm 0.5 \text{ (stat.)} \pm 1.3 \text{ (syst.) GeV} \quad . \tag{3.10}$$

Since the top quark mass is close to the scale of electroweak symmetry breaking, it can be used to investigate the SM predictions in less tested mass ranges and is believed to play an important part in beyond the SM (BSM) scenarios. However, all measurements so far are in good agreement with the predictions made by the SM.

BSM processes could show up in the production process as well as in the decays of top-antitop pairs. Since top-quarks are short-lived with $\tau_{\text{top}} = (3.3^{+1.3}_{-0.9}) \cdot 10^{-25}$ sec [15], they decay before any hadronisation process can take place: $\tau_{\text{hadr.}} = \mathcal{O}(10^{-23})$ sec. Hence their properties, such as charge, spin or polarisation are directly transferred to the decay products.
The top quark pair is produced unpolarised at tree-level[5] but their spins are predicted to be correlated [54, 55, 56]. This correlation has been recently observed by ATLAS using a dataset of 2.1 fb^{-1} of 7 TeV collision data in the dilepton channel [57]. CMS performed a similar measurement in the dilepton channel, using 5.0 fb^{-1}[58]. Both results are in full agreement with the SM predictions.
In order to analyse the spin of the top-quarks, the final state particles (charged leptons or down-type quarks) are used. The charged lepton is also used to analyse the decay vertex Wtb and to test its structure. This is the topic of this thesis. Therefore the properties of the Wtb vertex and useful observables are introduced, followed by a discussion of previous measurements and effective Lagrange densities that describe possible anomalous couplings.

3.4.1. The Structure of the Wtb Vertex

As shown in Chapter 2.2.2, the vertex factor for the weak charged current has the following form:

$$\frac{-ig_W}{2\sqrt{2}}\gamma^\mu(1-\gamma^5) \quad . \tag{3.11}$$

It has a vector (γ^μ) minus axial-vector ($\gamma^\mu\gamma^5$) form that is often called (V-A) structure. The term $\frac{1}{2}(1-\gamma^5)$ was already introduced in Chapter 2.2.2, as the projection operator $\mathrm{P_L}$. This means that the vertex for weak charged currents only couples to left-handed particles or right-handed antiparticles. The full matrix element for the top-quark decay is:

$$i\mathcal{M} = i|V_{tb}|\frac{g_W}{\sqrt{2}}\,\bar{b}\,\gamma^\mu\,P_L\,t\,\epsilon^W \quad . \tag{3.12}$$

[5] The top-pair polarisation has been recently measured by ATLAS [52] and CMS [53] and no deviation from the SM predictions has been observed.

W-boson polarisation

The massive W^+-boson that originates from a top-quark decay can be either left-handed, right-handed or longitudinally polarised. This is shown in Fig. 3.6: If the spin of the W$^+$-boson (indicated by the small arrows) is parallel to its direction of motion (large arrows) it is called right-handed, and left-handed for an anti-parallel configuration.

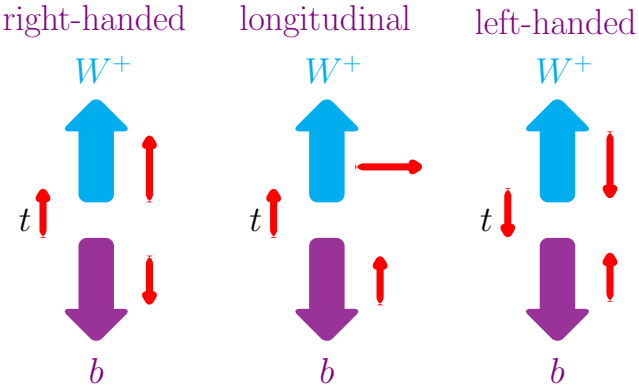

Figure 3.6.: Decay of the top quark into a W^+-boson and a b-quark in the top quark rest frame. The large arrows represent the momentum of the particles and the small arrows the spin. The probability for the top-quark to decay into a right-handed W^+-boson is suppressed by the ratio $m_\mathrm{b}^2/m_\mathrm{top}^2$.

The corresponding fractions are calculated as the ratio of the relative decay width to the total width:

$$F_i = \frac{\Gamma_i}{\sum_{k=0,L,R}\Gamma_k} \quad \text{with } i = 0, L, R. \tag{3.13}$$

The total decay width is calculated by applying *Fermis golden rule* and using the matrix element from Eq. 3.12:

$$\Gamma = \frac{2\pi}{\hbar}\int |\mathcal{M}|^2 d\phi \quad . \tag{3.14}$$

Taking the spins of the initial and final states into account and assuming the b-quark mass to be negligible, this results in[6]:

$$\Gamma = \frac{G_F}{8\sqrt{2}\pi}\, m_\mathrm{top}^3\, |V_{tb}|^2\, (1-x^2)^2(1+2x^2) \quad , \tag{3.15}$$

using the substitution $x = m_\mathrm{W}/m_\mathrm{top}$. When decomposing the last terms, the expression can be written as:

$$\Gamma = \frac{G_F}{8\sqrt{2}\pi}\, m_\mathrm{top}^3\, |V_{tb}|^2\, [\underbrace{(1-x^2)^2}_{\hat{\Gamma}_0} + \underbrace{2x^2(1-x^2)^2}_{\hat{\Gamma}_L}] \quad , \tag{3.16}$$

[6] Using $g_W^2 = 4\sqrt{2}G_F m_W^2$

where the first term describes longitudinally polarised W-bosons and the second part the left-handed W-bosons. Using the expression for x, one can see that Γ_0 is proportional to m_{top}^3 whereas F_{L} only increases linearly with the top quark mass. The direct comparison shows:

$$F_0 : F_L : F_R = \frac{1}{1+2x^2} : \frac{2x^2}{1+2x^2} : 0 \quad . \tag{3.17}$$

This enhancement of longitudinally polarised W-bosons is founded in the *Goldstone boson equivalence theorem* [59, 60]. This theorem states that, at high energies, the probability of the emission (absorption) of a longitudinally polarised gauge boson is the same as the probability to emit (absorb) the corresponding Goldstone boson [7].

Taking now into account also the b-quark mass, the total decay width can be expressed as (taken from [62]):

$$\Gamma = \frac{G_F\, m_W^2\, m_{top}}{8\sqrt{2}\pi}\, |V_{tb}|^2\, \sqrt{\lambda}\, \frac{(1-y^2)^2 + x^2(1-2x^2+y^2)}{x^2} \quad . \tag{3.18}$$

Using the expressions $y = m_b/m_{\text{top}}$ and $\lambda = 1 + x^4 + y^4 - 2x^2y^2 - 2x^2 - 2y^2$, the helicity fractions can be expressed in leading order as [62]:

$$\begin{aligned}
F_0 &= \frac{(1-y^2)^2 - x^2(1+y^2)}{(1-y^2)^2 + x^2(1-2x^2+y^2)} \ , \\
F_{\text{L}} &= \frac{x^2(1-x^2+y^2+\sqrt{\lambda})}{(1-y^2)^2 + x^2(1-2x^2+y^2)} \ , \\
F_{\text{R}} &= \frac{x^2(1-x^2+y^2-\sqrt{\lambda})}{(1-y^2)^2 + x^2(1-2x^2+y^2)} \\
&= y^2 \frac{2x^2}{(1-x^2)^2(1+2x^2)} + ...
\end{aligned} \tag{3.19}$$

The right-handed component is suppressed by m_b^2/m_{top}^2. In the limit of a vanishing b-quark mass, right-handed b-quarks are forbidden. Using the current measurements of $m_{\text{top}} = 173.18(94)$ GeV [16], $m_{\text{W}} = 80.385(15)$ GeV [15] and the b-quark pole mass $m_{\text{b}} = 4.65(3)$ GeV [15], the helicity fractions in LO amount to:

$$\begin{aligned}
F_0 &= 0.698 \ , \\
F_{\text{L}} &= 0.301 \ , \ , \\
F_{\text{R}} &= 0.0004 \quad .
\end{aligned}$$

A deviation from the values predicted by the SM can have several reasons. For vanishing b-quark mass, F_0 and F_{L} both change about 0.09% and the effect on F_{R} is even smaller. Therefore the dependence on the b-quark mass is tiny. Furthermore, the fractions could be altered by gluon radiation. The radiative corrections are $\mathcal{O}(\alpha_s) \approx$ 1-2 % for F_0 and F_{L} and smaller for F_{R} [62].

[7] More detailed explanations can be found in [61], p.743 ff.

There are several BSM models on the market that would explain the observation of sizable V+A contributions to the Wtb vertex. Since for the underlying analysis a model-independent approach was chosen to search for non-SM couplings, these models will not be discussed here in detail. Models like top-color assisted technicolor (TC2) [63], the minimal supersymmetric standard model (MSSM) [32] or a two-Higgs doublett model (2HDM) can alter the Wtb-vertex [64]. In the TC2 model, additional heavy particles (three top pions and a top-Higgs) are predicted. These particles can show up in loop corrections to the Wtb-vertex, which would lead to an enhanced contribution to F_{R}. In the 2HDM, the Higgs sector is extended to a total of five Higgs bosons (including two charged Higgs). In the case of lighter charged Higgs bosons, the top-quark could decay via $t \to H^+ b$ which would lead again to an alteration of the measured W-helicity fractions compared to the predicted values. Both models, however, would only have small contributions of $\mathcal{O}(1\ \%)$ or smaller [65].

To be able to draw conclusions on new physics models, the helicity fractions have to be known at higher order and large precision. Including corrections of $\mathcal{O}(\alpha_s^2)$ and leading electroweak corrections, the NNLO prediction can be performed with a relative precision of $\mathcal{O}(1\%)$ [66]:

$$\begin{aligned} F_0 &= 0.687(5) \ , \\ F_{\mathrm{L}} &= 0.311(5) \ , \\ F_{\mathrm{R}} &= 0.0017(1) \ . \end{aligned}$$

The charged lepton from the leptonic W-decay is used to analyse the W-boson polarisation. Several observables have been used in the past years. The first results from CDF in Run II have been obtained using the transverse momentum of the charged lepton [67]. Since a right-handed W-boson emits the charged lepton preferably into the direction of its momentum vector, while a left-handed W-boson emits the lepton in the opposite direction, lepton-p_{T} spectrum of left-handed W-bosons is much softer than the one of the right-handed ones. Another variable is the invariant mass of the lepton and the b-quark, m_{lb}^2, which has been used in CDF in Run I and II [68, 69]. This observable is correlated with the angular distribution of the charged lepton:

$$m_{lb}^2 \approx 2E_l E_b(1 - \cos\theta_{lb}) \ . \tag{3.20}$$

The angular distribution of the charged lepton, $\cos\theta^*$, has been used in most of the analyses performed at CDF and DØ [8], but also for the first measurements at ATLAS and CMS. As shown in Fig. 3.7a, θ^* is defined as the angle between the charged lepton and the negative direction of the b-quark in the W-boson rest frame. Fig. 3.7b shows the distribution for the left-handed (dotted line), right-handed (dashed line) and longitudinal distribution (solid line), which gives a good separation power between the three helicity states. The distributions can be parameterised as follows:

$$\frac{1}{\Gamma}\frac{d\Gamma}{d\cos\theta^*} = \frac{3}{8}(1+\cos\theta^*)^2 F_{\mathrm{R}} + \frac{3}{8}(1-\cos\theta^*)^2 F_{\mathrm{L}} + \frac{3}{4}\sin^2\theta^* F_0 \ . \tag{3.21}$$

An integration over $\cos\theta^*$ leads to:

$$1 = F_{\mathrm{R}} + F_{\mathrm{L}} + F_0 \ . \tag{3.22}$$

[8] Since the up and down type quarks cannot be easily distinguished experimentally, for the hadronically decaying W-boson the absolute value of $\cos\theta^*$ was used.

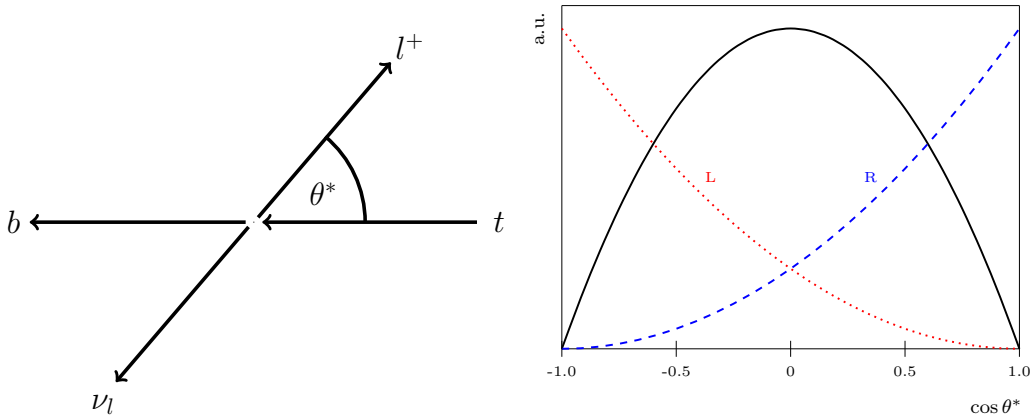

(a) (b)

Figure 3.7.: Left: The $\cos\theta^*$ variable defined as the angle between the charged lepton and the negative direction of the b-quark in the W-boson rest frame. Right: The angular distribution of the charged lepton in arbitrary units. The distributions are different for left-handed (dotted line), right-handed (dashed line), and longitudinally polarised W-bosons (solid).

3.4.2. Previous Measurements

The tables 3.3 and 3.4 compare the most precise results of ATLAS, CDF, CMS and DØ as well as the combination of the Tevatron results for a simultaneous measurement of the three W-helicity fractions (Tab. 3.3) and the measurements assuming Standard Model fractions ($F_{\mathrm{R}} = 0$, Tab. 3.4), respectively. The most precise results are obtained by the combination of two lepton+jets and two dilepton analyses performed at the ATLAS experiment. For the results used for the combination, two different analysis strategies were followed: For the first approach, the angular asymmetries are measured as defined in [70, 71]:

$$A_{\pm} = \frac{N(\cos\theta^* > z) - N(\cos\theta^* < z)}{N(\cos\theta^* > z) + N(\cos\theta^* < z)} \quad , \tag{3.23}$$

with $z = \pm(1 - 2^{2/3})$. For the forward-backward asymmetry ($z = 0$), A can be expressed by the W-helicity fractions:

$$A_{FB} = \frac{3}{4}(F_R - F_L) \quad . \tag{3.24}$$

The angular asymmetries can then be translated into the W-helicity fractions, using $\beta = 2^{\frac{1}{3}} - 1$:

$$\begin{aligned} F_0 &= -\frac{1+\beta}{1-\beta} + \frac{A_+ - A_-}{3\beta(1-\beta)} \quad , \\ F_{\mathrm{L}} &= \quad \frac{1}{1-\beta} - \frac{A_+ - \beta A_-}{3\beta(1-\beta^2)} \quad , \\ F_{\mathrm{R}} &= \quad \frac{1}{1-\beta} + \frac{A_- - \beta A_+}{3\beta(1-\beta^2)} \quad . \end{aligned} \tag{3.25}$$

For the second analysis[9], a template method was used to fully exploit the shape of the angular distribution. For the final result, the four measurements were combined using the BLUE [72, 73] method.

Experiment	$\sqrt{s}$ [TeV]	$\int dt\mathcal{L}$ [fb^{-1}]	Channel	Fraction	F $\pm$ stat. $\pm$ syst.	Ref.
ATLAS comb.	7	1.04	l+jets / dilepton	F_0	$0.67 \pm 0.03 \pm 0.06$	[3]
				F_R	$0.01 \pm 0.01 \pm 0.04$	
CMS	7	2.2	μ+jets	F_0	$0.57 \pm 0.07 \pm 0.05$	[74]
				F_R	$0.04 \pm 0.04 \pm 0.04$	
CDF	1.96	5.1	dilepton	F_0	$0.71^{+0.18}_{-0.17} \pm 0.06$	[75]
				F_R	$-0.07 \pm 0.09 \pm 0.03$	
CDF	1.96	8.7	l+jets	F_0	$0.73 \pm 0.07 \pm 0.07$	[76]
				F_R	$-0.05 \pm 0.04 \pm 0.06$	
DØ comb.	1.96	5.4	l+jets / dilepton	F_0	$0.67 \pm 0.08 \pm 0.07$	[77]
				F_R	$-0.02 \pm 0.04 \pm 0.03$	
Tevatron comb.	1.96	2.7-5.4	l+jets / dilepton	F_0	$0.72 \pm 0.06 \pm 0.05$	[78]
				F_R	$-0.03 \pm 0.03 \pm 0.03$	

Table 3.3.: Summary of previous measurements of the W-boson polarisation. In all results, simultaneous measurements of the three helicity fractions have been performed.

Experiment	$\sqrt{s}$ [TeV]	$\int dt\mathcal{L}$ [fb^{-1}]	Channel	Fraction	F_0 $\pm$ stat. $\pm$ syst.	Ref.
ATLAS	7	1.04	l+jets / dilepton	F_0	$0.66 \pm 0.03 \pm 0.04$	[3]
CMS	7	2.2	μ+jets	F_0	$0.64 \pm 0.03 \pm 0.05$	[74]
CDF	1.96	5.1	dilepton	F_0	$0.56 \pm 0.09 \pm 0.06$	[78]
CDF	1.96	8.7	l+jets	F_0	$0.69 \pm 0.04 \pm 0.04$	[76]
DØ comb.	1.96	5.4	l+jets / dilepton	F_0	$0.71 \pm 0.04 \pm 0.05$	[77]
Tevtron comb.	1.96	2.7-5.4	l+jets / dilepton	F_0	$0.68 \pm 0.04 \pm 0.05$	[78]

Table 3.4.: Summary of previous measurements of the W-boson polarisation. The analyses have been performed assuming F_R to be zero.

[9] Each analysis approach has been performed in the lepton+jets and the dilepton channel.

Effective Lagrangian

As stated in the previous chapter, there are several models that allow for a V+A admixture and significant deviations from the predicted W-helicity fractions. Instead of testing each model separately, a model-independent Ansatz is more straight-forward. Following the approach introduced in [79, 80], an effective Lagrangian describing physics processes at TeV scale and beyond can be written as:

$$\mathcal{L}_{\text{eff}} = \mathcal{L}_{SM} + \frac{1}{\Lambda}\mathcal{L}_1 + \frac{1}{\Lambda^2}\mathcal{L}_2 + ... \tag{3.26}$$

or as the sum of the operators $O_i^{(n)}$ of dimension n with their coefficients $C_i^{(n)}$, where the coefficients show the impact of the operator to the effective Lagrangian[10]:

$$\mathcal{L}_{\text{eff}} = \mathcal{L}_{SM} + \sum \frac{C_x^{(5)}}{\Lambda} O_x^{(5)} + \sum \frac{C_x^{(6)}}{\Lambda^2} O_x^{(6)} + ... \quad . \tag{3.27}$$

$\mathcal{L}_1$ and $\mathcal{L}_2$ contain five and six dimensional terms that are extensions of the SM Lagrangian. All Lagrangians have to be gauge invariant under the tranformations of the SM gauge group. $\mathcal{L}_1$ only contains one gauge-invariant dimension five operator that contributes only at very high energy scales ($\Lambda \propto 10^{15}$ GeV). Therefore, this dimension-five operator is not considered further for this analysis. In contrast to $\mathcal{L}_1$, $\mathcal{L}_2$ contains several gauge invariant dimension-six operators. There are, however, only two operators that affect the Wtb vertex and only one of them, O_{tW}, that can affect the measurement of the W-helicity fractions[11]. The Lagrangian extension is expressed as follows:

$$\mathcal{L}_{\text{eff}} = -\frac{2C_{tW}^{33}}{\Lambda^2} v\bar{b}\sigma_{\mu\nu}P_R t\partial_\nu W_\mu^- + \quad \text{h.c.} \tag{3.28}$$

Taking into account all interference effects and including the assumption of vanishing b-quark mass, the modified W-helicity fractions can be written as:

$$\begin{aligned} F_0 &= \frac{m_t^2}{m_t^2 + 2m_W^2} - \frac{4\sqrt{2}Re(C_{tW}^{33})v^2}{\Lambda^2 V_{tb}} \frac{m_t m_W (m_t^2 - m_W^2)}{(m_t^2 + 2m_W^2)^2} \\ F_L &= \frac{2m_W^2}{m_t^2 + 2m_W^2} + \frac{4\sqrt{2}Re(C_{tW}^{33})v^2}{\Lambda^2 V_{tb}} \frac{m_t m_W (m_t^2 - m_W^2)}{(m_t^2 + 2m_W^2)^2} \end{aligned} \tag{3.29}$$

These expressions can be used combined with the measured W-helicity fractions to set a limit on the coefficient C_{tW}^{33}. The result of the combined template fits presented in [3] allows to set the limit: $\frac{\text{Re}(C_{tW}^{33})}{\Lambda^2} \in [-0.9,\ 2.3]$ TeV^{-2}.

[10] Operators of higher order n are suppressed by $1/\Lambda^n$ and are therefore not considered in the following.
[11] The effect of the operator $O_{\phi q}^3$ cancels out when calculating the W-helicity fractions.

Anomalous couplings

In the previous subchapter, the W-helicity measurements were used to set a limit on dimension-6 operators under the assumption of a negligible b-quark mass. When the b-quark mass is taken into account, another set of limits on dimension-6 operators can be set. The Lagrangian of the Wtb-vertex can be expressed using a minimum set of four anomalous couplings that are introduced in [81]:

$$\mathcal{L}_{Wtb} = -\frac{g}{\sqrt{2}}\bar{b}\gamma^{\mu}(V_L P_L + V_R P_R)tW_{\mu}^{-} - \frac{g}{\sqrt{2}}\bar{b}\frac{i\sigma^{\mu\nu}q_{\nu}}{M_W}(g_L P_L + g_R P_R)tW_{\mu}^{-} + \text{h.c.} \ , \tag{3.30}$$

under the assumption of a non-vanishing b-quark mass. The Lagrangian contains two vector couplings V_L and V_R as well as two tensor couplings g_L and g_R. In the Standard model, V_L is the CKM matrix element V_{tb} whereas the other couplings vanish at tree level. Indirect limits on V_R, g_L and g_R have been set using $b \to s\gamma$ decays [82]. The four couplings can be expressed in the effective operator formalism introduced above:

$$\begin{aligned} V_L &= V_{tb} + C_{\phi q}^{(3,33)*}\frac{v^2}{\Lambda^2} \\ V_R &= \frac{1}{2}C_{\phi\phi}^{33}\frac{v^2}{\Lambda^2} \\ g_L &= \sqrt{2}C_{dW}^{33*}\frac{v^2}{\Lambda^2} \\ g_R &= \sqrt{2}C_{uW}^{33}\frac{v^2}{\Lambda^2} \quad . \end{aligned} \tag{3.31}$$

Measurements of angular asymmetries or W-helicity fractions can be used to set limits on the four anomalous couplings. The operators $O_{\phi\phi}^{33}$ and O_{dW}^{33*} are b-chirality flipping and would lead to a V+A admixture. The chirality flipping amplitude is proportional to the b-quark mass. Therefore, m_b must not be neglected in the calculation of the limits. The operator O_{uW}^{33} however is chirality conserving. Since it is ad-hoc not clear if one or more of these couplings exist, one as well as two dimensional limits on the couplings should be calculated. In the combination of the ATLAS results as presented in [3], the one-dimensional limits are as follows:

$$\begin{aligned} \mathrm{Re}(\mathrm{V_R}) \in [-0.20, 0.23] &\to \frac{\mathrm{Re}(\mathrm{C}_{\phi\phi}^{33})}{\Lambda^2} \in [-6.7, 7.8]\,\mathrm{TeV}^{-2} \quad , \\ \mathrm{Re}(\mathrm{g_L}) \in [-0.14, 0.11] &\to \frac{\mathrm{Re}(\mathrm{C}_{\mathrm{dW}}^{33})}{\Lambda^2} \in [-1.6, 1.2]\,\mathrm{TeV}^{-2} \quad , \\ \mathrm{Re}(\mathrm{g_R}) \in [-0.08, 0.04] &\to \frac{\mathrm{Re}(\mathrm{C}_{\mathrm{uW}}^{33})}{\Lambda^2} \in [-1.0, 0.5]\,\mathrm{TeV}^{-2} \quad . \end{aligned}$$

These limits are obtained using the TopFit [70, 83] program. The combination of four independent measurements allows for limits with good precision. Assuming $V_R = 0$ and $V_L = 1$, also the two dimensional limits are calculated. The results show that all anomalous couplings are consistent with zero.

4. Experimental Setup

The data used for the analysis presented in this thesis has been collected with the ATLAS detector in 7 TeV proton-proton collisions at the LHC. First, an introduction to the Large Hadron Collider (LHC) [84, 85] and its experiments is given, followed by a detailed presentation of the ATLAS experiment [86, 87] and its corresponding subcomponents. Furthermore, the magnet and the trigger systems are explained.

4.1. The Large Hadron Collider

The Large Hadron Collider (LHC) is a proton-proton and also Pb-Pb and p-Pb collider located at CERN, Geneva. It has a circumference of 27 km and is installed in the tunnel of the Large Electron-Positron collider (LEP) [88] that was operational until 2000. The LHC is installed at an average depth of 100 m and with an inclination of 1.4%.

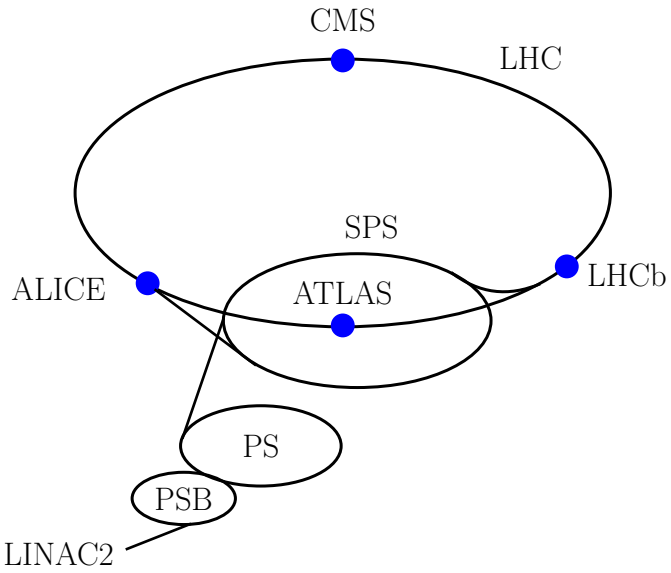

Figure 4.1.: The Large Hadron collider with its four main experiments ATLAS, Alice, CMS and LHCb and the preaccelerator chain.

The particles are brought to collision at four main experiments (see Fig. 4.1): ATLAS [86], ALICE [89], CMS [90] and LHCb [91]. The LHC produces either proton-proton, lead-lead or proton-lead collisions. The focus of the following chapter will mainly be placed on the proton-proton mode. ATLAS and CMS are multipurpose detectors designed to collect data for high-precision measurements of Standard Model processes and couplings, but also for the search of the Higgs boson and non-Standard Model processes such as the production of supersymmetric particles.

LHCb is a forward spectrometer with a characteristic asymmetric shape. The physics program is focused on the measurement of rare decays in strongly boosted $b\bar{b}$-systems. The nature of CP violation is studied in order to explain the asymmetry between matter and antimatter that has been produced in the Big Bang. In addition to that, ALICE was built to study the nature of quark-gluon plasma in PbPb collisions. To improve the knowledge of the quark-gluon structure within the colliding Pb-ions, data of proton-Pb collisions will be taken from beginning of 2013. First tests were already performed in September 2012. Furthermore, two smaller experiments are in operation that are focusing on diffractive physics, namely LHCf [92] and TOTEM [93].

The LHC and the preaccelerator chain are shown in Fig. 4.1. Protons are obtained from hydrogen atoms and are formed to bunches consisting of $\propto 10^{11}$ protons. These bunches are accelerated in the LINAC2 up to an energy of 50 MeV. The Proton Synchroton Booster (PBS) is increasing the proton energy up to 1.4 GeV. Afterwards they are accelerated in the Proton Synchrotron (PS) to 25 GeV before they are injected into the Super Proton Synchrotron (SPS). Here their energy is increased to 450 GeV. In the LHC, the protons are circulating for about 20 minutes until they are finally brought to collision at a centre-of-mass energy of 8 TeV (7 TeV in 2010 and 2011).
Sixteen superconducting radio-frequency cavities are used to accelerate the proton bunches within the LHC. To keep the particles on their track within the beam pipe 1,232 main dipole magnets are used whereas 392 main quadrupole magnets serve to focus the beam. These magnets are working at 1.9 K in order to maintain superconductivity and use Nb-Ti Rutherford cables. This is done using liquid helium and allows for magnetic fields of up to 8.3 T. To prevent collisions between the accelerated protons and gas atoms in the beam pipe, an ultrahigh vacuum is neccessary (p $\propto 10^{-13}$ atm) [85].

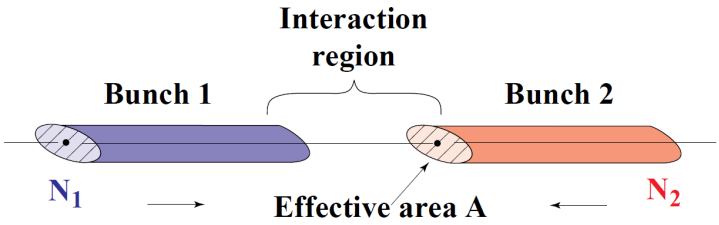

Figure 4.2.: The collision of two bunches 1 and 2 with N_1 and N_2 number of particles, respectively [94]. The hatched area shows the effective area A.

The luminosity depends on the number of particles per bunch (N_1 and N_2), the number of bunches in the two beams (n_1 and n_2), the revolution frequency f, the relativistic γ factor and the effective area A ($A = 4\pi\sigma_x\sigma_y$) with the cross sections σ_x and σ_y as shown in Fig. 4.2:

$$\mathscr{L} = \frac{N_1 N_2 n_1 n_2 f \gamma}{4\pi\sigma_x\sigma_y} \quad . \tag{4.1}$$

σ_x and σ_y can be obtained using van-der-Meer scans [95].

The two beams cross under an angle θ_c to avoid parasitic collisions. This leads to a luminosity reduction by a factor of $F(\theta_c)$:

$$\mathscr{L} = \frac{N_1 N_2 n_1 n_2 f \gamma}{4\pi\sigma_x\sigma_y} F(\theta_c) \quad . \tag{4.2}$$

For the design center-of-mass energy of 14 TeV with 2,808 bunches per beam and 1.15 $\cdot 10^{11}$ particles per bunch this leads to a luminosity of $\mathcal{O}(10^{34}\ \frac{1}{\mathrm{cm^2 s}})$.
For the 7 TeV runs of 2010/2011 and the 8 TeV run in 2012, the bunch spacing was 50 ns and about 1380 bunches per beam were used. The peak luminosity amounts to $3.65 \cdot 10^{34} \frac{1}{\mathrm{cm^2 s}}$ as discussed in Chapter 7.

Measurements at hadron colliders can be affected by in- and out-of-time pileup. In-time pileup describes additional proton-proton interactions within one bunch crossing and is increased by a stronger beam focus or by an increased number of protons per bunch. Out-of-time pileup describes additional proton-proton interactions that originate from subsequent (preceding) bunch crossings. The bunches are not uniformly distributed in the LHC ring but form so-called *bunch trains*. These bunch trains consist of several bunches with a spacing of 50 ns. In contrast to that, some of the subdetectors have a much larger read-out time (up to 600ns for the electromagnetic calorimeter). A decrease of the bunch spacing would lead to an increased amount of out-of-time pileup since the detector components cannot properly match the measured signal to the corresponding bunch crossing.

4.2. ATLAS Detector

The ATLAS experiment (**A** **T**oroidal **L**HC **A**pparatu**S**) is a multipurpose detector which is 44 m long, has a diameter of 25 m and a weight of 7,000 tons [86]. It has a typical onion-shell-like structure and covers almost the full 4π solid angle as shown in Fig. 4.3:

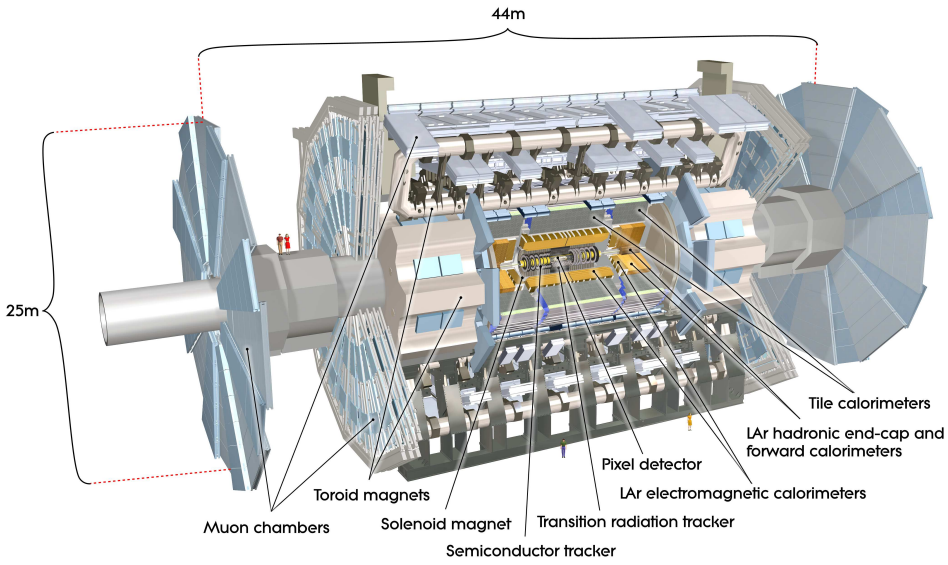

Figure 4.3.: The ATLAS detector with its subdetectors and magnet systems [86].

The tracks of the charged particles are measured by the Inner Detector (ID). It is installed close to the beam pipe and is encompassed in a solenoidal magnetic field of 2 T. The trajectories of charged particles are bent by the magnetic field which allows the determination of the sign of their charge and to improve the track reconstruction. Furthermore, the highly segmented structure provides a good spatial resolution to reconstruct primary and secondary vertices. The particles traverse the ID and may leave electromagnetic and hadronic showers in the calorimeter system. Electrons, photons and jets are fully stopped within the calorimeters. The outer part of the detector consists of the muon spectrometer which is embedded in the huge toroidal magnets that define the name and the characteristic look of the ATLAS detector. Muons traverse all detector components, while depositing only a small fraction of their energy. Their tracks and momenta are measured in the ID and again in the Muon Spectrometer (MS).

Coordinate system

The origin of the ATLAS coordinate system lies in the interaction point. ATLAS uses a right-handed system in which the x-component points towards the centre of the LHC ring, the y-component points upwards and the z-component points into the direction of the beampipe.
The polar angle θ is defined in the yz-plane and is measured from the z-axis. The azimuthal angle ϕ is defined in the xy-plane. The pseudorapidity is defined using the polar angle θ:

$$\eta = -\ln \tan\left(\frac{\theta}{2}\right) \tag{4.3}$$

The difference in pseudorapidity of two objects, $\Delta\eta$, is invariant under Lorentz-transformations. For massive objects such as jets, the difference in rapidity Δy[1] is used. The cone around a particle is expressed in $\Delta\eta$ and $\Delta\phi$:

$$\Delta R = \sqrt{(\Delta\eta)^2 + (\Delta\phi)^2} \quad . \tag{4.4}$$

The transverse momentum and energy of a particle are defined as:

$$p_T = \sqrt{p_x^2 + p_y^2} \quad \text{and} \quad E_T = E\sin(\theta) \quad . \tag{4.5}$$

4.2.1. Inner Detector

The Inner Detector (ID) is installed at a distance of 5 cm from the beam pipe and consists of the Pixel Detector, the Semiconductor Tracker (SCT) and the Transition Radiation Tracker (TRT) which have barrel and endcap components as shown in Fig. 4.4. The charged particles that traverse the ID ionise the detector material which allows to reconstruct the particle track as well as primary and secondary vertices (e.g. from b- or τ-decays).
Being closest to the beam pipe, the ID has to cope with high radiation. High granularity is of utmost importance to reconstruct the vertices as well as hundreds of different particle trajectories.

[1] $y = \frac{1}{2}\ln\left(\frac{E+p_z}{E-p_z}\right)$

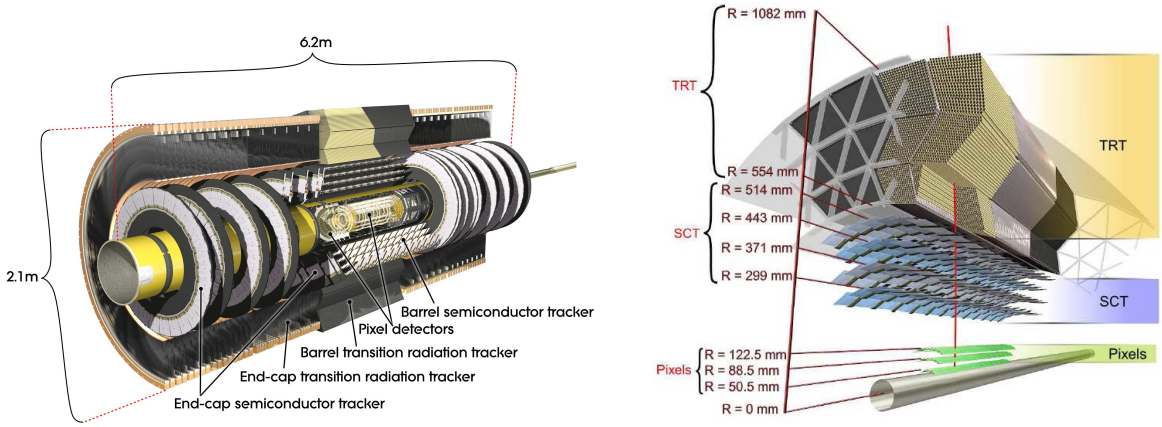

Figure 4.4.: The Inner Detector composed of the Pixel Detector, the Semiconductor Tracker and the Transition Radiation tracker [86]. Left: The barrel and endcap components of the ID. Right: Radial distance of the ID component from the beam pipe.

Pixel Detector

The Pixel Detector consists of 1,744 modules that are arranged around the beam pipe in three layers that have a radius of 50.5 - 122.5 mm. On each side of the barrel, three disks are installed perpendicular to the beam pipe. Since the innermost layer is important for the identification of secondary vertices (for example from b-decays), it is called b-layer. Each module contains 16 front-end chips (FE). The pixels are semiconductors made of silicon and have a size of 50×400 μm^2. The sensors between the FE chips are longer (50 × 600 μm^2). Bump-bonding is used for the connection to the read-out electronics.
80.4 million read-out channels (≈ 100 million for ATLAS in total) are installed for the pixel detector alone. Since the track density that close to the beam pipe is high, good spatial resolution (10 μm in R-ϕ and 115 μm in R) is neccessary to distinguish the different tracks.
During the shutdown from early 2013 - 2014, another layer of pixel sensors will be installed directly on the beam pipe to improve the identification of secondary vertices. It is there for called *insertable b-layer*.

Semiconductor Tracker

The Semiconductor Tracker (SCT) consists of four double layers of silicon strips in the barrel (2,112 modules) and nine disks for each endcap (988 modules each). Each strip is 12 cm long and made of two sensors that are connected back-to-back to another pair of sensors (double-layer). These two layers are rotated by a 40 mrad stereo angle. The strips have a pitch of 80 μm. The Pixel Detector and the SCT are cooled down to -7 °C using C_3F_8 and has 6.3 million read-out channels. It covers a region of up to $|\eta| < 2.5$. The resolution in the barrel is 17 μm in R-ϕ direction and 580 μm in z-direction (endcap: 17 μm in R-ϕ direction and 580 μm in R-direction).

Transition Radiation Tracker

The Transition Radiation Tracker (TRT) is installed at 55 - 110 cm distance from the beam pipe and covers a region of $|\eta| < 2.0$. The barrel part is divided into two parts that meet at $\eta = 0$. In each part, straws of a length of 0.7 m are used. The straws have a diameter of 4 mm and contain a tungsten wire in the middle. The tungsten wire serves as anode while the outer part of the tube serves as cathode. The straws are proportional chambers that are filled with a mixture of Xe, CO_2 and O_2. The barrel contains 52,544 straws while each endcap (consisting of 18 wheels) contains 122,880. This leads to a total of 351,000 read-out channels. The TRT provides on average 36 hits per track. The TRT is used to distinguish electrons from pions based on the different amount of transition radiation that they emit when traversing material with different dielectric constants. The resolution amounts to 130 μm in R-ϕ direction.

4.2.2. Calorimeter System

ATLAS uses sampling calorimeters for the electromagnetic and the hadronic calorimeters. An overview over the calorimeter system is given in Fig. 4.5. A sampling calorimeter consists of alternating layers of active and passive detector material. The particles interact with the passive material such as lead and induce a shower of secondary particles. The active material is ionised by the created particle shower and used for the signal read-out.

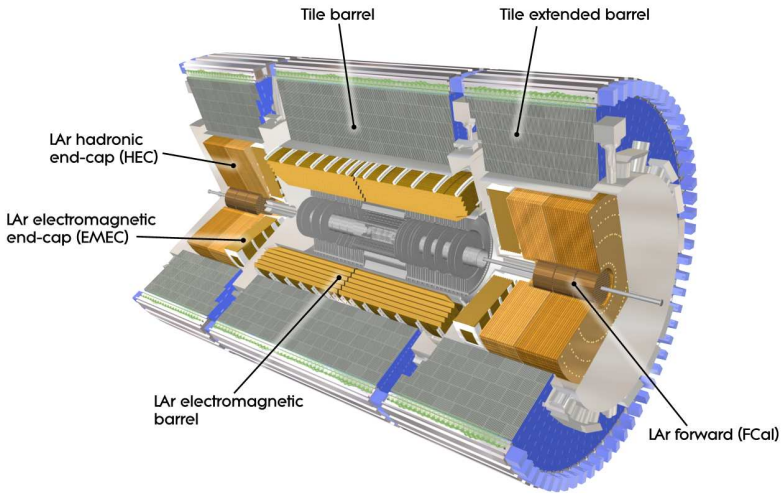

Figure 4.5.: The calorimeter system with central and forward calorimeters [86].

The energy resolution of a calorimeter can be parameterised as:

$$\frac{\sigma_E}{E} = \sqrt{\frac{a^2}{E} + \frac{b^2}{E^2} + c^2} \tag{4.6}$$

where a is the stochastic term, b the noise term and c a constant term that accounts for non-uniformities and miscalibrations. If not mentioned otherwise, the dominating terms are given in the following for each subdetector, being the stochastic and the constant term.
The depth of a calorimeter can be expressed using the radiation length. An electron/photon entering the calorimeter interacts with the detector material and creates particles via radiation of photons (Bremsstrahlung) or e^+e^--production. If the energy of one of the new particles is

above the critical energy E_c, it can itself create a pair of new particles. This leads to a large shower in the detector. If the particle energy is below E_c, the shower is stopped. After traversing a certain distance X_0 of the calorimeter, the average particle energy has been decreased by a factor of 1/e. This distance X_0 is called *radiation length* and depends on the chosen detector material. In order to avoid punch-through effects when particles leave the calorimeter, the depth of the calorimeter has to be chosen such that the shower is fully contained in the calorimeter.
A similar quantity is used for hadronic calorimeters, the *nuclear interaction length*, λ_I. The nuclear interaction length is defined as the distance λ_I that a particle travels within the detector until its energy is decreased by a factor of 1/e. In contrast to electromagnetic showers, hadronic showers are much broader and λ_I is typically larger than X_0. Therefore a hadronic calorimeter needs to have a larger transversal depth to ensure that the shower is fully contained in the calorimeter and no punch-through effects occur to the muon spectrometer. The distribution of material in measures of the nuclear interaction length is shown in Fig. 4.6 for the calorimeter system.

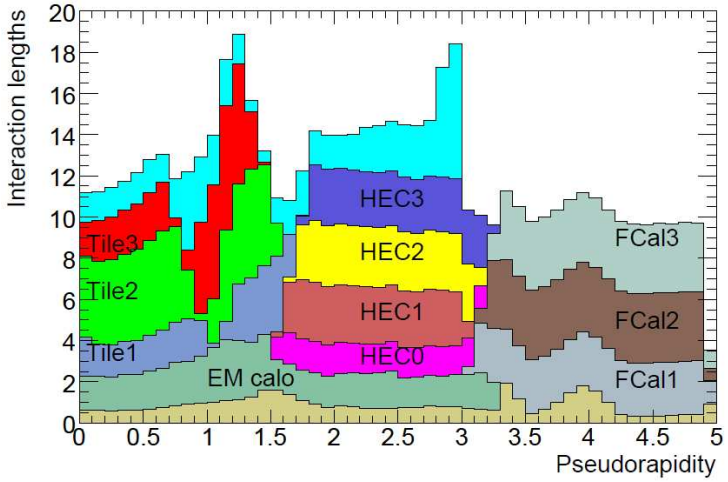

Figure 4.6.: Interaction length for the different components of the electromagnetic and hadronic calorimeters, dependent on the pseudorapidity [86]. For the hadronic calorimeters, each layer is shown separately. The distribution at the bottom shows the material distribution in front of the calorimeter system.

Electromagnetic Calorimeter

The electromagnetic (EM) calorimeter is a sampling calorimeter using liquid argon (LAr) as active and lead as passive material. Characteristic for the EM calorimeter is the accordeon-shaped structure with Kapton electrodes that provides full coverage in ϕ. A presampling calorimeter is installed between the electromagnetic calorimeter and the ID up to $|\eta| < 1.8$ to detect the energy loss of the particles due to interaction with the solenoid and the support structure of the detector, but also with the beampipe and the Inner Detector. The barrel part is divided into two parts with a gap of 4 mm between them. Each part has a length of 3.2 m and covers the range of $|\eta| < 1.475$. The liquid argon has been chosen as active material mainly due to it's stable response and radiation hardness. It is kept at a temperature of 87 K. It has a minimal depth of 22 X_0 at $\eta = 0$ and a maximum depth of 33 X_0 for larger η. The two endcaps cover the region of $1.385 < |\eta| < 3.2$ (with a minimum depth of 24 X_0 at $\eta = 1.475$ and a maximum

of 38 X_0 at $\eta = 2.5$) and consist of an inner and an outer wheel. The calorimeter has a high granularity with $\Delta\eta \times \Delta\phi = 0.025 \times 0.025$ in the barrel part and a bit coarser granularity in the endcaps. This leads to a total amount of 226,176 read-out channels for the barrel and the two endcaps. The electromagnetic calorimeter has an energy resolution of[2]:

$$\frac{\sigma_E}{E} = \frac{(10.1 \pm 0.4)\%\sqrt{\text{GeV}}}{\sqrt{E}} \oplus (0.2 \pm 0.1)\% \quad . \tag{4.7}$$

Hadronic Calorimeter

Jets originate from quarks and gluons. Their energy is measured both by the electromagnetic and the hadronic calorimeter, while they leave the largest part of their energy in the latter. The hadronic calorimeter consists of a tile calorimeter in the barrel ($|\eta| < 1.0$) and two extended barrels ($0.8 < |\eta| < 1.7$) as well as LAr calorimeters in the endcap and forward calorimeters. The tile calorimeters consist of alternating layers of scintillator tiles and steel. The tiles are parallel to the direction of the incoming particle and are arranged in three layers. When passing through the scintillator, photons are created and read out using wavelength shifters and photomultipliers. The calorimeter has a minimum depth in the barrel of 9.7 interaction length λ_I at a rapidity of $\eta = 0$. Further information for each calorimeter part can be found in Fig. 4.6.

The hadronic endcap (HEC, $1.5 < |\eta| < 3.2$) and the forward calorimeter (FCal, $3.1 < |\eta| < 4.9$) are overlapping. The HEC is a sampling calorimeter using copper as passive and LAr as active material. Since the forward calorimeter has to cope with a high particle flux, a radiation-hard construction consisting of one layer with copper/LAr and two layers of tungsten/LAr has been chosen. The resolution of the hadronic calorimeter has been measured in test beams using pions. The resolution for the tile calorimeter yields[3]:

$$\frac{\sigma_E}{E} = \frac{(56.4 \pm 0.4)\%\sqrt{\text{GeV}}}{\sqrt{E}} \oplus (5.5 \pm 0.1)\% \quad , \tag{4.8}$$

while the resolution for the hadronic endcap has been measured to[4]:

$$\frac{\sigma_E}{E} = \frac{(70.6 \pm 1.5)\%\sqrt{\text{GeV}}}{\sqrt{E}} \oplus (5.8 \pm 0.2)\% \quad . \tag{4.9}$$

[2] Taken from [86], p. 156.
[3] Taken from [86], p. 161.
[4] Taken from [86], p. 156.

4.2.3. Muon Spectrometer

The muon spectrometer (MS) consists of three concentric layers at a radius of 5 m, 7.5 m and 10 m. For each endcap, four wheels are installed at $|z| = 7.4$ m, 10.8 m, 14 m and 21.5 m and cover a region of $1.0 < |\eta| < 2.7$. It does not cover the full solid angle due to a gap at $|\eta| < 0.05$ for support material and the detector feet. The detector is embedded in a magnetic field created by the toroid magnets in the barrel ($|\eta| < 1.0$) and the two endcap magnets ($1.4 < |\eta| < 2.7$).

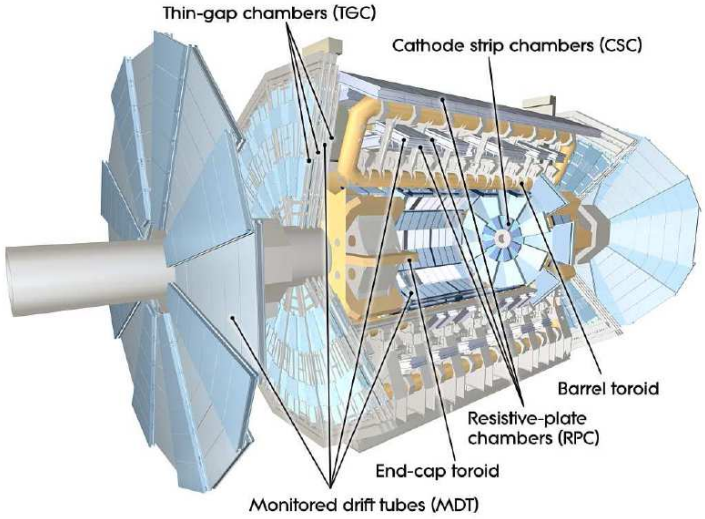

Figure 4.7.: The muon spectrometer with the high precision chambers MDT and CSC as well as the trigger chambers RPC and TGC [86].

Muons created in high-energy collisions at the LHC are minimum ionising particles and loose only a small fraction of their energy while traversing the detector without being absorbed. The design muon momentum resolution is about 10% for 1 TeV muons and 3% for 10-200 GeV muons [87]. To achieve these resolutions, the track of a particle has to be measured with high precision. The trajectory of muons that traverse the spectrometer are deflected by the magnetic field. In order to measure the particle track, the sagitta s has to be measured:

$$s = R(1 - \cos\left(\frac{\theta}{2}\right)) \tag{4.10}$$

For muons with a high transverse momentum, the trajectory has a larger bending radius, leading to a smaller sagitta. This measurement is done using Monitoring Drift Tubes (MDT) in the barrel, and MDTs and Cathode Strip Chambers (CSCs) in the forward region. These two detector components have a good spatial resolution but low timing resolution. To be able to distinguish between muons from different bunch crossings, Resistive Plate Chambers (barrel) and Thin Gap Chambers (endcap) provide fast trigger information. The spatial and timing resolution is listed for each component in Tab. 4.1[5].

[5]Taken from [86], p. 168.

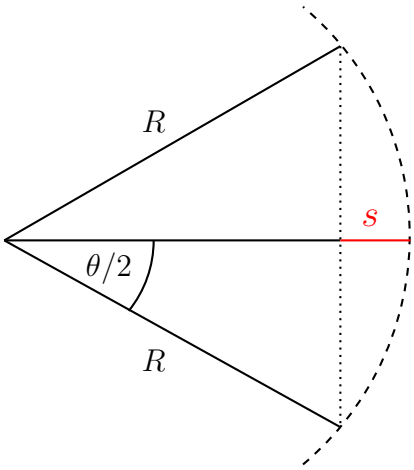

Figure 4.8.: The trajectories of muons in the MS are bent by the toroidal field and their track is measured using the sagitta s. The particle track is indicated by the dashed line, the radius of the track is denoted by R.

Monitoring Drift Tubes

Modules made of Monitoring Drift Tubes (MDTs) are 1-6 m long, 1-2 m wide and consist of 3-8 layers of aluminum tubes. These tubes have a diameter of 3 cm and contain a tungsten-rhenium wire. The volume is filled with a gas mixture of 93% Ar and 7% CO_2 at a pressure of 3 bar. The barrel part of the MDTs covers a region of up to $|\eta| < 1.0$ while the wheels in the endcap cover up to $|\eta| < 2.7$. Muons passing through the spectrometer create a signal by ionising the gas. The produced electrons have a drift time of 700 ns, therefore additional information has to be provided by the RPCs to differentiate between signals from different bunch crossings.

Resistive Plate Chambers

The Resistive Plate Chambers (RPCs) are made of two plates with a gas mixture of $C_2H_2F_4$ (94.7%), Iso-C_4H_{10} (5%) and SF_6 (0.3%) filled in the 2 mm gap between the plates. The RPCs have a good timing resolution and are therefore used for triggering in the barrel part of the MS. They also provide a measurement of the azimuthal angle ϕ.

Cathode Strip Chambers

Cathode Strip Chambers (CSCs) are multi-wire proportional chambers that are only installed in the first wheel of the muon spectrometer which is installed at $|z| = 7$ m. Being placed in the forward region of the spectrometer, the detector has to be radiation hard and is filled with Ar/CO_2 (80/20%). To provide a good coverage in the forward region, each disk is made of eight large and eight small modules that overlap.

Thin Gap Chambers

Thin Gap Chambers (TGCs) provide the trigger information in the forward region of the MS. They are multi-wire proportional chambers filled with a gas mixture of CO_2 and n-C_5H_{12}. The distance between the cathode and the anode is only 1.4 mm. In addition to the trigger information, TGCs also provide a measurement of the azimuthal angle ϕ.

	Function	Coverage	z/R	ϕ	time [ns]	Barrel	Endcap
MDT	tracking	$\lvert\eta\rvert < 2.7$	35 μm (z)	-	-	20	20
RPC	triggering	$\lvert\eta\rvert < 1.05$	10 mm (z)	10 mm	1.5	6	-
CSC	tracking	$2.0 < \lvert\eta\rvert < 2.7$	40 μm (R)	5 mm	7	-	4
TGC	triggering	$1.05 < \lvert\eta\rvert < 2.4$	2-6 mm (R)	3-7 mm	4	-	9

Table 4.1.: The different muon subdetectors with their function, η coverage and their spatial and timing resolution. The last two columns show the number of measurements per track provided by the separate detector components. The information has been taken from [86], p. 168.

4.2.4. Magnet System

The magnet system of ATLAS consists of a solenoid magnet comprising the Inner Detector (ID) and a large toroid magnet system that is part of the muon spectrometer (MS). A sketch of the magnet system is shown in Fig. 4.9. Charged particles traversing the ID or the MS are bent by the magnetic field. This allows not only to determine the sign of the particle charge but also to get a precise measurement of the particle momentum.

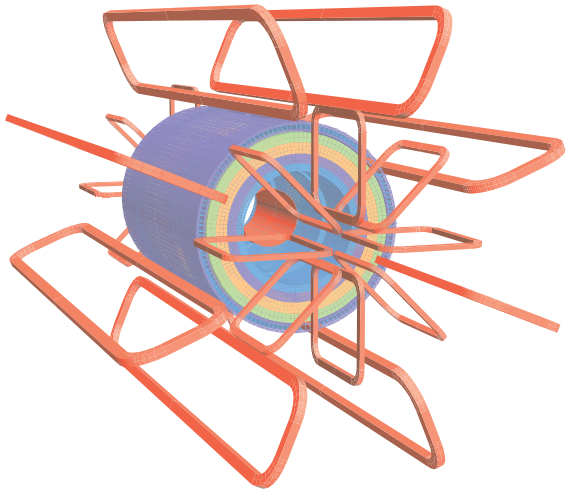

Figure 4.9.: The ATLAS magnet system with the ID comprising solenoid and the large toroid magnets in the MS [86].

The solenoid magnet is cooled with liquid helium to a temperature of 1.8 K. It provides a magnetic field of up to 2.6 T. Since it is installed directly in front of the electromagnetic calorimeter, its material budget had to be reduced. The toroid system consists of two endcaps and one barrel toroid, each made out of eight coils. It provides a non-uniform magnetic field of up to 4.7 T. In order to know the field strength of this non-uniform field, Hall sensors are installed. The transition region between barrel and endcap magnets is located at a pseudorapidity of $1.4 < \lvert\eta\rvert < 1.6$. In this region the bending power is decreased compared to the forward region (1-7.5 Tm) and barrel region (1.5-5.5 Tm) [86]. Each superconducting coil has an air core in order to suppress multiple scattering of the traversing muons.

4.2.5. Trigger and Data Aquisition System

The interaction rate of approximately 1 GHz leads to a huge amount of data produced at the LHC. Since only the interesting events should be selected and written to tape, ATLAS installed a three level trigger system, consisting of the hardware-based Level 1 trigger (L1) and the software based *High Level Trigger* (HLT) consisting of the Level 2 trigger (L2) and the Event Filter (EF). The full trigger system with the reduced data rates is shown in Fig. 4.10.

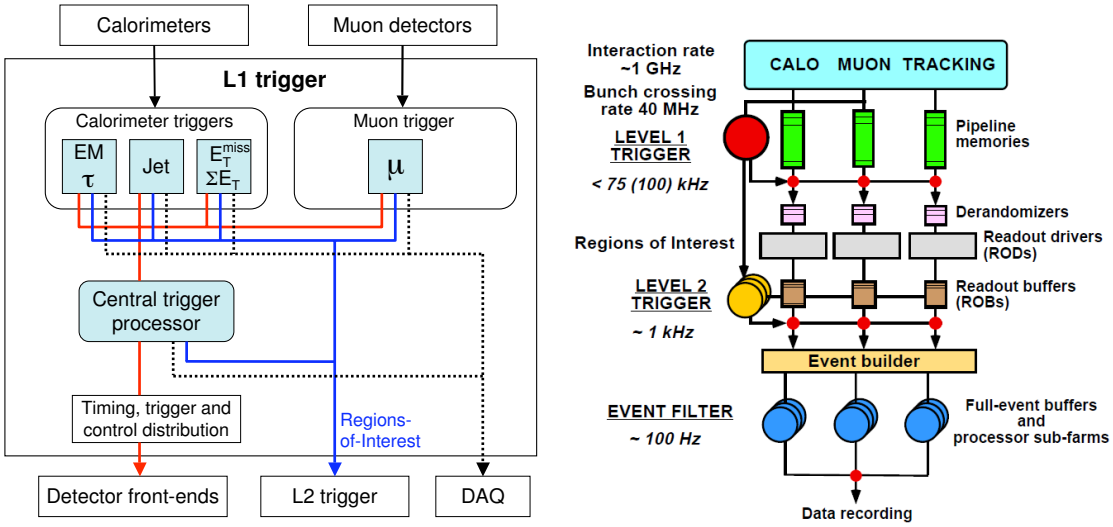

Figure 4.10.: The ATLAS trigger system with the hardware-based L1 trigger and the software based L2 and EF trigger [86].

The L1 trigger as shown in Fig. 4.10 (left) is hardware based and takes reduced calorimeter information as well as information from the muon trigger chambers (RPCs and TGCs). So-called *Regions of Interest* (RoIs) are defined in the detector and passed to the next trigger stages. Since events with large missing transverse energy (defined in Chapter 5.6) are interesting for SM analyses such as $t\bar{t}$-production but also for searches for Supersymmetry or other BSM processes, this is an important trigger object that defines an RoI for the L1 trigger. Furthermore high-p_T particles such as electrons, muons, jets etc. are identified and used in the decision process that takes about 2.5 μs. All RoI information of the accepted event is passed to the next trigger level. The selection of these RoI leads to a data rate reduction down to $\mathcal{O}$(75 kHz).
In the L2 trigger also the information of the Inner Detector (ID) is taken into account. Furthermore the RoI are analysed using detailed information of the calorimeters and the muon spectrometer (MS). In contrast to the hardware based L1 trigger, the HLT algorithms are running on computing farms. If an event is accepted by the L2 trigger (latency time about 10 ms) it is passed to the Event Filter. There it is fully reconstructed using all information available. The algorithms also contain track and vertex reconstruction methods. This last decision is taken in an average time of 4 seconds [86]. Events passing the EF decision are stored on tape for later analysis.

5. Object Definition

The objects used for this measurement are defined in the following and comprise electrons and muons as well as jets and missing transverse energy. Furthermore, b-tagging methods and calibrations are discussed. Since the tag-and-probe method is used for several objects to determine efficiencies, it is briefly described in the beginning.

5.1. Tag and Probe Method

The tag-and-probe method (TP method) is widely used to estimate trigger and reconstruction efficiencies. Leptonically decaying Z- or W-bosons as well as J/ψ- or Υ-mesons are used. In the following, the method is explained for the decay $Z \to l^+l^-$.

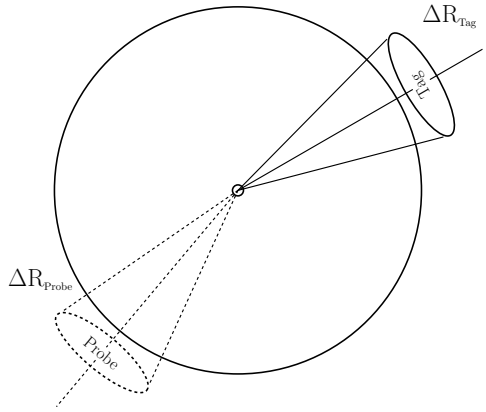

Figure 5.1.: Sketch of the Tag and Probe method that is used to determine trigger and reconstruction efficiencies. If the *tag* lepton passes the tight selection, a *probe* lepton with looser isolation criteria is looked for.

The event selection is perfomed with a tight selection for the lepton which is called *tag lepton*. If the tag lepton is found, another lepton with looser isolation criteria is searched for, called *probe lepton*. The probe lepton has to fulfill the same criteria as the lepton in the measurement where these scale factors are applied. The leptons used for the TP method have to have opposite charges to suppress background processes. The invariant mass of the lepton pair has to be close to the Z-boson mass. The corresponding efficiency is calculated as the ratio of the number of selected probe leptons, $N_{\text{Probe}}^{\text{selected}}$, and the total number of probe leptons, N_{Probe}:

$$\epsilon = \frac{N_{\text{Probe}}^{\text{selected}}}{N_{\text{Probe}}} \quad . \tag{5.1}$$

The efficiency is estimated both in data and MC events. The scale factor that is applied on the MC events in the analysis is calculated as:

$$SF = \frac{\epsilon_{Data}}{\epsilon_{MC}} \quad . \tag{5.2}$$

The scale factor is usually parameterised in η, p_T and/or ϕ of the object.

5.2. Electrons

An electron that is considered in this thesis is an object that has to fulfill certain quality criteria. These criteria and the performance of the object identification is explained in the following subchapters.

Definition and preselection

The transverse energy of the electron is defined based on the cluster energy and the track η:

$$E_{\mathrm{T}} = \frac{E_{\mathrm{cluster}}}{\cosh(\eta_{\mathrm{track}})} \quad . \tag{5.3}$$

The identification of electrons starts by searching for clusters with energy deposits $E_{\mathrm{T}} > 2.5$ GeV in the electromagnetic (EM) calorimeter [96]. The so-called *seed cluster* is found using the *sliding-window* algorithm [97]. Based on the granularity of the middle layer of the EM calorimeter, where a cell has a size of 0.025×0.025 (in $\eta \times \phi$), the window has a size of 3×5 cells. The window with the maximum amount of deposited energy is chosen as cluster center. Now the final cluster is built with longitudinal towers of the size of 3×7 cells.
The cluster energy is calculated whilst taking into account the energy loss due to interaction of the particles with material in front of the calorimeter and correcting for energy leaking out of the cone, as well as energy leaking out of the electromagnetic into the hadronic calorimeter. After identifying the seed cluster, at least one track has to be found that can be matched to the cluster. If more than one track can be matched, the closest track is taken.
Only objects in the central part of the detector are considered for further analysis. Therefore, the cluster pseudorapidity has to fulfill the condition: $0 \leq |\eta_{\mathrm{cluster}}| \leq 2.47$. The EM calorimeter, as introduced in Chapter 4, has a so-called *crack region*, which is the transition region between the EM barrel and endcap calorimeters. Electrons falling in the region of $1.37 \leq |\eta_{\mathrm{cluster}}| \leq 1.52$ are rejected.
Electrons are considered to be loose++, medium++ or tight++ based on requirements for the shower shapes, the E/p ratio or hadronic leakage that is used to suppress background from jets and photons. To reduce background due to misidentified leptons, track and calorimeter isolation criteria are applied to the cluster energy. Pileup and leakage corrections are applied. A cone with a radius of $\Delta R = 0.3$ (0.2) is defined around the electron for the track (calorimeter) isolation, respectively. In this cone, only a certain transverse momentum (energy) is allowed in order to consider the electron to be isolated. A TP method has been applied to retrieve the corresponding cut values. This allows to provide a uniform isolation efficiency of 90%.
In addition, jets overlapping with an electron within a cone of $\Delta R = 0.2$ are rejected. After this jet-electron overlap removal, the distance of the remaining jets with a transverse momentum of 20 GeV is calculated. If a jet is found in a cone of $\Delta R = 0.4$ around the electron, the electron is not considered for further analysis. Finally, a cut on the longitudinal impact parameter of the lepton ($|z_0| < 2$ mm) with respect to the primary vertex is applied. The data set is split into

different data taking periods according to the trigger requirements. The trigger with the lowest p_{T}-threshold is taken as long as it was unprescaled. Otherwise, the next higher unprescaled trigger was taken. The triggers with their respective data taking periods are listed in Tab. 5.1. For periods L-M, the EF_e22vh_medium1 trigger was used that is expected to not be efficient for very high transverse energies ($E_T \gg 100$ GeV) due to the hadronic core veto used at trigger level 1. For these high-E_T electrons, the EF_e45_medium1 was used. The electron has to have $E_{\mathrm{T}} > 25$ GeV in order to ensure a high trigger efficiency.

data period	trigger	special requirements
B-H	EF_e20_medium	
I-K	EF_e22_medium	
L-M	EF_e22vh_medium1 OR	
	EF_e45_medium1	$p_{\mathrm{T}} \gg 100$ GeV

Table 5.1.: Unprescaled electron event filter triggers used for the different data periods.

The electron energy was corrected in data events. The uncertainty of this correction is up to 1.6 % in the central part of the calorimeter [98]. The energy scale is estimated using Z or $\mathrm{J}/\psi \to e^+e^-$ events. Furthermore, $W \to e\nu$ events are used to study the E/p ratio. Figure 5.2 (left) shows the stability of the relative electron energy scale with respect to the average number of interactions per bunch crossing. In Fig. 5.2 (right), the invariant mass of the electron-positron pair is shown. The resolution in the simulated sample is different from the resolution in data, therefore the energy resolution had to be enlarged in data.

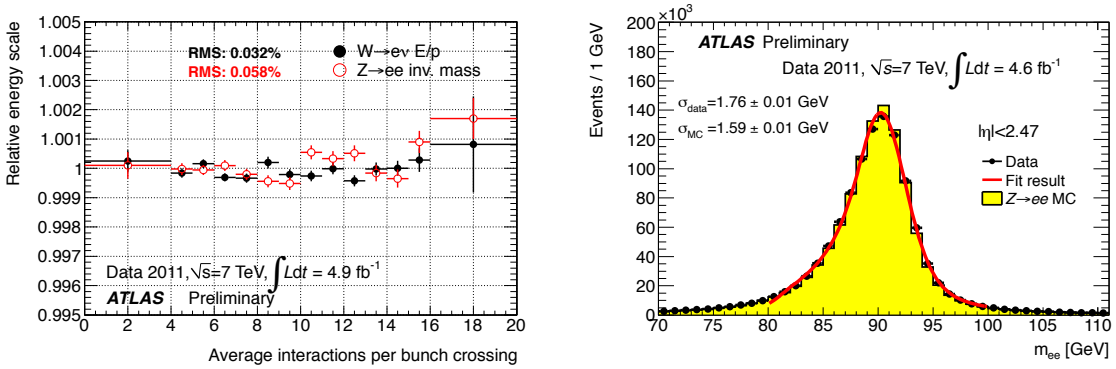

Figure 5.2.: Left: Stable energy electron response dependent on the average number of interactions per bunch crossing [99]. Right: Invariant mass of the electron-positron pair. The resolution is different for MC and data, therefore the MC events have to be smeared to achieve an improved data description [100].

Moreover, a correction for events that were reconstructed with fast simulation[1] is neccessary. Finally, all samples need a correction for electrons in the crack region. In the estimate of this correction, the crack region is defined as $1.42 \leq |\eta_{\mathrm{cluster}}| \leq 1.55$. Since electrons in the region $1.37 \leq |\eta_{\mathrm{cluster}}| \leq 1.52$ are rejected in the selection, this correction only applies to electrons within $1.52 \leq |\eta_{\mathrm{cluster}}| \leq 1.55$.
Table 5.2 shows the different corrections and calibrations that are applied.

[1] The fast simulation or ATLFASTII simulation is explained in more detail in Chapter 6.

Sample Type	Scaling	Smearing	Crack calibr.	Extra correction
Data	yes	no	yes	no
Full simulation	no	yes	yes	no
Fast simulation	no	yes	yes	fast sim. → full sim.

Table 5.2.: Corrections and calibrations applied to electrons in data and simulated events.

The acceptance loss due to malfunctioning front-end boards in some data periods (see Chapter 7), is modeled in the MC according to the respective luminosity. The reconstruction and trigger efficiencies were obtained using the TP method in $Z \rightarrow ee$ events both in MC and data. The scale factors were calculated as shown in Eq. 5.2. They were parameterised for the reconstruction (trigger) efficiencies in 9 (18) η bins. Furthermore, the trigger efficiencies got an additional correction that was parameterised in six E_T bins. The identification efficiencies were obtained using the TP method on $Z \rightarrow ee$ and $W \rightarrow e\nu$ events[2]. The scale factors were calculated for nine η and eleven E_T bins. Figure 5.3 shows the identification efficiencies for the selection in 2011 and 2012 on the number of primary vertices for loose++, medium++ and tight++ electrons. A clear dependence on the number of primary vertices can be seen for the 2011 selection. Due to lower cuts on the leakage out of the electromagnetic calorimeter and harder cuts on the shower shapes, the identification efficiency is much less dependent on pileup effects.

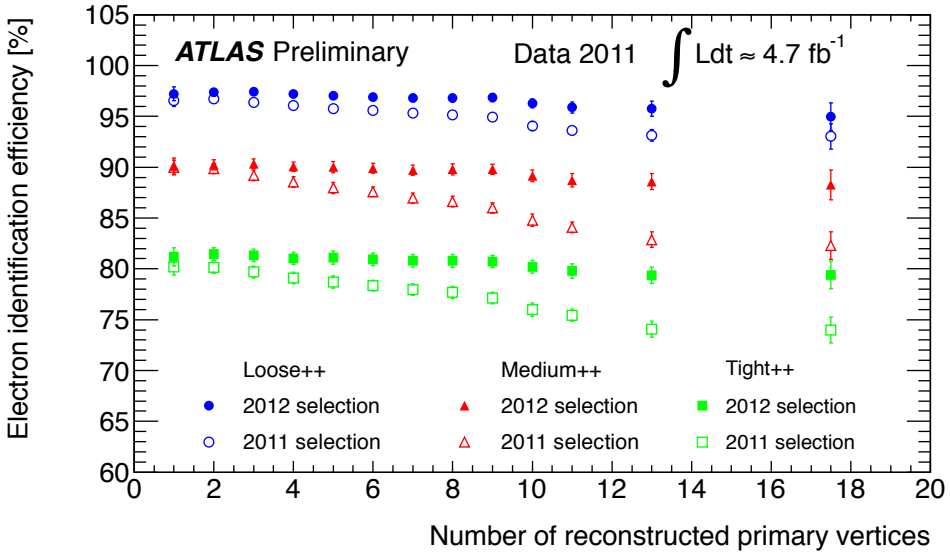

Figure 5.3.: Pileup dependence of the electron identification efficiency for loose++, medium++ and tight++ electrons, comparing the effects of the selection used in 2011 and 2012 [101]. The identification efficiency decreases significantly for the 2011 selection while it is more stable for the 2012 selection.

[2]The tag object is in this case the missing transverse energy.

5.3. Muons

A muon that is considered in this measurement is an object that has to fulfill certain quality criteria. These criteria and the performance of the object identification are explained in the following.

Definition and preselection

Muons considered in the underlying analysis are objects that have a track both in the Inner Detector (ID) and Muon Spectrometer (MS). The MuId algorithm [102, 103] is used for the track reconstruction using track information from the ID and the MS together to perform a combined fit. The unprescaled muon triggers used for the respective data taking periods are listed in Tab. 5.3. A cut on the transverse momentum of 20 GeV is applied to ensure stable trigger efficiencies on the trigger plateau. Furthermore, the muons have to be central: $|\eta| < 2.5$. To reject muons originating from heavy flavour decays, the muon has to be isolated. Thus, the additional allowed transverse energy (calorimeter isolation) or transverse momentum (track isolation) in a cone with a certain size around the muon has to be defined. The combination of $E_T^{\text{cone},20} < 4$ GeV and $p_T^{\text{cone},30} < 2.5$ GeV were shown to give good isolation efficiency and being stable against pile-up. $E_T^{\text{cone},20}$ describes the additional transverse energy that is allowed in a cone size of $\Delta R = 0.2$ around the muon. A jet-muon overlap-removal is performed with $\Delta R(\text{muon}, \text{jet}) < 0.4$. If a muon is found in the cone, it is disregarded for the further selection. To maintain a high efficiency of this overlap removal in collisions with higher pile-up conditions, only jets with a $p_T > 25$ GeV and a cut on the jet vertex fraction of $|\text{JVF}| > 0.75$ (details see Chapter 5.4.1) are considered.
Additional hit requirements for the ID track are neccessary. The muon is supposed to have one hit in the *b*-layer of the Pixel Detector unless it traverses an inactive area or a gap. Furthermore it should have at least two Pixel and six SCT hits. A cut on the longitudinal impact parameter $|z_0| < 2$ mm with respect to the primary vertex is applied. Trigger and isolation efficiencies are estimated in data applying the TP method on Z$\rightarrow \mu\mu$ events.

data period	trigger
B-I	EF_e18
J-M	EF_e18_medium

Table 5.3.: Unprescaled muon triggers used for the different data periods.

The resolution obtained from the $Z \rightarrow \mu\mu$ mass spectrum is compared in Fig. 5.4. A discrepancy between data and MC is observed. The results for the dimuon mass resolution for the different pile-up conditions agree within uncertainties both for data and MC, respectively. The discrepancy between data and MC observed is due to a small misalignment of the Inner Detector and Muon Spectrometer.
In order to get a good description of the data, the transverse momentum of muons in simulated events has to be smeared and the muon scale is corrected.

The identification, reconstruction and trigger efficiencies were obtained from $Z \rightarrow \mu\mu$ events and the corresponding scale factors that are applied to MC events are calculated dependent on η, p_T and ϕ. The identification scale factors are parameterised in 14 η and 16 p_T bins since the reconstruction scale factors are parameterised in 20 η bins. The trigger SF are split into three data periods B-I, J-K and L-M while a few runs in period L suffered from issues with the RPC timing which lead to a decreased trigger efficiency.

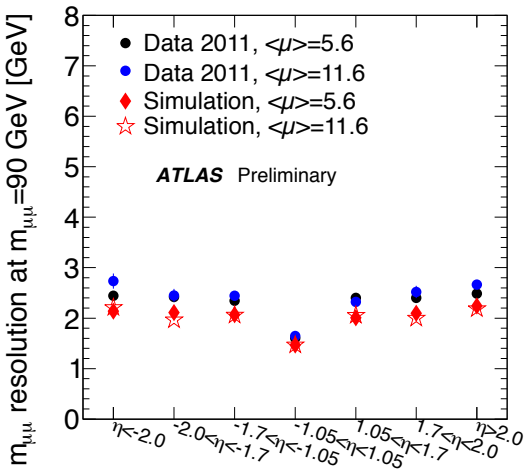

Figure 5.4.: Mass resolution in data and $Z \to \mu\mu$ events simulated with Pythia for different pile-up conditions [104].

5.4. Jets

High-energy collisions at the LHC are characterised by a multitude of high-p_{T} jets. These jets are complex objects whose identification, calibration, and corresponding performance is discussed in the following subchapter.

Definition and preselection

In the ATLAS analysis model, jets are reconstructed with the infrared- and collinear-safe anti-k$_t$ algorithm [105] with a distance parameter of $\Delta\mathrm{R} = 0.4$ and are based on topological clusters [106] (calorimeter jets) which are matched to reconstructed tracks in the Inner Detector (track jets). The reconstruction is done using the FastJet-software [107]. Calorimeter cells with a certain signal-over-noise ratio $S/N > 4$ are used as seeds[3]. The cells around this seed with $S/N > 2$ are added to the cluster and, in a final step, their next neighbours are taken into account. The clusters are first calibrated to the scale of the electromagnetic calorimeter. To get jets calibrated at the hadronic scale, they are corrected for pileup effects using an offset correction on the tranverse energy [108, 109] and then η and p_{T} dependent correction factors are applied which were obtained from simulated events. The dependence of the transverse jet momentum is shown in Fig. 5.5 for simulation and data, respectively. A clear dependence is observed that was corrected for. An additional calibration is applied to data which was obtained from in-situ measurements. The jet direction is corrected such that the jet does not point to the center of the ATLAS detector but to the primary vertex. Furthermore, the jets need a $p_{\mathrm{T}} > 25$ GeV and $|\eta| < 2.5$ where η is the pseudorapidity at EM scale. For the calculation of the missing transverse energy, jets are contributing to two terms. Jets with a $p_{\mathrm{T}} > 20$ GeV are considered in the jet term while jets with a p_{T} of 7-20 GeV are contributing to the *softjet* term.

[3] Due to the smaller bunch spacing in 2011 compared to 2012, the noise term does include both electronic and pile-up noise [108].

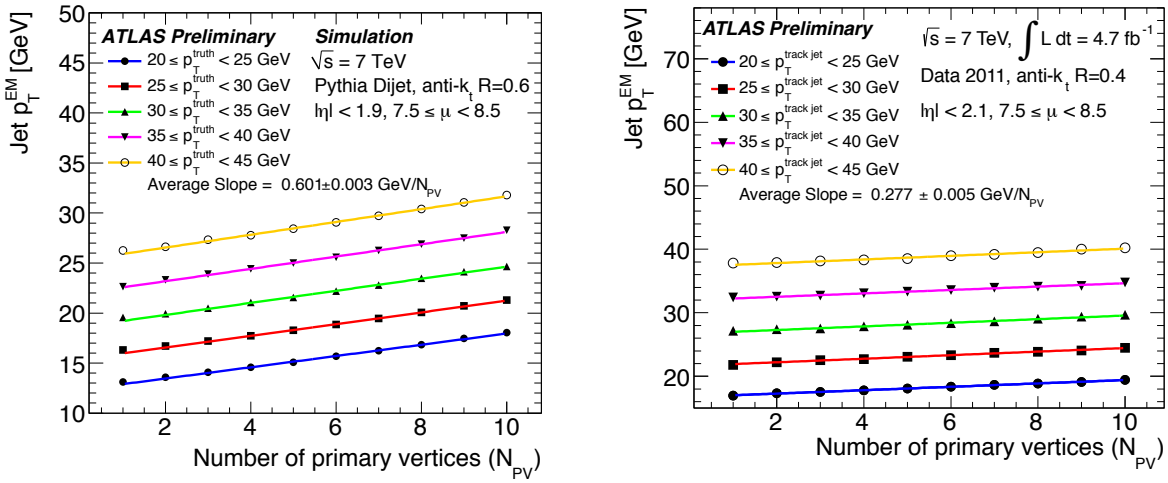

Figure 5.5.: The calorimeter clusters are corrected for jet p_{T} coming from in- and out-of-time pileup. The dependence of the jet-p_{T} on the number of primary vertices is shown for simulation (left) and in 2011 collision data (right) [108].

The uncertainty of the jet energy scale (JES) is parameterised in η and p_T. In the central part of the detector with $|\eta| < 1.2$, in-situ calibration methods were applied that exploit the p_T balance between γ/Z and a jet or, for jets with higher transverse momentum, the recoil of one high-p_{T} jet against low-p_{T} jets in the event [109]. The uncertainty on the jet energy scale is evaluated using simulated events, test beam measurements as well as measurements in proton-proton collisions. The uncertainty decreases with increasing transverse momentum, resulting in a relative uncertainty of 4.6 % for jets with $|\eta| < 0.8$ and $p_{\mathrm{T}} > 20$ GeV down to 2.5 % for jets with a transverse momentum between 60 and 800 GeV [109]. The presence of close-by jets, flavour composition and η-intercalibration are taken into account. The additional uncertainty due to the jet energy scale of b-jets is overall < 2.5 % and decreases with increasing jet p_T down to 1 %. This uncertainty is added in quadrature to the nominal JES term for true b-jets. The correction for pileup effects is taken into account by including an uncertainty of 0.5 GeV per additional primary vertex.
For the estimation of the Jet energy resolution (JER) on data and MC [110], the dijet balance [111] and the bisector method are used [112]. The corresponding uncertainty is larger for smaller jet p_{T} and for the central part with $|\eta| \geq 0.8$. The relative difference between the JER in data and MC is about 10 % [110]. The jet reconstruction efficiency (JRE) was estimated using the TP method on dijet events. The two jets are required to be back-to-back ($\Delta\phi > 2.8$). The track jet with the highest p_{T} is used as tag jet. The probe track jet is matched to the calorimeter based jet using $\Delta R < 0.4$ as matching radius. The estimated reconstruction efficiencies in data and MC differ by about 2% [113]. The effect is modeled in MC by randomly disregarding jets according to the estimated efficiencies.

5.4.1. The Jet Vertex Fraction

The measurement of the jet energy and the missing transverse energy of the event is strongly affected by events from in-time and out-of-time pileup (see Chapter 4.1). The minimum bias events do not only lead to a higher jet multiplicity and jet energy mismeasurement but also to a worse jet and E_T^{miss} resolution. It is therefore of utmost importance to distinguish between jets from pileup events and jets from the hard-scattering and to correct for a potential bias in the jet energy calculation. This is done using the so-called *Jet Vertex Fraction* which gives a probability for each jet to come from a specific vertex. For the calculation of this probability, the tracks and jets have to fulfil certain selection criteria. Only jets in the central region of the calorimeter with $|\eta| < 2.5$ are considered. A cone of $\Delta R = 0.4$ is defined around each jet in which the transverse momenta of the tracks are summed up as depicted in Fig. 5.6:

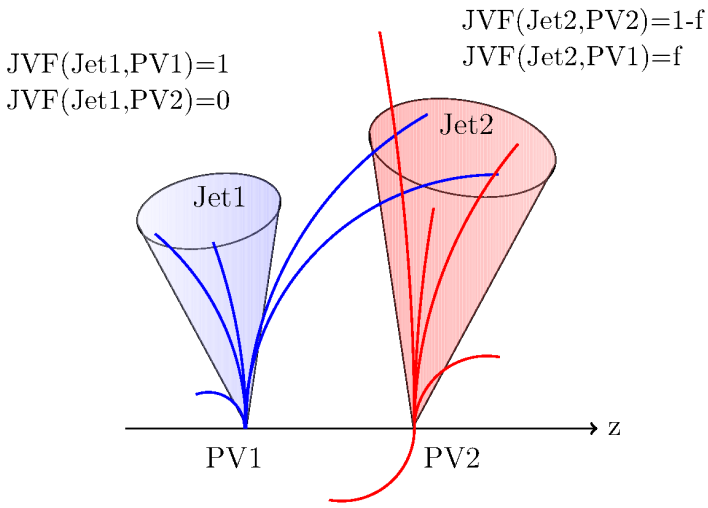

Figure 5.6.: Sketch of the jet vertex fraction: jet 1 only contains tracks that originate from vertex 1. Jet 2 however contains tracks originating from both vertices, leading to a decreased jet vertex fraction.

Each track within this cone is assigned to the corresponding jet and has to stem from a specific primary vertex. The contribution of the transverse momentum of each track to the primary vertex associated to the jet i is calculated for each vertex j:

$$\text{JVF}(\text{Jet}_\text{i}, \text{Vertex}_\text{j}) = \frac{\sum_\text{k} \text{p}_T(\text{Track}_\text{k}^{\text{Jet}_\text{i}}, \text{Vertex}_\text{j})}{\sum_\text{n} \sum_\text{l} \text{p}_T(\text{Track}_\text{l}^{\text{Jet}_\text{i}}, \text{Vertex}_\text{n})} \tag{5.4}$$

In Fig. 5.7 a simulation of the JVF distribution is shown. Jets with a JVF close to one are assumed to originate from the primary vertex of the hard scattering whereas jets with a JVF close to zero are assumed to come from the vertex of a minimum bias event. A cut value of JVF > 0.75 gives a good pileup rejection while keeping still a large fraction of the available statistics for $t\bar{t}$-analyses.

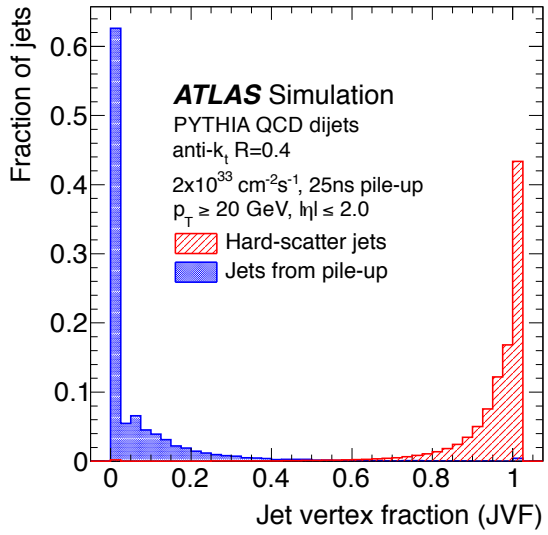

Figure 5.7.: Distribution of the jet vertex fraction for jets originating from the hard scattering (hatched area) and jets from pileup events (solid area) [114].

Efficiency of JVF cut

The efficiency of the JVF cut needs to be calculated in data and MC to obtain scale factors for each jet. This efficiency was obtained from $Z(\rightarrow e^+e^-)$+jets and $Z(\rightarrow \mu^+\mu^-)$+jets events via the TP method. Four different efficiencies are defined:

- ϵ_{hs} $\hat{=}$ efficiency for a jet from a hard-scatter to pass the JVF cut. This efficiency is called *tag rate* for jets from hard-scattering.
- 1 - $\epsilon_{\text{hs}}\hat{=}$ mistag rate for jets from hard-scattering.
- ϵ_{pu} $\hat{=}$ tag rate for jets from pileup events.
- 1 - $\epsilon_{\text{pu}}\hat{=}$ mistag rate for jets from pileup events.

To obtain tag and mistag rate for jets from hard scattering, events with a boosted Z-boson and a back-to-back jet are considered (pileup depleted sample). For the evaluation of the tag- and mistag rate of the pileup events, Z-bosons with a low transverse momentum and exactly one jet are considered (pileup enriched sample).

Since the pileup enriched sample still contains a fraction of hard-scattering jets, called f_{hs}, the measured pileup rejection efficiency needs to be corrected using this fraction:

$$\epsilon_{\text{pu}}^{\text{meas}} = \frac{\epsilon_{\text{pu}} N_{\text{pu}} + (1 - \epsilon_{\text{hs}} N_{\text{hs}})}{N_{\text{pu}} + N_{\text{hs}}} \tag{5.5}$$

Four scale factors are obtained for the tag and mistag rates. They have to be multiplied to calculate the total event weight for the JVF cut including those jets that fulfil all jet criteria except for the Jet Vertex Fraction cut.

Jet cleaning

In the analysis presented in this thesis, at least four high-p_{T} jets were selected. In order to suppress background from jets that are not produced in proton-proton collisions, *bad jets* with $E > 0$ GeV and $p_{\mathrm{T}} > 20$ GeV are defined which are expected to come from beam-gas or beam-halo events, cosmic rays or fake energy deposits from calorimeter noise or other hardware problems. The cut on bad jets is applied after the full event selection (see Chapter 7.2). If a bad jet is found, the event is disregarded for the analysis.

5.5. b-tagging

As already mentioned in Chapter 3, the top quark decays almost exclusively into a W-boson and a b-quark. Therefore the final state contains two b-quarks. An identification of one or more b-quarks leads to an improvement of the sample purity and a reduction of the combinatorial background. Hadrons containing b-quarks can be distinguished from light-jets and c-jets using their mean lifetime of $\mathcal{O}(1.6$ ps) [15]. Due to this long lifetime, b-jets decay at a mean distance of about $\mathcal{O}(0.5$ mm) from the primary vertex and are identified by the reconstruction of the secondary vertex. A sketch of the secondary vertex identification is shown in Fig. 5.8. In the r-ϕ-plane of the detector, a *distance of closest approach* is defined between the primary vertex and the track, along with the so-called *transverse and longitudinal impact parameters* d_0 and z_0. b-jets are more likely to have a positively signed transverse impact parameter than light- or c-jets. The impact parameter significance of d_0/σ_{d0} also gives a good separation.

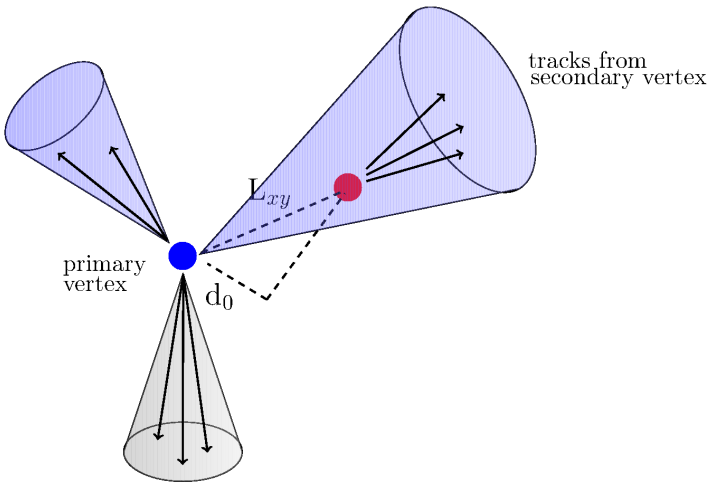

Figure 5.8.: Identification of b-jets by reconstruction of the secondary vertex.

Several b-tagging algorithms were developed at the ATLAS experiment and their performance has been studied in detail [115]. All b-tagging algorithms provide weights that are used to decide if a jet is considered tagged or not. For a certain cut value w_{cut}, the b-tagging efficiency and the light jet rejection is evaluated. The comparison of the light- and c-jet rejection as a function of the b-tagging efficiency is shown in Fig. 5.9. While the c-jet rejection is slightly better for the JetFitterCombNNc tagger, the MV1 tagger provides generally a higher light-jet rejection.

Quantity	value
Cut value	0.602
b-tagging efficiency	0.696
light-rejection	134
c-rejection	5

Table 5.4.: b-tagging peformance of the MV1 tagger for the working point with a b-tagging efficiency of about 70%.

The MV1 tagger is used for the analysis of the full 2011 data set. It makes use of the tagging weights of three different b-tagging algorithms: SV1, IP3D and JetFitter. These three weights are used as input to a neural network along with the jet p_{T} and η values. A short summary of the three tagging algorithms is given in the following:

SV1

SV1 is a secondary vertex tagger that provides a weight based on a likelihood ratio. Three input variables are used in the likelihood approach:

- All tracks that belong to the vertex are used to calculate the invariant mass.
- $\sum_i \mathrm{E}(\mathrm{track}_i,\mathrm{vertex})/\sum_j \mathrm{E}(\mathrm{track}_j,\ \mathrm{jet})$
- Number of vertices with two tracks.

IP3D

The IP3D tagger is also based on a likelihood approach and uses the 2D distribution of the transverse and longitudinal impact parameter significance.

JetFitter

The JetFitter algorithm is based on a Kalman Filter [116]. The algorithm searches for a line that contains the primary vertex as well as the vertices from b- and c-jets. Vertex information such as mass, momentum, track multiplicity and flight length significances are used in the likelihood.

5.5.1. b-tagging calibration

To account for differences between data and MC, the total b-tagging scale factor is calculated while taking into account the tagging and mistagging efficiencies per jet. This scale factor depends on the jet flavour and the b-tagging weight: if the weight for a b-jet is larger than the cut value that has been defined for a certain working point, the efficiency scale factor is applied. If it is smaller than this cut value, the inefficiency scale factor is used. Therefore scale factors have been evaluated for the tag- and mistag-rate for each jet flavour and a specific b-tagging efficiency:

$$SF_{\mathrm{flavour}}(p_T,\eta) = \frac{\epsilon^{data}_{\mathrm{flavour}}(p_T,\eta)}{\epsilon^{MC}_{\mathrm{flavour}}(p_T,\eta)} \quad . \tag{5.6}$$

The total event weight is then calculated as the product of the scale factors for each jet. The b-tagging efficiencies are obtained from the p_T^{rel} and the *system8* method while using jets in which muons originate from semileptonic decays of b-hadrons [117]. The $p_{\text{T}}{}^{\text{rel}}$ variable is the transverse momentum of the muon relative to the muon-jet axis [117] which gives a harder distribution for b-jets while providing similar results for c- and light jets. The *system8* method is less dependent on MC and uses a system of eight equations and variables to calculate the trigger efficiencies. The results from the $p_{\text{T}}{}^{\text{rel}}$ and *system8* method are combined. The total uncertainties on the scale factors range from 5% up to 19% for high-p_{T} bins. The efficiencies for c-jets are obtained from the decay of D^{*+} mesons with a total uncertainty of 12-25% [118]. The scale factors for the light jets have an uncertainty of 18-49% [119].

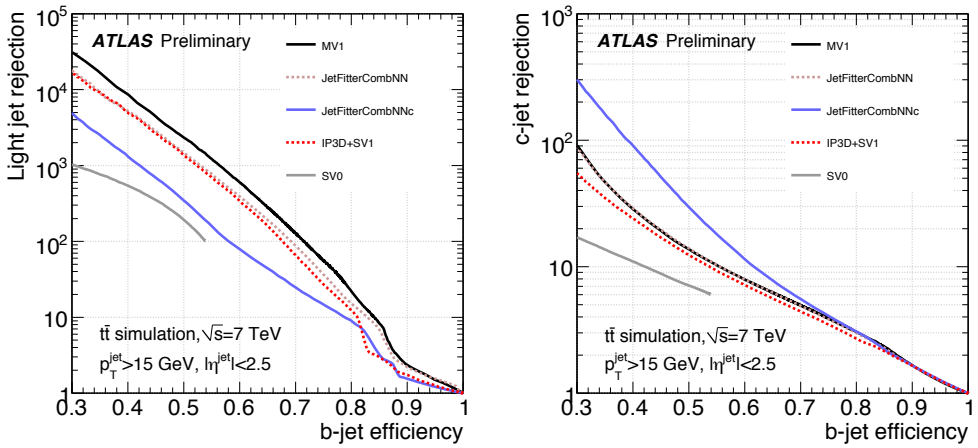

Figure 5.9.: Comparison of the performance for different b-tagging algorithms [117]. The light jet rejection (left) and the c-jet rejection (right) are shown as a function of the b-jet efficiency.

The b-,c- and light-quark jet scale factors are assumed to be uncorrelated and the systematic uncertainty has to be evaluated for each of these flavours separately. When calculating the uncertainty for one flavour, the efficiency and inefficiency scale factors belonging to this flavour need to be treated anti-correlated. If the jet-p_{T} is larger than the maximum p_{T}-value shown in Tab. 5.5, the SF from the last bin is used. The combined scale factors for the $p_{\text{T}}{}^{rel}$ and *system8* method are compared in Fig. 5.10 to the scale factors of other calibration methods.

jet flavour	dependence	SF type	p_{T}-range [GeV]
b	p_{T},η	efficiency	20-200
b	p_{T},η	inefficiency	20-200
c	p_{T},η	efficiency	20-200
c	p_{T},η	inefficiency	20-200
light	p_{T},η	efficiency	20-750
light	p_{T},η	inefficiency	20-200

Table 5.5.: Range of the jet-p_{T} for the efficiency and inefficiency scale factors for b-, c- and light-quark jets.

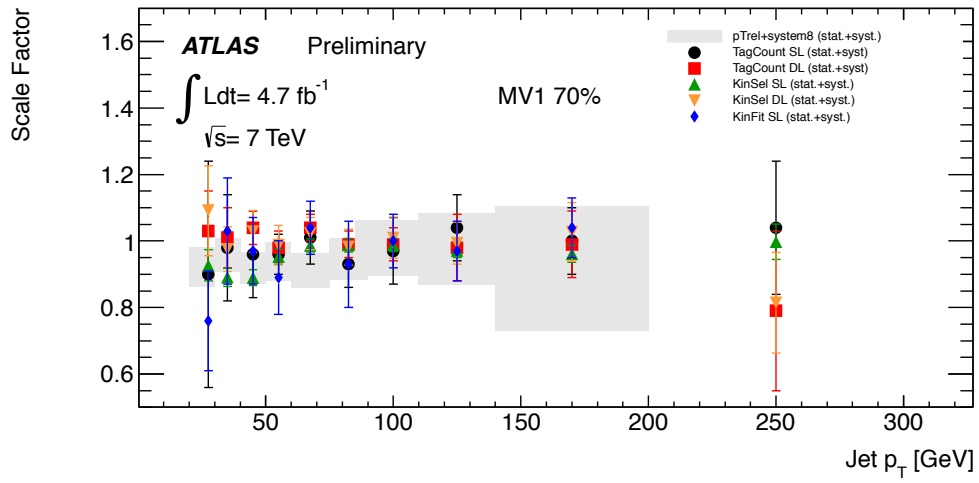

Figure 5.10.: Comparison of the b-tagging scale factor and the total uncertainties evaluated for the MV1 tagger for a b-tagging efficiency of about 70% for different calibration methods [120]. The combination of the $p_{\mathrm{T}}{}^{\mathrm{rel}}$ and *system8* methods is used for the analysis presented in this thesis.

5.6. Missing transverse energy

The vectorial sum of the particle momenta in the plane transverse to the beam axis created in the collision needs to be zero. Since neutrinos do not interact with the detector material, the so-called *missing transverse energy* E_T^{miss} is defined from the sum of all reconstructed objects:

$$-E_{x,y}^{miss} = E_{x,y}^{\mathrm{RefEle}} + E_{x,y}^{\mathrm{RefJet}} + E_{x,y}^{\mathrm{RefSoftJet}} + E_{x,y}^{\mathrm{RefMuon}} + E_{x,y}^{\mathrm{RefCellOut}} \tag{5.7}$$

The total missing transverse energy is then calculated from the respective x and y components:

$$E_T^{miss} = \sqrt{(E_x^{miss})^2 + (E_y^{miss})^2} \quad . \tag{5.8}$$

Calorimeter cells with an energy deposit are associated with one high-p_{T} object. The order of this association is as follows: electrons, jets, soft jets, muons. The cell is than calibrated according to the object calibration. If no object is found for a cluster, it is calibrated at EM scale and is considered in the cellout term. As explained in Chapter 5.4, all jets with $p_{\mathrm{T}} > 20$ GeV are calibrated to the EM+JES scale and contribute to the *jets* term while jets with p_{T} between 7-20 GeV are calibrated to the EM scale and contribute to the *soft jets* term. Tight electrons with $p_{\mathrm{T}} > 10$ GeV are included in the electron term. The muon term includes combined muons with $|\eta| < 2.5$ with a separate treatment for isolated and non-isolated muons. For the isolated muons (ΔR(muon track, jet) > 0.3) the calorimeter energy is included in the cellout term while for the non-isolated muons it is included in the jet term.

6. Signal and Background Modelling

The proper simulation of signal and background processes is essential for searches and precision measurements in high energy physics. The hard scattering process is simulated using Monte Carlo generators while the non-perturbative parts such as parton showering and hadronisation are modeled using PYTHIA [121] (which uses the Lund string fragmentation model) or HERWIG [122] (which is based on cluster hadronisation). The process chain for MC production continues with the detector simulation, digitisation of the calorimeter entries and tracker hits and the reconstruction of the full event. The computing model is based on the ATHENA framework [123, 124]. For the MC processes, the interaction of particles with the detector material is simulated using the GEANT4 package [125, 126], taking into account stable particles with $c\tau > 10$ mm.

Two different types of MC samples are created: fully simulated events and fast simulation with ATLFASTII which is used mainly for systematic studies but also for the production of the signal templates used in this thesis. The fast simulation is less CPU intensive and therefore samples with higher statistics can be generated. The fast simulation can be done in two ways. The first approach is to take the fast simulation both for the inner detector and muon spectrometer (based on the FATRAS code [127]) as well as fast calorimeter simulation. This leads to an event production faster by a factor of 100 [124]. The second approach uses the fast simulation only for the calorimeter, leading to an improvement by a factor of about 10 in contrast to the full simulation with GEANT4 [124]. The reconstruction of the MC events is done using the same algorithms as for data.

The MC samples used for this thesis are part of the MC11c campaign that uses Pythia6 [128] to simulate minimum bias events with the ATLAS AMBT2B(CTEQ6L1) tune [129]. The bunch spacing used in the simulation is 50 ns according to the conditions in data. The MC is reweighted according to the average number of interactions per bunch crossing, called $< \mu >$. As explained in Chapter 7, the data set needs to be split into four different data-taking periods corresponding to the detector conditions. The acceptance loss due to dead or unreachable modules is properly simulated in the MC samples according to the amount of data where they occur. In the baseline $t\bar{t}$-samples, the top mass was fixed to 172.5 GeV. Furthermore, the vector boson masses used in the generators were $m_W = 80.399$ GeV and $m_Z = 91.1876$ GeV. If not stated otherwise, the masses according to the PDG2010 values [130] were used. For m_b and m_c, the masses of the respective generator were used. The width of the W/Z-bosons are calculated perturbatively by PYTHIA6, whereas the top width is set to the NLO value of 1.320 GeV.
An overview over the simulated signal and background samples is given, followed by a description of the data-driven estimates. A detailed list of Monte Carlo samples used for the analysis can be found in Chapter A.3.

6.1. Signal Monte Carlo

The baseline $t\bar{t}$-sample is generated with MC@NLO version 4.01 [131] using HERWIG6.520 [122] for the hadronisation and showering and JIMMYv4.31 [132] for the underlying event model. The PDF used in this sample is CT10 [133]. The generator has been tuned with the JIMMY ATLAS AUET2 tune [134]. The theoretical production cross section for $t\bar{t}$-events at $\sqrt{s} = 7$ TeV yields at approximate NNLO precision: $166.78^{+16.5}_{-17.8}$ pb using HATHOR1.2 [39]. In the calculation, the MSTW2008 90 % NNLO PDF sets were used [135] that include the uncertainties on the PDFs and α_S according to [136]. This number was cross-checked using a NLO+NNLL calculation [137] implemented in the TOP++v1.0 tool [138].

For the templates used in the W-helicity analysis, the LO generator PROTOS [70, 139] has been interfaced with PYTHIA using the CTEQ6L1 PDF [140] set. These samples were simulated using the ATLFASTII package. PROTOS is the only generator available that allows to produce samples with either left-handed, right-handed or longitudinal polarisation of the W-bosons. The samples were generated separately for the lepton+jets and dilepton channel. Each sample contains about 500,000 events, leading to a sample size of about 7 fb^{-1} for each lepton+jets and 29 fb^{-1} for each dilepton sample. Further $t\bar{t}$-samples were used for the evaluation of systematic uncertainties. These are described in detail in Chapter 8.5.

6.2. Background Monte Carlo

The production of a W-boson with additional jets with the W-boson decaying into a charged lepton and its corresponding neutrino is the dominant background process for $t\bar{t}$-events. Samples with W+n light partons[1], W+$c\bar{c}/b\bar{b}$+m partons [2] and W+c+n partons are generated using the leading order MC generator ALPGEN [141] interfaced with HERWIG [122]. Since processes with n and with n+1 partons can lead to the same final state due to radiation of extra jets, the MLM matching [141] is applied which removes overlaps in phase space. The phase space overlap in the production of the W+light and W+heavy-flavour samples is also removed. The events are produced with a minimum transverse momentum of 15 GeV. The cross sections are corrected at NNLO using a k-factor of 1.52 for the $W + c$-samples and a k-factor of 1.2 for all other flavours. The overall normalisation is not taken from simulation but from a data-driven estimate that is explained in detail in Chapter 6.3.2. The heavy-flavour composition is taken from data as well, as described in Chapter 6.3.3.

The production of single top quarks has been simulated in two ways. The s-channel production as well as the associated production as described in Chapter 3.2 are produced using MC@NLO with the same settings as shown in Sec.6.1. Due to problems with the modelling in MC@NLO and HERWIG, however, the t-channel process was simulated using ACERMCv3.8 [142] interfaced to PYTHIA. To remove final states that are generated both for $t\bar{t}$- and Wt-channels, the diagram removal scheme is applied [143]. The corresponding production cross-sections are at approximate next-to-next-to leading order: $64.6^{+2.7}_{-2.0}$ pb [144] (t-channel), 4.6 ± 0.2 pb [145] (s-channel) and 15.7 ± 1.1 pb [146] (associated production).
The production of a Z-boson/γ^* with additional jets where the Z-boson decays into two charged leptons is generated using ALPGEN+HERWIG. In addition to the Z+n light parton samples with up to 5 inclusive partons, heavy-flavour samples are also generated, using Z+$b\bar{b}$ + m partons (m = 0,1,2,3-jet exclusive and 4-jet inclusive) events. The samples with light jets are again

[1] n = 0,1,2,3,4 excl and 5incl
[2] m = 0,1,2,3 excl and 4incl

splitted in samples with low Z masses (10 GeV $< M(l,l) <$ 40 GeV) and samples with higher masses (40 GeV $< M(l,l) <$ 2,000 GeV). The overlap in phase space between the samples with light and with heavy-flavour jets is removed. The cross sections are corrected at NNLO using k-factors of 1.25 for all samples. The uncertainty on the cross section is increasing with the jet bin according to the Berends-Giele scaling [147], leading to an uncertainty of 48 % for events with four jets.
Diboson production, namely WW, WZ and ZZ, is simulated using the leading order HERWIG generator. The cross sections are corrected with k-factors of 1.48 (WW), 1.3 (ZZ) and 1.6 (WZ). The uncertainty on the cross section is 5% as described in [148].

6.3. Data driven background estimates

6.3.1. Fake lepton background

The analysis presented in this thesis is carried out in the lepton+jets channel where one high-p_{T} electron or muon is expected. Apart from the prompt leptons that originate from the decay of a W- or Z-boson, mis-identified leptons can be selected for several reasons. Leptons, as defined in Chapter 5, are required to be isolated to reject leptons that are contained in heavy-flavour jets. Some of these jets however contain leptons that pass the selection criteria (so-called *fake isolation*). Another source of non-prompt leptons are pion and kaon decays. In the e+jets channel, the lepton can be *faked* by photon conversion or neutral pions, hence the background due to non-prompt leptons is often called *fake lepton* background. The cross section for jet production is large, leading to a non-negligible production of mis-identified leptons. These processes cannot be properly simulated by MC generators. Thus, a data-driven approach is used to measure the production rate and estimate the contribution to the analysis.

Matrix method

A widely used method is the so called *matrix method* that is applied both for the e+jets and μ+jets channel in the context of this thesis. To estimate the rate of the fake lepton background, samples containing loose and tight leptons are selected that differ in the isolation criteria. The specific criteria for the individual estimates are described below. The number of selected events with a loose lepton is expressed as the sum of events with a prompt (*real*) lepton and the number of events containing a *fake* lepton:

$$N^{\mathrm{loose}} = N^{\mathrm{loose}}_{\mathrm{real}} + N^{\mathrm{loose}}_{\mathrm{fake}} \quad . \tag{6.1}$$

Accordingly, the number of tight leptons is:

$$N^{\mathrm{tight}} = N^{\mathrm{tight}}_{\mathrm{real}} + N^{\mathrm{tight}}_{\mathrm{fake}} \quad . \tag{6.2}$$

The number of tight leptons can be expressed using the efficiencies of the real and loose leptons to survive the isolation cuts:

$$N^{\mathrm{tight}} = \epsilon_{\mathrm{real}} N^{\mathrm{loose}}_{\mathrm{real}} + \epsilon_{\mathrm{fake}} N^{\mathrm{loose}}_{\mathrm{fake}} \quad , \tag{6.3}$$

while the efficiencies are defined as:

$$\epsilon_{\mathrm{real}} = \frac{N^{\mathrm{tight}}_{\mathrm{real}}}{N^{\mathrm{loose}}_{\mathrm{real}}} \quad , \quad \epsilon_{\mathrm{fake}} = \frac{N^{\mathrm{tight}}_{\mathrm{fake}}}{N^{\mathrm{loose}}_{\mathrm{fake}}} \quad . \tag{6.4}$$

The rate of fake leptons that survive the tighter cuts can now be derived as:

$$N_{\text{fake}}^{\text{tight}} = \frac{\epsilon_{\text{fake}}}{\epsilon_{\text{real}} - \epsilon_{\text{fake}}}(N^{\text{loose}}\epsilon_{\text{real}} - N^{\text{tight}}) \quad . \tag{6.5}$$

An event weight is now calculated from Eq. 6.5. If the loose selection is applied, the event weight is calculated as:

$$w_{\text{loose}} = \frac{\epsilon_{\text{fake}}\epsilon_{\text{real}}}{\epsilon_{\text{real}} - \epsilon_{\text{fake}}} \quad , \tag{6.6}$$

while the event weight for the tight selection is calculated as:

$$w_{\text{tight}} = \frac{\epsilon_{\text{fake}}(\epsilon_{\text{real}} - 1)}{\epsilon_{\text{real}} - \epsilon_{\text{fake}}} \quad . \tag{6.7}$$

Events that also pass the tight selection are identical with the events in the data sample and have negative weights, while the loose events contribute with a positive weight. Therefore the matrix method allows also to model the shape of the fake lepton background.

μ+jets channel For the μ+jets channel, two different fake lepton estimates were used that are both based on the matrix method. The control region for the first method was chosen orthogonal to the signal region by inverting the transverse mass and triangular cut described in Chapter 7.2. The selection for the tight sample is otherwise the same as for the default selection. For the selection of the loose sample, the track and calorimeter isolation criteria were dropped. The jet-muon overlap removal was applied to both samples. The fake efficiency was estimated in the control region while the signal efficiency was obtained from a tag-and-probe method using $Z \to \mu^+\mu^-$ events. The efficiencies are parameterised in η and p_{T}.
The second method makes use of the fact that muons in heavy-flavour jets have a relatively large impact parameter. The impact parameter significance was therefore used to distinguish between real and non-prompt leptons. The average of the two estimates was taken as default value. The statistical uncertainty for events with one b-tag is 20 % while events with ≥ 2 b-tags have an uncertainty of 40 %. The shape uncertainty is evaluated by a comparison of the two separate methods to the averaged distribution.

e+jets channel The tight sample in the e+jets channel was selected using the standard event selection described in Chapter 7.2. For the loose sample, no isolation criteria were applied. Instead of tight electrons, medium electrons were used and a veto on electrons from converted photons was applied. The signal efficiency was estimated using a tag-and-probe method on $Z \to e^+e^-$ events. The fake efficiency was derived in a control region that was defined by an inverted E_T^{miss}-cut: $E_T^{\text{miss}} < 20$ GeV. The statistical uncertainty of the estimate amounts to 50 %. The systematic uncertainties on the fake efficiency was obtained from a 5 GeV variation of the E_T^{miss}-cut that defines the control region. The uncertainty on the signal efficiency was obtained from a variation of the fit and signal region that were used in the tag-and-probe method.

6.3.2. Data driven W+jets normalisation

The dominating background process in the lepton+jets channel is the production of a W-boson with additional jets. The uncertainties on the corresponding cross sections are rather large $\mathcal{O}(50\ \%)$. To decrease these uncertainties, a data driven estimate is applied to obtain the overall normalisation of the W+jets process from data, while the shape of the distributions are modeled by MC. In proton-proton interactions at the LHC, the production rate for W^+-bosons is about a factor of 2 larger than the rate for W^--bosons due to the higher parton density of u-quarks compared to d-quarks. Although the production cross sections for the W+n+jets processes have large uncertainties, the ratio $r = \sigma(pp \to W^+)/\sigma(pp \to W^-)$ can be more precisely calculated [135, 149]. This is used in the following for the data-driven estimate.
The same event selection that is used for the measurement of the W-helicity fractions is applied. Leptonically decaying W-bosons allow to identify the charge of the boson by identifying the charge of the corresponding lepton. Events from single-top production are subtracted since they also lead to a charge-asymmetric contribution. The data-driven heavy-flavour scale factors that are described in Sec. 6.3.3 are applied to correct the heavy-flavour composition. The pretag W+jets yield can be expressed as the sum of positively and negatively charged W-bosons:

$$N_W = N_{W^+} + N_{W^-} = \left(\frac{N_{W^+}^{MC} + N_{W^-}^{MC}}{N_{W^+}^{MC} - N_{W^-}^{MC}} \right) (D^+ - D^-) \tag{6.8}$$

$$= \left(\frac{r_{MC} + 1}{r_{MC} - 1} \right) (D^+ - D^-) \quad , \tag{6.9}$$

with $r_{MC} = \sigma(pp \to W^+)/\sigma(pp \to W^-)$ and $D^{\pm}$ describing the data events identified bye the charge of their respective lepton in the final state. The estimate was performed in the 2-jet exclusive bin on pretag events. The estimates and their uncertainties for higher jet bins were extrapolated and a correction factor for b-tagged events was applied. The final scale factor for the 4-jet inclusive bin was estimated to 0.825 for the e+jets channel and 0.874 for the μ+jets channel with an overall uncertainty of 17 %. This uncertainty is dominated by the uncertainty on the heavy-flavour composition and the fake lepton background. The former will be discussed in following.

6.3.3. W+jets heavy-flavour composition

While the method described in Section 6.3.2 only gives an estimate for the total W+jets yield normalisation, another set of scale factors is neccessary to correct the heavy-flavour composition of the generated samples. To extract this heavy-flavour composition from data, an event selection was performed to select W+jets events. The respective yields for the data-driven fake lepton estimate and the simulated $t\bar{t}$, single top, diboson and Z+jets estimates were subtracted. The scale factors for the $b\bar{b}$ and $c\bar{c}$ processes were derived simultaneously under the assumption that the ratio SF($b\bar{b}$)/SF($c\bar{c}$) is constant. The scale factors were evaluated on the pretag sample for the 2-jet exclusive bin as shown in Tab. 6.1 and were extrapolated into the higher jet bins while taking into account an additional 25 % uncertainty per jet bin. This additional uncertainty was evaluated by varying the factorisation and renormalisation scale as well as the parton density function in the ALPGEN generator. The scale factors only change the heavy-flavour composition of the pretag/tagged W+jets estimate, while the pretag normalisation is unchanged.

The uncertainty of the scale factors is dominated by uncertainties due to the jet energy scale, fake lepton normalisation and flavour tagging. The scale factors for events with exactly two jets are listed along with the corresponding uncertainties in Tab. 6.1.

Channel	SF($b\bar{b}/c\bar{c}$)	SF(c)	SF(light)
e+jets	1.22 ± 0.29	0.95 ± 0.23	0.98 ± 0.07
μ+jets	1.36 ± 0.30	0.71 ± 0.31	1.01 ± 0.08

Table 6.1.: Scale factors for the different heavy-flavour processes estimated for events with exactly two jets. The uncertainties shown contain statistical and systematic uncertainties.

7. Data Sample and Event Selection

7.1. Description of the Data Set

The data analysed for the measurement presented in this thesis was recorded with the ATLAS experiment in 2011 in proton-proton collisions at $\sqrt{s} = 7$ TeV. A total amount of 5.61 fb^{-1} of data were delivered by the LHC and 5.25 fb^{-1} were recorded by the ATLAS experiment (see Fig. 7.1). This leads to a data-taking efficiency of about 93.6%. Only data with fully operational detector and good beam and data quality is used in the analysis. The runs which fulfil the requirements are summarised in so-called *GoodRunLists*. These GoodRunLists are provided for the full 2011 data set. The total integrated luminosity that fulfilled all data-quality requirements amounts to 4656 $\pm$ 84 pb^{-1} (relative uncertainty of 1.8 % [150]). The bunch spacing is 50 ns with a maximum number of bunches per beam of 1380.

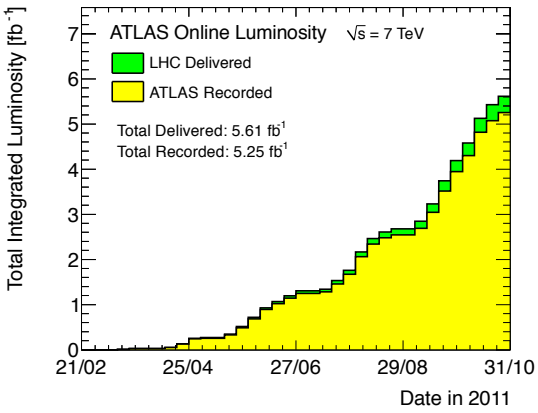

Figure 7.1.: Development of luminosity delivered and recorded by the ATLAS experiment in 2011 [151].

Data periods

The data periods are split into four parts, depending on the different detector conditions as shown in Tab. 7.1. In the beginning of period E, six front-end boards (FEBs) were unreachable due to failing optical links. These FEBs are located in the barrel part of the EM LAr calorimeter[1] in layer 2 (four FEBs) and layer 3 (two FEBs). The four FEBs in layer 2 were recovered in the beginning of period I. Furthermore, modules in the tile calorimeter and the pixel detector died during the data taking period. The acceptance loss due to the non-operational modules is simulated in the MC samples (see beginning of Sec. 6).

[1] The dead FEBs are located at $0 < \eta < 1.475$, $-0.791 < \phi < -0.595$.

Data period	Run Numbers	Lumi	Fraction of total Lumi [%]	Number of dead/missing modules LAr calo	Tile calo	Pixel	b-layer
B-D	178044–180481	176.25	3.79	0	5	54	7
E-H	180614–184169	937.71	20.14	6	6	56	7
I-K	185353–187815	1140.00	24.49	2	7	62	10
L-M	188902–189751	2401.77	51.59	2	9	63	10

Table 7.1.: Data periods summarised in periods with similar detector conditions. The missing/dead modules are correctly simulated in the MC samples.

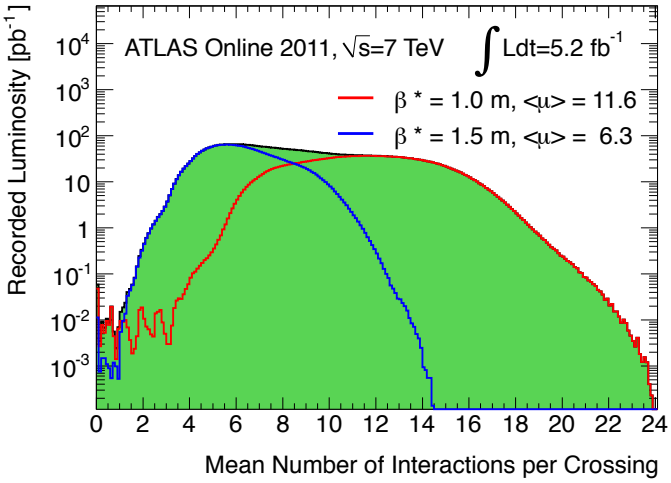

Figure 7.2.: Increasing number of the average proton-proton interactions per bunch crossing [152]. The blue distribution describes the conditions in the first part of the data-taking period while the red distribution shows the conditions after the beam was focused by decreasing the emittance β during the technical stop in September 2011.

Pileup conditions

Measurements at the LHC can be affected by in- and out-of-time pileup, as described in Chapter 4.1. In the first part of the data-taking period in 2011, as shown in Fig. 7.2, the average number of interactions per bunch crossing, $< \mu >$, was 6.3. After the beam emittance was decreased, $< \mu >$ increased to 11.6. The measurement must be tested for a possible dependence on the number of primary vertices or on the average number of interactions per bunch crossing. This is further described in Chapter 8.5.

7.2. Event Selection

The measurement presented in this thesis is carried out in the lepton+jets channel which is characterised by one high-p_{T} lepton, at least four high-p_{T} jets and missing transverse energy due to the undetected neutrino.
For the selection of data events, a *GoodRunList* is defined that ensures the selection of events with good data quality and stable data taking conditions for the ATLAS detector. As explained in the respective object definitions in Chapter 5, corrections are applied to the simulated events for the leptons, jets and missing transverse energy before performing the event selection described below. The following criteria are used both for the e+jets and for the μ+jets channel if not stated otherwise.

- The EventFilter trigger has to be fired for the respective data taking periods as explained in Tab. 5.1 and Tab. 5.3.
- To reject non-collision background, a good primary vertex with at least five tracks is required.
- Electrons and muons are selected according to the definitions introduced in Chapter 5. Only events with exactly one good electron (muon) are selected.
- The selected offline electron (muon) needs to match the trigger object using the matching criterion: ΔR(offline lepton, trigger lepton) < 0.15.
- A combined muon is not allowed to share an inner detector track with a good electron.
- The full event is rejected if it contains a loose bad jet with $p_{\mathrm{T}} > 20$ GeV and E > 0.
- The transverse mass[2] of the W-boson has to fullfil $m_{T,W} > 30$ GeV in the e+jets channel. In the μ+jets channel, a triangular cut is applied to reduce background from fake isolation: $E_T^{\mathrm{miss}} + m_{T,W} > 60$ GeV (μ+jets).
- The cuts for the missing transverse energy are $E_T^{\mathrm{miss}} > 30$ GeV (20 GeV) for the e+jets (μ+jets) channel.
- Using the jet definition introduced in Chapter 5.4, at least four good jets are required for the event to be selected. An additional cut on the Jet Vertex Fraction ($|\mathrm{JVF}| > 0.75$) is applied, leading to a reduced influence of in-time pileup.
- At least one of the jets selected in the event has to have a b-tag (using the MV1 tagger and cut values as explained in Sec. 5.5).

An additional cut is applied that is related to the reconstruction of $t\bar{t}$-events that will be described in more detail in Chapter 8.1. In the reconstruction, a kinematic likelihood fit is performed, while the fit is carried out using the Minuit package. If this fit does not converge, the event is not considered in the analysis. This effect on the event yield is on average 0.2 %, as described in Appendix A.3. The event yields and control distributions for the pretag selection are shown in the Appendix A.1.

[2] The transverse W-mass is defined as $m_{T,W} = \sqrt{2p_T^l p_T^\nu (1 - \cos(\phi^l - \phi^\nu))}$, with p_T^ν being the missing transverse momentum.

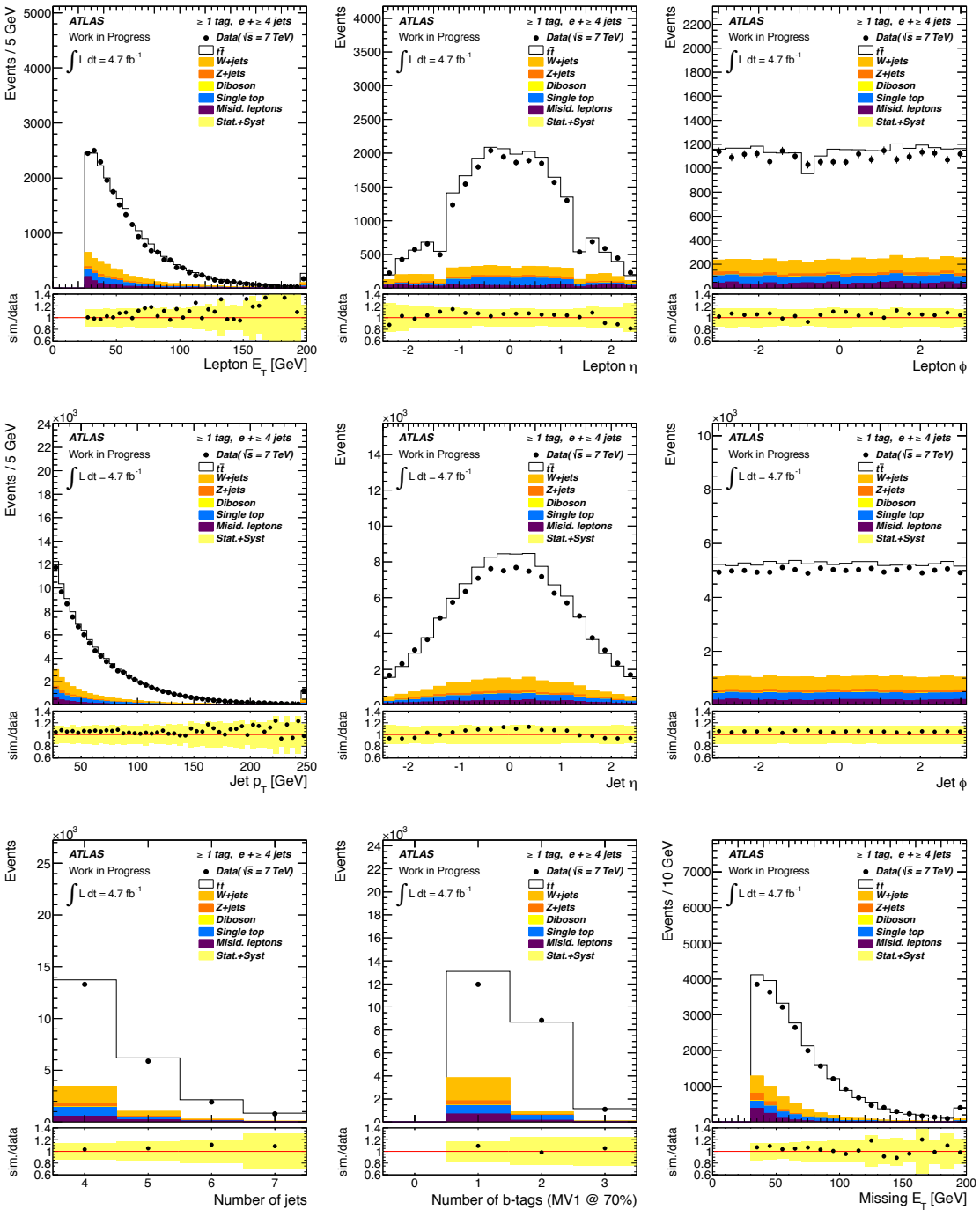

Figure 7.3.: Comparison between data and MC prediction in the e+jets channel for lepton and jet quantities as well as the missing transverse energy while using events with at least one b-tag. The yellow band in the residual distributions contains beside the statistical uncertainty further uncertainties on the cross-section normalisation, jet and lepton energy scales and resolutions, scale factors and the luminosity. For the W+jets contribution, also the shape and heavy flavour uncertainties are included.

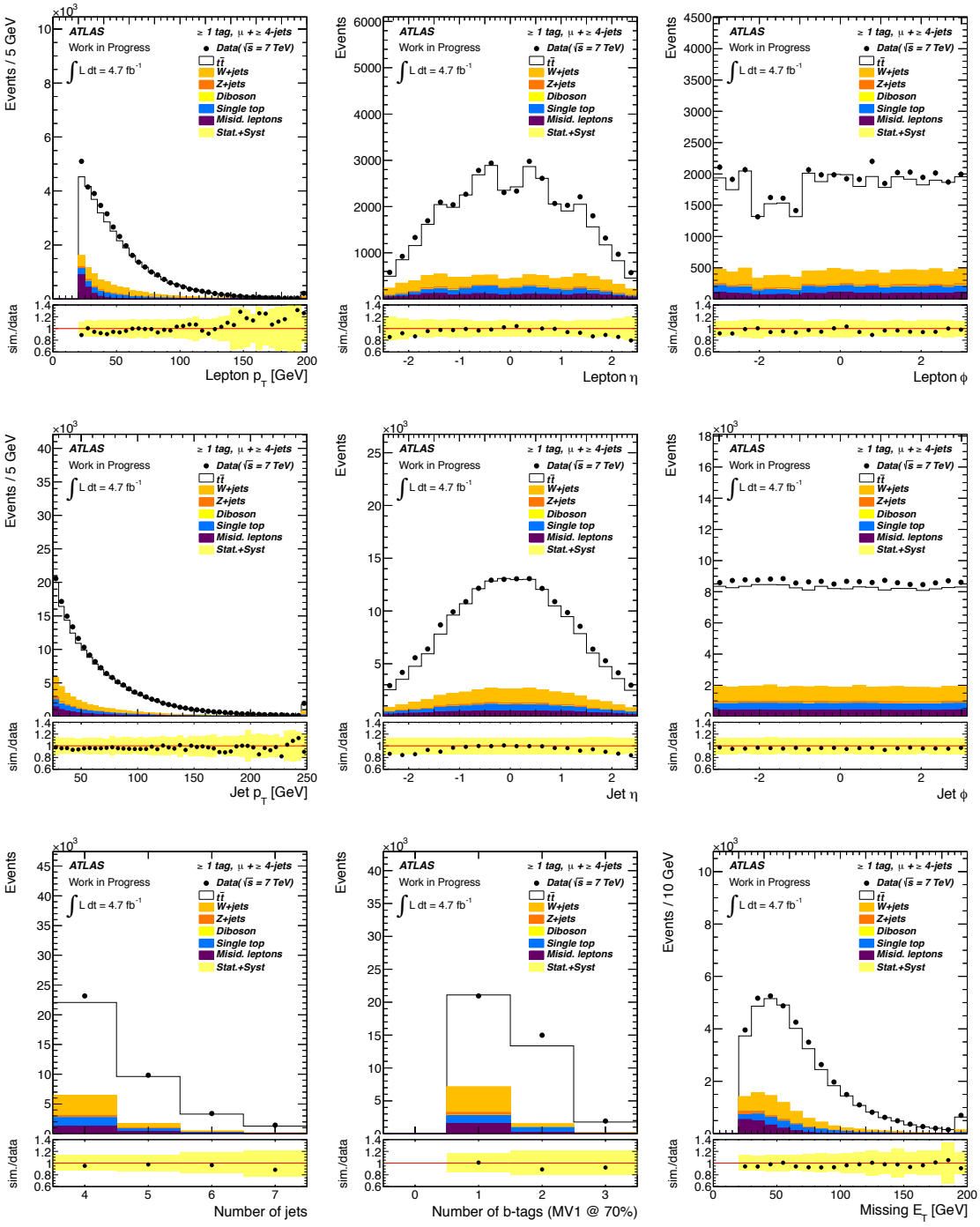

Figure 7.4.: Data/MC comparison in the μ+jets channel for lepton and jet quantities as well as the missing transverse energy while using events with at least one b-tag. The yellow band in the residual distributions contains beside the statistical uncertainty further uncertainties on the cross-section normalisation, jet and lepton energy scales and resolutions, scale factors and the luminosity. For the W+jets contribution, also the shape and heavy flavour uncertainties are included.

Table 7.2 shows the event yields for the e+jets (left) and the μ+jets channel (right). The PROTOS generator is used for the simulation of the $t\bar{t}$-events. The uncertainties shown in the table contain the statistical uncertainty as well as the uncertainties due to the jet and lepton energy scales and resolutions, the lepton and b-tagging scale factors and the luminosity uncertainty of 1.8% [150]. For the W+jets contribution, also the shape and heavy flavour uncertainties are included. The simulated samples are normalised to the cross sections described in Chapter 6. The relative normalisation uncertainties are therefore 10.7 % on the $t\bar{t}$-sample and 17 % on the W+jets contribution according to the data-driven estimate. The Z+jets cross section uncertainty is interpolated according to the Behrends-Giele scaling from an overall 4% uncertainty to the higher jet bins adding 24 % uncertainty per jet bin in quadrature. This results into 48% for the 4 jet bin. The overall normalisation uncertainties for the single top and diboson processes are 7 % and 5 %, respectively. The normalisation uncertainties on the data-driven estimate for the misidentified leptons is 50 % for the e+jets channel. For the μ+jets channel, 20% uncertainty is applied to events with exactly one b-tag and 40% to events with more than one b-tag, leading to an overall uncertainty of 23 %.

	e+jets		μ+jets	
Process	Events	Uncertainty	Events	Uncertainty
$t\bar{t}$ (PROTOS)	18129	2868	27500	4155
W+jets (DD norm.)	2294	1574	4457	3022
Misid. leptons (DD)	843	422	1774	406
Single Top	1178	217	1965	343
Z+jets	445	299	479	358
Diboson	46	23	73	36
Total predicted	22935	3319	36248	5178
Observed	21906		37845	
S/B	3.77		3.14	

Table 7.2.: Event yields for the e+jets (left) and μ+jets channel (right) after the selection of events with at least four jets, one charged lepton and missing transverse energy. At least one of the selected jets is required to have a b-tag.

In the e+jets channel, the number of predicted events is larger than the number of observed events while for the μ+jets channel more events are observed than predicted. In both channels, the difference is covered by the overall uncertainty.
When comparing the data/MC distributions for the jets and the leptons shown in Fig. 7.3 and 7.4, one observes that the differences are covered by uncertainties for most of the distributions. However, the systematic uncertainties are assumed to be fully uncorrelated which could lead to an overestimation of the total uncertainty. In the lepton-p_{T} (E_T) spectrum, larger discrepancies are seen at high p_{T}. To test the influence of these badly modelled events, the data fit has been performed for the full data set as well as for a subset of events with a $p_{\mathrm{T}}/E_T < 150$ GeV. The comparison is shown in Appendix A.5. The two-dimensional fit was performed on both samples. A small change was visible which was however covered by the statistical uncertainty. For the μ+jets channel, a larger discrepancy is observed at low p_{T} pointing to problems in the muon isolation. Since a LO generator (with LO PDF) is used for the signal modelling, additional effects can be seen in the shapes of the jet-rapidity. The use of an NLO PDF is expected to improve the data/MC agreement.

8. Analysis Strategy and Uncertainty Evaluation

The measurement described in the following is carried out in the lepton+jets channel. At least four jets are required in the selection, while at least one of them has to have a b-tag. The observable used to extract the W-helicity fractions is the angular distribution of the charged lepton in the rest frame of the W-boson (see Chapter 3.4.1). The reconstruction method and its performance are discussed in Section 8.1, followed by the description of the template method in Section 8.2. The validation of the template method is presented in Section 8.3. Finally, the evaluation of the statistical and systematic uncertainties are described in Section 8.4 and 8.5, respectively.

8.1. Event Reconstruction

To calculate the angle between the charged lepton and the negative direction of the b-quark in the W-boson rest frame, the $t\bar{t}$-event needs to be fully reconstructed. The four jets with the highest transverse momentum are chosen for the reconstruction. The most probable jet-parton association has to be found. Since the two light jets from the hadronically decaying W-boson are indistinguishable, twelve possible jet-parton assignments are considered. To get the best permutation for the calculation of $\cos\theta^*$, a kinematic likelihood approach is used. First, the likelihood used in the kinematic fit is introduced. The separate components of the likelihood are discussed and performance studies of the method are presented.

8.1.1. Kinematic Likelihood Fits

The information of the selected lepton, jets and missing transverse energy are used in the event reconstruction. The corresponding likelihood is defined in Eq. 8.1 [153] and is the product of several subcomponents that will be explained in the following. This reconstruction method is part of the KLFitter package.

$$\begin{aligned}\mathcal{L} = & BW(m_{q_1q_2}|m_W,\Gamma_W)\cdot BW(m_{l\nu}|m_W,\Gamma_W)\cdot \\ & BW(m_{q_1q_2b_{had}}|m_{top},\Gamma_{top})\cdot BW(m_{l\nu b_{lep}}|m_{top},\Gamma_{top})\cdot \\ & W(\tilde{E}_{jet_1}|E_{b_{had}})W(\tilde{E}_{jet_2}|E_{b_{lep}})W(\tilde{E}_{jet_3}|E_{q_1})W(\tilde{E}_{jet_4}|E_{q_2})\cdot \\ & W(\tilde{E}_x^{miss}|p_{x,\nu})W(\tilde{E}_y^{miss}|p_{y,\nu})\cdot \\ & \left\{ \begin{array}{ll} W(\tilde{E}_l|E_l) & (l \mathrel{\hat{=}} \text{electron}) \\ W(\tilde{p}_{T,l}|p_{T,l}) & (l \mathrel{\hat{=}} \text{muon}) \end{array} \right\}\end{aligned} \tag{8.1}$$

The four-vectors of the measured jets and leptons are used as input for the likelihood. The direction of the particles are assumed to be well-measured. The measured energies $\tilde{E_{\text{jet}}}$, $\tilde{E}_l$ and the momenta $\tilde{p}_{T,l}$ and $\tilde{E}_x^{miss}$,$\tilde{E}_y^{miss}$ are mapped to the quantities of the final state particles using *transfer functions* W. Further information of these transfer functions is given in Chapter 8.1.2.

Breit-Wigner terms, BW, are used for the W-bosons and the top-quarks, respectively. The W-boson mass is fixed to 80.4 GeV with a width of 2.1 GeV.
The pole-mass of the top-quark, m_{top}, can either be used as a free parameter in the fit or be fixed to a certain value. The top-quark width is set to 1.5 GeV. The log-likelihood is now calculated for all possible permutations. The corresponding event probability is multiplied by the b-tag weight w_{btag} for each jet. Since two of the jets in the final state are supposed to be b-jets, the b-tagging information can be used to increase the reconstruction efficiency. As explained in Chapter 5.5, the b-tagging efficiency of the used algorithm is $\epsilon = 0.7$ with a light jet rejection rate of R = 134. If now a b-tagged jet takes the position of a b-jet, the corresponding weight is multiplied to the event probability. If it takes the position of a light jet, the weight is 1/R. The weighting factors for each possible scenario are shown in Eq. 8.2:

$$w_{\mathrm{btag}} = \left\{ \begin{array}{c} \epsilon,\ b_{\mathrm{had}} \text{ was } b\text{-tagged} \\ (1-\epsilon), b_{\mathrm{had}} \text{ was not } b\text{-tagged} \end{array} \right\} \cdot \left\{ \begin{array}{c} \epsilon,\ b_{\mathrm{lep}} \text{ was } b\text{-tagged} \\ (1-\epsilon), b_{\mathrm{lep}} \text{ was not } b\text{-tagged} \end{array} \right\} \cdot \left\{ \begin{array}{c} \frac{1}{R},\ q_1 \text{ was } b\text{-tagged} \\ (1-\frac{1}{R}), q_1 \text{ was not } b\text{-tagged} \end{array} \right\} \cdot \left\{ \begin{array}{c} \frac{1}{R},\ q_2 \text{ was } b\text{-tagged} \\ (1-\frac{1}{R}), q_2 \text{ was not } b\text{-tagged} \end{array} \right\} \tag{8.2}$$

The jet-parton assignment with the highest probability is chosen for the event reconstruction. The log-likelihood distribution for the e+jets and μ+jets channel is shown in Fig. 8.1 for data and simulated events. The distributions agree well within the uncertainties that are shown by the yellow band.

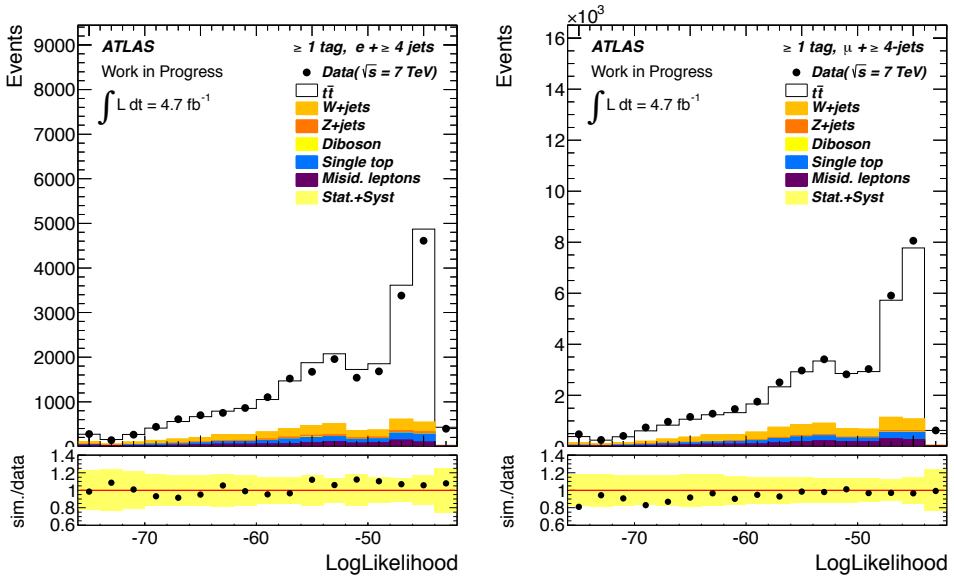

Figure 8.1.: Distribution of the logarithmic likelihood values obtained from the kinematic likelihood for the best jet-parton assignment for the e+jets (left) and the μ+jets channel (right). The yellow error band contains besides the statistical uncertainties also the normalisation uncertainties as well as the uncertainties due to JES, JER, b-tagging, LES, LER and the luminosity uncertainty of 1.8%. For the W+jets contribution, also the shape and heavy-flavour uncertainties are included.

8.1.2. Transfer Functions

Transfer functions are extracted from simulation which relate the energies and momenta from particle to parton level. The transfer functions are obtained from $t\bar{t}$-events generated with the MC@NLO generator[1], separately for light jets, b-jets, electrons and muons. The parameterisation is chosen differently for separate η-regions according to the detector geometry and for different energies. The reconstructed objects used for the transfer functions are defined as explained in Chapter 5. In addition to the standard $t\bar{t}$-selection described in Chapter 7.2, the selected reconstructed objects are required to be matched to the truth objects. The matching criteria are discussed in the following.

Matching criteria

The matching criterion for the jets used for the transfer function extraction is based on the distance parameter ΔR between the jet and the parton. The following condition has to be fulfilled:

$$\Delta\mathrm{R}(\text{jet, parton}) < 0.3 \quad .$$

An event is therefore called *fully matched*, if all jets can be matched unambiguously to their respective partons. For this analysis it is not neccessary to distinguish between the light jets coming from the hadronically decaying W-boson, therefore the term *fully matched* describes the correct matching of the b-jets and the W-boson. The matching procedure is required to be bijective: each jet is only allowed to be matched to one parton and vice versa, otherwise the event is considered to be *unmatched*. The matching efficiency is $\mathcal{O}(28\ \%)$ as shown in Tab. 8.1.

Parameterisation

The transfer functions are parameterised using the sum of two Gaussian distributions:

$$W(\Delta E) = \frac{1}{\sqrt{2\pi}(p_2 + p_3 p_5)} \left[e^{\frac{-(\Delta E - p_1)^2}{2p_2^2}} + p_3 \cdot e^{-\frac{(\Delta E - p_4)^2}{2p_5^2}} \right] \quad , \tag{8.3}$$

with $\Delta E = (E_{\text{true}} - E_{\text{reco}})/{E_{\text{true}}}^2$. The parameters p_i are also dependent on E_{true}:

$$\begin{aligned} p_1 &= a_1 + b_1 \cdot E_{\text{truth}} \\ p_2 &= a_2/\sqrt{E_{\text{truth}}} + b_2 \\ p_3 &= a_3 + b_3 \cdot E_{\text{truth}} \\ p_4 &= a_4 + b_4 \cdot E_{\text{truth}} \\ p_5 &= a_5 + b_5 \cdot E_{\text{truth}} \quad . \end{aligned}$$

For each particle type and η-region, the parameters a_i and b_i are obtained by a global fit. Since for high particle energies the Monte Carlo statistics is very small, the transfer functions are extrapolated in those regions. In contrast to the electrons and jets, the transfer functions for

[1] Having the highest sample statistics (about 15 million events), MC@NLO was chosen do derive the transfer functions.

[2] E_{true} describes either the parton or the electron energy.

muons are dependent on the transverse momentum. All parameters p_i have a linear dependence on $p_{\mathrm{T,\,truth}}$:

$$p_i = a_i + b_i \cdot p_{\mathrm{T,\,truth}} \quad .$$

For a given true energy (transverse momentum), the integral over the reconstructed quantity is normalised to unity. Figure 8.2 shows example transfer functions for light jets and b-jets in different η-regions.

8.1.3. Performance of the Kinematic Fit

The performance of a reconstruction algorithm is measured by the so-called *reconstruction efficiency* ϵ_{reco}. It is defined as follows:

$$\epsilon_{\mathrm{reco}} = \frac{\text{Number of correctly reconstr. events}}{\text{Number of fully matched events}} \quad . \tag{8.4}$$

Only events that pass the standard $t\bar{t}$-selection as described in Chapter 7.2 are considered in the following. The number of fully matched events contains by definition only lepton+jets events with an electon or muon in the final state. The kinematic fit for the underlying analysis is performed with the four highest p_{T} jets. The matching efficiency for this scenario is $\mathcal{O}(28$ %) both for e+jets and μ+jets events as shown in Tab. 8.1. Furthermore, the reconstruction efficiency can be significantly increased by fixing the top-quark mass instead of using it as a free parameter. Comparisons are shown in Tab. 8.1 and in Fig. 8.3. The absolut increase in the reconstruction efficiency is about 7.5 % in the e+jets channel and 8.2% in the μ+jets channel when fixing the top-quark mass. If the jets are assigned randomly to the partons, the reconstruction efficiency is significantly lower: $\epsilon_{\mathrm{reco}} = 8.33$ %.

channel	m_{top} [GeV]	$\epsilon_{\mathrm{matching}}$	ϵ_{reco} (full event)	ϵ_{reco} (b_{lep})
e+jets	free	0.2839(1)	0.6905(1)	0.7846(1)
e+jets	fixed to 172.5	0.2836(1)	0.7663(1)	0.8556(1)
μ+jets	free	0.2859(1)	0.6832(1)	0.7773(1)
μ+jets	fixed to 172.5	0.2855(1)	0.7651(1)	0.8541(1)

Table 8.1.: Reconstruction efficiencies for the e+jets and μ+jets channel where the kinematic fit is either performed using the top-quark mass as a free parameter or fixing the mass to 172.5 GeV. The corresponding uncertainties are shown. The setup with the fixed top-quark mass leads to a significant improvement of ϵ^{reco} by more than 7 % in the e+jets channel and more than 8 % in the μ+jets channel. The last column shows the reconstruction efficiency for the b-quark from the leptonic side only.

To improve the reconstruction efficiency, the setup with fixed top-quark mass is used for the following analysis.

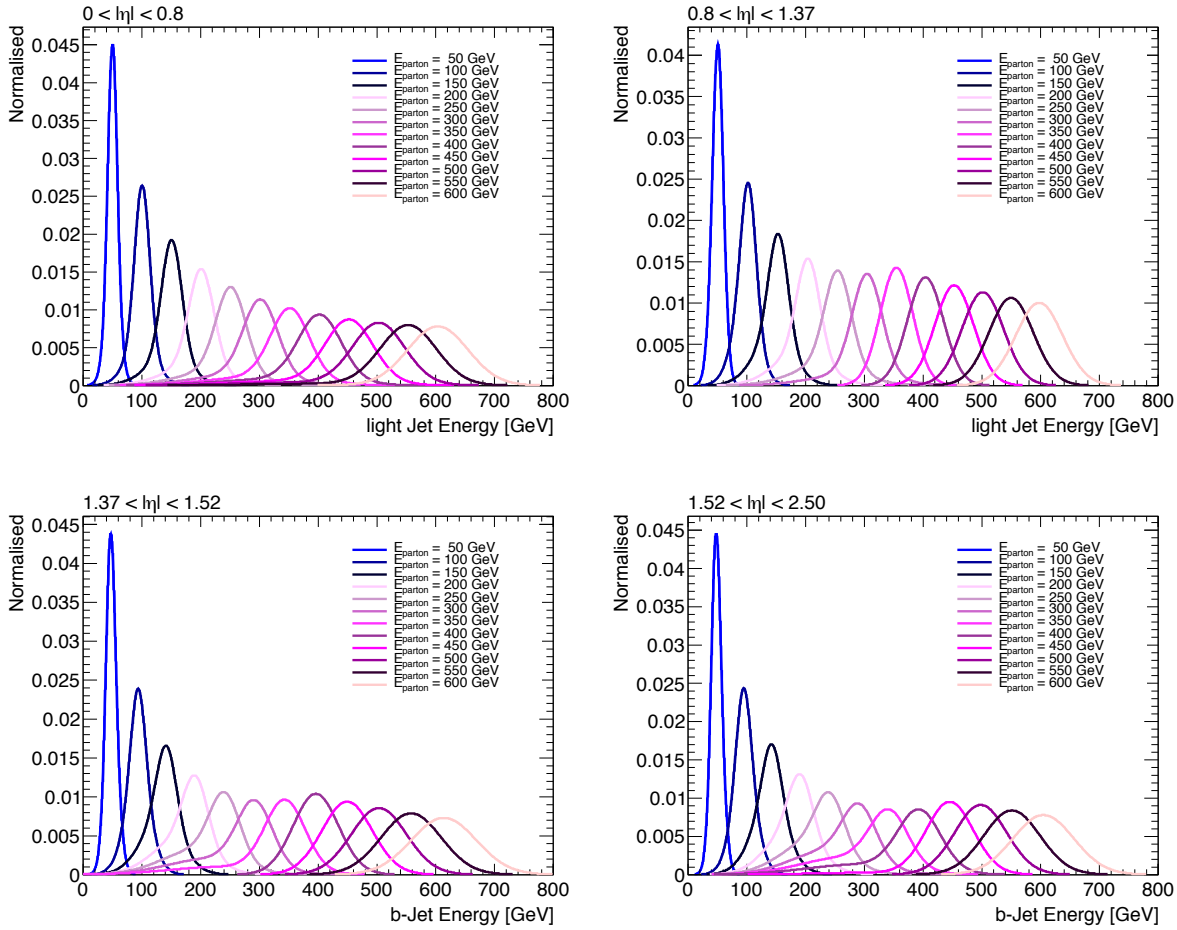

Figure 8.2.: Transfer functions for light jets (upper plots) and b-jets (lower plots) extracted from Monte Carlo simulation in steps of 50 GeV for the parton energy. The transfer functions are determined for different $|\eta|$-regions that are chosen such that they match the detector geometry.

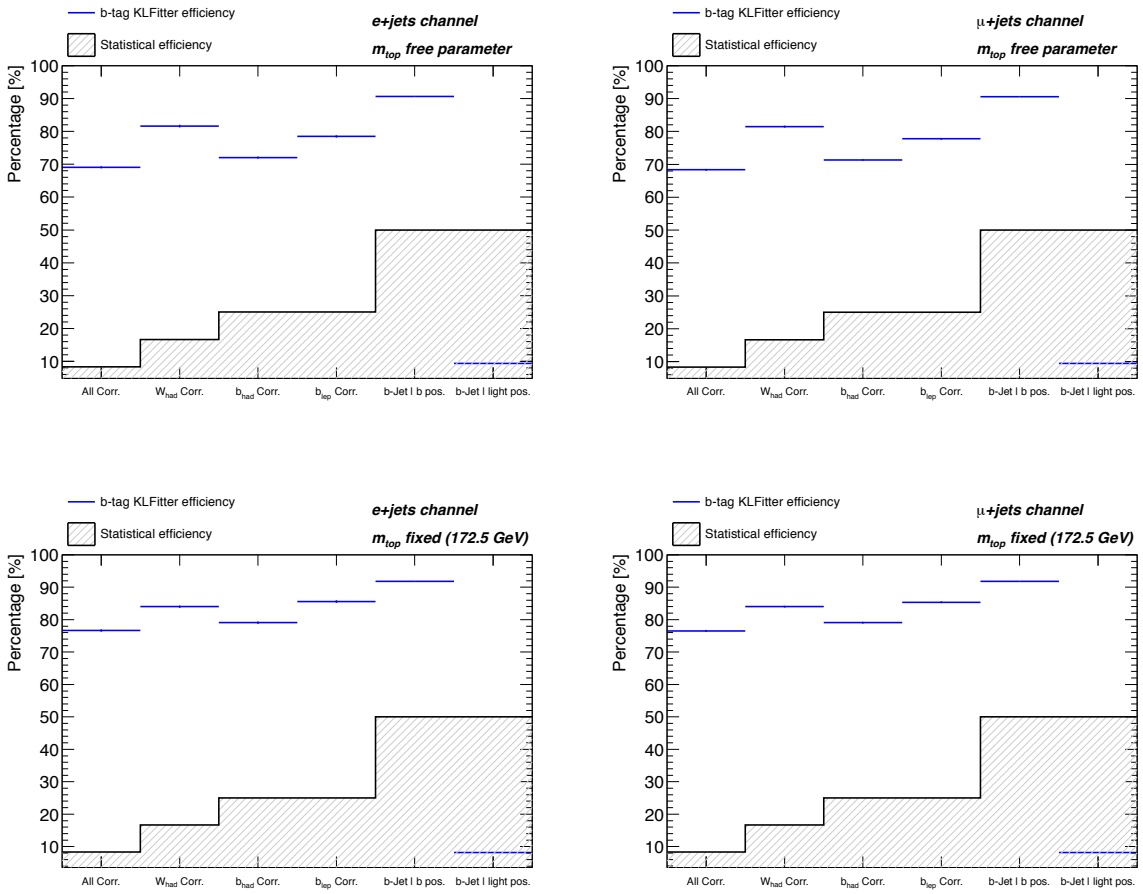

Figure 8.3.: Comparison of the reconstruction efficiency (only fully matched events are considered) for random jet-parton assignments (hatched area) and the efficiency of the kinematic likelihood fit. b-tagging information is used to find the best jet-parton assignment. The upper plots show the reconstruction efficiencies for a likelihood where the top-quark mass is a parameter of the kinematic fit while the lower plots show the reconstruction efficiencies for a likelihood where the top-quark mass has been fixed to 172.5 GeV. The setup with the fixed top-quark mass shows a significant increase of correctly reconstructed $t\bar{t}$-events.

8.2. Template Fit

For the results presented in this thesis, the W-helicity fractions are obtained by comparing the shape of data and simulated distributions using a binned likelihood fit. This allows to fully exploit the shape of the angular distribution of the lepton. Three signal and three background templates were created which are compared in Fig. 8.4 for the e+jets channel (left) and the μ+jets channel (right). The event reconstruction presented in the previous subchapter was applied. As described in Eq. 3.19, the W-helicity fractions are dependent on the top-quark mass. The kinematic is performed with the top-pole mass fixed to 172.5 GeV to increase the reconstruction efficiency. A possible bias due to the chosen top-quark mass in the kinematic fit is studied in Chapter A.6. The jet-parton permutation with the highest probability was chosen to calculate the $\cos\theta^*$ values.

8.2.1. Template distributions

The LO Monte Carlo generator Protos [70, 139], as described in Chapter 6.1, was used to create the signal templates. It allows to create separate samples for longitudinal, left-handed and right-handed polarised W-bosons. The signal templates contain events from the lepton+jets samples as well as dilepton events that pass the lepton+jets selection. The latter also contain information about the W-boson polarisation and are therefore considered in the signal distributions. Since no samples for single-top production were available for the different polarisation states, single-top events are considered in the background templates.

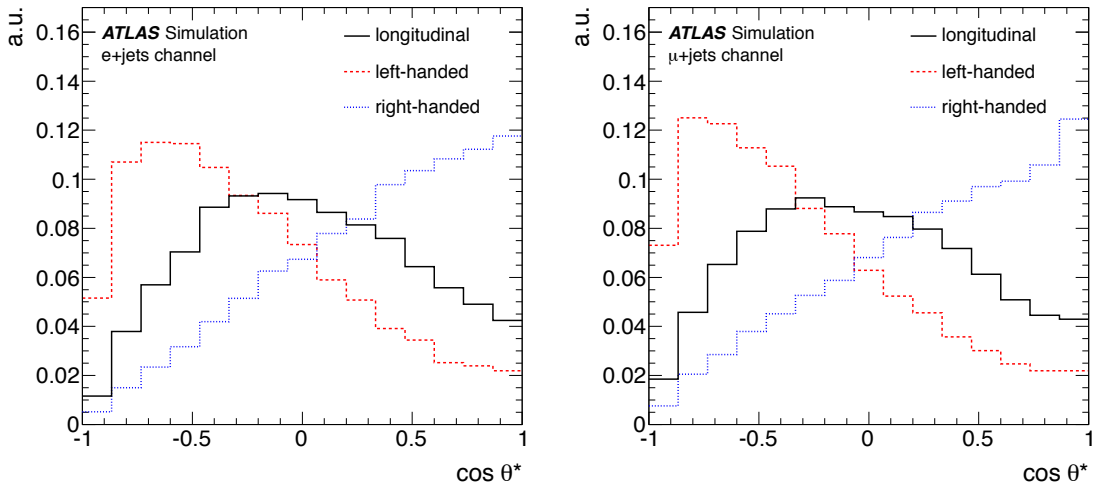

Figure 8.4.: Signal template distributions for the e+jets channel (left) and the μ+jets channel (right). The plots show the distribution for the longitudinal (solid line), left-handed (dashed line) and right-handed (dotted line) template, respectively.

Figure 8.4 shows the three signal distributions for the e+jets channel (left) and the μ+jets channel (right). The templates for the e+jets channel show less pronounced peaks for high and low values of the $\cos\theta^*$-distribution than the equivalent distributions for the μ+jets channel. These effects are caused by the different selection cuts in the two channels and will be discussed in Chapter 8.2.2. The selection efficiencies for the different samples are shown in Tab. 8.2. Since

leptons emitted from left-handed W-bosons are emitted preferentially opposite to the momentum direction of the W-boson, their transverse momentum is on average smaller. Hence, less events from the left-handed sample pass the event selection. The fitted number of signal events have to be corrected for these selection efficiencies before calculating the W-helicity fractions. This is explained in more detail in Chapter 8.2.3.

Selection eff.	e+jets	μ+jets
ϵ_0	0.0469(3)	0.0716(4)
ϵ_L	0.0343(3)	0.0563(4)
ϵ_R	0.0459(3)	0.0688(4)

Table 8.2.: Selection efficiencies for the e+jets and μ+jets channel with their corresponding statistical uncertainties.

The background templates are shown in Fig. 8.5 for the e+jets channel (left) and the μ+jets channel (right). One background template describes the W+jets process using MC simulation for the shape and the data-driven normalisation as described in Chapter 6.3.2. For the background due to misidentified leptons, the data driven estimates as described in Chapter 6.3.1 are used. The third background template contains the sum of the smaller background contributions, namely single-top, Z+jets and diboson production.

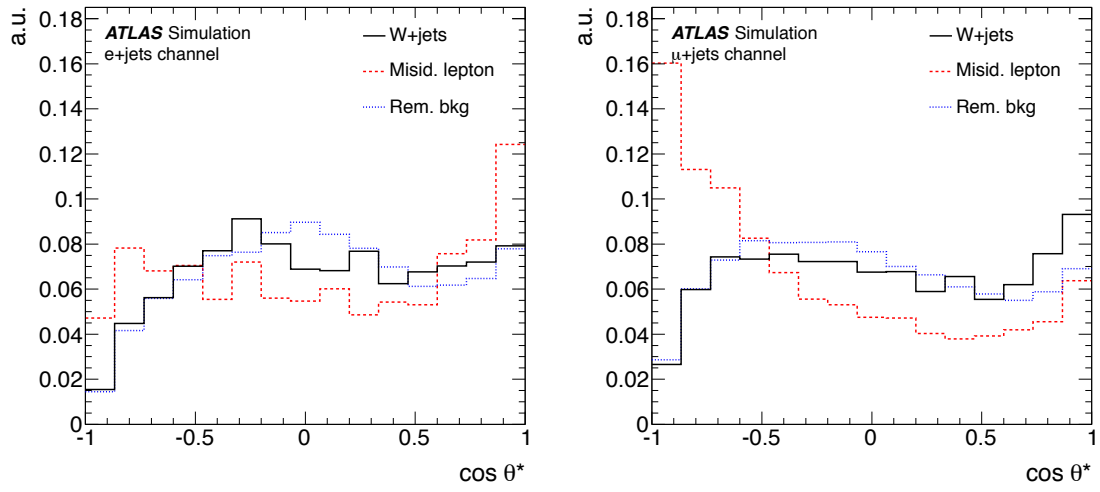

Figure 8.5.: Background template distributions for the e+jets channel (left) and the μ+jets channel (right). The plots show the distribution for W+jets production (solid line), background from misidentified leptons (dashed line) and the sum of the smaller background contributions (dotted line).

The background templates, especially the templates for the background due to misidentified leptons, show strong peaks for the high and low end of the $\cos\theta^*$-spectrum. In these bins, the signal templates suffer from reduced sensitivity as explained in the following. Furthermore, the strong peak at negative $\cos\theta^*$-values for the misidentified leptons in the μ+jets channel is assumed to be caused by the isolation as discussed in Chapter 7.2.

8.2.2. Acceptance effects

The $\cos\theta^*$-distributions are distorted due to acceptance effects caused by the event selection. As described in Chapter 7.2, the missing transverse energy cut is higher in the e+jets channel ($E_T^{\text{miss}} > 30$ GeV) than in the μ+jets channel ($E_T^{\text{miss}} > 20$ GeV). This mostly affects the right side of the $\cos\theta^*$-spectrum, leading to a distortion mainly in the template for the right-handed template. To show the impact of this cut on the angular distribution, it has been varied between 0 and 40 GeV and the resulting shapes are compared in Fig. 8.6. For an increasing E_T^{miss} cut, the peak in the last bin decreases significantly, leading to a dip for values above 35 GeV. Since the E_T^{miss} cut used in the default selection is larger in the e+jets channel, the sensitivity on the corresponding right-handed template is reduced compared to the μ+jets channel.

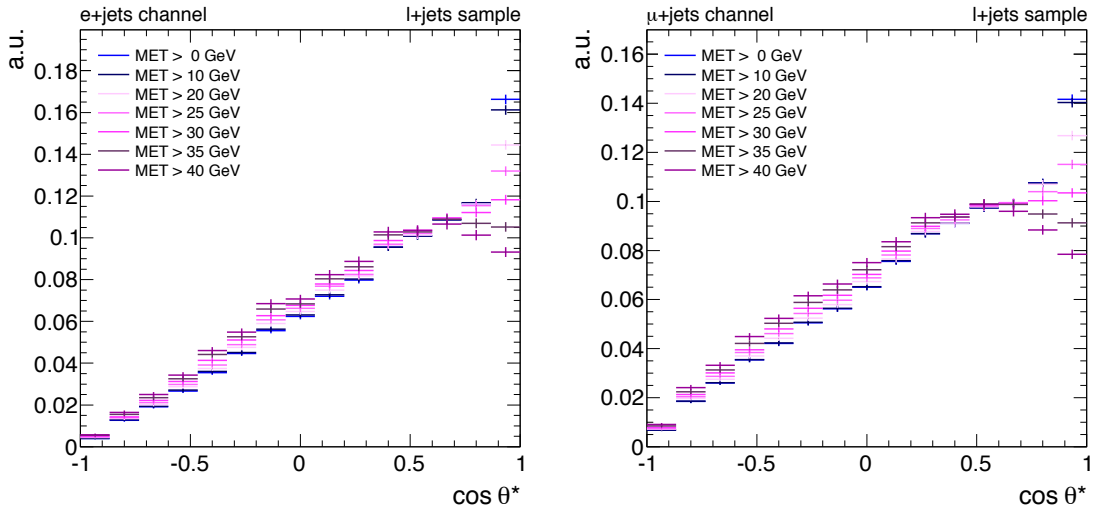

Figure 8.6.: Shape dependence of the right-handed $\cos\theta^*$ template on the E_T^{miss} cut.

Furthermore, a higher E_T cut of 25 GeV is chosen for the electrons while the muon p_{T} cut is at 20 GeV. To study the effect of this cut on the template shapes, the p_{T}-cut is increased starting from the default value up to 40 GeV. The resulting shapes are compared in Fig. 8.7. For all three polarisation states, large distortions are observed especially for lower $\cos\theta^*$ values. These distortions are different for the three polarisation states. The peak on the left side of the distribution is significantly decreased and moves towards higher $\cos\theta^*$ values. As already explained in Chapter 3.4.1, charged leptons emitted from left-handed W-bosons have a softer p_{T}-spectrum than those emitted from right-handed W-bosons, since they are emitted opposite to the momentum direction of the W-boson. Therefore the effect on the left-handed templates is more pronounced than for the other templates. Again, the templates for the e+jets channel are more strongly affected by these distortions due to the tighter cuts that are applied.

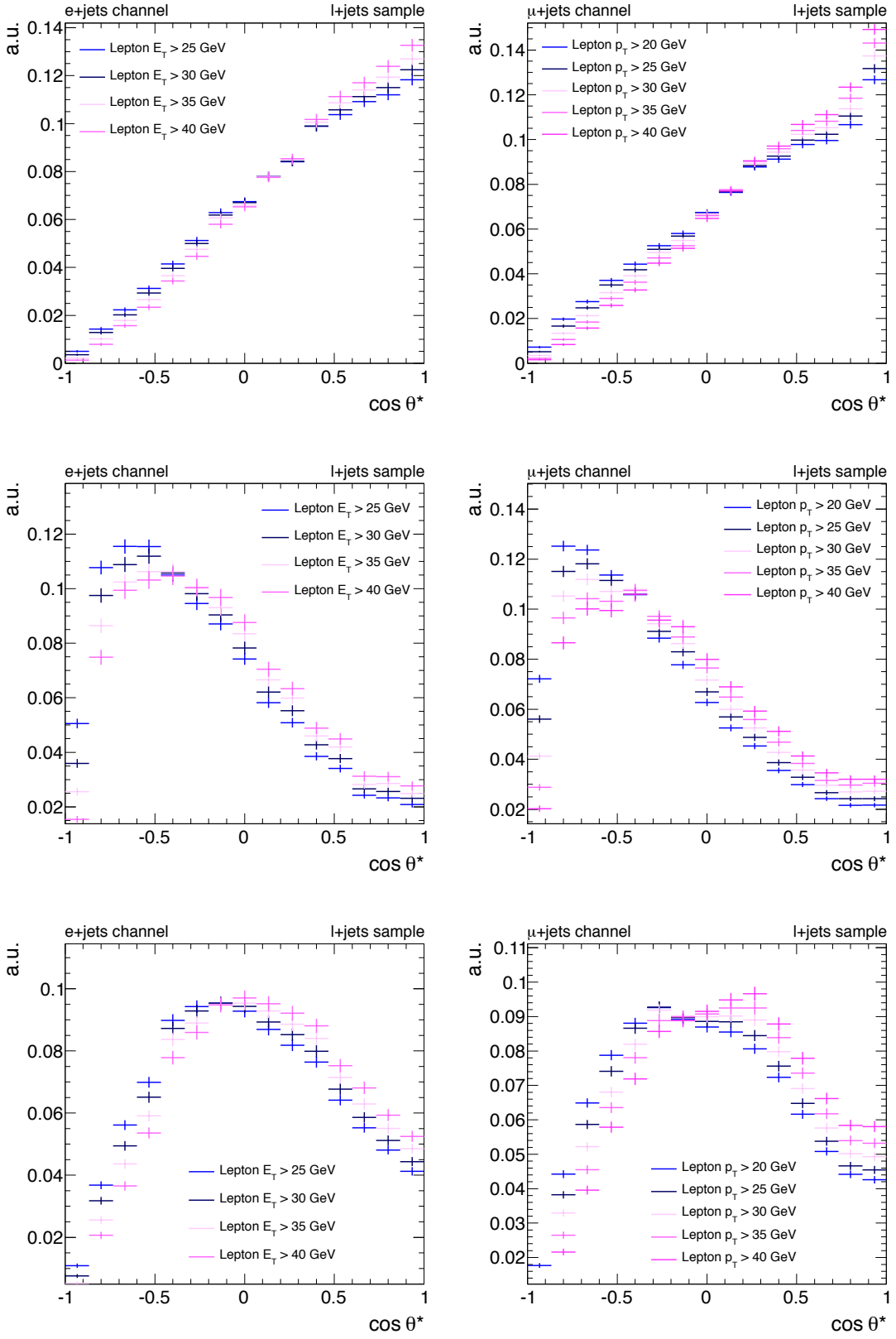

Figure 8.7.: Shape dependence of the right-handed (upper plots), left-handed (middle) and longitudinal (lower plots) distributions on the lepton p_{T} cut. Starting from the default selection (20 GeV for muons and 25 GeV for electrons), the cut is increased in steps of 5 GeV up to 40 GeV.

8.2.3. Likelihood fit

The binned likelihood fit is performed using the templates shown in Fig. 8.4 and 8.5. The fit procedure is based on the MINUIT package used within ROOT [154]. The background contributions are constrained by Gaussian priors that allow the normalisations to float within their uncertainties. These Gaussian priors are set to the values according to their MC normalisation for the small background contributions, or to their data-driven normalisations for W+jets and the background due to misidentified leptons. The normalisations and uncertainties were shown in Tab. 7.2. The number of events in the signal templates is expressed as the product of efficiencies, acceptances and the number of events before applying the selection. The latter are the parameter in the likelihood fit, called N_i. The product of efficiency and acceptance effects is summarised in the term *selection efficiency*, ϵ^{sel}, in the following. Since the selection efficiencies are different for the three polarisation states, they have to be taken into account in the template fit. These efficiencies are shown in Tab. 8.2. The number of events in the respective signal template is therefore:

$$n_{\mathrm{i,templ.}} = \epsilon_i^{sel} \cdot N_i \quad \text{with i = 0, L, R.} \tag{8.5}$$

The sum of all template normalisations is calculated as:

$$n_{\mathrm{exp,templ}} = n_{\mathrm{0,templ.}} + n_{\mathrm{L,templ.}} + n_{\mathrm{R,templ.}} + n_{\mathrm{W+jets}} + n_{\mathrm{Misid.leptons}} + n_{\mathrm{RemBkg}} \quad , \tag{8.6}$$

and the sum of these distributions is compared to the data distribution in the Likelihood fit:

$$L = \prod_{i=1}^{N_{bins}} \mathrm{Poisson}(n_{\mathrm{data,i}}; n_{\mathrm{exp,i}}) \prod_{j=1}^{N_{bkg}} \frac{1}{\sqrt{2\pi}\sigma_{\mathrm{bkg,j}}} e^{\frac{-(n_{\mathrm{bkg,j}} - \bar{n}_{\mathrm{bkg,j}})^2}{2\sigma^2_{\mathrm{bkg,j}}}} \quad . \tag{8.7}$$

The W-helicity fractions are then obtained from the ratio:

$$F_i = \frac{N_{\mathrm{i}}}{N_0 + N_L + N_R} \text{ for i = 0, L, R.} \tag{8.8}$$

For the combined likelihood fit, the signal templates for the respective polarisation states are combined while each background contribution is fitted separately. The selection efficiencies for the combined templates are adjusted accordingly. Hence, the combined template fit uses either eight or nine templates.

8.2.4. Ensemble tests

For the estimation of systematic and expected statistical uncertainties, so-called *pseudo-data* distributions are used. This pseudo-data is obtained from MC simulation by varying the parameters under study within one standard deviation. So-called *ensembles* are obtained by fluctuating each bin of the pseudo-data distribution according to Poissonian statistics. A template fit is performed to each ensemble (*pseudo-experiment*). Usually 5,000 pseudo-experiments are performed if not stated otherwise and the resulting fit parameters are histogrammed. The mean values of N_0 , N_{L} and N_{R} are used to calculate the specific W-helicity fractions for each pseudo data distribution. The difference between the fractions obtained from the nominal distribution to the fractions obtained from the up- and down-variations are calculated, respectively. In case of asymmetric uncertainties, the largest deviation is taken and the uncertainty is symmetrised. If only one variation is studied (when for example comparing MC Generators), the full difference is taken as symmetric uncertainty.

8.3. Method validation

The method is validated by performing linearity tests and creating pull distributions. The pull for a parameter N is defined as:

$$\text{Pull} = \frac{N_j - N_{\text{nom}}}{\sigma_{N_j}} \quad . \tag{8.9}$$

To test the linearity of the method, ensemble tests are performed on pseudo-data distributions. The W-helicity fractions are calculated from the mean of the distributions:

$$F_i = \frac{< N_i >}{< N_0 > + < N_L > + < N_R >} \text{ for i = 0, L, R.} \tag{8.10}$$

The result for the fractions and parameters are now plotted dependent on their input values. For an unbiased estimator, a slope of 1 and an offset of zero are expected. The distributions for the N_i are plotted symmetrically around zero. The background contributions are expected to be stable and the absolute difference of the fit result to the expectation value is drawn dependent on the input values for F_0. A slope and an offset of zero are expected. The calibration curves are created using 5,000 ensembles per calibration point. The longitudinal W-helicity fraction is varied between 0.4 and 1.0. If it is varied up by 0.1, the two other fractions are both decreased by 0.05. The mean values of the pull distributions are also drawn for each calibration point as well as the pull width.
The measurement is performed following two different approaches. First, the analysis is carried out under the assumption that the b-quark mass is zero, leading to a vanishing right-handed component. Since only two signal samples are considered in this approach, it is called *two-dimensional fit* in the following. For the second part of the analysis, all three helicity fractions are estimated simultaenously. This approach is hence called *three-dimensional fit*. The method validation is performed for both approaches.
The results for the signal parameters and helicity fractions are summarised in Tab. 8.3 for the two-dimensional fit and in Tab. 8.4 for the three-dimensional fit. The corresponding tables for the background contribution can be found in Tab. A.15 and A.16. The distributions for the two-dimensional fit in the combined channel are shown in Fig. 8.8. The calibration curves are unbiased, only small deviations are shown. The RMS dependence plots, however, show that the RMS is not 1 but smaller for all parameter. This can be explained with the Gaussian priors that are used. Just to show the consistency of the method, the fit has been performed with signal templates only and the results are schon in Appendix A.7 for the combined fit for the three-dimensional approach. The slope for all RMS dependence plots are consistent with 1.

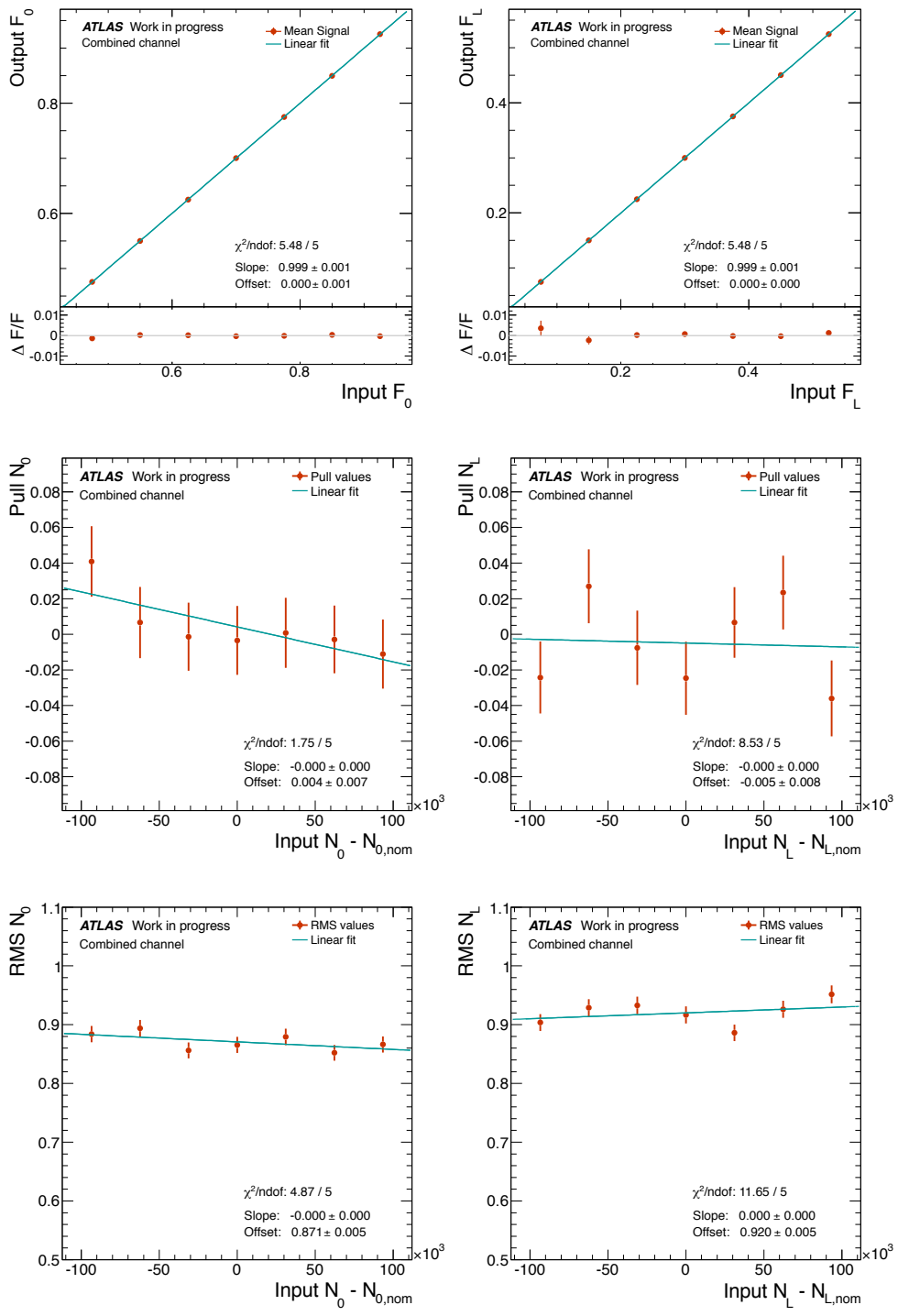

Figure 8.8.: Calibration curves are shown in the upper plots for F_0 and F_L respectively, together with the pull dependence plots in the middle for the fit parameters N_0 and N_L and the corresponding RMS distributions below. The two-dimensional fit was used, while performing a combined likelihood fit. 2,000 ensembles were used. No bias is observed.

		Linearity tests		Pull		RMS	
Parameter	Channel	Slope	Offset	Slope	Offset	Slope	Offset
F_0	e+jets	1.000 ± 0.001	0.000 ± 0.001				
F_L	e+jets	1.000 ± 0.001	0.000 ± 0.000				
N_0	e+jets	0.999 ± 0.001	46 ± 65	$< 10^{-6}$	0.003 ± 0.004	$< 10^{-6}$	0.748 ± 0.003
N_L	e+jets	1.000 ± 0.001	-92 ± 41	$< 10^{-6}$	-0.015 ± 0.005	$< 10^{-6}$	0.924 ± 0.003
F_0	μ+jets	1.000 ± 0.001	0.000 ± 0.001				
F_L	μ+jets	1.000 ± 0.001	0.000 ± 0.001				
N_0	μ+jets	1.000 ± 0.001	-18 ± 49	$< 10^{-6}$	-0.001 ± 0.005	$< 10^{-6}$	0.908 ± 0.004
N_L	μ+jets	1.000 ± 0.001	-22 ± 38	$< 10^{-6}$	-0.004 ± 0.005	$< 10^{-6}$	0.869 ± 0.003
F_0	Combined	0.999 ± 0.001	0.000 ± 0.001				
F_L	Combined	0.999 ± 0.001	0.000 ± 0.001				
N_0	Combined	1.000 ± 0.001	45 ± 40	$< 10^{-6}$	0.005 ± 0.005	$< 10^{-6}$	0.866 ± 0.003
N_L	Combined	1.000 ± 0.005	30 ± 28	$< 10^{-6}$	0.004 ± 0.005	$< 10^{-6}$	0.909 ± 0.003

Table 8.3.: Results of the linear fits to the calibration curves, pull and RMS values using 5,000 ensembles per calibration point for the e+jets, the μ+jets and the combined lepton+jets channel. The two-dimensional fit is used. No bias is observed.

		Linearity tests		Pull		RMS	
Parameter	Channel	Slope	Offset	Slope	Offset	Slope	Offset
F_0	e+jets	1.002 ± 0.001	-0.001 ± 0.001				
F_L	e+jets	1.001 ± 0.001	0.000 ± 0.001				
F_R	e+jets	1.002 ± 0.002	0.000 ± 0.000				
N_0	e+jets	1.001 ± 0.001	-118 ± 69	$< 10^{-6}$	-0.007 ± 0.004	$< 10^{-6}$	0.761 ± 0.003
N_L	e+jets	1.002 ± 0.002	30 ± 67	$< 10^{-6}$	-0.000 ± 0.004	$< 10^{-6}$	0.790 ± 0.003
N_R	e+jets	1.002 ± 0.002	4 ± 59	$< 10^{-6}$	0.000 ± 0.004	$< 10^{-6}$	0.786 ± 0.003
F_0	μ+jets	1.005 ± 0.002	-0.003 ± 0.001				
F_L	μ+jets	1.005 ± 0.002	-0.001 ± 0.001				
F_R	μ+jets	1.005 ± 0.005	-0.000 ± 0.001				
N_0	μ+jets	1.001 ± 0.001	-12 ± 54	$< 10^{-6}$	-0.001 ± 0.005	$< 10^{-6}$	0.889 ± 0.003
N_L	μ+jets	1.002 ± 0.002	-22 ± 70	$< 10^{-6}$	-0.001 ± 0.004	$< 10^{-6}$	0.763 ± 0.003
N_R	μ+jets	1.001 ± 0.002	-66 ± 66	$< 10^{-6}$	-0.005 ± 0.005	$< 10^{-6}$	0.830 ± 0.003
F_0	Combined	1.001 ± 0.001	0.000 ± 0.001				
F_L	Combined	1.001 ± 0.001	0.000 ± 0.001				
F_R	Combined	1.001 ± 0.001	0.000 ± 0.001				
N_0	Combined	1.000 ± 0.001	77 ± 42	$< 10^{-6}$	0.009 ± 0.005	$< 10^{-6}$	0.866 ± 0.003
N_L	Combined	1.000 ± 0.001	-105 ± 49	$< 10^{-6}$	-0.010 ± 0.004	$< 10^{-6}$	0.786 ± 0.003
N_R	Combined	1.000 ± 0.001	-111 ± 44	$< 10^{-6}$	-0.011 ± 0.005	$< 10^{-6}$	0.809 ± 0.003

Table 8.4.: Results of the linear fits to the calibration curves, pull and RMS values using 5,000 ensembles per calibration point for the e+jets, the μ+jets and the combined lepton+jets channel. The three-dimensional fit is used. No bias is observed.

8.4. Statistical Uncertainty

The statistical uncertainties are obtained from a fit to the data distribution. MINUIT provides the fitted number of events and the corresponding statistical uncertainties. The fractions are calculated from the parameters N_0, N_L and N_R. These parameters are highly correlated. The correlations $\rho(N_i, N_j)$ are evaluated using ensemble tests. For the error propagation, the correlations between the parameters have to be taken into account. To perform the error propagation, the correlation matrix $\underline{C}$ and the vector of derivatives $\vec{d}$ are introduced:

$$\underline{C} := \begin{pmatrix} \sigma^2_{N_0} & \sigma_{N_0}\,\sigma_{N_\mathrm{L}}\,\rho(N_0\,,N_\mathrm{L}\,) & \sigma_{N_0}\,\sigma_{N_\mathrm{R}}\,\rho(N_0\,,N_\mathrm{R}\,) \\ \sigma_{N_\mathrm{L}}\,\sigma_{N_0}\,\rho(N_\mathrm{L}\,,N_0\,) & \sigma^2_{N_\mathrm{L}} & \sigma_{N_\mathrm{L}}\,\sigma_{N_\mathrm{R}}\,\rho(N_\mathrm{L}\,,N_\mathrm{R}\,) \\ \sigma_{N_\mathrm{R}}\,\sigma_{N_0}\,\rho(N_\mathrm{R}\,,N_0\,) & \sigma_{N_\mathrm{R}}\,\sigma_{N_\mathrm{L}}\,\rho(N_\mathrm{R}\,,N_\mathrm{L}\,) & \sigma^2_{N_\mathrm{R}} \end{pmatrix}$$

$$\vec{d} := \begin{pmatrix} \partial F_i/\partial N_0 \\ \partial F_i/\partial N_\mathrm{L} \\ \partial F_i/\partial N_\mathrm{R} \end{pmatrix} \quad \text{for } i = 0,\,\mathrm{L},\,\mathrm{R}\;.$$

Therefore the uncertainty on F_i results in:

$$\sigma^2_{F_i} = \vec{d}\,\underline{C}\,\vec{d}^{\,T} = \sum_{j=0,L,R}\sum_{k=0,L,R} \frac{\partial F_i}{\partial N_j}\frac{\partial F_i}{\partial N_k}\sigma_j\sigma_k\rho(N_j,N_k) \quad \text{for } i = 0,\,\mathrm{L},\,\mathrm{R}\;. \tag{8.11}$$

Two-dimensional fit

The fit to the data distribution is performed and the statistical uncertainty is extracted first for the two-dimensional fit. F_0 and F_L are fully anti-correlated. Ensemble tests are performed to estimate the expected statistical uncertainty. The comparison between expected and observed uncertainties is shown in Tab. 8.5. Since F_0 and F_L are fully anti-correlated, their absolute uncertainties are identical.

	e+jets		μ+jets		Comb.	
Fraction	Exp.	Obs.	Exp.	Obs.	Exp.	Obs.
F_0	0.026	0.027	0.021	0.022	0.016	0.016
F_L	0.026	0.027	0.021	0.022	0.016	0.016

Table 8.5.: Comparison between expected and observed statistical uncertainty for the three channels using the two-dimensional fit. Only small differences are observed. Due to the higher cuts in the e+jets channel and the corresponding smaller event yield, the statistical uncertainty is larger than in the μ+jets channel.

Three-dimensional fit

The procedure is repeated and the parameter N_{R} is included in the fit. The correlations between the parameters are obtained from ensemble tests. They are shown in Tab. 8.6. The correlations are used to calculate the uncertainties on the W-helicity fractions. The expected and observed statistical uncertainties are compared in Fig. 8.9 for the combined fit and in Tab. 8.7 for all three channels. The statistical uncertainty of F_0 and F_{R} in the μ+jets channel is higher than in the e+jets channel despite the larger event yield. This is founded in the larger anti-correlations observed in the μ+jets channel (see Tab. 8.6) that leads to larger uncertainties. In both channels, the observed and expected uncertainties are in good agreement.

e+jets			
	N_0	N_{L}	N_{R}
N_0	1.00	-0.51	-0.32
N_{L}	-0.51	1.00	0.78
N_{R}	-0.32	0.78	1.00
μ+jets			
	N_0	N_{L}	N_{R}
N_0	1.00	-0.57	-0.40
N_{L}	-0.57	1.00	0.85
N_{R}	-0.40	0.85	1.00
Combined			
	N_0	N_{L}	N_{R}
N_0	1.00	-0.53	-0.34
N_{L}	-0.53	1.00	0.83
N_{R}	-0.34	0.83	1.00

Table 8.6.: Correlation coefficients for the parameters N_0 , N_{L} and N_{R}. The correlations are estimated using 5,000 ensembles. The anti-correlations between N_0 and N_{L} as well as between N_0 and N_{R} are larger in the μ+jets channel, leading to larger statistical uncertainties.

	e+jets		μ+jets		Comb.	
Fraction	Exp.	Obs.	Exp.	Obs.	Exp.	Obs.
F_0	0.041	0.038	0.043	0.044	0.030	0.029
F_{L}	0.022	0.020	0.019	0.020	0.015	0.014
F_{R}	0.026	0.024	0.029	0.029	0.020	0.019

Table 8.7.: Comparison between expected and observed statistical uncertainty for the three channels using the three-dimensional fit.

e+jets			
	F_0	F_L	F_R
F_0	1.00	-0.85	-0.89
F_L	-0.85	1.00	0.52
F_R	-0.89	0.52	1.00
μ+jets			
	F_0	F_L	F_R
F_0	1.00	-0.84	-0.93
F_L	-0.84	1.00	0.59
F_R	-0.93	0.59	1.00
Combined			
	F_0	F_L	F_R
F_0	1.00	-0.84	-0.91
F_L	-0.84	1.00	0.55
F_R	-0.91	0.55	1.00

Table 8.8.: Correlation coefficients for the three helicity fractions F_0 , F_L and F_R . The correlations are estimated using 5,000 ensembles. Strong anti-correlations are observed between F_0 and F_L as well as between F_0 and F_R whereas the fractions F_L and F_R are positively correlated.

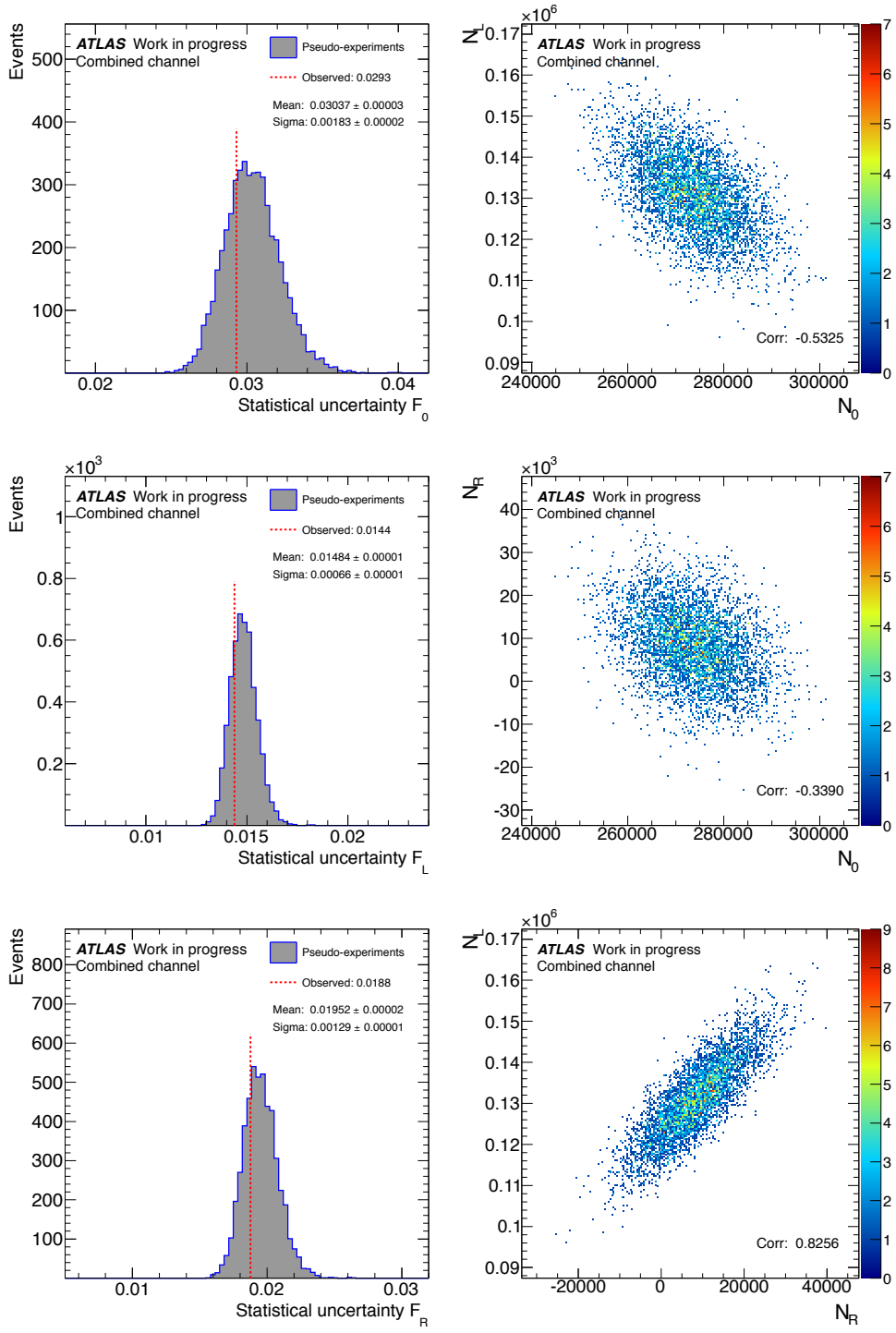

Figure 8.9.: Comparison between expected and observed statistical uncertainties for the three-dimensional fit, using a combined likelihood fit. 5,000 ensembles were created to calculate the correlations shown on the right-hand side that are used in the error propagation. N_0 and N_L as well as N_0 and N_R are anti-correlated whereas N_L and N_R are highly correlated.

8.5. Systematic Uncertainties

With the large number of $t\bar{t}$-events produced at the LHC, the measurements of most top-quark properties are limited by systematic uncertainties. Therefore, it is crucial to identify the dominating uncertainties and to develop methods that allow for their reduction. The different sources of systematic uncertainties are presented in the following. For large effects on the shape, the respective distributions are shown. The normalisation effects are shown in Chapter A.8. If the systematic uncertainty affects only the signal process, the distributions only contain the signal process (Label: *Signal Only*), otherwise also the background distributions are included (Label: *Pseudo data*). The systematic uncertainties are evaluated using ensemble tests as described in Chapter 8.2.4.

8.5.1. Signal modelling

Several sources of systematic uncertainties are caused by the signal modelling. These uncertainties are discussed in the following in more detail. While the differences in normalisation (see Tab. A.12) should have no influence on the systematic uncertainties, the shape of the pseuo-data distributions change the result of the ensemble tests.

Monte Carlo generators

The impact of the signal MC generator has been studied by performing two comparisons. In case 1, MC@NLO is compared to the LO ALPGEN generator [141]. In case 2, the NLO generators MC@NLO [131] and POWHEG [3] [155] are compared. All generators are interfaced to HERWIG [122]. The W-helicity fractions are obtained from ensemble tests to the pseudo-data distributions and the difference between the helicity fractions is calculated for both sets of generators. The largest uncertainty of the two is symmetrised and taken as systematic uncertainty. Figure 8.10 shows the corresponding normalised pseudo data distributions for the e+jets (left) and μ+jets channel (right). While the effect on the shape is very similar in both channels, the effect on the normalisation is larger in the μ+jets channel (see Tab. A.12).

[3] For the sample generated with Powheg+Herwig, Tauola does not include the tau polarisation in the simulation. Therefore this uncertainty can be slightly overestimated.

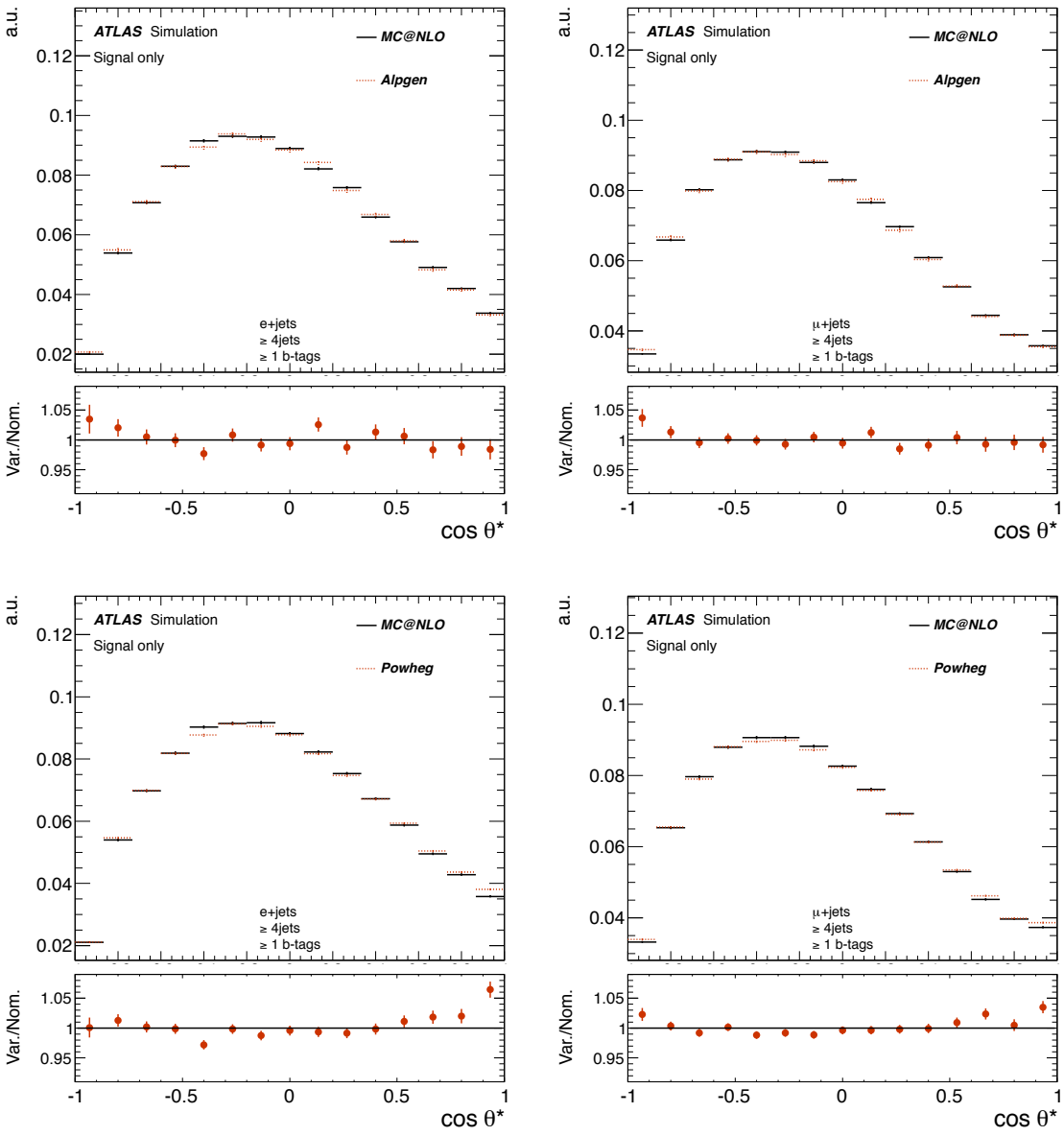

Figure 8.10.: Shape comparison of the $t\bar{t}$-distributions for the e+jets channel (left) and the μ+jets channel (right). The upper plots show the comparison between the NLO generator MC@NLO with the LO generator ALPGEN. The lower plots show the comparison of MC@NLO with the NLO generator POWHEG. Larger shape deviations are observed for the comparison with POWHEG.

Parton showering

To evaluate the impact of the parton shower model, the POWHEG generator is used. Two pseudo data distributions are created, one using POWHEG interfaced to HERWIG, the other using POWHEG with PYTHIA. While PYTHIA is based on the Lund string fragmentation model [121], HERWIG uses a cluster hadronisation model. The full difference between the obtained W-helicity fractions is symmetrised and taken as systematic uncertainty. The corresponding $t\bar{t}$-distributions are compared in Fig. 8.11. While the shape difference is similar in the e+jets and μ+jets channel, the impact on the normalisation is larger in the e+jets channel (see Tab. A.12).

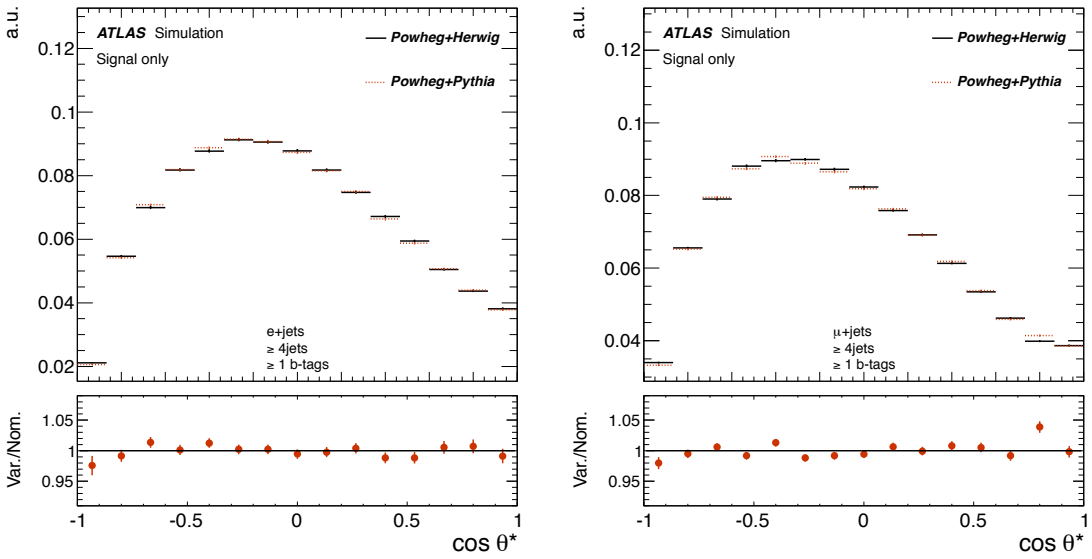

Figure 8.11.: Comparison between the $t\bar{t}$-distributions for the samples generated with POWHEG+HERWIG (solid line) and POWHEG+PYTHIA (dotted line) for the e+jets channel (left) and the μ+jets channel (right), respectively. The impact on the shape is rather similar, while the effect on the normalisation is slightly larger in the e+jets channel (see Tab. A.12).

Initial and final state radiation

The impact of initial state and final state radiation (ISR/FSR) is estimated using the ACERMC [142] generator. ACERMC is based on a LO matrix element and the MRST LO** PDF [156] is used. For the showering, PYTHIA is used. In the W-helicity analysis published in [3], the uncertainty due to ISR/FSR in the lepton+jets template method was one of the largest systematic uncertainties. This effect could be significantly reduced by using the results of the jet gap fraction analysis presented in [157]. This analysis performs a measurement using the $t\bar{t}$ dilepton channel with the requirement of two b-tags. No additional central jet is allowed with a p_{T} that exceeds a certain value. The gap fraction is calculated as the ratio between the number of events without such a central jet and the total number of selected events. In Fig. 8.12 the gap fraction is shown as a function of the p_{T} threshold for the central jet. Comparing the data distribution and the uncertainty on the jet gap fraction with the previously used ACERMC central and variation samples, a large deviation is observed that shows that the uncertainty on the initial state radiation was highly overestimated.

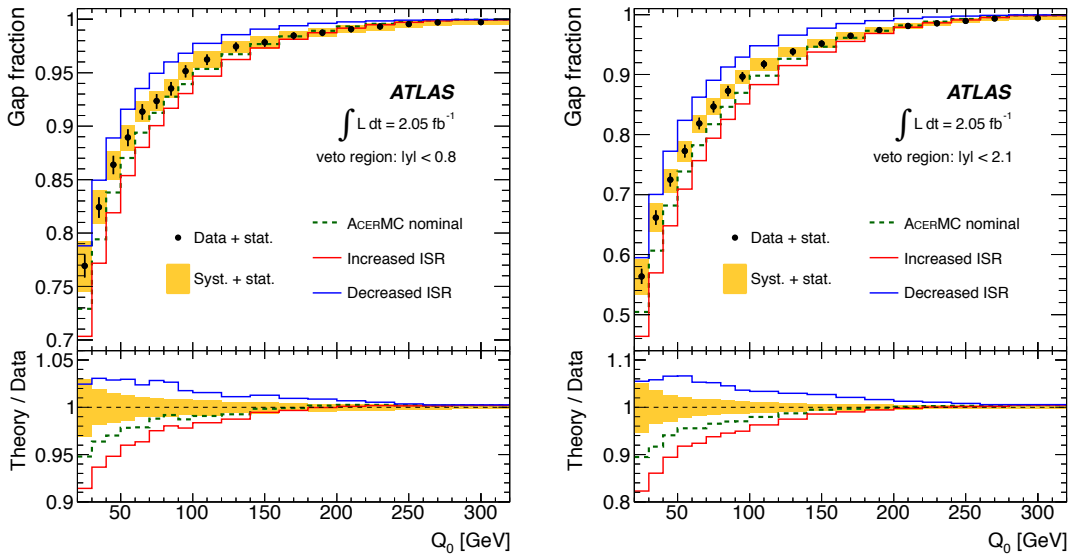

Figure 8.12.: The jet gap fraction as a function of the p_{T} threshold compared to the previously used central AcerMC samples and the corresponding ISR up and down variations. The figures are taken from [157]. The uncertainties from these samples are strongly overestimated. The measurement has been used to tune the ISR parameters which leads to a decrease of the corresponding uncertainty.

The results obtained in the jet gap fraction analysis allowed to tune the ISR parameters, leading to a significantly decreased systematic influence. The pseudo data distributions used for the current W-helicity measurement are shown in Fig. 8.13.

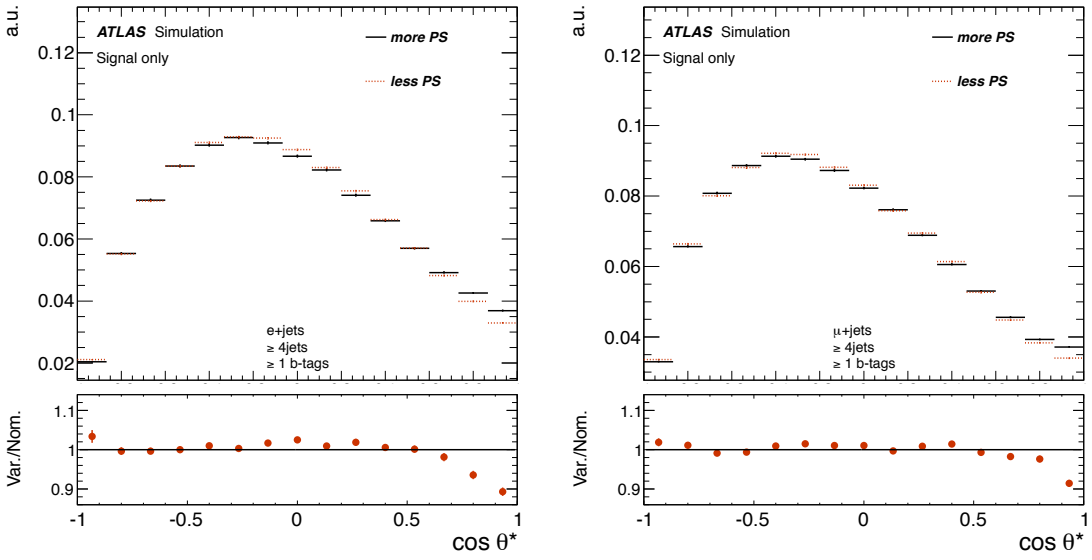

Figure 8.13.: Comparison between two samples generated with AcerMC using Pythia for the parton showering. The ISR and FSR parameters are varied simultaneously up and down, leading to samples with more and less parton showering.

The parton showering activity has been varied up and down simultaneously for the ISR and FSR parameters. Since no nominal distribution is available, the difference between the W-helicity fractions obtained from these two variations is calculated and half of this difference is taken as systematic uncertainty. The impact on the $\cos\theta^*$ distribution is larger for the e+jets channel (left), where deviations are observed on both ends of the $\cos\theta^*$ spectrum.

Underlying event

The uncertainty due to the underlying event is modelled using ACERMC interfaced to PYTHIA. Measurements of underlying event observables such as the charged particle multiplicity in data taken at the LHC with a centre-of-mass energy of $\sqrt{s} = 900$ GeV and $\sqrt{s} = 7$ TeV [158] allowed for an improved MC tuning. The AUET2B LO** PDF [129] tune was used in the simulation and two samples were created in which the underlying event activity was increased/decreased by about 10% using the PROFESSOR tool [159]. The effect on the shape is small in both channels, the corresponding distributions are compared in Fig. A.7. Since no nominal sample is available, the W-helicity fractions are obtained from the up and down variation and half of the difference is taken as systematic uncertainty.

Colour reconnection

The samples for the evaluation of the colour reconnection uncertainty are generated with the ACERMC generator interfaced to PYTHIA. The samples use the Perugia2011 tunes that are described in [160]. Data from SPS, LEP and the Tevatron were used to tune the parameters. Two samples are created: one is using the standard Perugia2011 tune while the other is simulated without colour reconnection effects. The full difference between the W-helicity fractions that are obtained from the two pseudo data sets are used as symmetric uncertainty. Small changes are observed in both channels that are slightly larger in the μ+jets channel. The distributions are compared in Fig. A.8.

Top-quark mass

The systematic uncertainty due to the top-quark mass is estimated using pseudo data distributions where $t\bar{t}$- and single-top samples with different top-quark masses. Samples with generated top-quark masses between 167.5 and 177.5 GeV in steps of 2.5 GeV are used. The W-helicity fractions are obtained from ensemble tests to each pseudo data distribution and plotted as a function of the top-quark mass. A linear fit is performed to the resulting distribution and the uncertainty on each fraction is obtained from the slope, corresponding to the 0.9 GeV uncertainty of the Tevatron combination result [16]. The corresponding pseudo-data distributions are shown in Fig. 8.14. The upper plots show the comparison of baseline samples (generated using a top-quark mass of 172.5 GeV) with samples based on lower top-quark masses. The lower plots show the comparison with higher top-quark masses. As expected due to the direct mass dependence, a strong change of the shape is observed. Another test has been performed to estimate the influence of the top-quark mass that has been used as fixed value within the kinematic likelihood fit in the event reconstruction. The results are shown in th Appendix A.6. The effect is relatively small and hence it will not be included in the total uncertainty.

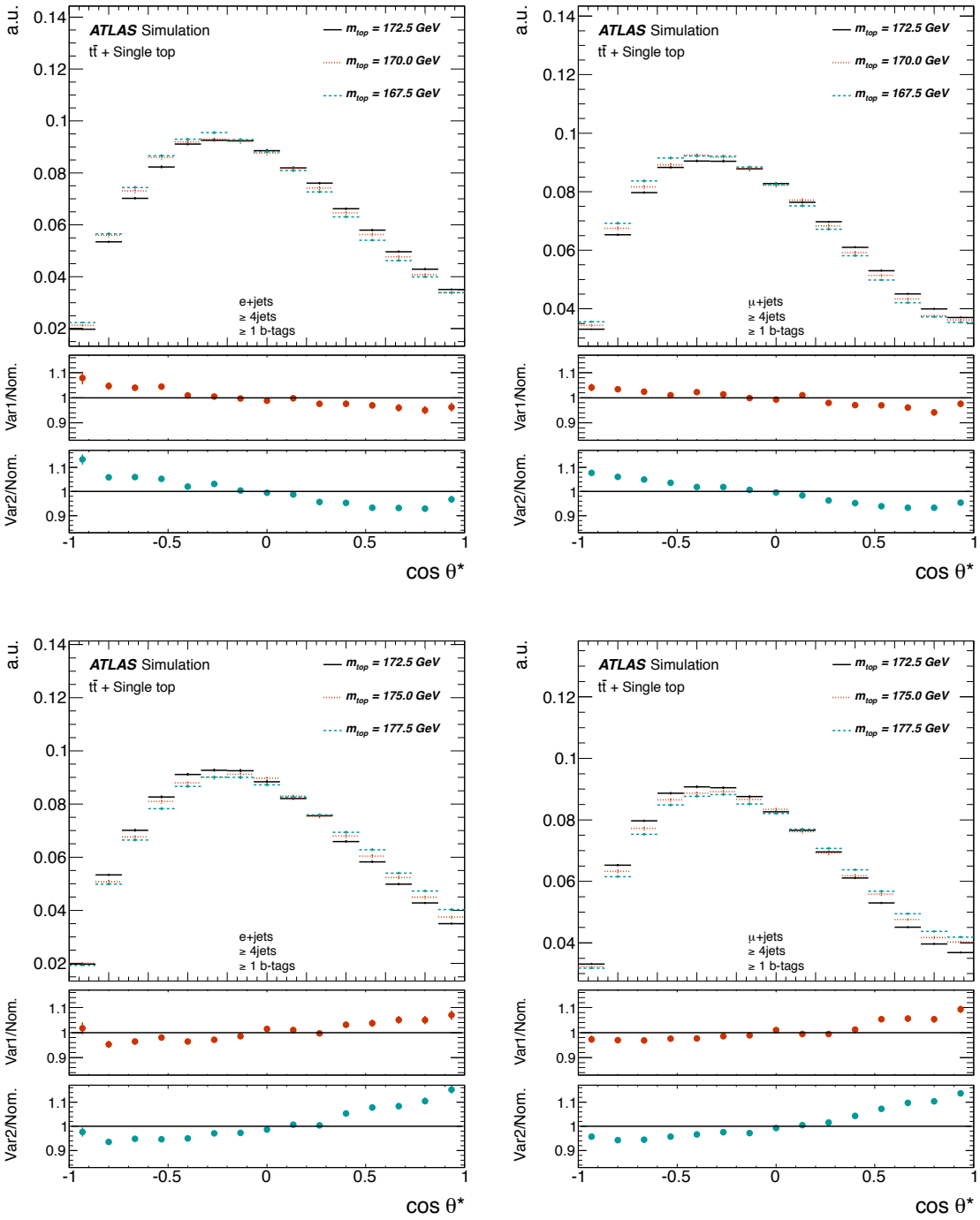

Figure 8.14.: Comparison between pseudo-data distributions consisting of $t\bar{t}$- and single top samples that are generated with different top-quark masses. The upper plots show the deviation of samples for lower top-quark masses from the nominal distribution while the lower plots show the comparison of samples with higher top-quark masses.

Parton density functions

For the uncertainty due to the parton density functions (PDFs), three different sets of PDFs are compared, namely CT10 [35], MSTW [36] and NNPDF20 [37]. Each PDF set is provided together with its corresponding uncertainties (52 uncertainties for CT10, 40 for MSTW and 100 for NNPDF20). The simulated events of the pseudo-data distribution are reweighted using the LHAPDF tool [161] for each uncertainty provided. This reweighting leads to a new pseudo-data distribution which is evaluated using 2,000 ensemble tests. The uncertainty for each PDF set is estimated using three different approaches. For CT10, the symmetric Hessian is used. If $F_{k,+}$ and $F_{k,-}$ are the fractions obtained from the k-th uncertainty pair, the total uncertainty is:

$$\sigma_{F_i} = 0.5 \sqrt{\sum_{k=1}^{26} (F_{k,+} - F_{k,-})^2} \quad , \tag{8.12}$$

For MSTW, the up and down variations are calculated separately using the asymmetric Hessian:

$$\sigma_{F_{i,up}} = \sqrt{\sum_{k} (F_k - F_0)^2} \quad \text{for } F_k - F_0 > 0 \tag{8.13}$$

and

$$\sigma_{F_{i,down}} = \sqrt{\sum_{k} (F_k - F_0)^2} \quad \text{for } F_k - F_0 < 0 \quad . \tag{8.14}$$

For NNPDF20, the results are averaged over all 100 PDF sets for each polarisation state and the corresponding uncertainty is the standard deviation from this averaged value. The total uncertainty due to the PDFs is obtained by calculating the envelope of the three estimates. The half width of the envelope is taken as systematic uncertainty.

8.5.2. Background modelling

Background normalisation

As described in Chapter 8.2, the background normalisations are estimated in the fit while they are constrained within the predicted uncertainties. Therefore the normalisation uncertainty is included in the statistical uncertainty of the fit.

Fake lepton shape

e+jets channel The fake lepton background is obtained using a matrix method as described in Chapter 6.3.1. The shape uncertainty of this estimate is obtained by varying the fake and real efficiencies independently while keeping the normalisation of the contribution to the default value. The W-helicity fractions are obtained from ensemble tests for each variation and the uncertainties are added in quadrature.

μ+jets channel As explained in Chapter 6.3.1, two different matrix methods for the fake lepton estimate in the μ+jets channel exist. Three different pseudo data sets are obtained, one for each method and the average of the two methods as nominal distribution. The largest difference between the W-helicity fractions is taken as symmetric uncertainty.

W+jets shape

The shape of the W+jets distribution depends on the parameters used within the ALPGEN generator. For the evaluation of the corresponding uncertainty, scale factors that account for the change of the two parameters with the largest impact are provided. The minimum transverse momentum of the light quarks is set to 15 GeV in the default setup. For the variation, it is lowered to 10 GeV. Furthermore, a modified factorisation scale ($Q^2 = m_W^2 + p_{T,W}$) is used instead of the default scale $Q^2 = m_W^2 + \sum_i p_T(\text{jets})$. Pseudo data sets with these modifications in the W+jets contribution were created and ensemble tests are performed. The difference of the resulting W-helicity fractions to the nominal fractions is calculated. The two uncertainties are added in quadrature.

W+jets HF fraction

As explained in Chapter 6.3.2, scale factors are applied to correct for the flavour composition of the W+jets samples. The scale factors are applied on pretag level such that the flavour composition is changed to match those in data while the overall W+jets normalisation remains unchanged. To take into account the systematic uncertainties on these estimates, different pseudo data sets are created. First, the scale factors F_{bb} and F_c are varied within one standard deviation in an anti-correlated way while adjusting the fraction of light events accordingly to keep the overall normalisation fixed. This is done for the up and down variation and for each jet bin separately. In addition, pseudo-data sets are created while varying only either F_{bb} or F_c while again the normalisation remains constant. Since the scale factors are obtained in the jet bin containing only 2 jets, an additional uncertainty of 25 % per jet bin is applied. For each up/down variation pair, the maximum deviation from the nominal fractions is calculated. The uncertainties for the different variations are then added in quadrature.

8.5.3. Detector modelling

Jet energy scale

The uncertainty on the jet energy scale has been discussed in Chapter 5.4. The uncertainties due to close-by jets, flavour composition, η-intercalibration and b-JES are taken into account. Furthermore, a pileup-correction is applied [162]. The jet energy scale is varied within one standard deviation and the event selection and reconstruction is applied to these varied samples. The two pseudo data distributions are compared to the nominal distribution in Fig. 8.15. For both channels, a shape dependence is observed for the up and down variations. While the effect on the down variation is similar in both channels, the e+jets channel shows larger deviations in the distribution for the up variation as well. The difference of the estimated W-helicity fractions is calculated for the up and down variation and the largest deviation is taken as systematic uncertainty.

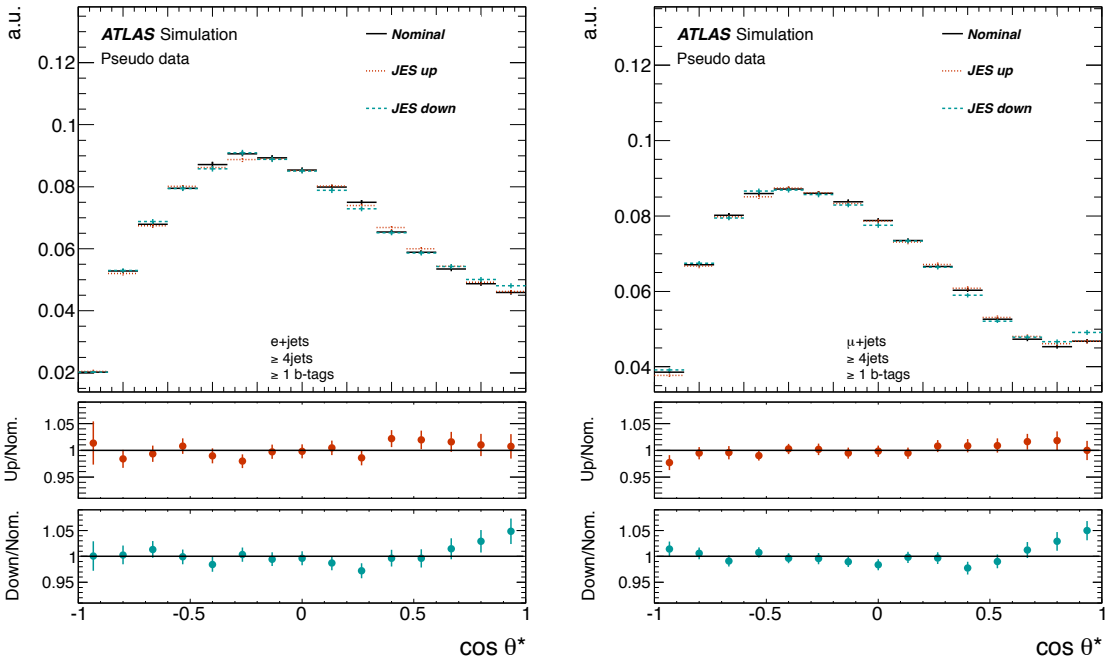

Figure 8.15.: Comparison of the nominal pseudo data distribution with jet energy scale up and down variations for the e+jets (left) and μ+jets channel (right). The effect on the down variation is similar in both channels while the impact for the up variation is more pronounced in the e+jets channel.

Jet energy resolution

The jet energy resolution, as described in Chapter 5.4 has an overall uncertainty of about 10% [110]. To evaluate the impact of this uncertainty on the measurement of the W-helicity fractions, the transverse momentum of the jets is smeared according to this uncertainty and the event selection and reconstruction is applied on these samples. The corresponding pseudo data distributions are compared in Fig. 8.16. The impact on the shape is large in both channels but more pronounced in the upper end of the angular distribution for the e+jets channel. The full difference between the evaluated W-helicity fractions is taken as symmetric uncertainty.

Jet reconstruction efficiency

According to the uncertainty on the jet reconstruction efficiency of about 2 %, jets are randomly dropped in the selection and the event selection and reconstruction is applied. The impact on the shape is small as shown in Fig. 8.17, but larger for the μ+jets channel. The full difference between the evaluated W-helicity fractions is taken as symmetric uncertainty.

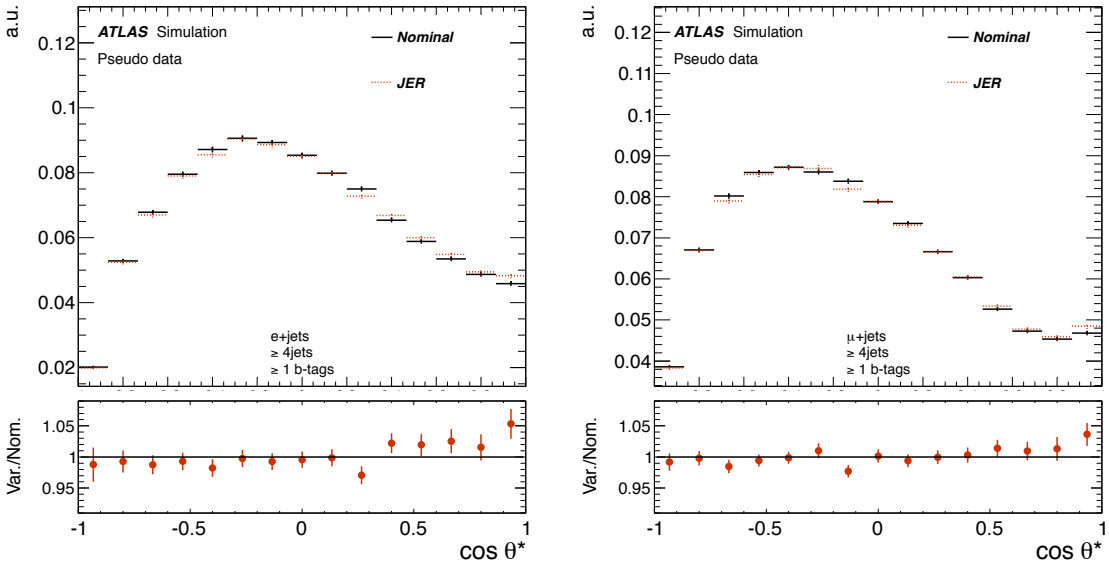

Figure 8.16.: Comparison of the nominal pseudo data distribution with distributions where the jet energy resolution is varied within one standard deviation for the e+jets (left) and μ+jets channel (right). The impact is large in both channels but more pronounced in the e+jets channel.

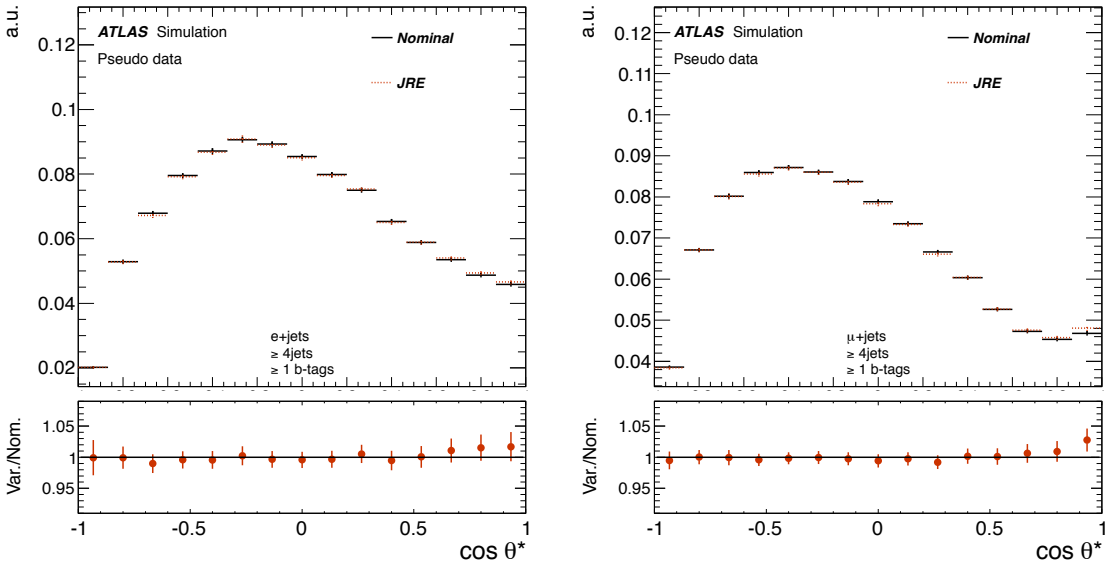

Figure 8.17.: Comparison of the nominal pseudo data distribution with distributions where the jet reconstruction efficiency is varied within one standard deviation for the e+jets (left) and μ+jets channel (right). The impact is small in both channels but more pronounced in the μ+jets channel.

Lepton energy and momentum scale

The lepton energy and momentum scale is corrected by default in the simulated events. An estimate of the systematic uncertainty on this correction was provided based on $Z \to ee$ and $Z \to \mu\mu$ events for the e+jets and μ+jets channel, respectively. For the muon momentum scale, the pseudo data distribution with the default scale is compared to the distribution where the correction is not applied as shown in Fig. 8.19. For the e+jets channel, the electron energy scale is varied up and down within one standard deviation as shown in Fig. 8.18. The comparison with the nominal distribution shows a change in the shape for both channels. The deviation in the up variation of the electron energy scale is however much more pronounced. The maximum difference is taken as systematic uncertainty in the e+jets channel while the full difference in the μ+jets channel is taken as symmetric uncertainty. In the combined likelihood fit, the uncertainties for the e+jets and μ+jets channel are evaluated separately and are added in quadrature.

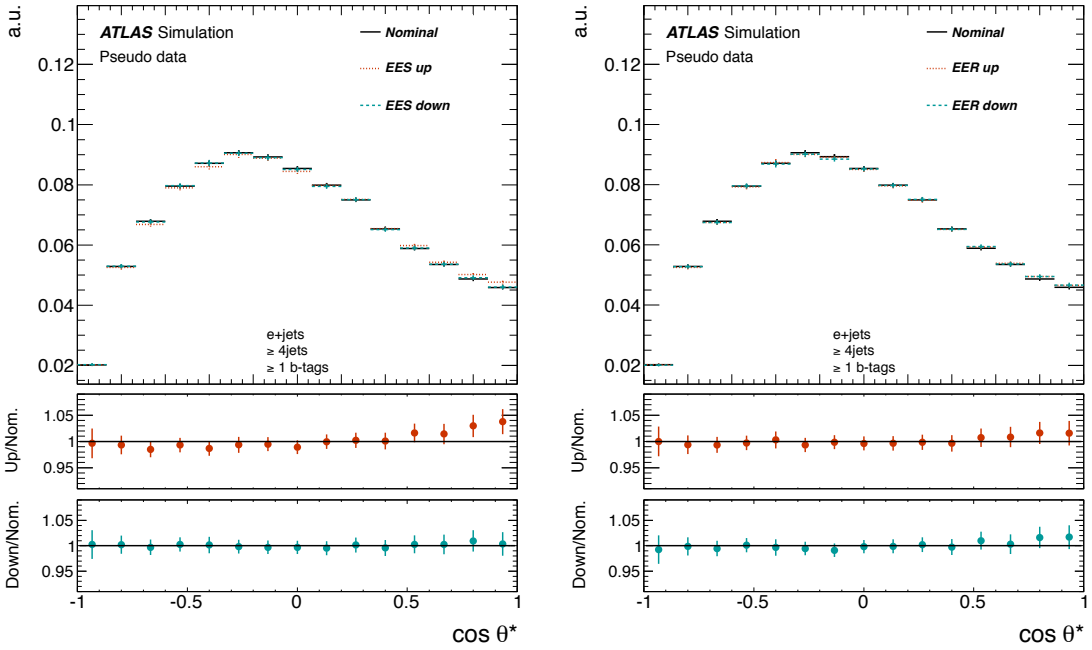

Figure 8.18.: Comparison of the nominal pseudo data distribution with distributions where the electron energy scale (left) and electron energy resolution (right) is varied up and down within one standard deviation.

Lepton energy and momentum resolution

The lepton energy and momentum resolution is corrected by default in the simulated events. $Z \to ee$ and $Z \to \mu\mu$ events were taken to evaluate the systematic uncertainty on this correction. The up- and down-variations of these corrections are applied and new pseudo data distribution are created that are compared with the nominal distributions in Fig. 8.18 (right) and Fig. 8.19 (upper plots). For the e+jets channel, the maximum deviation is taken as symmetric uncertainty while for the μ+jets channel the uncertainty contribution from the inner detector and muon spectrometer resolution are added in quadrature. In the combined likelihood fit, the uncertainties for the e+jets and μ+jets channel are evaluated separately and are added in quadrature.

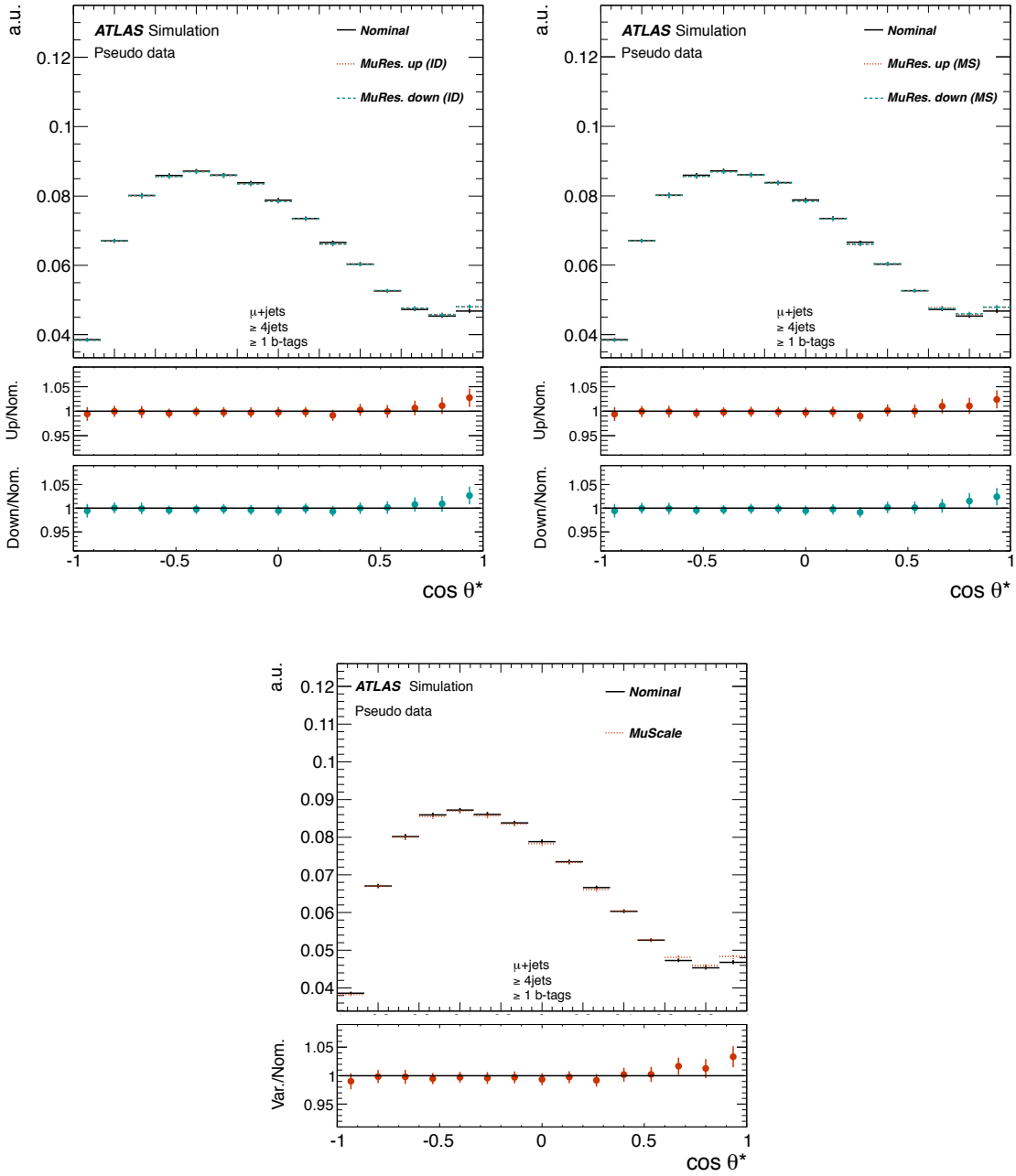

Figure 8.19.: Comparison of the nominal pseudo data distribution with distributions where the muon resolution is varied up and down within one standard deviation in the inner detector (left) and the muon spectrometer (right). The lower plot shows the comparison with the muon momentum scale. The shape changes for the muon momentum resolution are small except for the last bin, a larger effect is observed for the muon momentum scale.

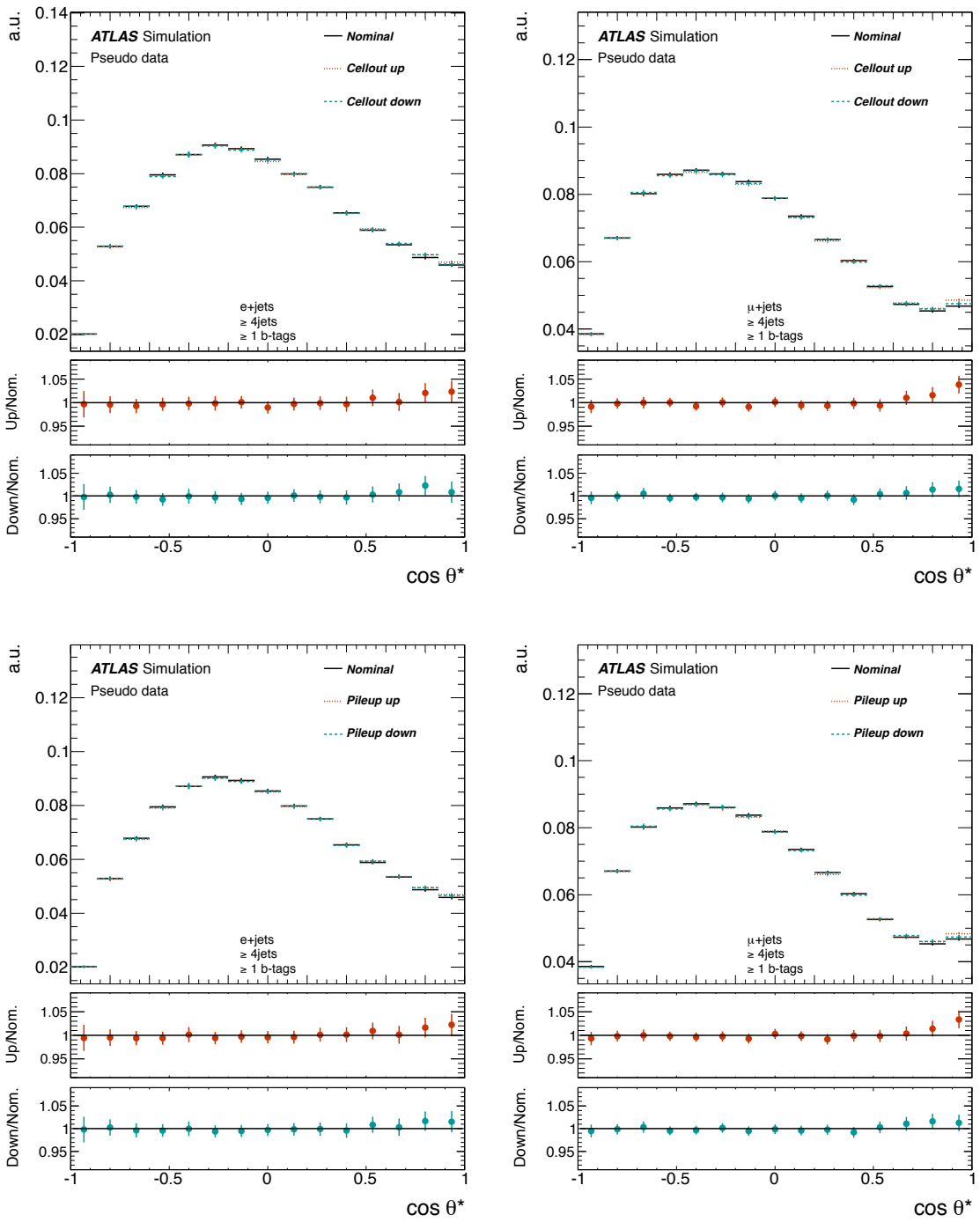

Figure 8.20.: Shape dependence of the $\cos\theta^*$ distribution due to uncertainties on the missing transverse energy. The upper two plots show the effect of the variation of the cellout and softjet term while the lower plots show the comparison with the variation of the pileup term.

Lepton efficiency scale factors

The lepton scale factors for the identification, reconstruction and trigger efficiencies are varied independently within their uncertainties and the systematic uncertainties are added in quadrature. Since they have only a very small impact on the shape of the distribution, they are not shown here separately. In the combined likelihood fit, the uncertainties for the e+jets and μ+jets channel are evaluated separately and are added in quadrature.

Missing transverse energy

When changing the energy scale and resolution of the jets and leptons as explained above, the missing transverse energy has to be corrected accordingly. As explained in Chapter 5.6, additional cellout and softjets terms are taken into account in the calculation of the missing transverse energy. The impact of these terms is evaluated while varying them fully correlated within one standard deviation (see upper plots in Fig. 8.20). In addition, the uncertainty due to pileup effects is evaluated (see lower plots in Fig. 8.20) and the uncertainties on the W-helicity fractions are added in quadrature.

B-tagging efficiency

For the evaluation of the b-tagging uncertainty, the separate uncertainties for b-tag, c-tag and mistag are varied within one standard deviation. This leads to new weights that are applied to each jet and the total event weight is recalculated using the procedure described in Chapter 5.5. The uncertainties are evaluated separately for these three cases and added in quadrature for the total uncertainty. Since the effects on the shape are small, the distributions are not shown here.

Luminosity

As described in Chapter 8.2, the luminosity uncertainty of 1.8 % is included in the uncertainties that are constraining the background normalisation and is hence included in the statistical uncertainty. The impact of the luminosity is fully correlated between the three signal contributions. Therefore the effect cancels out when calculating the W-helicity fractions.

Pileup uncertainty

As discussed in Chapter 6, the MC events are reweighted to match the pileup conditions in data. The average number of interactions per bunch crossing, $< \mu >$, is used for this reweighting. In order to test a possible pileup-dependence of our measurement, the data set is split into six smaller samples according to $< \mu >$ or to the number of primary vertices, $N_{\text{Prim.}}$. A finer binning was not possible due to the limited MC statistics available to create the templates.
The templates are fitted to each of the six data distributions and the corresponding helicity fractions are drawn dependent on $< \mu >$ or $N_{\text{Prim.}}$ as shown in Fig. 8.21. A linear fit is carried out and the slope of the linear fit is taken to test the pileup dependence. The results are shown in Tab. 8.9 for the two-dimensional and in Tab. 8.10 for the three-dimensional fit. All slopes are in agreement with zero within 1.3 standard deviations. Therefore no additional uncertainty is assigned.

Fraction	Variable	e+jets	μ+jets	Combined
F_0	$N_{\text{Prim.}}$	0.011 ± 0.013	-0.003 ± 0.011	0.003 ± 0.008
F_0	$< \mu >$	0.003 ± 0.006	-0.000 ± 0.005	0.002 ± 0.004

Table 8.9.: Slope of the linear fit to the W-helicity fractions dependent on the number of primary vertices, $N_{\text{Prim.}}$, or the average number of interactions per bunch crossing, $< \mu >$. The two-dimensional fit is used.

Fraction	Variable	e+jets	μ+jets	Combined
F_0	$N_{\text{Prim.}}$	0.028 ± 0.021	-0.024 ± 0.019	0.003 ± 0.014
F_{L}	$N_{\text{Prim.}}$	-0.018 ± 0.013	0.008 ± 0.010	-0.003 ± 0.008
F_{R}	$N_{\text{Prim.}}$	0.012 ± 0.012	0.012 ± 0.012	0.000 ± 0.009
F_0	$< \mu >$	-0.004 ± 0.010	-0.005 ± 0.009	0.003 ± 0.007
F_{L}	$< \mu >$	-0.001 ± 0.006	0.002 ± 0.005	0.000 ± 0.004
F_{R}	$< \mu >$	0.004 ± 0.006	0.002 ± 0.006	0.003 ± 0.004

Table 8.10.: Slope of the linear fit to the W-helicity fractions dependent on the number of primary vertices, $N_{\text{Prim.}}$, or the average number of interactions per bunch crossing, $< \mu >$. The three-dimensional fit is used.

8.5.4. Method specific uncertainties

Template statistics

Six different templates are used in the binned likelihood fit. After applying the event selection, the number of events in the sample used to create these templates is significantly reduced. To account for possible fluctuations in the templates, ensemble tests are performed. In these ensemble tests, the pseudo data distribution is not changed, but the template distributions are fluctuated within their sample statistics assuming Poisson statistics. The width of the distributions for the W-helicity fractions are taken as a measure of the uncertainty that arises due to this limited template statistics.

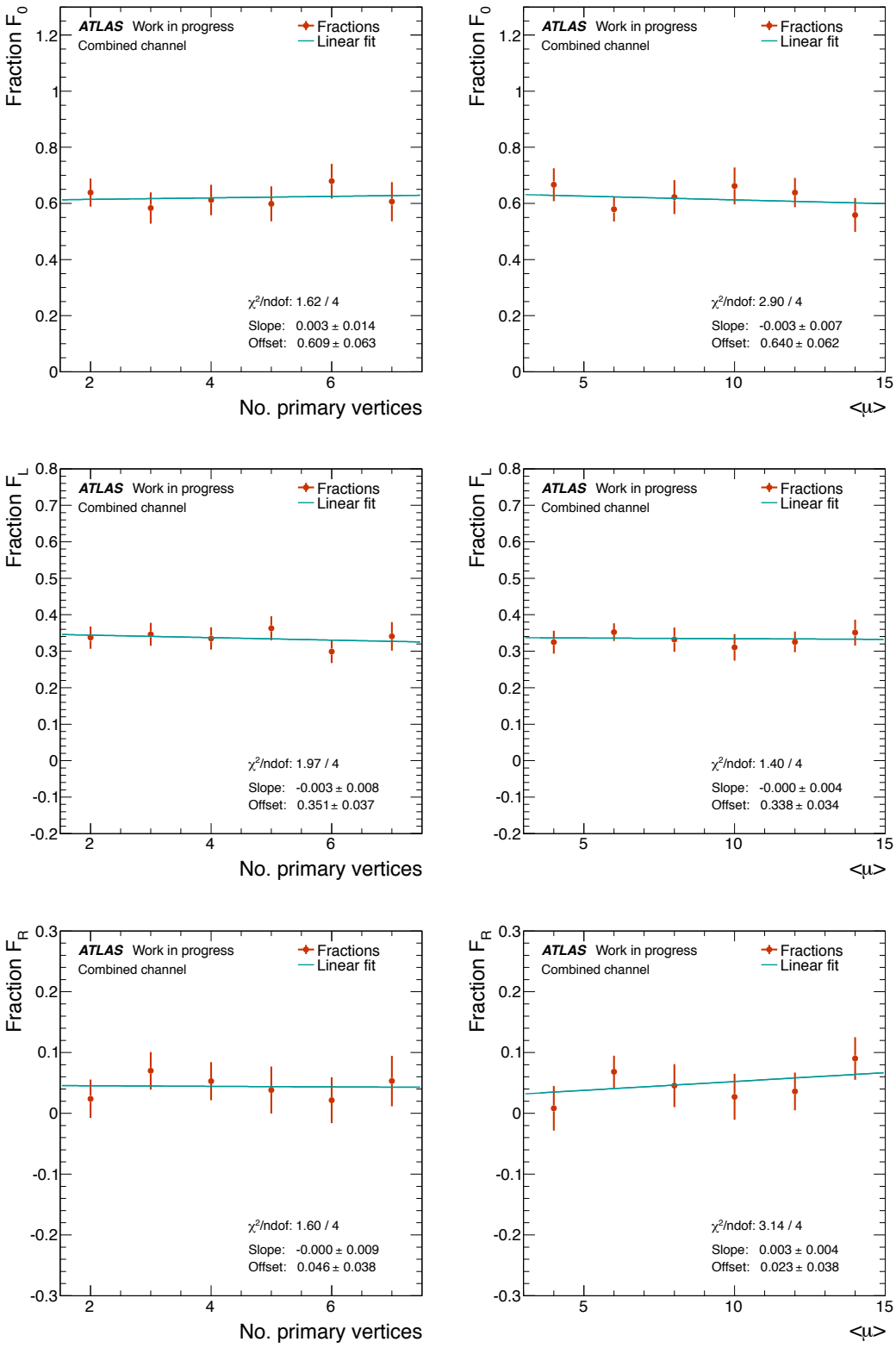

Figure 8.21.: Measurement of the W-helicity fractions dependent on the number of primary vertices, $N_{\text{Prim.}}$, or the average number of interactions per bunch crossing, $< \mu >$. The three-dimensional fit is used in the combined channel.

9. Results

A template method as described in Chapter 8.2 is used to measure the W-helicity fractions based on a data set collected with the ATLAS detector at a centre-of-mass energy of $\sqrt{s} = 7$ TeV. The integrated luminosity of the data set amounts to $\int dt\mathcal{L} = 4.7$ fb^{-1}. The statistical uncertainties are obtained from the best-fit results to the data distribution. The systematic uncertainties are evaluated by comparing the ensemble test results from nominal and systematically varied pseudo-data distributions as described in Chapter 8.2.4. First, the results for the two-dimensional fit are presented in Chapter 9.1. The measurement is performed under the assumption that the b-quark mass vanishes and the right-handed fraction is zero[1]. The measurement is carried out both in the e+jets and μ+jets channel as well as in a combined likelihood fit. The result from the combined fit is used to set a limit on the coefficient of the dimension-six operator O_{tW}^{33} that was introduced in Chapter 3.4.2. In the second part of this chapter, the three-dimensional fit is used to perform a simultaneous measurement of all three polarisation states. Again, the fit is performed in the separate lepton channels and in a combined likelihood fit. The corresponding results are presented in Chapter 9.2. The result of the combined likelihood fit, allows to set limits on the anomalous Wtb-couplings.

9.1. Two-dimensional fit

9.1.1. W-helicity fractions

In Fig. 9.1, the best-fit results for the e+jet channel (left) and for the μ+jets channel (right) are shown by the solid line and are compared to the respective data distributions (black markers). The statistical and systematic uncertainties are shown by the hatched area. The solid area represents the sum of the three background contributions.

Fraction/Param.	Sim.	σ(Sim.)	Fit	σ(Fit)	Diff. [$\sigma_{\text{Sim.}}$]
F_0			0.698	0.027	
F_L			0.302	0.027	
N_0			278288	16206	
N_L			120197	8108	
N(W+jets)	2294	1574	2376	833	0.05
N(Fake lepton)	843	422	670	337	0.41
N(RemBkg)	1669	370	1687	359	0.05

Table 9.1.: Best-fit results for the e+jets channel using the two-dimensional fit. The extracted W-helicity fractions are shown with their statistical uncertainties. The predicted and fitted background normalisations are compared. The relative difference between them is shown in units of the standard deviation from the background prediction.

[1] Following the approach in [79, 80].

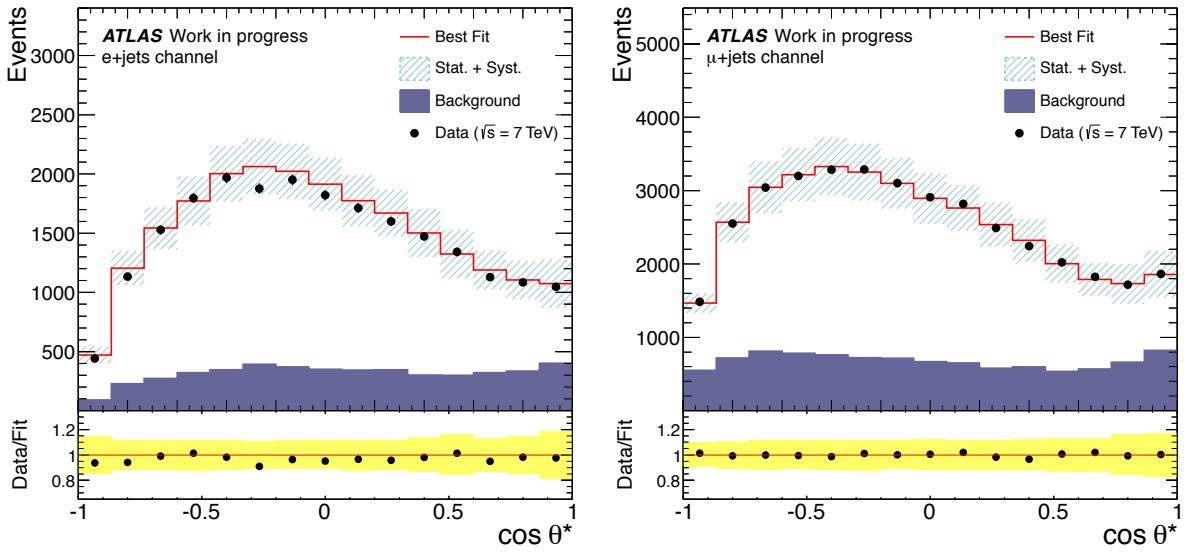

Figure 9.1.: Result of the data fit in the e+jets channel (left) and the μ+jets channel (right) using the two-dimensional fit. The data distributions (black markers) are shown together with the best-fit result (solid line) and the background distribution (solid area). The statistical and systematic uncertainties are shown by the hatched area. In the lower part of the plot, the residual distribution with the corresponding uncertainties are drawn.

The Tables 9.1 and 9.2 show the extracted W-helicity fractions and their statistical uncertainties for the e+jets and μ+jets channel, respectively. Furthermore, the fitted background normalisations are compared with the predicted values alongside their respective uncertainties. The fitted background contributions are in agreement with the predicted values within their uncertainties.

Fraction/Param.	Sim.	σ(Sim.)	Fit	σ(Fit)	Diff. [$\sigma_{\text{Sim.}}$]
F_0			0.685	0.022	
F_L			0.315	0.022	
N_0			284021	10316	
N_L			130612	8255	
N(W+jets)	4457	3022	5532	691	0.36
N(Fake lepton)	1774	406	2063	291	0.71
N(RemBkg)	2517	497	2570	493	0.11

Table 9.2.: Best-fit results for the μ+jets channel using the two-dimensional fit. The extracted W-helicity fractions are shown with their statistical uncertainties. The predicted and fitted background normalisations are compared. The relative difference between them is shown in units of the standard deviation from the background prediction.

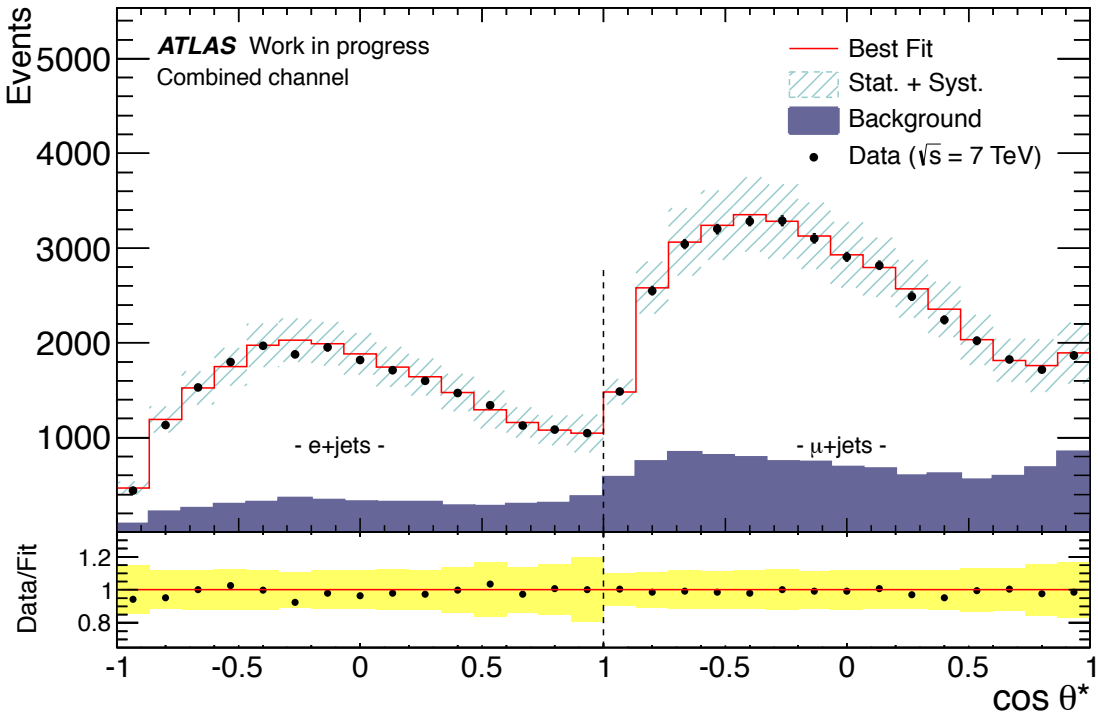

Figure 9.2.: Result of the data fit in the combined lepton+jets channel using the two-dimensional fit. The data distributions (black markers) are shown together with the best-fit result (solid line) and the background distribution (solid area). The statistical and systematic uncertainties are shown by the hatched area. In the lower part of the plot, the residual distribution with the corresponding uncertainties are drawn.

Figure 9.2 shows the best-fit result of the combined likelihood fit compared to the data distribution. The corresponding W-helicity fractions and their statistical uncertainties are summarised in Tab. 9.3. Two signal and six background templates are used in the fit, as each background component is allowed to float separately within its uncertainty. As graphically shown by the residual distribution, the best-fit result is in good agreement with the data distribution. The extracted W-helicity fractions and their statistical uncertainties are shown together with the predicted and observed background normalisations. The statistical uncertainties on the fractions are reduced by the combined fit.

Fraction/Param.	Sim.	σ(Sim.)	Fit	σ(Fit)	Diff. [$\sigma_{\text{Sim.}}$]
F_0			0.695	0.016	
F_L			0.305	0.016	
N_0			283526	8645	
N_L			124545	5715	
N(W+jets) e+jets	2294	1574	2037	590	0.16
N(W+jets) μ+jets	4457	3022	5626	646	0.39
N(Fake lepton) e+jets	843	422	690	299	0.36
N(Fake lepton) μ+jets	1774	406	2199	255	1.05
N(RemBkg) e+jets	1669	370	1642	349	0.07
N(RemBkg) μ+jets	2517	497	2683	482	0.33

Table 9.3.: Best-fit results for the combined likelihood fit using the two-dimensional fit. The extracted W-helicity fractions are shown with their statistical uncertainties. The predicted and fitted background normalisations are compared. The relative difference between them is shown in units of the standard deviation from the background prediction.

The systematic uncertainties for the three measurements are compared in Tab. 9.4. For easier comparison, they are also shown graphically in Fig. 9.3. Only one result is shown for each channel since by construction, the uncertainties of F_0 and F_L are identical when performing the two-dimensional fit. For the e+jets and μ+jets channel, the statistical and systematic uncertainties are of similiar size. The systematic uncertainties in all measurements are mainly driven by the uncertainty on the top-quark mass, followed by the jet energy scale and jet resolution uncertainties. This large impact of the top-quark mass uncertainty is expected since the W-helicity fractions have a direct mass dependence as shown in Eq. 3.19. The larger impact of the jet energy scale and resolution on the e+jets channel can be explained when comparing the effect of these uncertainties for each process separately as shown in Chapter 8.5.3. The distributions for the e+jets channel show a stronger shape dependency which can be explained by the tighter cuts on lepton p_{T} and E_T^{miss} which leads to a larger distortion of the templates as described in Chapter 8.2.

A large difference in uncertainty is also observed for the uncertainty due to parton showering, initial and final state radiation as well as the underlying event activity, where the effect on the e+jets channel is higher than in the μ+jets channel. The corresponding pseudo-data distributions are compared in Chapters 8.5.1 and A.9. For all three uncertainties, the effect on the

e+jets channel is much more pronounced. The effect for the parton showering can be explained with the mis-modelling in the HERWIG sample as mentioned in the previous chapter. HERWIG uses TAUOLA for the τ decay. However, the polarisation of the τ-lepton is not accounted for in the decay. Therefore the electrons and muons from the semileptonic τ-decay have on average a softer transverse momentum which again affects the e+jets channel stronger due to the high E_T-cut.

If the uncertainties estimated for the single lepton channels are of different size, the uncertainty from the combined likelihood fit is expected to be inbetween as observed for example for the jet energy scale and resolution. In case of the lepton-related uncertainties, the different sources are estimated individually (for example electron and muon resolution), and the evaluated uncertainties are added in quadrature. Since the selection cuts in the μ+jets channel are less tight than in the e+jets channel, the higher event yield leads to a smaller statistical uncertainty. The final results for the W-helicity fractions using the two-dimensional fit are in summary:

$$F_0 = 0.698 \pm 0.027\ (\text{stat.}) \pm 0.031\ (\text{syst.}) \qquad [e\text{+jets channel}]$$
$$F_L = 0.302 \pm 0.027\ (\text{stat.}) \pm 0.031\ (\text{syst.}) \qquad [e\text{+jets channel}]$$

$$F_0 = 0.685 \pm 0.022\ (\text{stat.}) \pm 0.027\ (\text{syst.}) \qquad [\mu\text{+jets channel}]$$
$$F_L = 0.315 \pm 0.022\ (\text{stat.}) \pm 0.027\ (\text{syst.}) \qquad [\mu\text{+jets channel}]$$

$$F_0 = 0.695 \pm 0.016\ (\text{stat.}) \pm 0.029\ (\text{syst.}) \quad [\text{lepton+jets channel}]$$
$$F_L = 0.305 \pm 0.016\ (\text{stat.}) \pm 0.029\ (\text{syst.}) \quad [\text{lepton+jets channel}]$$

The result from the combined likelihood fit is limited by the systematic uncertainties, while the uncertainty due to the top-quark mass as well as due to the jet energy scale and resolution have the largest impact. When comparing this result above with the measurement published in [3] using 1.04 fb^{-1}, the overall uncertainty is decreased by about 34% results are in good agreement with the SM prediction.

Category	e+jets	μ+jets	comb.
Statistical unc.	0.027	0.022	0.016
Detector modelling			
Jet energy scale	0.014	0.010	0.011
Jet energy res.	0.015	0.008	0.011
Jet reconstruction eff.	0.002	0.003	0.001
JVF SF	0.001	0.000	0.001
Lepton energy scale	0.009	0.000	0.008
Lepton energy res.	0.003	0.004	0.005
Lepton SF	0.002	0.001	0.003
b-tagging	0.003	0.003	0.003
Missing E_T	0.005	0.006	0.003
Signal and background modelling			
MC Generator	0.004	0.005	0.007
Parton showering	0.004	0.001	0.000
ISR/FSR	0.005	0.002	0.001
Underlying event	0.003	0.000	0.001
Color reconnection	0.003	0.004	0.004
Top mass (0.9 GeV)	0.014	0.014	0.014
PDF	0.004	0.004	0.003
W+jets shape	0.001	0.004	0.003
W+jets HF	0.005	0.012	0.008
Fake lepton shape	0.002	0.001	0.001
Method uncertainties			
Template stat.	0.011	0.010	0.011
Total uncertainty	0.041	0.035	0.033

Table 9.4.: Summary of statistical and systematic uncertainties using the two-dimensional fit. The results are shown for the e+jets (left column) the μ+jets (middle) and the combined lepton+jets channel (right column). The total uncertainties of the W-helicity fractions are dominated by the statistical and the top-quark mass uncertainty (assuming a top-mass uncertainty of 0.9 GeV in the systematics evaluation). For the total uncertainty, all sources of uncertainty are added in quadrature.

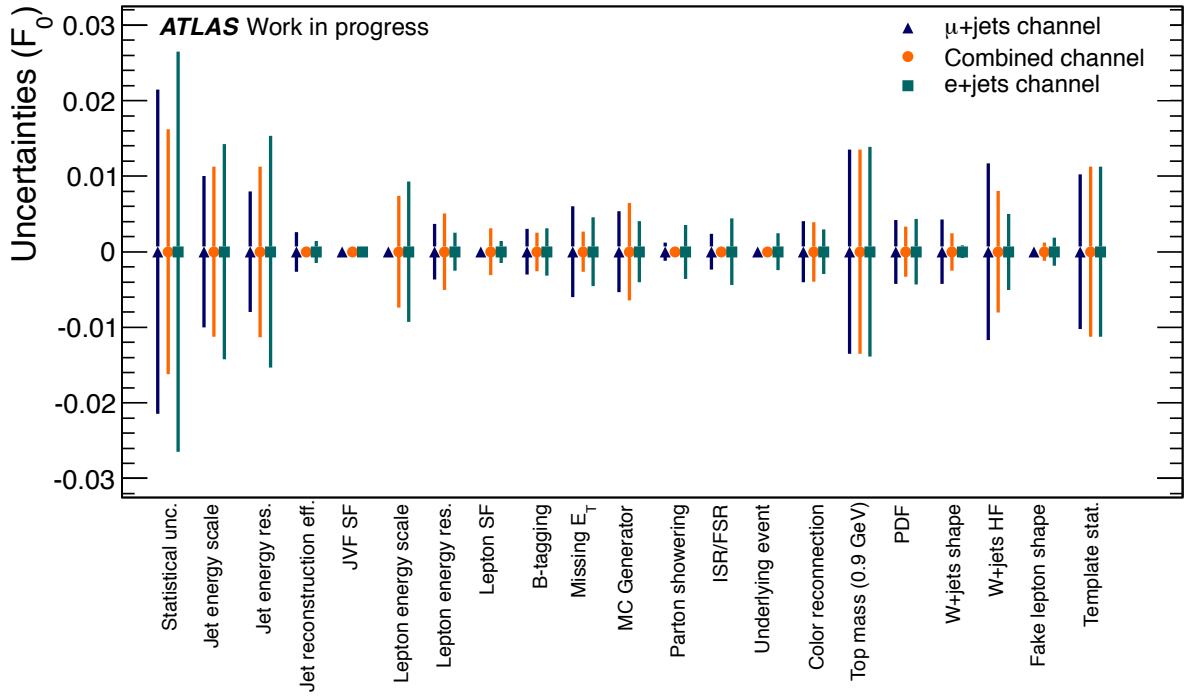

Figure 9.3.: Graphical comparison of the different sources of uncertainty for the μ+jets (triangle), the combined lepton+jets channel (circle) and the e+jets channel (squarel), using the two-dimensional fit. The total uncertainty of the combined likelihood fit is mainly driven by systematic uncertainties, while the uncertainty due to the top-quark mass has the largest impact.

9.1.2. Limit on C_{tW}^{33}

The result of the two-dimensional fit allows to set a limit on the coefficient of the dimension-six operator O_{tW}^{33} that was introduced in Chapter 3.4.2. As shown in Equation 3.29, this operator can lead to an alteration of the Wtb vertex. The limit on C_{tW}^{33} is obtained using a Bayesian approach, using the top-quark and W-boson mass as well as the widths of the W-boson and C_{tW}^{33} itself as parameters. The masses and widths are allowed to float within their uncertainties while C_{tW}^{33} is constrained by the precision of the F_0 measurement. The CKM matrix element V_{tb} is set to 1.

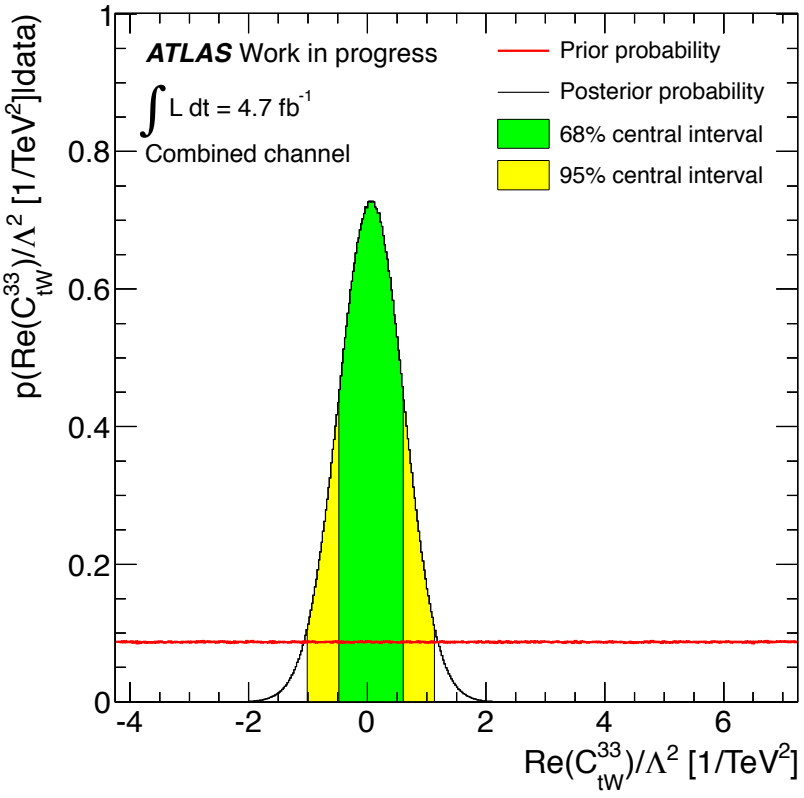

Figure 9.4.: Result for the fit parameter $\mathrm{Re}(C_{tW}^{33})/\Lambda^2$ showing the prior probability distribution (red line) as well as the distribution of the posterior probability (black line). The posterior probability density is integrated symmetrically around the peak to obtain the 68% (green) and 95% (yellow) probability interval, respectively.

The fit is carried out using Markov Chain Monte Carlo [163]. The method is implemented in the *BAT* package [164]. The central 68% and 95% probability intervals on C_{tW}^{33} were obtained from an integration over the marginalised distribution shown in Fig. 9.4. The limit set at 95% probability is:

$$\frac{\mathrm{Re}(C_{tW}^{33})}{\Lambda^2} \in [-1.01,\ 1.14]\ \mathrm{TeV}^{-2}.$$

The coefficient C_{tW}^{33} is hence consistent with zero.

9.2. Three-dimensional fit

The measurement is repeated using a three-dimensional fit while fitting the contributions of all three polarisation states simultaneously. Therefore three signal and three background templates (six background templates for the combined likelihood) are used in the fit.

9.2.1. W-helicity fractions

The best-fit results for the e+jets and for the μ+jets channel in Fig. 9.5 are represented by the solid line and are compared to the respective data distributions (black markers). The statistical and systematic uncertainties are shown by the hatched area on top of the best-fit result. The solid area represents the sum of the three background contributions. The best-fit result is in good agreement with the data distribution. The best-fit parameters and the W-helicity

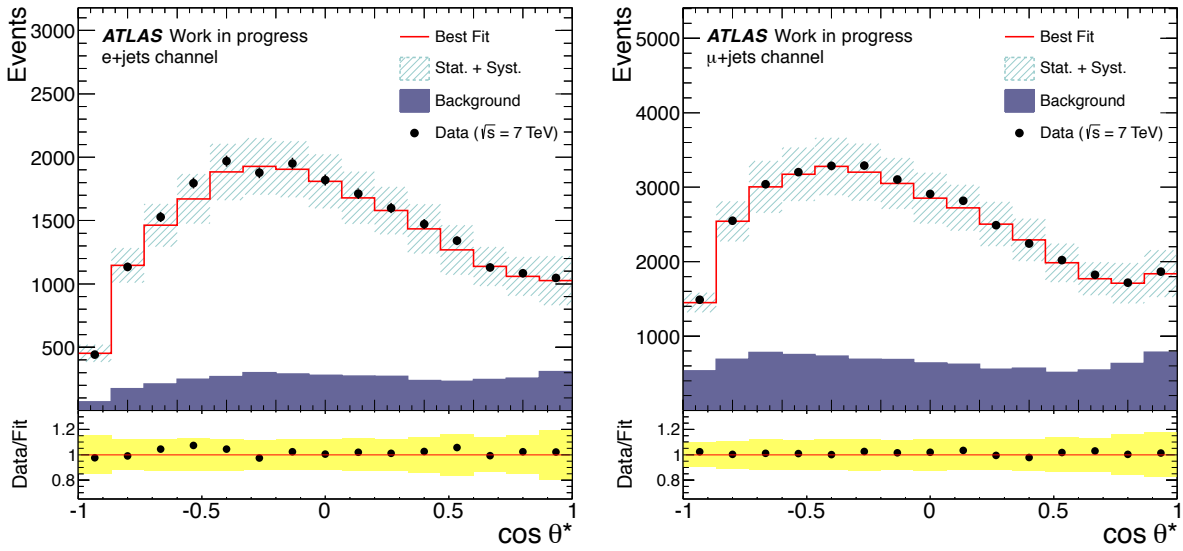

Figure 9.5.: Result of the data fit in the e+jets channel (left) and the μ+jets channel (right) using the three-dimensional fit. The data distributions (black markers) are shown together with the best-fit result (solid line) and the background distribution (solid area). The statistical and systematic uncertainties are shown by the hatched area.

fractions along with their statistical uncertainties are shown in Tab. 9.5 and Tab. 9.6 for the e+jets and the μ+jets channel, respectively. The fitted background normalisations agree with their predictions within the corresponding uncertainties. Although the data set for the μ+jets channel is larger, a smaller statistical uncertainty is observed in the e+jets channel. As discussed in Chapter 8.4, the large anti-correlations that are observed in the μ+jets channel lead to a higher uncertainty. Moreover, the observed statistical uncertainty in the e+jets channel is smaller than expected, while in the μ+jets channel the observed uncertainty is larger than expected. The systematic uncertainties are compared in Tab. 9.7. The measurements are dominated by the systematic uncertainty while the statistical uncertainties are still large. The reason for these large statistical contributions in both channels are the large uncertainties that constrain the background normalisation in the likelihood fit and the additional degree of fredom due to the additional parameter N_R.

Fraction/Param.	Sim.	σ(Sim.)	Fit	σ(Fit)	Diff. [$\sigma_{\text{Sim.}}$]
F_0			0.641	0.038	
F_L			0.320	0.020	
F_R			0.039	0.024	
N_0			273335	16743	
N_L			136217	15677	
N_R			16633	13906	
N(W+jets)	2294	1574	1554	1080	0.47
N(Fake lepton)	843	422	457	381	0.92
N(RemBkg)	1669	370	1641	361	0.08

Table 9.5.: Best-fit results for the e+jets channel using the three-dimensional fit. The extracted W-helicity fractions are shown with their corresponding statistical uncertainties. The predicted and fitted background normalisations are compared. The relative difference between them is shown in units of the standard deviation from the background prediction.

Fraction/Param.	Sim.	σ(Sim.)	Fit	σ(Fit)	Diff. [$\sigma_{\text{Sim.}}$]
F_0			0.669	0.044	
F_L			0.320	0.020	
F_R			0.011	0.029	
N_0			282502	11520	
N_L			135171	17461	
N_R			4432	14957	
N(W+jets)	4457	3022	5128	1527	0.22
N(Fake lepton)	1774	406	2023	321	0.61
N(RemBkg)	2517	497	2561	494	0.09

Table 9.6.: Best-fit results for the μ+jets channel using the three-dimensional fit. The extracted W-helicity fractions are shown with their corresponding statistical uncertainties. The predicted and fitted background normalisations are compared. The relative difference between them is shown in units of the standard deviation from the background prediction.

The systematic uncertainty is dominated by the jet energy scale and resolution, the missing transverse energy and the MC generators. Furthermore, the limited number of MC events for all templates leads to a sizable contribution. In agreement with the observation made for the two-dimensional fit, the e+jets channel is more affected by the systematics. This was explained by the tight cuts that lead to larger distortions of the angular distribution. When varying the jet and lepton energy scale and resolution, the changes are propagated into the calculation of the missing transverse energy. The tighter E_T^{miss} cut in the e+jets channel leads then to a reduced sensitivity at large $\cos\theta^*$ values. This effect is especially large for the jet energy scale and reconstruction but is also observed for the lepton energy/momentum scale and for the ISR/FSR uncertainty: Fig. 8.13 (left) in Chapter 8.5.1 shows a larger discrepancy of the pseudo-data distributions at high $\cos\theta^*$ values for the e+jets distribution. Hence, a much larger uncertainty is observed in the e+jets channel. In contrast to that, the μ+jets channel has larger uncertainties due to the colour reconnection and the MC generator comparisons. The corresponding pseudo-data distributions are compared in Chapter 8.5.1 and in the Appendix A.9.

$$
\begin{aligned}
F_0 &= 0.641 \pm 0.038\ (\text{stat.}) \pm 0.080\ (\text{syst.}) && [e\text{+jets channel}] \\
F_L &= 0.320 \pm 0.020\ (\text{stat.}) \pm 0.030\ (\text{syst.}) && [e\text{+jets channel}] \\
F_R &= 0.039 \pm 0.024\ (\text{stat.}) \pm 0.067\ (\text{syst.}) && [e\text{+jets channel}]
\end{aligned}
$$

$$
\begin{aligned}
F_0 &= 0.669 \pm 0.044\ (\text{stat.}) \pm 0.072\ (\text{syst.}) && [\mu\text{+jets channel}] \\
F_L &= 0.320 \pm 0.020\ (\text{stat.}) \pm 0.026\ (\text{syst.}) && [\mu\text{+jets channel}] \\
F_R &= 0.011 \pm 0.029\ (\text{stat.}) \pm 0.055\ (\text{syst.}) && [\mu\text{+jets channel}]
\end{aligned}
$$

	e+jets			μ+jets		
Category	F_0	F_L	F_R	F_0	F_L	F_R
Statistical unc.	0.038	0.020	0.024	0.044	0.020	0.029
Detector modelling						
Jet energy scale	0.047	0.017	0.041	0.034	0.008	0.027
Jet energy res.	0.027	0.001	0.028	0.022	0.003	0.020
Jet reconstruction eff.	0.000	0.001	0.001	0.004	0.004	0.000
JVF SF	0.000	0.001	0.001	0.001	0.001	0.001
Lepton energy scale	0.022	0.005	0.021	0.010	0.004	0.007
Lepton energy res.	0.013	0.003	0.010	0.007	0.004	0.003
Lepton SF	0.001	0.001	0.001	0.001	0.000	0.001
b-tagging	0.004	0.002	0.004	0.004	0.003	0.003
Missing E_T	0.024	0.008	0.017	0.020	0.010	0.010
Signal and background modelling						
MC Generator	0.028	0.012	0.016	0.036	0.011	0.025
Parton showering	0.012	0.001	0.011	0.001	0.001	0.000
ISR/FSR	0.013	0.008	0.006	0.001	0.002	0.001
Underlying event	0.004	0.003	0.001	0.002	0.001	0.002
Color reconnection	0.011	0.001	0.010	0.016	0.002	0.014
Top mass (0.9 GeV)	0.004	0.008	0.012	0.007	0.007	0.014
PDF	0.009	0.004	0.006	0.014	0.006	0.010
W+jets shape	0.002	0.001	0.002	0.001	0.003	0.003
W+jets HF	0.011	0.002	0.010	0.011	0.008	0.012
Fake lepton shape	0.003	0.001	0.002	0.005	0.002	0.003
Method uncertainties						
Template stat.	0.028	0.014	0.018	0.031	0.013	0.021
Total uncertainty	0.089	0.036	0.071	0.084	0.033	0.062

Table 9.7.: Summary of statistical and systematic uncertainties using the three-dimensional fit. The results are shown for the e+jets channel (left) and for the μ+jets channel (right).

Combined likelihood fit

The combined likelihood fit using the three-dimensional fit is performed with three signal and six background templates, allowing the individual background normalisations to float within their uncertainties. The result of the datafit is shown in Fig. 9.6. The corresponding helicity fractions and background normalisations are summarised in Tab. 9.8. The fitted background contributions are in agreement with their corresponding predicted values. The statistical uncertainties are decreased by the combined fit with respect to the separate e+jets and μ+jets channels. In Tab. 9.9, the systematic uncertainties of the combined likelihood are shown. The

Fraction/Param.	Sim.	σ(Sim.)	Fit	σ(Fit)	Diff. [$\sigma_{\text{Sim.}}$]
F_0			0.659	0.029	
F_L			0.317	0.014	
F_R			0.024	0.019	
N_0			280169	9268	
N_L			134882	11647	
N_R			10384	10186	
N(W+jets) e+jets	2294	1574	1527	774	0.49
N(W+jets) μ+jets	4457	3022	4675	1135	0.07
N(Fake lepton) e+jets	843	422	554	328	0.69
N(Fake lepton) μ+jets	1774	406	2113	269	0.84
N(RemBkg) e+jets	1669	370	1614	350	0.15
N(RemBkg) μ+jets	2517	497	2666	483	0.30

Table 9.8.: Best-fit results for the combined likelihood fit using the three-dimensional fit. The extracted W-helicity fractions are shown with their corresponding statistical uncertainties. The predicted and fitted background normalisations are compared. The relative difference between them is shown in units of the standard deviation from the background prediction.

total uncertainty is mainly driven by the jet energy scale and resolution, missing transverse energy and MC generators as well as the uncertainty due to limited MC statistics. In Figs. 9.7, 9.8 and 9.9, the uncertainties of the three measurements presented above are compared graphically for F_0, F_L and F_R, respectively. The overall uncertainties on F_L are smaller and its dominating uncertainties are due to uncertainties on the jet energy scale, missing transverse energy, MC generator and due to limited template statistics. The uncertainty due to the choice of the parton shower model is much larger in the e+jets than in the μ+jets channel. As explained in the previous subchapter, the mis-modelling of the HERWIG sample is expected to be the cause of this difference. The difference in jet energy scale and resolution as well as for the missing transverse energy uncertainty were discussed in detail above.

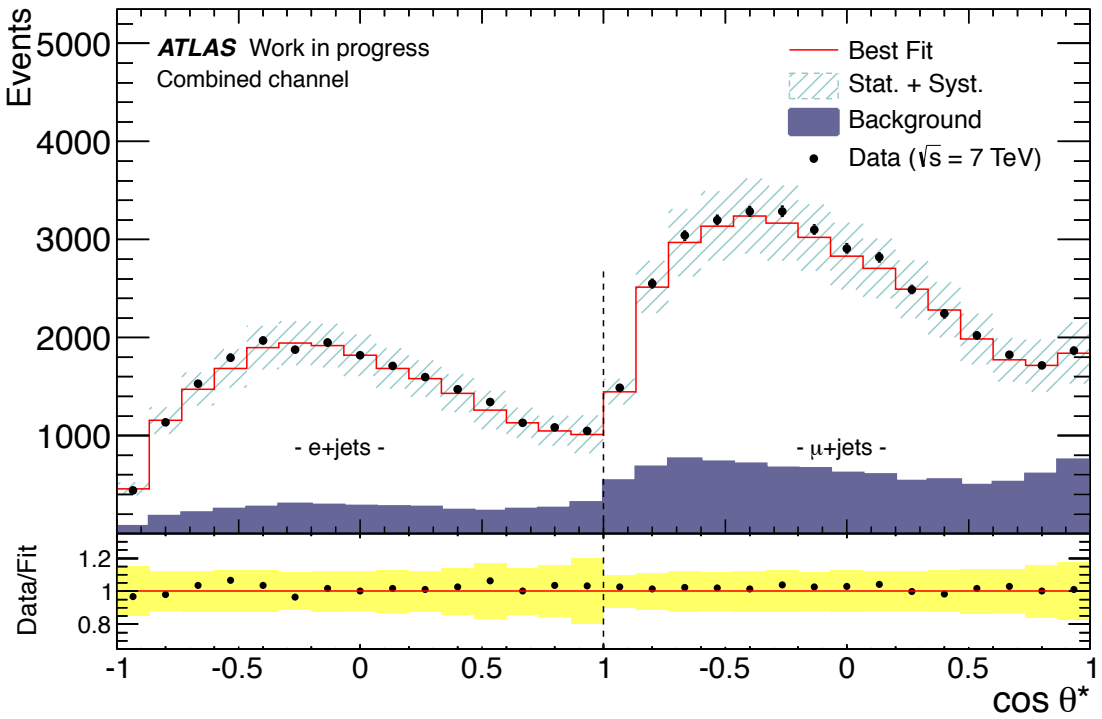

Figure 9.6.: Result of the data fit in the combined lepton+jets channel using the three-dimensional fit. The data distributions (black markers) are shown together with the best-fit result (solid line) and the background distribution (solid area). The statistical and systematic uncertainties are shown by the hatched area. In the lower part of the plot, the residual distribution with the corresponding uncertainties are drawn.

Category	F_0	F_L	F_R
Statistical unc.	0.029	0.014	0.019
Detector modelling			
Jet energy scale	0.041	0.012	0.034
Jet energy res.	0.024	0.001	0.024
Jet reconstruction eff.	0.002	0.001	0.001
JVF SF	0.001	0.000	0.001
Lepton energy scale	0.010	0.004	0.010
Lepton energy res.	0.007	0.005	0.005
Lepton SF	0.005	0.004	0.002
b-tagging	0.004	0.002	0.003
Missing E_T	0.022	0.008	0.014
Signal and background modelling			
MC Generator	0.030	0.011	0.021
Parton showering	0.008	0.002	0.006
ISR/FSR	0.004	0.002	0.003
Underlying event	0.003	0.001	0.002
Color reconnection	0.012	0.001	0.011
Top mass (0.9 GeV)	0.006	0.007	0.013
PDF	0.007	0.003	0.006
W+jets shape	0.003	0.003	0.000
W+jets HF	0.011	0.005	0.009
Fake lepton shape	0.003	0.001	0.002
Method uncertainties			
Template stat.	0.028	0.014	0.018
Total uncertainty	0.077	0.030	0.060

Table 9.9.: Summary of statistical and systematic uncertainties using the three-dimensional fit. The results are shown for the combined likelihood fit.

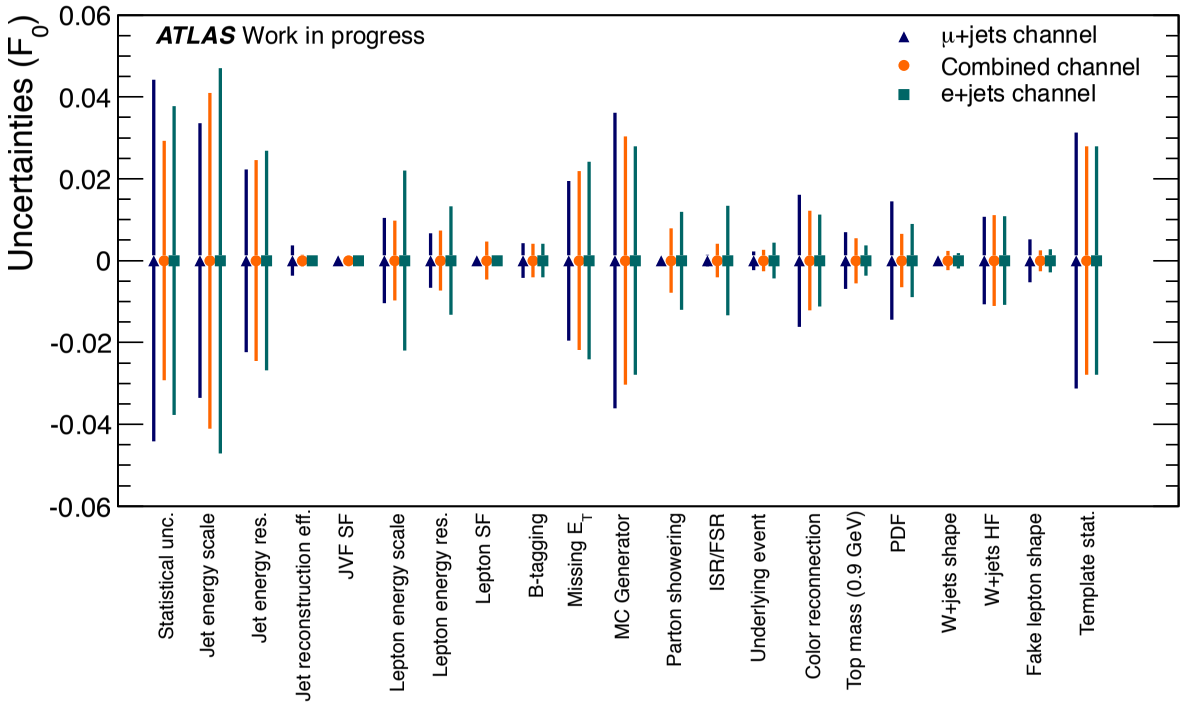

Figure 9.7.: Graphical comparison of the different sources of uncertainty on the longitudinal fraction F_0 for the μ+jets (triangle), the combined (circle) and the e+jets channel (square) using the three-dimensional fit.

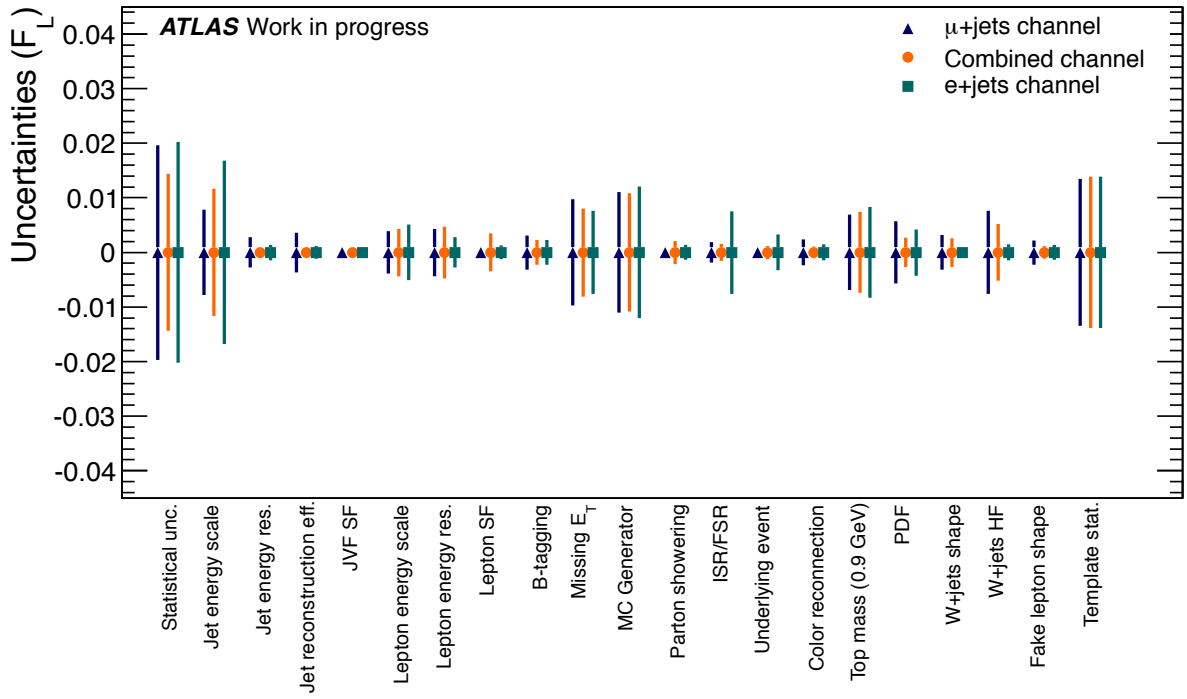

Figure 9.8.: Graphical comparison of the different sources of uncertainty on the longitudinal fraction F_{L} for the μ+jets (triangle), the combined (circle) and the e+jets channel (square) using the three-dimensional fit.

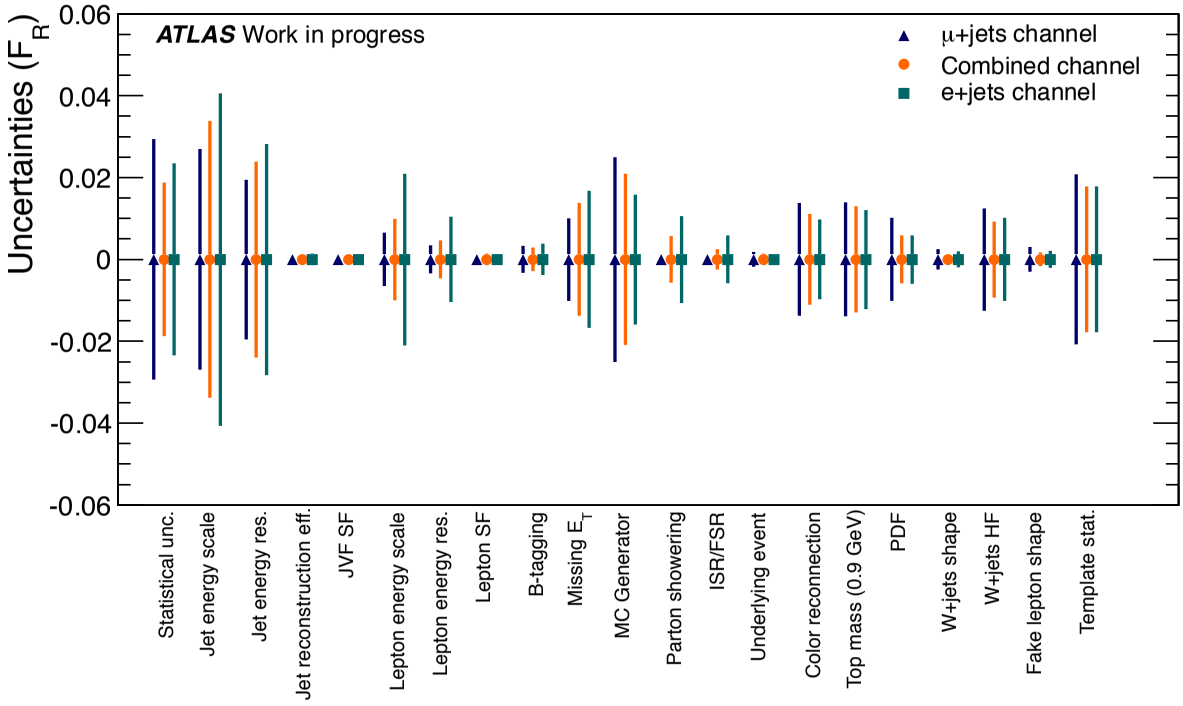

Figure 9.9.: Graphical comparison of the different sources of uncertainty on the longitudinal fraction F_{R} for the μ+jets (triangle), the combined (circle) and the e+jets channel (square) using the three-dimensional fit.

The final result of the three-dimensional fit is shown below. Figure 9.10 shows the graphical comparison of the individual measurements and the combined result with the Standard Model expectation in the F_0-F_L-plane. The fit result for the e+jets channel is shown (triangle up) together with the error ellipse (dashed line). The uncertainties in the e+jets channel are slightly higher due to the tighter cuts that lead to a decrease of sensitivity on both sides of the $\cos\theta^*$ spectrum. The uncertainties for the μ+jets channel are smaller and the error ellipse is drawn using a dotted line. Finally, the error ellipse for the combination is drawn (solid line) together with the uncertainties in x- and y-direction. The black error bars show the statistical uncertainty while the red error bars show the total uncertainty. All measurements are consistent with each other and in good agreement with the SM prediction. They are also consistent with the results obtained for the two-dimensional fit. The correlations between F_0 and F_L shown in Figure 9.10 are obtained from the total uncertainties and are determined to ρ = -0.66 (e+jets), ρ = -0.78 (μ+jets) and ρ = -0.70 (combined fit).

$$
\begin{aligned}
F_0 &= 0.659 \pm 0.029\ \text{(stat.)} \pm 0.071\ \text{(syst.)}\ \ \text{[lepton+jets channel]}\ , \\
F_L &= 0.317 \pm 0.014\ \text{(stat.)} \pm 0.026\ \text{(syst.)}\ \ \text{[lepton+jets channel]}\ , \\
F_R &= 0.024 \pm 0.019\ \text{(stat.)} \pm 0.057\ \text{(syst.)}\ \ \text{[lepton+jets channel]}\ .
\end{aligned}
$$

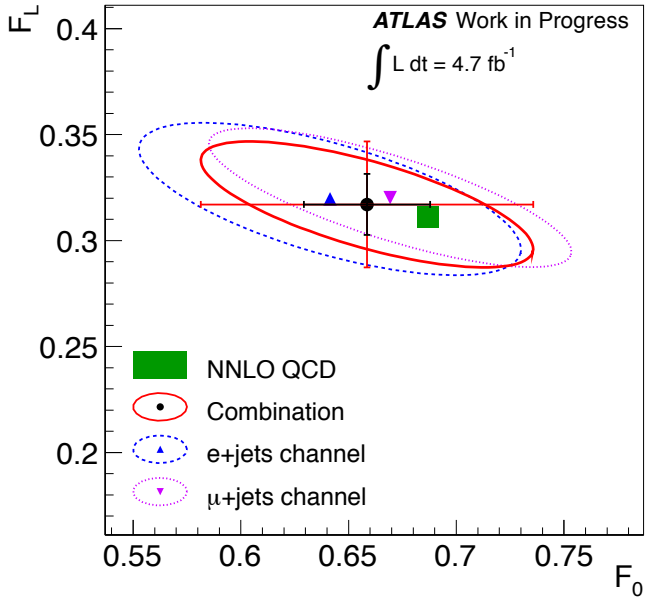

Figure 9.10.: Summary of the best-fit results and the corresponding error ellipse in the e+jets channel (triangle up, dashed line), the μ+jets channel (triangle down, dotted line) and the combination for the lepton+jets channel (circle, solid line). The results are compared with the Standard Model prediction at NNLO (green square) [66]. The results are in good agreement with the Standard Model prediction.

9.2.2. Limits on anomalous Wtb couplings

The W-helicity fractions obtained from the three-dimensional fit are now used to determine limits on the anomalous couplings introduced in Chapter 3.4.2. In contrast to the chirality conserving operator O_{uW}^{33}, the operators O_{dW}^{33*} and $O_{\phi\phi}^{33}$ are chirality flipping. In contrast to the approach followed in Section 9.1.2, the b-quark mass has to be taken into account when calculating the limits on the anomalous couplings. The calculation is done with the TopFit program using an acceptance-rejection method [70, 83]. The one-dimensional limits are obtained under the assumption that $V_L = 1$ and that all but one coupling vanish. These limits can be directly translated into limits on the operator coefficients as described in Eq. 3.31. The results at 95% confidence level are:

$$\begin{aligned}
\mathrm{Re}(\mathrm{V_R}) \in [-0.34, 0.34] &\rightarrow \frac{\mathrm{Re}(\mathrm{C}_{\phi\phi}^{33})}{\Lambda^2} \in [-11.3, 11.3]\,\mathrm{TeV}^{-2} \\
\mathrm{Re}(\mathrm{g_L}) \in [-0.23, 0.20] &\rightarrow \frac{\mathrm{Re}(\mathrm{C}_{\mathrm{dW}}^{33})}{\Lambda^2} \in [\ -2.7,\ \ 2.4]\,\mathrm{TeV}^{-2} \\
\mathrm{Re}(\mathrm{g_R}) \in [-0.10, 0.07] &\rightarrow \frac{\mathrm{Re}(\mathrm{C}_{\mathrm{uW}}^{33})}{\Lambda^2} \in [\ -1.1,\ \ 0.8]\,\mathrm{TeV}^{-2} \quad .
\end{aligned}$$

Two dimensional limits on the g_L-g_R plane are calculated under the assumption that $V_L = 1$ and $V_R = 0$. The result can be seen in Fig. 9.11. The yellow region shows the 95% confidence level and the green distribution the 68% confidence level. The smaller upper region is only shown here for completeness. Such large g_R values would only be possible if the single-top cross section was much larger than observed, therefore this region is already excluded [165, 166, 167]. Both the one-dimensional and two-dimensional limits are in agreement with vanishing anomalous couplings. No deviation from SM expectations is observed.

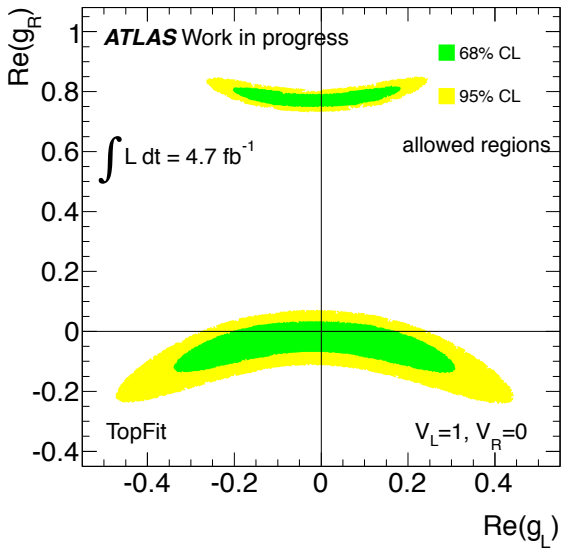

Figure 9.11.: Two-dimensional region for the anomalous Wtb couplings g_L and g_R at 68% and 95% confidence level. The upper region is excluded by the size of the single-top cross section. The results for the operators are consistent with zero. No deviation from SM expectations is observed.

10. Summary and Conclusions

The polarisation of W-bosons in top-quark decays was studied using events containing top-antitop pairs. The measurements were based on a dataset corresponding to an integrated luminosity of 4.7 fb^{-1} that was collected with the ATLAS detector in 2011 in proton-proton interactions with a centre-of-mass energy of 7 TeV. The W-helicity fractions were measured in the lepton+jets channel, characterised by the presence of one high-p_{T} lepton, missing transverse energy and at least four high-p_{T} jets with at least one b-tagged jet. The background is composed of the production of W-bosons with additional jets, background due to misidentified leptons as well as single top, Z+jets and diboson production. The requirement to have at least one b-tagged jet leads to a significant improvement of the signal-to-background ratio.

The events were reconstructed using a kinematic likelihood approach. The four jets with highest transverse momentum were considered for the event reconstruction. b-tagging information was used to improve the event reconstruction. Furthermore, the top-quark mass was fixed in the kinematic fit which leads to a significant increase of the reconstruction efficiency. The jet-parton assignment with the highest probability was chosen for the analysis.

In order to measure the W-helicity fractions, the angular distribution of the charged lepton, $\cos\theta^*$, was used. This variable is defined as the angle between the charged lepton and the negative direction of the b-quark in the rest frame of the W-boson. The variable can be calculated using the best fit results of the kinematic likelihood fit and provides good separation power between the three polarisation states.

The W-helicity fractions were measured using a template method. This approach allows to fully exploit the shape of the angular distribution. Two different measurements were performed. First, a two-dimensional fit was performed where the right-handed fraction is fixed to zero. This allows to set limits on the dimension-six Operator C_{tW}^{33} that was introduced in an effective Lagrangian approach and would lead to an alteration of the W-helicity fractions. Furthermore, a three-dimensional measurement is carried out where the three helicity fractions were measured simultaneously. Taking into account the b-quark mass, limits on anomalous couplings were set.

Two-dimensional fit

From the combined likelihood fit to the e+jets and μ+jets distribution, the results for F_0 and F_{L} are obtained:

$$\begin{aligned} F_0 &= 0.695 \pm 0.016\ (\text{stat.}) \ \pm\ 0.029\ (\text{syst.}) \quad , \\ F_L &= 0.305 \pm 0.016\ (\text{stat.}) \ \pm\ 0.029\ (\text{syst.}) \quad . \end{aligned}$$

This measurement is limited by the systematic uncertainty. A comparison of this result with the measurement published in [3] using 1.04 fb^{-1} shows an improvement of the total uncertainty by 34%. This leads to an improved limit on the operater coefficient C_{tW}^{33}. The result at 95% probability is $\frac{\mathrm{Re}(C_{tW}^{33})}{\Lambda^2} \in [-1.01,\ 1.14]$ TeV^{-2}. All results are in good agreement with the SM prediction.

Three-dimensional fit

The three-dimensional fit was performed while extracting all three helicity fractions simultaneously. The result of the combined likelihood fit is:

$$\begin{aligned} F_0 &= 0.659 \pm 0.029 \text{ (stat.)} \pm 0.071 \text{ (syst.)} \\ F_L &= 0.317 \pm 0.014 \text{ (stat.)} \pm 0.026 \text{ (syst.)} \\ F_R &= 0.024 \pm 0.019 \text{ (stat.)} \pm 0.057 \text{ (syst.)} \quad . \end{aligned}$$

The total fit result is compared with the most precise measurements from ATLAS [3], CMS [74], and the Tevatron combination[1] [78] in Fig. 10.1. The yellow band shows the result presented in this thesis while the green line shows the values from the SM prediction [66]. While the uncertainty on F_0 is of similar size as the results from the ATLAS and Tevatron combination, the uncertainty on F_R is larger. When compared directly to the result of the template method in the lepton+jets channel with 1.04 fb^{-1}, the uncertainties are reduced by about 27% for F_0 , 40% for F_L and 10% for F_R. Therefore the result presented here is the most precise single measurement of the W-helicity fractions to date.

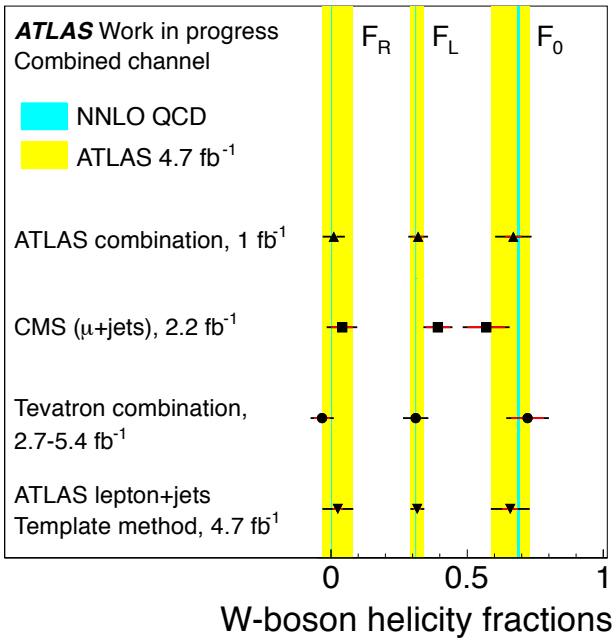

Figure 10.1.: Comparison of the best fit results presented in this thesis (triangle down) with the combination of Tevatron measurements [78] (circle), CMS [74] (square) and the previous ATLAS combination that was perfomed based on a data set of 1.04 fb^{-1} [3] (triangle up). The NNLO prediction is shown with the green line [66]. For easier comparison, the measurement presented in this thesis is shown in addition by the yellow band.

[1] The left-handed helicity fraction and corresponding uncertainty has been calculated from the uncertainties and correlations of F_0 and F_R.

Prospects for future measurements

As shown in the results summarised above, the measurements are limited by systematic uncertainties. The main contributions are the uncertainties due to the jet energy scale and resolution. These uncertainties could be reduced by introducing nuisance parameters in a profile likelihood approach. The uncertainty due to the limited template statistics can be reduced by increasing the number of generated MC events for the template distributions. Furthermore, the statistical uncertainy in the three-dimensional fit is still relatively large due to the large uncertainties on the background prediction. This could be improved by including a background dominated region in a combined likelihood fit. One possible channel could be defined as events that do not have a b-tag, since this channel is dominated by W+jets production.

A. Appendix

A.1. Pretag selection

Event yields and kinematic distributions for the lepton+jets channel using the pretag selection (see Chapter 7.2). The discrepancies in normalisation that are shown in Tab. A.1 are covered by the uncertainties. The uncertainty bands in Fig. A.1 and A.2 contain the statistical uncertainty as well as the normalisation and luminosity uncertainty of 1.8%. The PROTOS generator is used for the signal modelling. In the e+jets channel, deviations at higher lepton E_T are observed.

	e+jets		μ+jets	
Process	Events	Uncertainty	Events	Uncertainty
$t\bar{t}$(Protos)	21141	2340	32070	3526
W+jets	13214	2284	26322	4526
Misid. leptons	3923	1962	6282	1438
Single Top	1475	116	2460	187
Z+jets	2900	1396	2911	1401
Diboson	231	16	375	24
Total predicted	42884	4062	70419	6082
Observed	40738		71385	
S/B	0.97		0.84	

Table A.1.: Event yields for the e+jets (left) and μ+jets channel (right) after the selection of events with at least four jets, one charged lepton and missing transverse energy.

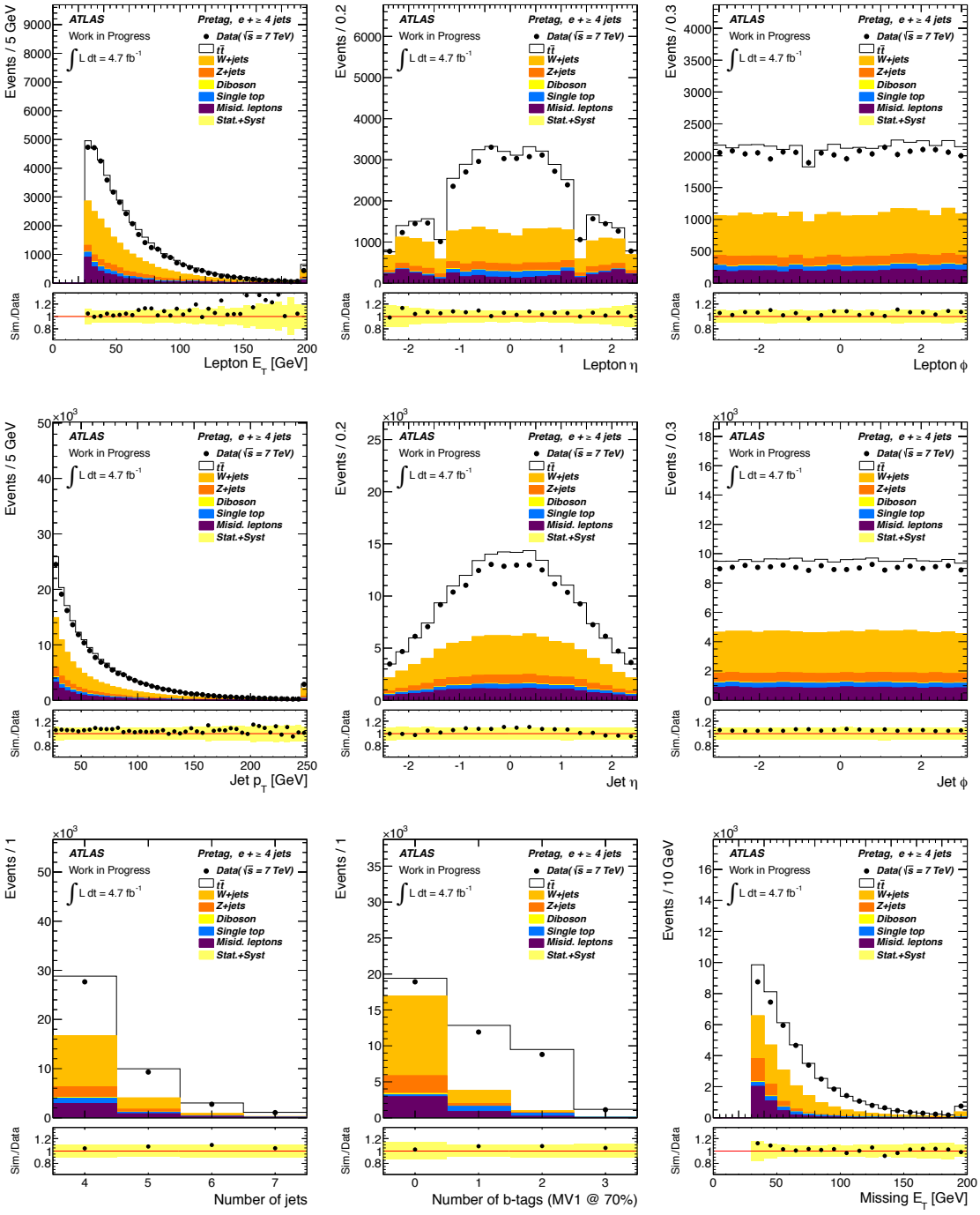

Figure A.1.: Comparison of data and simulated events in the e+jets channel for lepton and jet quantities as well as the missing transverse energy after the pretag selection. The yellow band in the residual distributions contains beside the statistical uncertainty further uncertainties on the cross-section normalisation and on the luminosity.Data and MC agree within the uncertainties.

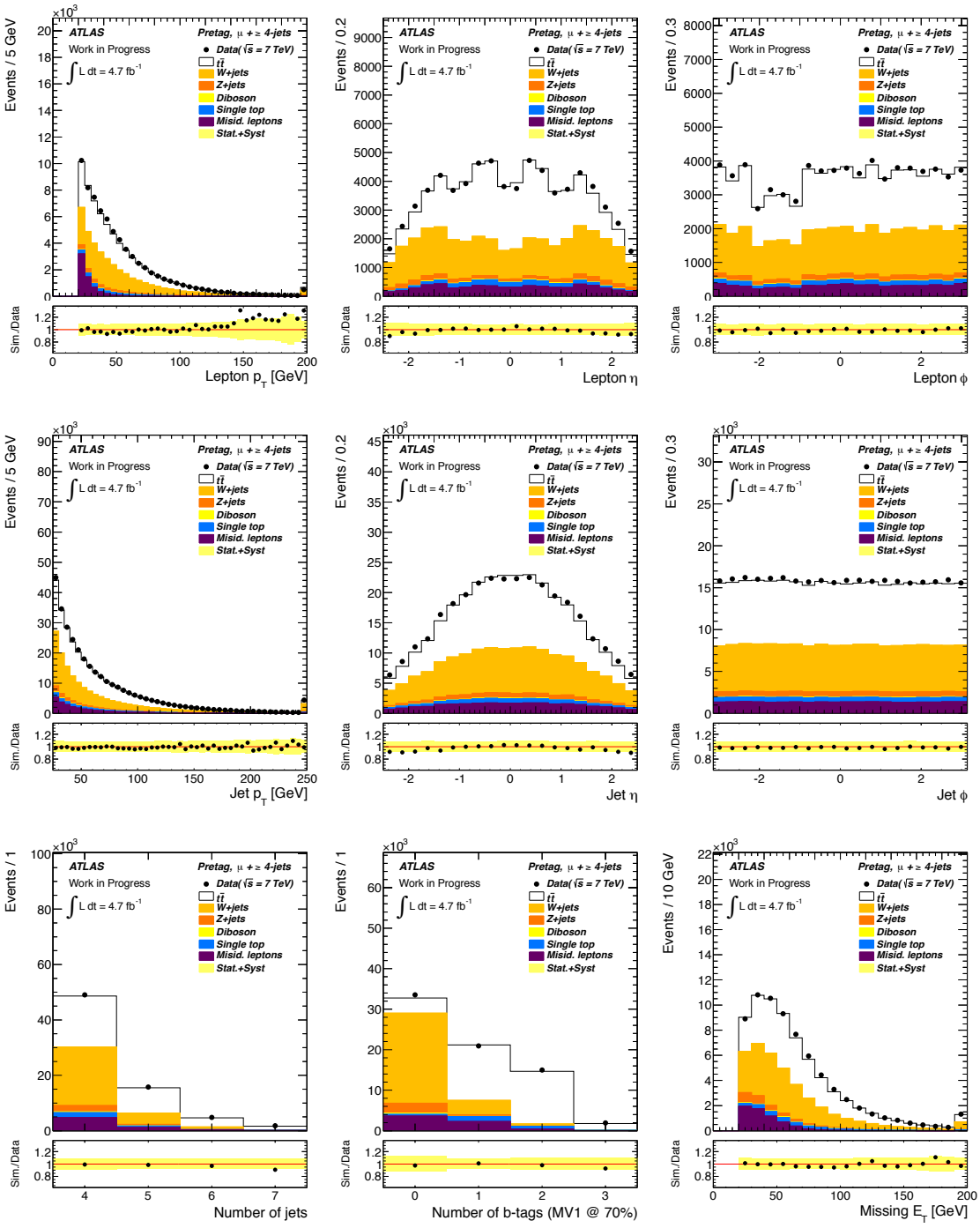

Figure A.2.: Comparison of data and simulated events in the μ+jets channel for lepton and jet quantities as well as the missing transverse energy after the pretag selection. The yellow band in the residual distributions contains beside the statistical uncertainty further uncertainties on the cross-section normalisation and on the luminosity. Data and simulation agree within the uncertainties.

A.2. Kinematics of Reconstructed Top Quarks

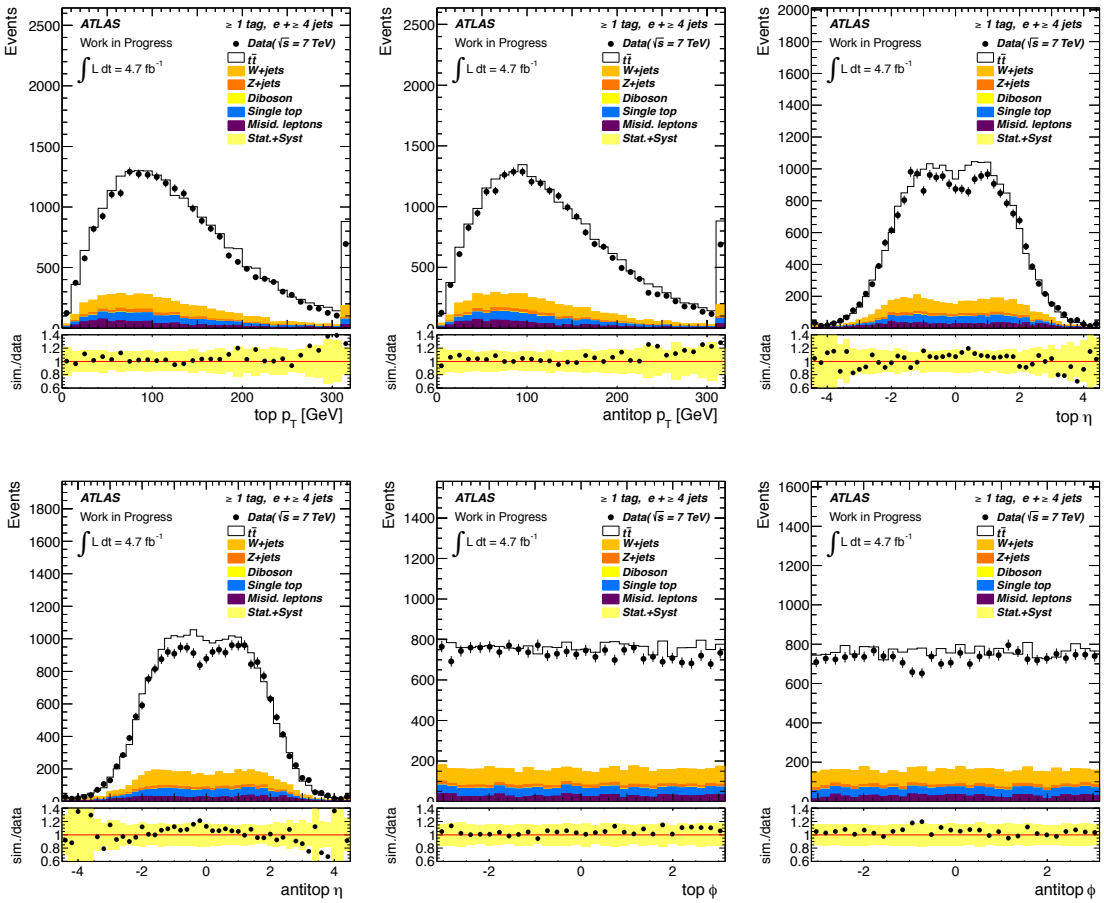

Figure A.3.: Comparison of top-/antitop-distributions for data and simulated events in the e+jets channel that are reconstructed using a kinematic likelihood fit.

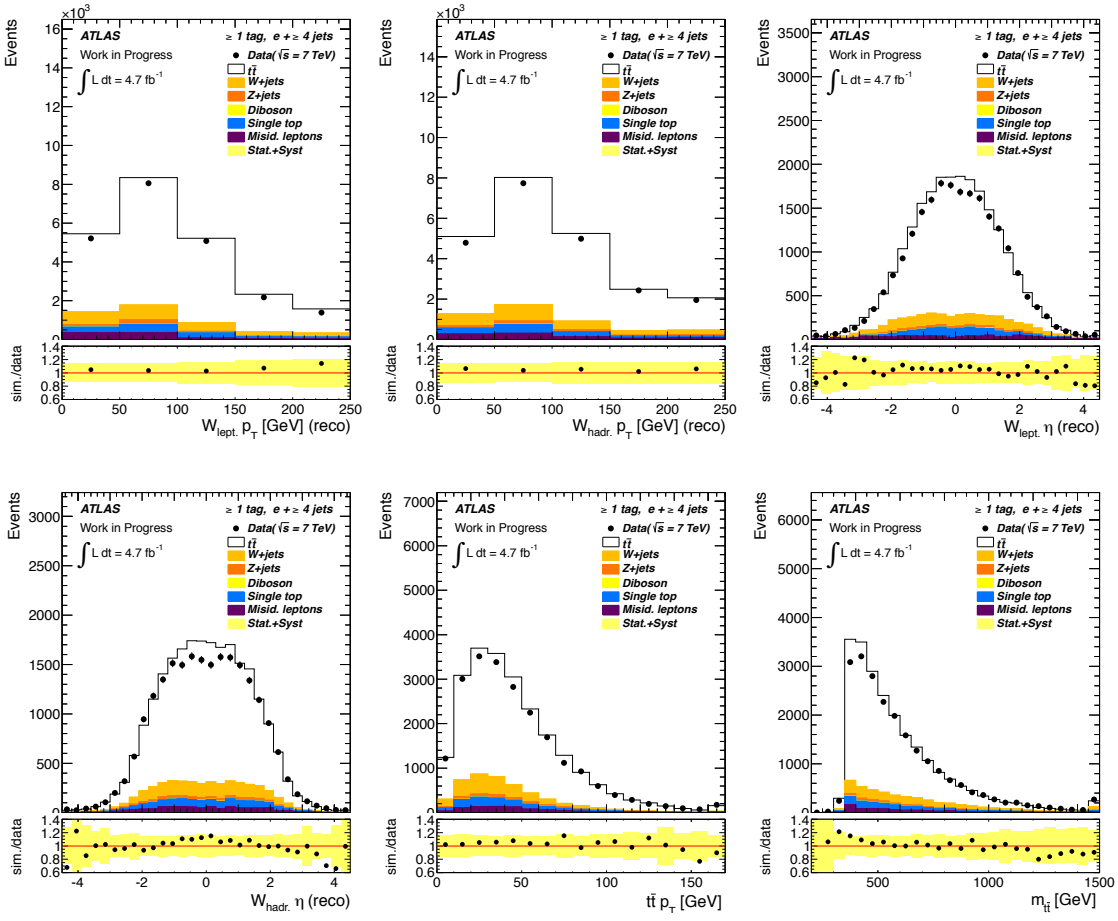

Figure A.4.: Comparison of W-boson and $t\bar{t}$-distributions for data and simulated events in the e+jets channel that are reconstructed using a kinematic likelihood fit.

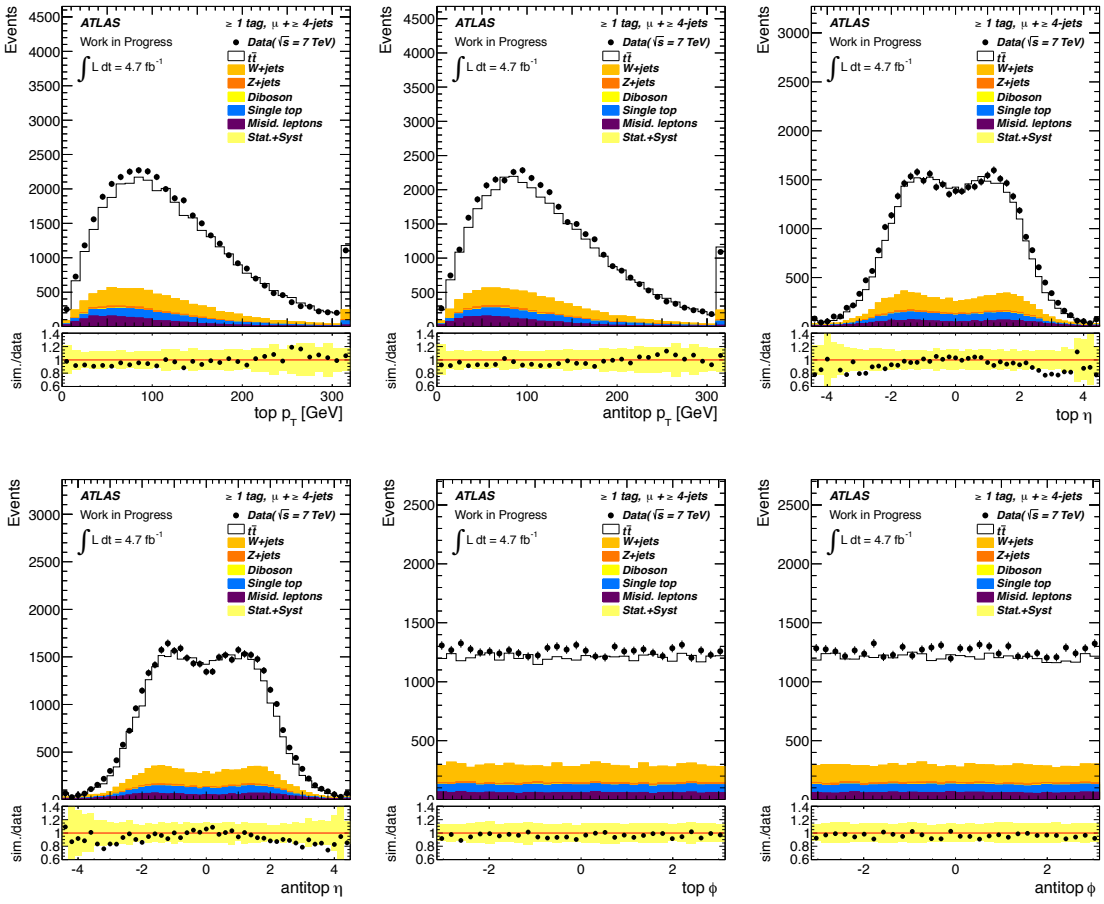

Figure A.5.: Comparison of top-/antitop-distributions for data and simulated events in the μ+jets channel that are reconstructed using a kinematic likelihood fit.

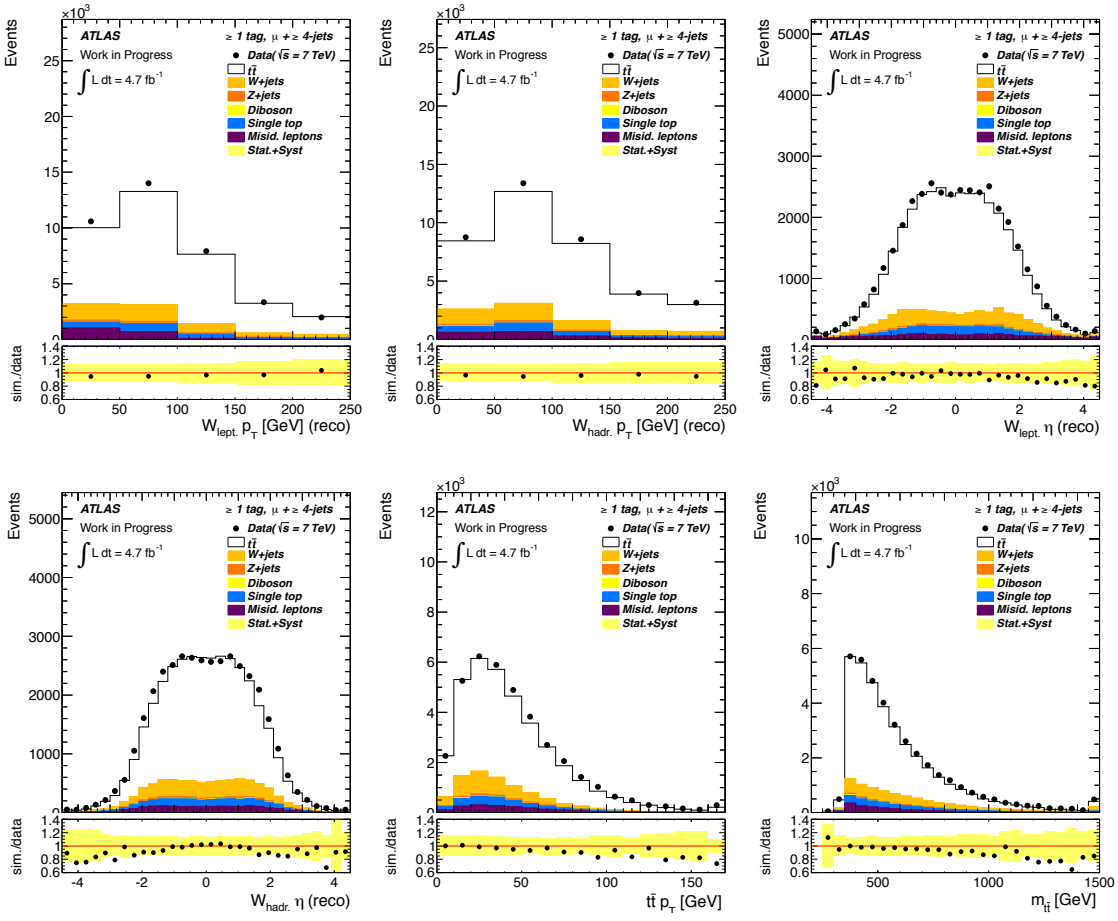

Figure A.6.: Comparison of W-boson and $t\bar{t}$-distributions for data and simulated events in the μ+jets channel that are reconstructed using a kinematic likelihood fit.

A.3. Monte Carlo samples

Process	Generator	Showering	PDF	Nr(Events)	$\int \mathcal{L}dt$ [fb^{-1}]
$W(\to e\bar{\nu_e})$ Np0	Alpgen	Herwig	CTEQ6L1	6952874	0.8
$W(\to e\bar{\nu_e})$ Np1	Alpgen	Herwig	CTEQ6L1	4998487	3.2
$W(\to e\bar{\nu_e})$ Np2	Alpgen	Herwig	CTEQ6L1	3768632	8.3
$W(\to e\bar{\nu_e})$ Np3	Alpgen	Herwig	CTEQ6L1	1008947	8.3
$W(\to e\bar{\nu_e})$ Np4	Alpgen	Herwig	CTEQ6L1	744998	24.3
$W(\to e\bar{\nu_e})$ Np5	Alpgen	Herwig	CTEQ6L1	419947	50.2
$W(\to \mu\bar{\nu_\mu})$ Np0	Alpgen	Herwig	CTEQ6L1	6962239	0.8
$W(\to \mu\bar{\nu_\mu})$ Np1	Alpgen	Herwig	CTEQ6L1	4988236	3.2
$W(\to \mu\bar{\nu_\mu})$ Np2	Alpgen	Herwig	CTEQ6L1	3768737	8.3
$W(\to \mu\bar{\nu_\mu})$ Np3	Alpgen	Herwig	CTEQ6L1	1008446	8.3
$W(\to \mu\bar{\nu_\mu})$ Np4	Alpgen	Herwig	CTEQ6L1	754898	24.6
$W(\to \mu\bar{\nu_\mu})$ Np5	Alpgen	Herwig	CTEQ6L1	418496	50.0
$W(\to \tau\bar{\nu_\tau})$ Np0	Alpgen	Herwig	CTEQ6L1	3418296	0.4
$W(\to \tau\bar{\nu_\tau})$ Np1	Alpgen	Herwig	CTEQ6L1	2499194	1.6
$W(\to \tau\bar{\nu_\tau})$ Np2	Alpgen	Herwig	CTEQ6L1	3750928	8.3
$W(\to \tau\bar{\nu_\tau})$ Np3	Alpgen	Herwig	CTEQ6L1	1009946	8.3
$W(\to \tau\bar{\nu_\tau})$ Np4	Alpgen	Herwig	CTEQ6L1	249998	8.1
$W(\to \tau\bar{\nu_\tau})$ Np5	Alpgen	Herwig	CTEQ6L1	65000	7.8
Wbb Np0	Alpgen	Herwig	CTEQ6L1	474997	8.4
Wbb Np1	Alpgen	Herwig	CTEQ6L1	205000	4.8
Wbb Np2	Alpgen	Herwig	CTEQ6L1	174499	8.4
Wbb Np3	Alpgen	Herwig	CTEQ6L1	69999	7.7
Wcc Np0	Alpgen	Herwig	CTEQ6L1	1274846	8.3
Wcc Np1	Alpgen	Herwig	CTEQ6L1	1049847	8.4
Wcc Np2	Alpgen	Herwig	CTEQ6L1	524947	8.4
Wcc Np3	Alpgen	Herwig	CTEQ6L1	170000	8.4
Wc Np0	Alpgen	Herwig	CTEQ6L1	6497837	6.6
Wc Np1	Alpgen	Herwig	CTEQ6L1	2069646	6.6
Wc Np2	Alpgen	Herwig	CTEQ6L1	519974	6.7
Wc Np3	Alpgen	Herwig	CTEQ6L1	115000	6.6
Wc Np4	Alpgen	Herwig	CTEQ6L1	30000	7.0
WW	Alpgen	Herwig	MRST	2489242	146.3
ZZ	Alpgen	Herwig	MRST	249999	197.8
WZ	Alpgen	Herwig	MRST	999896	180.4

Table A.2.: List of generators used for the production of W+jets samples including heavy-flavour samples for different number of parton multiplicities and diboson samples.

Process	Gen.	Shower.	PDF	Nr(Events)	$\int \mathcal{L}dt$ [fb^{-1}]
$Z(\rightarrow e^+e^-)$ Np0	Alpgen	Herwig	CTEQ6L1	6618284	7.9
$Z(\rightarrow e^+e^-)$ Np1	Alpgen	Herwig	CTEQ6L1	1334897	7.9
$Z(\rightarrow e^+e^-)$ Np2	Alpgen	Herwig	CTEQ6L1	2004195	39.6
$Z(\rightarrow e^+e^-)$ Np3	Alpgen	Herwig	CTEQ6L1	549949	39.4
$Z(\rightarrow e^+e^-)$ Np4	Alpgen	Herwig	CTEQ6L1	149948	41.7
$Z(\rightarrow e^+e^-)$ Np5	Alpgen	Herwig	CTEQ6L1	50000	48.2
$Z(\rightarrow \mu^+\mu^-)$ Np0	Alpgen	Herwig	CTEQ6L1	6615230	7.9
$Z(\rightarrow \mu^+\mu^-)$ Np1	Alpgen	Herwig	CTEQ6L1	1334296	8.0
$Z(\rightarrow \mu^+\mu^-)$ Np2	Alpgen	Herwig	CTEQ6L1	1999727	39.7
$Z(\rightarrow \mu^+\mu^-)$ Np3	Alpgen	Herwig	CTEQ6L1	549896	39.3
$Z(\rightarrow \mu^+\mu^-)$ Np4	Alpgen	Herwig	CTEQ6L1	150000	43.6
$Z(\rightarrow \mu^+\mu^-)$ Np5	Alpgen	Herwig	CTEQ6L1	50000	51.9
$Z(\rightarrow \tau^+\tau^-)$ Np0	Alpgen	Herwig	CTEQ6L1	10613179	12.7
$Z(\rightarrow \tau^+\tau^-)$ Np1	Alpgen	Herwig	CTEQ6L1	3334137	19.8
$Z(\rightarrow \tau^+\tau^-)$ Np2	Alpgen	Herwig	CTEQ6L1	1004847	19.9
$Z(\rightarrow \tau^+\tau^-)$ Np3	Alpgen	Herwig	CTEQ6L1	509847	36.3
$Z(\rightarrow \tau^+\tau^-)$ Np4	Alpgen	Herwig	CTEQ6L1	144999	41.6
$Z(\rightarrow \tau^+\tau^-)$ Np5	Alpgen	Herwig	CTEQ6L1	45000	46.8
$Z(\rightarrow e^+e^-)$ Np0 (m_{ll} =10-40 GeV)	Alpgen	Herwig	CTEQ6L1	994949	0.3
$Z(\rightarrow e^+e^-)$ Np1 (m_{ll} =10-40 GeV)	Alpgen	Herwig	CTEQ6L1	299998	2.8
$Z(\rightarrow e^+e^-)$ Np2 (m_{ll} =10-40 GeV)	Alpgen	Herwig	CTEQ6L1	9999461	9.3
$Z(\rightarrow e^+e^-)$ Np3 (m_{ll} =10-40 GeV)	Alpgen	Herwig	CTEQ6L1	149998	14.3
$Z(\rightarrow e^+e^-)$ Np4 (m_{ll} =10-40 GeV)	Alpgen	Herwig	CTEQ6L1	40000	17.3
$Z(\rightarrow e^+e^-)$ Np5 (m_{ll} =10-40 GeV)	Alpgen	Herwig	CTEQ6L1	10000	17.4
$Z(\rightarrow \mu^+\mu^-)$ Np0 (m_{ll} =10-40 GeV)	Alpgen	Herwig	CTEQ6L1	999849	0.3
$Z(\rightarrow \mu^+\mu^-)$ Np1 (m_{ll} =10-40 GeV)	Alpgen	Herwig	CTEQ6L1	300000	2.8
$Z(\rightarrow \mu^+\mu^-)$ Np2 (m_{ll} =10-40 GeV)	Alpgen	Herwig	CTEQ6L1	999992	19.3
$Z(\rightarrow \mu^+\mu^-)$ Np3 (m_{ll} =10-40 GeV)	Alpgen	Herwig	CTEQ6L1	150000	14.3
$Z(\rightarrow \mu^+\mu^-)$ Np4 (m_{ll} =10-40 GeV)	Alpgen	Herwig	CTEQ6L1	39999	17.3
$Z(\rightarrow \mu^+\mu^-)$ Np5 (m_{ll} =10-40 GeV)	Alpgen	Herwig	CTEQ6L1	10000	17.4
$Z(\rightarrow \tau^+\tau^-)$ Np0 (m_{ll} =10-40 GeV)	Alpgen	Herwig	CTEQ6L1	999649	0.3
$Z(\rightarrow \tau^+\tau^-)$ Np1 (m_{ll} =10-40 GeV)	Alpgen	Herwig	CTEQ6L1	299999	2.8
$Z(\rightarrow \tau^+\tau^-)$ Np2 (m_{ll} =10-40 GeV)	Alpgen	Herwig	CTEQ6L1	498899	9.6
$Z(\rightarrow \tau^+\tau^-)$ Np3 (m_{ll} =10-40 GeV)	Alpgen	Herwig	CTEQ6L1	150000	14.4
$Z(\rightarrow \tau^+\tau^-)$ Np4 (m_{ll} =10-40 GeV)	Alpgen	Herwig	CTEQ6L1	39999	17.3
$Z(\rightarrow \tau^+\tau^-)$ Np5 (m_{ll} =10-40 GeV)	Alpgen	Herwig	CTEQ6L1	10000	17.4

Table A.3.: List of generators used for the production of Z+jets samples for different number of parton multiplicities.

Process	Generator	Showering	PDF	Nr(Events)	$\int \mathcal{L}dt$ [fb^{-1}]
$Z(\rightarrow e^+e^-)$bb Np0	Alpgen	Herwig	CTEQ6L1	409832	49.9
$Z(\rightarrow e^+e^-)$bb Np1	Alpgen	Herwig	CTEQ6L1	160000	51.6
$Z(\rightarrow e^+e^-)$bb Np2	Alpgen	Herwig	CTEQ6L1	60000	53.9
$Z(\rightarrow e^+e^-)$bb Np3	Alpgen	Herwig	CTEQ6L1	30000	61.5
$Z(\rightarrow \mu^+\mu^-)$bb Np0	Alpgen	Herwig	CTEQ6L1	409949	50.0
$Z(\rightarrow \mu^+\mu^-)$bb Np1	Alpgen	Herwig	CTEQ6L1	155000	50.2
$Z(\rightarrow \mu^+\mu^-)$bb Np2	Alpgen	Herwig	CTEQ6L1	60000	53.9
$Z(\rightarrow \mu^+\mu^-)$bb Np3	Alpgen	Herwig	CTEQ6L1	29999	61.5
$Z(\rightarrow \tau^+\tau^-)$bb Np0	Alpgen	Herwig	CTEQ6L1	150000	18.3
$Z(\rightarrow \tau^+\tau^-)$bb Np1	Alpgen	Herwig	CTEQ6L1	99999	32.1
$Z(\rightarrow \tau^+\tau^-)$bb Np2	Alpgen	Herwig	CTEQ6L1	40000	36.0
$Z(\rightarrow \tau^+\tau^-)$bb Np3	Alpgen	Herwig	CTEQ6L1	9000	18.5

Table A.4.: List of generators used for the production of Z+jets heavy-flavour samples for different number of parton multiplicities.

Process	Generator	Showering	PDF	Nr(Events)	$\int \mathcal{L}dt$ [fb^{-1}]
$t\bar{t}$ (lepton+jets)	Protos	Pythia	CTEQ6L1	498999	6.9
$t\bar{t}$ (dilepton)	Protos	Pythia	CTEQ6L1	499500	29.2
Single Top (s-chan. $W \rightarrow e\bar{\nu_e}$)	Mc@Nlo	Herwig	CT10	253410	506.7
Single Top (s-chan. $W \rightarrow \mu\bar{\nu_\mu}$)	Mc@Nlo	Herwig	CT10	253594	507.1
Single Top (s-chan. $W \rightarrow \tau\bar{\nu_\tau}$)	Mc@Nlo	Herwig	CT10	253511	506.9
Single Top (associated Wt)	Mc@Nlo	Herwig	CT10	797024	50.6
Single Top (t-chan. $W \rightarrow e\bar{\nu_e}$)	AcerMC	Pythia	MRST	843473	121.0
Single Top (t-chan. $W \rightarrow \mu\bar{\nu_\mu}$)	AcerMC	Pythia	MRST	844230	121.1
Single Top (t-chan. $W \rightarrow \tau\bar{\nu_\tau}$)	AcerMC	Pythia	MRST	845149	121.4

Table A.5.: List of generators used for the production of $t\bar{t}$ and single-top quark samples.

A.4. KLFitter Performance

The kinematic likelihood fitter performs the fit using the Minuit package. If the fit does not converge, an error flag is written out. The analysis is only performed on events that survive this cut on the convergence criterion. Tab. A.6 and A.7 show the effect of the cut on the event yields whereas Tab. A.8 shows the impact on the selection efficiency. MC@NLO was used for the signal modelling. The observed effect is on sub-percent level and hence no uncertainty has to be assigned.

Process	without Minuit Cut	with Minuit Cut	Difference [%]
$t\bar{t}$ MC@NLO	16145	16113	0.2
W+jets (DD)	2298	2294	0.2
Single Top	1180	1178	0.2
Fake lepton (DD)	847	843	0.5
Z+jets	446	445	0.2
Diboson	46	46	0.0
Total predicted	20962	20920	0.2
Observed	21956	21906	0.2

Table A.6.: Event yields before and after the cut on non-converged Minuit fits for the e+jets channel.

Process	without Minuit Cut	with Minuit Cut	Difference [%]
$t\bar{t}$ MC@NLO	26548	26490	0.2
W+jets (DD)	4464	4457	0.2
Single Top	1969	1965	0.2
Fake lepton (DD)	1778	1774	0.2
Z+jets	481	479	0.4
Diboson	73	73	0.0
Total predicted	35312	35238	0.2
Observed	37919	37845	0.2

Table A.7.: Event yields before and after the cut on non-converged Minuit fits for the μ+jets channel.

Fraction	w/o Cut	w Cut	Difference [%]	w/o Cut	w Cut	Difference [%]
F_0	0.04699	0.0469	0.19	0.07176	0.0716	0.27
F_L	0.03438	0.0343	0.23	0.05636	0.0563	0.20
F_R	0.04611	0.0459	0.30	0.06903	0.0688	0.33

Table A.8.: Selection efficiencies before and after the cut on non-converged Minuit fits for the e+jets channel (left) and the μ+jets channel (right).

A.5. Lepton modelling

As observed in the pretag and b-tag control plots, the transverse momentum/energy of the lepton in the simulated samples does not match the data distribution for high values. To test the effect on the central value, a cut at $p_T = 150$ GeV was applied and the central value with the corresponding statistical uncertainties are evaluated for the two-dimensional fit. For the e+jets channel, the data yield is reduced by about 3 % while for the μ+jets channel the reduction is about 2 %. The central values increase after applying the cut and the statistical uncertainty decrease a bit. However the changes are still within statistical uncertainties.

		w/o cut		with cut	
Fraction	Channel	F_i	Stat.	F_i	Stat.
F_0	e+jets	0.698	0.027	0.711	0.022
F_0	μ+jets	0.685	0.022	0.703	0.020

Table A.9.: Best-fit result for the W-helicity fractions with statistical uncertainties for the two-dimensional fit. A cut on the transverse energy/momentum was applied at 150 GeV.

A.6. Mass Dependence

The event reconstruction is performed using the KLFitter with a fixed top-quark mass of 172.5 GeV. The W-helicity fractions are top-quark mass dependent and a large uncertainty is observed due to the top-quark mass. Hence, the influence of the choice of the fixed top-quark masses in the kinematic likelihood fit has to be studied. The mass was set to 171 GeV and 174 GeV in the kinematic fit. The events are reconstructed and a fit was performed to the pseudo-data distribution reconstructed with the same mass as the templates. Ensemble tests were performed using 2,000 ensembles for each mass point. The helicity fractions in the μ+jets channel barely change, whereas a small shift is observed for the e+jets channel. However, the mass range here is three times larger than the uncertainty on the current world-average mass. Hence, the uncertainty due to the fixed top mass is small compared to the systematic uncertainty already considered.

	F_0		F_L		F_R	
m_top [GeV]	(e+jets)	(μ+jets)	(e+jets)	(μ+jets)	(e+jets)	(μ+jets)
171	0.710	0.681	0.296	0.325	-0.006	-0.006
174	0.693	0.681	0.302	0.323	0.005	-0.003

Table A.10.: W-helicity fractions extracted from pseudo experiments with different top-quark masses used in the kinematic likelihood fit. For each mass point, 2,000 ensembles are used.

A.7. Calibration Curves

When validating the analysis method, Pull and RMS distributions were created. The RMS distributions showed for all parameters a smaller RMS than the expected result 1. This is due to the background constraints in the Likelihood. To test that the method does estimate the uncertainties properly, the calibration curves were obtained by fitting only the signal distributions. The RMS distributions are fitted with a straight line and the slope and offset of these fits are summarised in Tab. A.11. The distributions have a spread of 1 and a mean of zero, hence to bias is observed.

Parameter	Slope	Offset
N_0	$< 10^{-6}$	1.001 ± 0.007
N_L	$< 10^{-6}$	1.004 ± 0.004
N_R	$< 10^{-6}$	0.995 ± 0.004

Table A.11.: Fit results from RMS dependence test in the combined lepton+jets channel using the three-dimensional fit only for signal templates.

A.8. Systematic normalisation effects

		e+jets			μ+jets		
Uncertainty	Sample 1/Sample 2	S1	S2	Diff. [%]	S1	S2	Diff. [%]
MC gen.	MC@NLO/ALPGEN	16,113	16,150	0.23	26,490	26,310	0.68
MC gen.	MC@NLO/POWHEG	16,220	16,764	3.35	25,931	26,935	3.87
Showering	HERWIG/PYTHIA	16,764	16,649	0.69	26,935	27,012	0.29
ISR/FSR	More/Less PS	17,486	18,364	5.02	28,136	28,598	1.64
Colour rec.	CR / no CR	18,383	18,469	0.47	29,234	29,239	0.02
Underl. event	More/Less UE	17,816	18,004	1.06	28,638	28,554	0.30

Table A.12.: The grey shaded area shows the relative difference in normalisaton for the two generators that are compared for the different signal modelling uncertainties.

Ã§

Systematic	$t\bar{t}$	W+jets	Fake Lepton	Single Top	Z+jets	Diboson
JES	7.6/-9.6	35/-7.4	-	12/-15	31/-10	39/-9.1
JER	-0.31/–0.31	17/-17	-	0.87/-0.87	24/-24	16/-16
JEFF	-1.2/–1.2	11/-11	-	-1.8/–1.8	9.7/-9.7	10/-10
JVFSF	1.3/-1.5	1.5/-1.5	-	1.2/-1.4	1.8/-1.7	1.4/-1.5
ID-SF	2.2/-2.2	2.3/-2.3	-	2.2/-2.2	2.3/-2.3	2.3/-2.3
Reco-SF	0.88/-0.88	0.79/-0.79	-	0.88/-0.88	0.82/-0.82	0.83/-0.83
Trigger-SF	0.56/-0.56	0.57/-0.57	-	0.56/-0.56	0.56/-0.56	0.56/-0.56
b-tag	4/-4.4	2.1/-2.1	-	4.8/-5.1	2.7/-2.8	1.2/-1.3
c-tag	0.39/-0.39	6.2/-6.3	-	0.45/-0.46	4.1/-4.2	8.1/-8.2
mis-tag	0.33/-0.33	5.9/-5.9	-	0.46/-0.46	6.6/-6.7	4.5/-4.4
JVFSF	1.3/-1.5	1.5/-1.5	-	1.2/-1.4	1.8/-1.7	1.4/-1.5
Wjets (HF1)	-	20/-1	-	-	-	-
Wjets (HF2)	-	14/-1	-	-	-	-
Wjets (HF3)	-	16/5	-	-	-	-
Wjets (HF4)	-	12/5	-	-	-	-
Wjets (HF5)	-	16/7	-	-	-	-
Wjets (HF6)	-	28/-5.5	-	-	-	-
Wjets (ptjmin10)	-	11/-11	-	-	-	-
Wjets (iqop3)	-	11/-11	-	-	-	-
Norm.	11/-11	17/-17	50/-50	7/-7	48/-48	5/-5

Table A.13.: Effect of different systematic uncertainties on the normalisation of the different processes in the e+jets channel. The cross-section uncertainty is included in the statistical uncertainty and therefore only mentioned here for completeness.

Systematic	$t\bar{t}$	W+jets	Fake Lepton	Single Top	Z+jets	Diboson
JES	6.7/-9	34/-7.5	-	11/-14	40/-5.4	38/-11
JER	-0.9/–0.9	15/-15	-	-0.19/–0.19	27/-27	16/-16
JEFF	-1.1/–1.1	12/-12	-	-1.9/–1.9	12/-12	10/-10
JVFSF	1.3/-1.5	1.6/-1.6	-	1.2/-1.4	1.9/-1.7	1.5/-1.5
b-tag	4/-4.4	1.8/-1.9	-	4.7/-5.1	2.3/-2.4	1.3/-1.4
c-tag	0.4/-0.4	6.8/-6.8	-	0.51/-0.51	4/-4	7.8/-7.9
mis-tag	0.32/-0.32	6/-5.9	-	0.32/-0.32	8.5/-8.4	4.6/-4.5
MUID	-1/-1	12/12	-	-1.9/-1.9	13/13	10/9.8
MUMS	-1/-1.1	12/12	-	-1.9/-1.9	13/13	10/10
MUSC	-0.91/–0.91	12/-12	-	-1.7/–1.7	14/-14	11/-11
ID-SF	0.74/-0.74	0.74/-0.74	-	0.74/-0.74	0.73/-0.73	0.74/-0.74
Reco-SF	0.32/-0.32	0.34/-0.34	-	0.32/-0.32	0.34/-0.34	0.34/-0.34
Trigger-SF	1.3/-1.3	1.2/-1.2	-	1.3/-1.3	1.2/-1.2	1.3/-1.3
Wjets (HF1)	-	19/1.7	-	-	-	-
Wjets (HF2)	-	14/1.7	-	-	-	-
Wjets (HF3)	-	19/3.8	-	-	-	-
Wjets (HF4)	-	14/3.8	-	-	-	-
Wjets (HF5)	-	14/8.7	-	-	-	-
Wjets (HF6)	-	25/-0.87	-	-	-	-
Wjets (ptjmin10)	-	12/-12	-	-	-	-
Wjets (iqop3)	-	12/-12	-	-	-	-
Norm.	11/-11	17/-17	23/-23	7/-7	48/-48	5/-5

Table A.14.: Effect of different systematic uncertainties on the normalisation of the different processes in the e+jets channel. The cross-section uncertainty is included in the statistical uncertainty and therefore only mentioned here for completeness.

		Linearity tests		Pull		RMS	
Parameter	Channel	Slope	Offset	Slope	Offset	Slope	Offset
$N(W$+jets)	e+jets	14 ± 18	-11 ± 13	0.017 ± 0.022	-0.013 ± 0.016	0.021 ± 0.016	0.604 ± 0.011
N(Misid. lept.)	e+jets	8 ± 5	-6 ± 4	0.023 ± 0.016	-0.019 ± 0.012	-0.002 ± 0.012	0.455 ± 0.008
N(Rem. Bkg)	e+jets	-2 ± 3	1 ± 2	-0.004 ± 0.007	0.002 ± 0.005	-0.033 ± 0.005	0.218 ± 0.004
$N(W$+jets)	μ+jets	9 ± 21	-6 ± 15	0.015 ± 0.031	-0.013 ± 0.022	0.061 ± 0.022	0.820 ± 0.015
N(Misid. lept.)	μ+jets	-17 ± 7	12 ± 5	-0.062 ± 0.025	0.043 ± 0.018	0.107 ± 0.018	0.623 ± 0.012
N(Rem. Bkg)	μ+jets	1 ± 1	-1 ± 1	0.002 ± 0.003	-0.001 ± 0.002	-0.015 ± 0.002	0.088 ± 0.002
$N(W$+jets, e+j)	Combined	-4 ± 13	-2 ± 10	-0.007 ± 0.023	-0.004 ± 0.016	0.045 ± 0.016	0.610 ± 0.012
$N(W$+jets, μ+j)	Combined	5 ± 18	-8 ± 13	0.008 ± 0.029	-0.013 ± 0.020	0.052 ± 0.020	0.769 ± 0.015
N(Misid. lept. e+j)	Combined	6 ± 7	-5 ± 5	0.019 ± 0.023	-0.016 ± 0.017	-0.006 ± 0.016	0.655 ± 0.012
N(Misid. lept. μ+j)	Combined	7 ± 7	-7 ± 5	0.025 ± 0.027	-0.023 ± 0.019	0.073 ± 0.019	0.714 ± 0.014
N(Rem. Bkg e+j)	Combined	-1 ± 4	1 ± 3	-0.002 ± 0.010	0.003 ± 0.007	-0.051 ± 0.007	0.308 ± 0.005
N(Rem. Bkg μ+j)	Combined	2 ± 3	-2 ± 3	0.004 ± 0.007	-0.003 ± 0.005	-0.019 ± 0.005	0.205 ± 0.004

Table A.15.: Result for the background estimates for the calibration curves and pull values using 5,000 ensembles per calibration point for the e+jets, the μ+jets and the combined lepton+jets channel. A two-dimensional fit is performed. No bias is observed.

		Linearity tests		Pull		RMS	
Parameter	Channel	Slope	Offset	Slope	Offset	Slope	Offset
$N(W$+jets)	e+jets	3 ± 20	4 ± 15	0.002 ± 0.019	0.004 ± 0.014	-0.039 ± 0.013	0.733 ± 0.010
N(Misid. lept.)	e+jets	6 ± 4	-6 ± 3	0.017 ± 0.011	-0.016 ± 0.008	0.015 ± 0.008	0.389 ± 0.006
N(Rem. Bkg)	e+jets	5 ± 2	-5 ± 2	0.014 ± 0.005	-0.013 ± 0.004	-0.000 ± 0.004	0.201 ± 0.003
$N(W$+jets)	μ+jets	8 ± 34	1 ± 25	0.006 ± 0.022	0.001 ± 0.016	0.017 ± 0.016	0.831 ± 0.012
N(Misid. lept.)	μ+jets	3 ± 5	-4 ± 4	0.008 ± 0.016	-0.011 ± 0.012	0.029 ± 0.012	0.588 ± 0.008
N(Rem. Bkg)	μ+jets	-1 ± 1	0 ± 1	-0.001 ± 0.002	0.001 ± 0.002	-0.005 ± 0.002	0.085 ± 0.001
$N(W$+jets, e+j)	Combined	-1 ± 15	5 ± 11	-0.001 ± 0.020	0.006 ± 0.015	0.007 ± 0.014	0.754 ± 0.010
$N(W$+jets, μ+j)	Combined	11 ± 24	1 ± 18	0.010 ± 0.021	-0.000 ± 0.016	0.007 ± 0.015	0.804 ± 0.011
N(Misid. lept. e+j)	Combined	-1 ± 5	0 ± 4	-0.004 ± 0.016	0.001 ± 0.011	0.047 ± 0.011	0.552 ± 0.008
N(Misid. lept. μ+j)	Combined	-6 ± 5	3 ± 4	-0.024 ± 0.019	0.011 ± 0.014	0.039 ± 0.014	0.691 ± 0.010
N(Rem. Bkg e+j)	Combined	1 ± 3	1 ± 2	-0.004 ± 0.008	0.004 ± 0.006	-0.025 ± 0.005	0.297 ± 0.004
N(Rem. Bkg μ+j)	Combined	-3 ± 3	2 ± 2	0.006 ± 0.005	0.005 ± 0.004	0.005 ± 0.004	0.190 ± 0.003

Table A.16.: Result for the background estimates for the calibration curves and pull values using 2,000 ensembles per calibration point for the e+jets, the μ+jets and the combined lepton+jets channel. A three-dimensional fit is performed. No bias is observed.

A.9. Additional systematic distributions

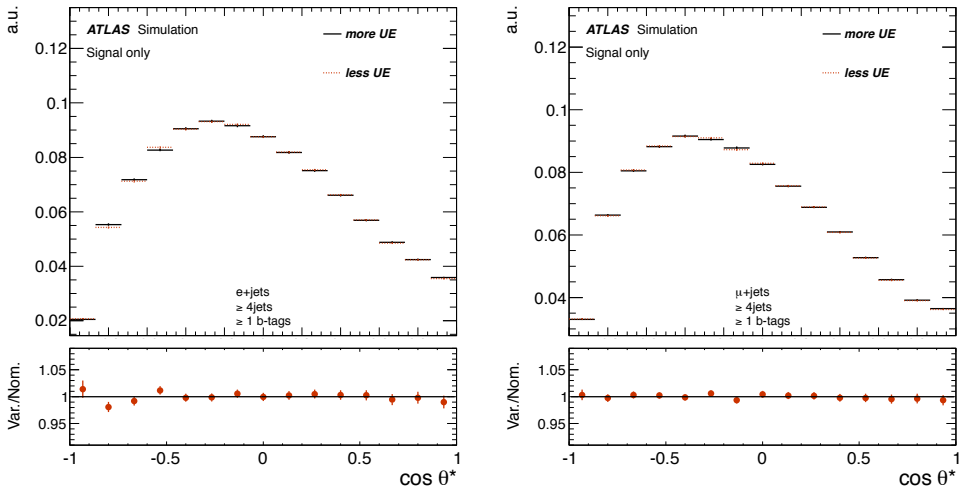

Figure A.7.: Comparison between the $t\bar{t}$-distributions for the samples generated with more/less underlying event activity for the e+jets channel (left) and the μ+jets channel (right), respectively. The impact on the shape is small for both channels, but a bit larger for the e+jets channel.

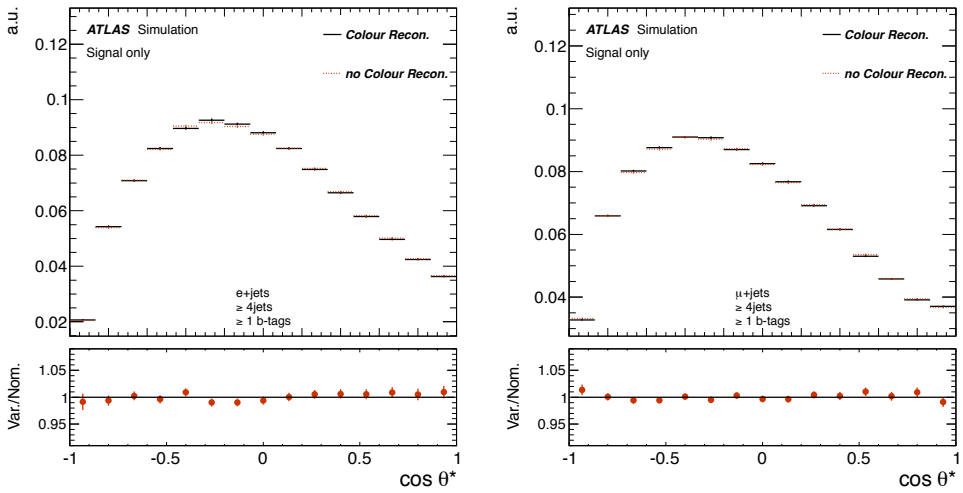

Figure A.8.: Comparison between the $t\bar{t}$-distributions for the samples generated with CR for the e+jets channel (left) and the μ+jets channel (right), respectively. The impact on the shape is small for both channels.

Bibliography

[1] *Measurement of the W-boson polarisation in top quark decays in pp collision data at $\sqrt{s}$ = 7 TeV using the ATLAS detector*, Tech. Rep. ATLAS-CONF-2011-037, CERN, Geneva, Mar, 2011. 1

[2] ATLAS Collaboration, *Measurement of the W boson polarisation in top quark decays in 0.70 fb^{-1} of pp collisions at $\sqrt{s}$ =7 TeV with the ATLAS detector*, Tech. Rep. ATLAS-CONF-2011-122, CERN, Geneva, Aug, 2011. 1

[3] ATLAS Collaboration, G. Aad et al., *Measurement of the W boson polarization in top quark decays with the ATLAS detector*, JHEP **1206** (2012) 088, `arXiv:1205.2484 [hep-ex]`. 1, 3.4.2, 3.4.2, 3.4.2, 3.4.2, 8.5.1, 9.1.1, 10, 10, 10.1, A.9

[4] H. D. Politzer, *Reliable Perturbative Results for Strong Interactions?*, Phys.Rev.Lett. **30** (1973) 1346–1349. 2.1

[5] H. D. Politzer, *Asymptotic Freedom: An Approach to Strong Interactions*, Phys.Rept. **14** (1974) 129–180. 2.1

[6] D. J. Gross and F. Wilczek, *Asymptotically Free Gauge Theories. I*, Phys. Rev. D **8** (Nov, 1973) 3633–3652. 2.1, 2.2.1

[7] S. Glashow, *Partial Symmetries of Weak Interactions*, Nucl.Phys. **22** (1961) 579–588. 2.1, 2.2.2

[8] A. Salam and J. C. Ward, *Electromagnetic and weak interactions*, Phys.Lett. **13** (1964) 168–171. 2.1, 2.2.2

[9] S. Weinberg, *A Model of Leptons*, Phys.Rev.Lett. **19** 1264–1266. 2.1, 2.2.2

[10] ATLAS Collaboration, G. Aad et al., *Observation of a new particle in the search for the Standard Model Higgs boson with the ATLAS detector at the LHC*, Phys.Lett. **B716** (2012) 1–29, `arXiv:1207.7214 [hep-ex]`. 2.1, 2.2.4, A.9

[11] CMS Collaboration, S. Chatrchyan et al., *Observation of a new boson at a mass of 125 GeV with the CMS experiment at the LHC*, Phys.Lett. **B716** (2012) 30–61, `arXiv:1207.7235 [hep-ex]`. 2.1, 2.2.4, A.9

[12] ALEPH Collaboration, DELPHI Collaboration, L3 Collaboration, OPAL Collaboration, SLD Collaboration, LEP Electroweak Working Group, SLD Electroweak Group, SLD Heavy Flavour Group Collaboration, S. Schael et al., *Precision electroweak measurements on the Z resonance*, Phys.Rept. **427** (2006) 257–454, `arXiv:hep-ex/0509008 [hep-ex]`. 2.1

[13] The ATLAS Collaboration, *Search for exotic same-sign dilepton signatures (b' quark, $T_{5/3}$ and four top quarks production) in 4.7/fb of pp collisions at $\sqrt{s}$ = 7 TeV with the ATLAS detector*, Tech. Rep. ATLAS-CONF-2012-130, CERN, Geneva, Sep, 2012. 2.1

[14] The ATLAS Collaboration, G. Aad et al., *Search for pair production of heavy top-like quarks decaying to a high-pT W boson and a b quark in the lepton plus jets final state at $\sqrt{s} = 7$ TeV with the ATLAS detector*, arXiv:1210.5468 [hep-ex]. 2.1

[15] J. Beringer et al., *Review of Particle Physics, 2012-2013. Review of Particle Properties*, Phys. Rev. D **86** (2012) No. 1, 010001. 2.1, 2.2, 6, 2.2.1, 12, 2.2.3, 3.2, 3.4, 3.4.1, 5.5, A.9

[16] CDF Collaboration, D0 Collaboration, T. Aaltonen et al., *Combination of the top-quark mass measurements from the Tevatron collider*, Phys.Rev. **D86** (2012) 092003, arXiv:1207.1069 [hep-ex]. 2.1, 3, 3.4, 3.4.1, 8.5.1

[17] R. Ellis, W. Stirling, and B. Webber, *QCD and Collider Physics*, Cambridge Monographs (2003) . 2.2.1, 2

[18] F. Halzen and A. Martin, *Quarks and Leptons: An Introductory Course in Modern Particle Physics*, John Wiley and Sons. (1984) 46. 9

[19] P. W. Higgs, *Broken symmetries, massless particles and gauge fields*, Phys.Lett. **12** (1964) 132–133. 2.2.3

[20] P. W. Higgs, *Broken Symmetries and the Masses of Gauge Bosons*, Phys.Rev.Lett. **13** (1964) 508–509. 2.2.3

[21] G. Guralnik, C. Hagen, and T. Kibble, *Global Conservation Laws and Massless Particles*, Phys.Rev.Lett. **13** (1964) 585–587. 2.2.3

[22] F. Englert and R. Brout, *Broken Symmetry and the Mass of Gauge Vector Mesons*, Phys.Rev.Lett. **13** (1964) 321–323. 2.2.3

[23] ALEPH Collaboration, CDF Collaboration, D0 Collaboration, DELPHI Collaboration, L3 Collaboration, OPAL Collaboration, SLD Collaboration, LEP Electroweak Working Group, Tevatron Electroweak Working Group, SLD Electroweak and Heavy Flavour Groups Collaboration, *Precision Electroweak Measurements and Constraints on the Standard Model*, arXiv:1012.2367 [hep-ex]. 2.2.4

[24] LEP Working Group for Higgs boson searches, ALEPH Collaboration, DELPHI Collaboration, L3 Collaboration, OPAL Collaboration Collaboration, R. Barate et al., *Search for the standard model Higgs boson at LEP*, Phys.Lett. **B565** (2003) 61–75, arXiv:hep-ex/0306033 [hep-ex]. 2.2.4

[25] Tevatron New Physics Higgs Working Group, CDF Collaboration, D0 Collaboration, C. Group, D. Collaborations, the Tevatron New Physics, and H. Working, *Updated Combination of CDF and D0 Searches for Standard Model Higgs Boson Production with up to 10.0 fb^{-1} of Data*, arXiv:1207.0449 [hep-ex]. 2.2.4

[26] CDF Collaboration, D0 Collaboration, T. Aaltonen et al., *Evidence for a particle produced in association with weak bosons and decaying to a bottom-antibottom quark pair in Higgs boson searches at the Tevatron*, Phys.Rev.Lett. **109** (2012) 071804, arXiv:1207.6436 [hep-ex]. 2.2.4

[27] ATLAS Collaboration, *An update of combined measurements of the new Higgs-like boson with high mass resolution channels*, ATLAS-CONF-2012-170 (Dec, 2012) . 2.2.4, 2.3, 2.2.4, A.9

[28] CMS Collaboration, *Combination of standard model Higgs boson searches and measurements of the properties of the new boson with a mass near 125 GeV*, CMS-PAS-HIG-12-045 (2012) . 2.2.4, 2.4, A.9

[29] L. Landau, *The moment of a 2-photon system*, Dokl. Akad. Nauk USSR **60** (1948) 207. 2.2.4

[30] C.-N. Yang, *Selection Rules for the Dematerialization of a Particle Into Two Photons*, Phys.Rev. **77** (1950) 242–245. 2.2.4

[31] The ATLAS Collaboration, *Observation and study of the Higgs boson candidate in the two photon decay channel with the ATLAS detector at the LHC*, Tech. Rep. ATLAS-CONF-2012-168, CERN, Geneva, Dec, 2012. 2.2.4

[32] S. P. Martin, *A Supersymmetry primer*, `arXiv:hep-ph/9709356 [hep-ph]`. 2.2.5, 3.4.1

[33] CDF Collaboration, F. Abe et al., *Observation of top quark production in $p\bar{p}$ collisions with the Collider Detector at Fermilab*, tech. rep., 1995. 3

[34] D0 Collaboration, S. Abachi et al., *Observation of the top quark*, Phys. Rev. Lett. **74** (1995) 2632–2637, `arXiv:hep-ex/9503003`. 3

[35] H.-L. Lai, M. Guzzi, J. Huston, Z. Li, P. M. Nadolsky, et al., *New parton distributions for collider physics*, Phys.Rev. **D82** (2010) 074024, `arXiv:1007.2241 [hep-ph]`. 3.1, 3.2, 8.5.1, A.9

[36] G. Watt and R. Thorne, *Study of Monte Carlo approach to experimental uncertainty propagation with MSTW 2008 PDFs*, JHEP **1208** (2012) 052, `arXiv:1205.4024 [hep-ph]`. 3.1, 8.5.1

[37] NNPDF Collaboration Collaboration, R. D. Ball et al., *Unbiased global determination of parton distributions and their uncertainties at NNLO and at LO*, Nucl.Phys. **B855** (2012) 153–221, `arXiv:1107.2652 [hep-ph]`. 3.1, 8.5.1

[38] ATLAS and CMS Collaboration, *Combination of ATLAS and CMS top-quark pair cross section measurements using proton-proton collisions at $\sqrt{s} = 7$ TeV*, CMS-PAS-TOP-12-003 (2012) . 3.1

[39] M. Aliev, H. Lacker, U. Langenfeld, S. Moch, P. Uwer, et al., *HATHOR: HAdronic Top and Heavy quarks crOss section calculatoR*, Comput.Phys.Commun. **182** (2011) 1034–1046, `arXiv:1007.1327 [hep-ph]`. 3.1, 6.1

[40] The ATLAS Collaboration, *Statistical combination of top quark pair production cross-section measurements using dilepton, single-lepton, and all-hadronic final states at $\sqrt{s} = 7$ TeV with the ATLAS detector*, Tech. Rep. ATLAS-CONF-2012-024, CERN, Geneva, Mar, 2012. 3.3, A.9

[41] D0 Collaboration, Abazov et al., *Observation of Single Top-Quark Production*, Phys. Rev. Lett. **103** (Aug, 2009) 092001. 3.2

[42] CDF Collaboration, T. Aaltonen et al., *First Observation of Electroweak Single Top Quark Production*, Phys.Rev.Lett. **103** 092002. 3.2

[43] ATLAS Collaboration, *Evidence for the associated production of a W boson and a top quark in ATLAS at*, Physics Letters B **716** (2012) No. 1, 142 – 159. 3.2, 3.2, 3.2

[44] CMS Collaboration, S. Chatrchyan et al., *Evidence for associated production of a single top quark and W boson in pp collisions at 7 TeV*, Phys.Rev.Lett. (2012) , arXiv:1209.3489 [hep-ex]. 3.2

[45] ATLAS Collaboration, G. Aad et al., *Measurement of the t-channel single top-quark production cross section in pp collisions at $\sqrt{s} = 7$ TeV with the ATLAS detector*, Physics Letters B **717** (2012) 330–350, arXiv:1205.3130 [hep-ex]. 3.2, 3.2, 3.2

[46] N. Kidonakis, *Next-to-next-to-leading-order collinear and soft gluon corrections for t-channel single top quark production*, Phys.Rev. **D83** (2011) 091503, arXiv:1103.2792 [hep-ph]. 3.2

[47] ATLAS Collaboration, *Measurement of the t-channel single top-quark and top-antiquark production cross-sections and their ratio in pp collisions at $\sqrt{s} = 7$ TeV*, Tech. Rep. ATLAS-CONF-2012-056, CERN, Geneva, Jun, 2012. 3.2

[48] N. Kidonakis, *Two-loop soft anomalous dimensions for single top quark associated production with a W- or H-*, Phys.Rev. **D82** (2010) 054018, arXiv:1005.4451 [hep-ph]. 3.2

[49] N. Kidonakis, *NNLL resummation for s-channel single top quark production*, Phys.Rev. **D81** (2010) 054028, arXiv:1001.5034 [hep-ph]. 3.2

[50] ATLAS Collaboration, *Search for s-Channel Single Top-Quark Production in pp Collisions at $\sqrt{s} = 7$ TeV*, Tech. Rep. ATLAS-CONF-2011-118, CERN, Geneva, Aug, 2011. 3.2

[51] ATLAS and CMS Collaboration, *Combination of ATLAS and CMS results on the mass of the top quark using up to 4.9 fb^{-1} of data*, CMS-PAS-TOP-12-001 (2012) . 3.4

[52] ATLAS Collaboration, *Measurement of top quark polarisation in $t\bar{t}$ events with the ATLAS detector in proton-proton collisions at $\sqrt{s} = 7$ TeV*, . 5

[53] CMS Collaboration, *Measurement of the top polarization in the dilepton final state*, Tech. Rep. CMS-PAS-TOP-12-016, CERN, Geneva, 2012. 5

[54] G. Mahlon and S. Parke, *Angular correlations in top quark pair production and decay at hadron colliders*, Phys. Rev. D **53** (May, 1996) 4886–4896. 3.4

[55] T. Stelzer and S. Willenbrock, *Spin correlation in top-quark production at hadron colliders*, Physics Letters B **374** (1996) No. 1-3, 169–172. 3.4

[56] W. Bernreuther and Z.-G. Si, *Distributions and correlations for top quark pair production and decay at the Tevatron and LHC.*, Nucl.Phys. **B837** (2010) 90–121, arXiv:1003.3926 [hep-ph]. 3.4

[57] ATLAS Collaboration, *Observation of Spin Correlation in $t\bar{t}$ Events from pp Collisions at $\sqrt{s} = 7$ TeV Using the ATLAS Detector*, Phys. Rev. Lett. **108** (May, 2012) 212001. 3.4

[58] CMS Collaboration, *Measurement of Spin Correlations in ttbar production*, CMS-PAS-TOP-12-004 (2012) . 3.4

[59] M. S. Chanowitz and M. K. Gaillard, *The TeV physics of strongly interacting W's and Z's*, Nuclear Physics B **261** (1985) No. 0, 379 – 431. 3.4.1

[60] J. M. Cornwall, D. N. Levin, and G. Tiktopoulos, *Derivation of gauge invariance from high-energy unitarity bounds on the S matrix*, Phys. Rev. D **10** (Aug, 1974) 1145–1167. 3.4.1

[61] M. Peskin and D. Schroeder, *An Introduction to Quantum Field Theory*, ABP, Westview Press (1995) 743–750. 7

[62] M. Fischer, S. Groote, J. G. Körner, and M. C. Mauser, *Longitudinal, transverse-plus and transverse-minus W bosons in unpolarized top quark decays at $\mathcal{O}(\alpha_s)$*, Phys. Rev. D **63** (Jan, 2001) 031501. 3.4.1, 3.4.1, 3.4.1

[63] C. T. Hill, *Topcolor assisted technicolor*, Phys.Lett. **B345** (1995) 483–489, `arXiv:hep-ph/9411426 [hep-ph]`. 3.4.1

[64] W. Bernreuther, P. Gonzalez, and M. Wiebusch, *The Top Quark Decay Vertex in Standard Model Extensions*, Eur.Phys.J. **C60** (2009) 197–211, `arXiv:0812.1643 [hep-ph]`. 3.4.1

[65] S. Etesami, M. Khatiri Yanehsari, and M. Mohammadi Najafabadi, *The effects of standard model extensions on W-boson helicity ratios in top quark decay*, Int.J.Theor.Phys. **51** (2012) 3694–3700. 3.4.1

[66] A. Czarnecki, J. G. Korner, and J. H. Piclum, *Helicity fractions of W bosons from top quark decays at NNLO in QCD*, Phys.Rev. **D81** (2010) 111503, `arXiv:1005.2625 [hep-ph]`. 3.4.1, 9.10, 10, 10.1, A.9

[67] CDF Collaboration, A. Abulencia et al., *Measurement of the helicity of W bosons in top-quark decays*, Phys.Rev. **D73** (2006) 111103, `arXiv:hep-ex/0511023 [hep-ex]`. 3.4.1

[68] CDF Collaboration, D. Acosta and T. Affolder, *Measurement of the W boson polarization in top decay at CDF at $\sqrt{s} = 1.8$ TeV*, Phys. Rev. D **71** (Feb, 2005) 031101. 3.4.1

[69] CDF Collaboration, A. Abulencia and others", *Search for $V + A$ Current in Top-Quark Decays in $p\overline{p}$ Collisions at $\sqrt{s} = 1.96$ TeV*, Phys. Rev. Lett. **98** (Feb, 2007) 072001. 3.4.1

[70] J. Aguilar-Saavedra, J. Carvalho, N. F. Castro, F. Veloso, and A. Onofre, *Probing anomalous Wtb couplings in top pair decays*, Eur.Phys.J. **C50** (2007) 519–533, `arXiv:hep-ph/0605190 [hep-ph]`. 3.4.2, 3.4.2, 6.1, 8.2.1, 9.2.2

[71] F. del Aguila and J. Aguilar-Saavedra, *Precise determination of the Wtb couplings at CERN LHC*, Phys.Rev. **D67** (2003) 014009, `arXiv:hep-ph/0208171 [hep-ph]`. 3.4.2

[72] L. Lyons, D. Gibaut, and P. Clifford, *How to combine correlated estimates of a single physical quantity*, Nucl. Instrum. Meth. **A270** (1988) 110. 3.4.2

[73] A. Valassi, *Combining correlated measurements of several different physical quantities*, Nucl. Instrum. Meth. **A500** (2003) 391–405. 3.4.2

[74] CMS Collaboration, *W helicity in top pair events*, CMS-PAS-TOP-11-020 (2012) . 3.4.2, 3.4.2, 10, 10.1, A.9

[75] CDF Collaboration, T. Aaltonen et al., *W boson polarization measurement in the $t\bar{t}$ dilepton channel using the CDF II Detector*, arXiv:1205.0354 [hep-ex]. 3.4.2

[76] CDF Collaboration Collaboration, T. Aaltonen et al., *Measurement of W-Boson Polarization in Top-quark Decay using the Full CDF Run II Data Set*, arXiv:1211.4523 [hep-ex]. 3.4.2, 3.4.2

[77] D0 Collaboration, V. M. Abazov et al., *Measurement of the W boson helicity in top quark decays using 5.4 fb^{-1} of ppbar collision data*, Phys.Rev. **D83** (2011) 032009, arXiv:1011.6549 [hep-ex]. 3.4.2, 3.4.2

[78] CDF Collaboration, D0 Collaboration, T. Aaltonen et al., *Combination of CDF and D0 measurements of the W boson helicity in top quark decays*, Phys.Rev. **D85** (2012) 071106, arXiv:1202.5272 [hep-ex]. 3.4.2, 3.4.2, 10, 10.1, A.9

[79] W. Buchmuller and D. Wyler, *Effective Lagrangian Analysis of New Interactions and Flavor Conservation*, Nucl.Phys. **B268** (1986) 621. 3.4.2, 1

[80] C. Zhang and S. Willenbrock, *Effective-Field-Theory Approach to Top-Quark Production and Decay*, Phys.Rev. **D83** (2011) 034006, arXiv:1008.3869 [hep-ph]. 3.4.2, 1

[81] J. Aguilar-Saavedra, *A Minimal set of top anomalous couplings*, Nucl.Phys. **B812** (2009) 181–204, arXiv:0811.3842 [hep-ph]. 3.4.2

[82] B. Grzadkowski and M. Misiak, *Anomalous Wtb coupling effects in the weak radiative B-meson decay*, Phys.Rev. **D78** (2008) 077501, arXiv:0802.1413 [hep-ph]. 3.4.2

[83] J. Aguilar-Saavedra and J. Bernabeu, *W polarisation beyond helicity fractions in top quark decays*, Nucl.Phys. **B840** (2010) 349–378, arXiv:1005.5382 [hep-ph]. 3.4.2, 9.2.2

[84] O. Bruening, H. Burkhardt, and S. Myers, *The Large Hadron Collider*, Progress in Particle and Nuclear Physics **67** (2012) No. 3, 705 – 734. 4

[85] L. Evans and P. Bryant, *LHC Machine*, Journal of Instrumentation **3** No. 08, S08001. 4, 4.1

[86] ATLAS Collaboration, *The ATLAS Experiment at the CERN Large Hadron Collider*, Journal of Instrumentation **3** No. 08, S08003. 4, 4.1, 4.2, 4.3, 4.4, 4.5, 4.6, 2, 3, 4, 4.7, 5, 4.1, 4.9, 4.2.4, 4.10, 4.2.5, A.9, A.9

[87] *ATLAS detector and physics performance: Technical Design Report, 1.* Technical Design Report ATLAS. CERN, Geneva, 1999. Electronic version not available. 4, 4.2.3

[88] *LEP design report.* No. CERN-LEP-84-01. CERN, Geneva, 1983. By the LEP Injector Study Group. 4.1

[89] The ALICE Collaboration, *The ALICE experiment at the CERN LHC*, Journal of Instrumentation **3** No. 08, S08002. 4.1

[90] CMS Collaboration, *The CMS Experiment at the CERN LHC*, Journal of Instrumentation **3** No. 08, S08004. 4.1

[91] The LHCb Collaboration, *The LHCb Detector at the LHC*, Journal of Instrumentation **3** No. 08, S08005. 4.1

[92] The LHCf Collaboration, *The LHCf detector at the CERN Large Hadron Collider*, Journal of Instrumentation **3** No. 08, S08006. 4.1

[93] The TOTEM Collaboration, *The TOTEM Experiment at the CERN Large Hadron Collider*, Journal of Instrumentation **3** No. 08, S08007. 4.1

[94] H. Burkhardt and P. Grafstroem, *Absolute Luminosity from Machine Parameters.*, LHC-PROJECT-Report-1019. CERN-LHC-PROJECT-Report-1019 (2007) . 4.2, A.9

[95] S. van der Meer, *Calibration of the effective beam height in the ISR*, Tech. Rep. CERN-ISR-PO-68-31. ISR-PO-68-31, CERN, Geneva, 1968. 4.1

[96] The ATLAS Collaboration, *Expected electron performance in the ATLAS experiment*, Tech. Rep. ATL-PHYS-PUB-2011-006, CERN, Geneva, Apr, 2011. 5.2

[97] ATLAS Collaboration, *Electron performance measurements with the ATLAS detector using the 2010 LHC proton-proton collision data*, The European Physical Journal C **72** (2012) 1–46. 5.2

[98] ATLAS Collaboration, *Electron performance measurements with the ATLAS detector using the 2010 LHC proton-proton collision data*, The European Physical Journal C **72** (2012) . 5.2

[99] https://atlas.web.cern.ch/Atlas/GROUPS/PHYSICS/EGAMMA/PublicPlots/20121403/StabilityPlots/ATL-COM-PHYS-2012-259. 5.2, A.9

[100] https://atlas.web.cern.ch/Atlas/GROUPS/PHYSICS/EGAMMA/PublicPlots/20110512/CalibratedZee/ATL-COM-PHYS-2011-1637. 5.2, A.9

[101] https://atlas.web.cern.ch/Atlas/GROUPS/PHYSICS/EGAMMA/PublicPlots/20110512/EfficiencyPileup/ATL-COM-PHYS-2011-1636. 5.3, A.9

[102] ATLAS Collaboration, *Muon Performance in Minimum Bias pp Collision Data at* $\sqrt{s} =$ *7 TeV with ATLAS*, Tech. Rep. ATLAS-CONF-2010-036, CERN, Geneva, Jul, 2010. 5.3

[103] ATLAS Collaboration, *Muon reconstruction efficiency in reprocessed 2010 LHC proton-proton collision data recorded with the ATLAS detector*, Tech. Rep. ATLAS-CONF-2011-063, CERN, Geneva, Apr, 2011. 5.3

[104] https://atlas.web.cern.ch/Atlas/GROUPS/ PHYSICS/MUON/PublicPlots/2011/Dec. 5.4, A.9

[105] M. Cacciari, G. P. Salam, and G. Soyez, *The Anti-k(t) jet clustering algorithm*, JHEP **0804** (2008) 063, `arXiv:0802.1189 [hep-ph]`. 5.4

[106] W. Lampl, S. Laplace, D. Lelas, P. Loch, H. Ma, et al., *Calorimeter clustering algorithms: Description and performance*, ATL-LARG-PUB-2008-002, ATL-COM-LARG-2008-003 (2008) . 5.4

[107] M. Cacciari and G. P. Salam, *Dispelling the* N^3 *myth for the* k_t *jet-finder*, Phys.Lett. **B641** (2006) 57–61, `arXiv:hep-ph/0512210 [hep-ph]`. 5.4

[108] ATLAS Collaboration, *Pile-up corrections for jets from proton-proton collisions at $\sqrt{s} = 7$ TeV in ATLAS in 2011*, Tech. Rep. ATLAS-CONF-2012-064, CERN, Geneva, Jul, 2012. 5.4, 3, 5.5, A.9

[109] ATLAS Collaboration, G. Aad et al., *Jet energy measurement with the ATLAS detector in proton-proton collisions at $\sqrt{s} = 7$ TeV*, `arXiv:1112.6426 [hep-ex]`. 5.4, 5.4

[110] ATLAS Collaboration, G. Aad et al., *Jet energy resolution in proton-proton collisions at $\sqrt{s} = 7$ TeV recorded in 2010 with the ATLAS detector*, `arXiv:1210.6210 [hep-ex]`. 5.4, 8.5.3

[111] D0 Collaboration, B. Abbott et al., *High-p_T jets in $\bar{p}p$ collisions at $\sqrt{s} = 630$ GeV and 1800 GeV*, Phys.Rev. **D64** (2001) 032003, `arXiv:hep-ex/0012046 [hep-ex]`. 5.4

[112] UA2 Collaboration, Bern-CERN-Copenhagen-Orsay-Pavia-Saclay Collaboration Collaboration, P. Bagnaia et al., *Measurement of Jet Production Properties at the CERN anti-p p Collider*, Phys.Lett. **B144** (1984) 283. 5.4

[113] ATLAS Collaboration, *Jet energy resolution and selection efficiency relative to track jets from in-situ techniques with the ATLAS Detector Using Proton-Proton Collisions at a Center of Mass Energy $\sqrt{s} = 7$ TeV*, Tech. Rep. ATLAS-CONF-2010-054, CERN, Geneva, Jul, 2010. 5.4

[114] https://twiki.cern.ch/twiki/bin/view/AtlasPublic/JetEtmissApproved2011PileupOffsetAndJVF. 5.7, A.9

[115] ATLAS Collaboration, *Commissioning of the ATLAS high-performance b-tagging algorithms in the 7 TeV collision data*, Tech. Rep. ATLAS-CONF-2011-102, CERN, Geneva, Jul, 2011. 5.5

[116] R. E. Kalman, *A New Approach to Linear Filtering and Prediction Problems*, Transactions of the ASME–Journal of Basic Engineering **82** (1960) No. Series D, 35–45. 5.5

[117] ATLAS Collaboration, *Measurement of the b-tag Efficiency in a Sample of Jets Containing Muons with 5^{-1} of Data from the ATLAS Detector*, Tech. Rep. ATLAS-CONF-2012-043, CERN, Geneva, Mar, 2012. 5.5.1, 5.9, A.9

[118] ATLAS Collaboration, *b-jet tagging calibration on c-jets containing D^{*+} mesons*, Tech. Rep. ATLAS-CONF-2012-039, CERN, Geneva, Mar, 2012. 5.5.1

[119] The ATLAS Collaboration, *Measurement of the Mistag Rate with 5 fb^{-1} of Data Collected by the ATLAS Detector*, Tech. Rep. ATLAS-CONF-2012-040, CERN, Geneva, Mar, 2012. 5.5.1

[120] The ATLAS Collaboration, *Measuring the b-tag efficiency in a top-pair sample with 4.7 fb^{-1} of data from the ATLAS detector*, Tech. Rep. ATLAS-CONF-2012-097, CERN, Geneva, Jul, 2012. 5.10, A.9

[121] B. Andersson, G. Gustafson, G. Ingelman, and T. Sjoestrand, *Parton fragmentation and string dynamics*, Physics Reports **97** (1983) No. 2-3, 31 – 145. 6, 8.5.1

[122] G. Corcella et al., *HERWIG 6: An Event generator for hadron emission reactions with interfering gluons (including supersymmetric processes)*, JHEP **0101** (2001) 010, `hep-ph/0011363`. 6, 6.1, 6.2, 8.5.1

[123] *Atlas Computing: technical design report.* No. ATLAS-TDR-17 ; CERN-LHCC-2005-022. CERN, Geneva, 2005. 6

[124] G. Aad, B. Abbott, J. Abdallah, A. A. Abdelalim, A. Abdesselam, O. Abdinov, B. Abi, M. Abolins, H. Abramowicz, H. Abreu, and et al., *The ATLAS Simulation Infrastructure*, European Physical Journal C **70** (Dec., 2010) 823–874, `arXiv:1005.4568 [physics.ins-det]`. 6

[125] S. Agostinelli et al., *Geant4 - A Simulation Toolkit*, Nucl. Instr. and Meth. **A506** (2003) 250. 6

[126] J. Allison, K. Amako, J. Apostolakis, H. Araujo, and Dubois, *Geant4 developments and applications*, Nuclear Science, IEEE Transactions on **53** (feb., 2006) 270 –278. 6

[127] J. Mechnich, *FATRAS - the ATLAS Fast Track Simulation project*, Tech. Rep. ATL-SOFT-PROC-2011-008, CERN, Geneva, Jan, 2011. 6

[128] T. Sjostrand and S. Mrenna and P.Z. Skands, *PYTHIA 6.4 Physics and Manual*, JHEP **05** (2006) 026, `hep-ph/0603175`. 6

[129] *ATLAS tunes of PYTHIA 6 and Pythia 8 for MC11*, ATL-PHYS-PUB-2011-009, ATL-COM-PHYS-2011-744 (2011) . 6, 8.5.1

[130] K. Nakamura and P. D. Group, *Review of Particle Physics*, Journal of Physics G: Nuclear and Particle Physics **37** No. 7A, 075021. 6

[131] S. Frixione and B.R. Webber, *Matching NLO QCD computations and parton shower simulations*, JHEP **0206** (2002) 029, `hep-ph/0204244`. 6.1, 8.5.1

[132] J. M. Butterworth, J. R. Forshaw, and M. H. Seymour, *Multiparton interactions in photoproduction at HERA*, Z. Phys. **C72** (1996) 637–646, `arXiv:hep-ph/9601371`. 6.1

[133] H.-L. Lai, M. Guzzi, J. Huston, Z. Li, P. M. Nadolsky, et al., *New parton distributions for collider physics*, Phys.Rev. **D82** (2010) 074024, `arXiv:1007.2241 [hep-ph]`. 6.1

[134] *New ATLAS event generator tunes to 2010 data*, Tech. Rep. ATL-PHYS-PUB-2011-008, CERN, Geneva, Apr, 2011. 6.1

[135] A. Martin, W. Stirling, R. Thorne, and G. Watt, *Parton distributions for the LHC*, Eur.Phys.J. **C63** (2009) 189–285, `arXiv:0901.0002 [hep-ph]`. 6.1, 6.3.2

[136] A. Martin, W. Stirling, R. Thorne, and G. Watt, *Uncertainties on alpha(S) in global PDF analyses and implications for predicted hadronic cross sections*, Eur.Phys.J. **C64** (2009) 653–680, `arXiv:0905.3531 [hep-ph]`. 6.1

[137] M. Cacciari, M. Czakon, M. Mangano, A. Mitov, and P. Nason, *Top-pair production at hadron colliders with next-to-next-to-leading logarithmic soft-gluon resummation*, Phys.Lett. **B710** (2012) 612–622, `arXiv:1111.5869 [hep-ph]`. 6.1

[138] M. Czakon and A. Mitov, *Top++: a program for the calculation of the top-pair cross-section at hadron colliders*, arXiv:1112.5675 [hep-ph]. 6.1

[139] J. Aguilar-Saavedra, *Single top quark production at LHC with anomalous Wtb couplings*, Nucl.Phys. **B804** (2008) 160–192, arXiv:0803.3810 [hep-ph]. 6.1, 8.2.1

[140] J. Pumplin, D. Stump, J. Huston, H. Lai, P. M. Nadolsky, et al., *New generation of parton distributions with uncertainties from global QCD analysis*, JHEP **0207** (2002) 012, arXiv:hep-ph/0201195 [hep-ph]. 6.1

[141] M.L. Mangano et al., *ALPGEN, a generator for hard multiparton processes in hadronic collisions*, JHEP **0307** (2003) 001, hep-ex/0206293. 6.2, 8.5.1

[142] B. P. Kersevan and E. Richter-Was, *The Monte Carlo event generator AcerMC version 2.0 with interfaces to PYTHIA 6.2 and HERWIG 6.5*, arXiv:hep-ph/0405247 [hep-ph]. 6.2, 8.5.1

[143] S. Frixione, E. Laenen, P. Motylinski, B. R. Webber, and C. D. White, *Single-top hadroproduction in association with a W boson*, JHEP **0807** (2008) 029, arXiv:0805.3067 [hep-ph]. 6.2

[144] N. Kidonakis, *Next-to-next-to-leading-order collinear and soft gluon corrections for t-channel single top quark production*, Phys. Rev. **D83** (2011) 091503, arXiv:1103.2792[hep-ph]. 6.2

[145] N. Kidonakis, *NNLL resummation for s-channel single top quark production*, Phys. Rev. **D81** (2010) 054028, arXiv:1001.5034[hep-ph]. 6.2

[146] N. Kidonakis, *Two-loop soft anomalous dimensions for single top quark associated production with a W- or H-*, Phys. Rev. **D82** (2010) 054018, arXiv:1005.4451[hep-ph]. 6.2

[147] F. Berends, H. Kuijf, B. Tausk, and W. Giele, *On the production of a W and jets at hadron colliders*, Nuclear Physics B **357** (1991) No. 1, 32 – 64. 6.2

[148] Atlas Collaboration, G. Aad et al., *Measurement of the top quark-pair production cross section with ATLAS in pp collisions at* $\sqrt{s} = 7$ *TeV*, Eur.Phys.J. **C71** (2011) 1577, arXiv:1012.1792 [hep-ex]. 6.2

[149] C.-H. Kom and W. J. Stirling, *Charge asymmetry in W + jets production at the LHC*, Eur.Phys.J. **C69** (2010) 67–73, arXiv:1004.3404 [hep-ph]. 6.3.2

[150] ATLAS Collaboration, *Improved Luminosity Determination in* **pp** *Collisions at* $\sqrt{\mathbf{s}} = \mathbf{7}$ *TeV using the ATLAS Detector at the LHC*, Tech. Rep. ATLAS-CONF-2012-080, CERN, Geneva, Jul, 2012. 7.1, 7.2

[151] ATLAS Collaboration, *https://atlas.web.cern.ch/Atlas/GROUPS/DATAPREPARATION/PublicPlots/2011/DataSummary/figs/sumLumiByWeek.eps*, tech. rep., as of Feb. 2013. 7.1, A.9

[152] ATLAS Collaboration, *https://twiki.cern.ch/twiki/pub/AtlasPublic/LuminosityPublicResults/mu_2011-2_1.eps*, tech. rep., as of Feb. 2013. 7.2, A.9

[153] ATLAS Collaboration, G. Aad et al., *Measurement of the top quark mass with the template method in the $t\bar{t} \to$ lepton + jets channel using ATLAS data*, Eur.Phys.J. **C72** (2012) 2046, arXiv:1203.5755 [hep-ex]. 8.1.1

[154] R. Brun and F. Rademakers, *ROOT - An object oriented data analysis framework*, Nuclear Instruments and Methods in Physics Research Section A: Accelerators, Spectrometers, Detectors and Associated Equipment **389** (1997) No. 1-2, 81 – 86. 8.2.3

[155] S. Frixione, P. Nason and C. Oleari, *Matching NLO QCD computations with Parton Shower simulations: the POWHEG method*, JHEP **0711** (2007) 070, arXiv:0709.2092[hep-ph]. 8.5.1

[156] A. Sherstnev and R. Thorne, *Different PDF approximations useful for LO Monte Carlo generators*, arXiv:0807.2132 [hep-ph]. 8.5.1

[157] ATLAS Collaboration, G. Aad et al., *Measurement of $t\bar{t}$ production with a veto on additional central jet activity in pp collisions at $\sqrt{s}$ = 7 TeV using the ATLAS detector*, Eur.Phys.J. **C72** 2043. 8.5.1, 8.12, A.9

[158] Atlas Collaboration, G. Aad et al., *Measurement of underlying event characteristics using charged particles in pp collisions at $\sqrt{s} = 900GeV$ and 7 TeV with the ATLAS detector*, Phys.Rev. **D83** (2011) 112001, arXiv:1012.0791 [hep-ex]. 8.5.1

[159] A. Buckley, H. Hoeth, H. Lacker, H. Schulz, and J. E. von Seggern, *Systematic event generator tuning for the LHC*, Eur.Phys.J. **C65** (2010) 331–357, arXiv:0907.2973 [hep-ph]. 8.5.1

[160] P. Z. Skands, *Tuning Monte Carlo Generators: The Perugia Tunes*, Phys.Rev. **D82** (2010) 074018, arXiv:1005.3457 [hep-ph]. 8.5.1

[161] M. Whalley, D. Bourilkov, and R. Group, *The Les Houches accord PDFs (LHAPDF) and LHAGLUE*, arXiv:hep-ph/0508110 [hep-ph]. 8.5.1

[162] ATLAS Collaboration, *Close-by Jet Effects on Jet Energy Scale Calibration in pp Collisions at $\sqrt{s}$ = 7 TeV with the ATLAS Detector*, Tech. Rep. ATLAS-CONF-2011-062, CERN, Geneva, Apr, 2011. 8.5.3

[163] N. Metropolis, A. W. Rosenbluth, M. N. Rosenbluth, A. H. Teller, and E. Teller, *Equation of State Calculations by Fast Computing Machines*, J. Chem. Phys. **21** (June, 1953) 1087–1092. 9.1.2

[164] A. Caldwell, D. Kollár, and K. Kröninger, *BAT - The Bayesian analysis toolkit*, Computer Physics Communications **180** (Nov., 2009) 2197–2209, arXiv:0808.2552 [physics.data-an]. 9.1.2

[165] J. A. Aguilar-Saavedra, *Single top quark production at LHC with anomalous Wtb couplings*, Nuclear Physics B **804** (Nov., 2008) 160–192, arXiv:0803.3810 [hep-ph]. 9.2.2

[166] Tevatron Electroweak Working Group, for the CDF Collaboration, and the D0 Collaboration, *Combination of CDF and D0 Measurements of the Single Top Production Cross Section*, ArXiv e-prints (Aug., 2009) , arXiv:0908.2171 [hep-ex]. 9.2.2

[167] D0 Collaboration, V. M. Abazov, B. Abbott, B. S. Acharya, M. Adams, T. Adams, G. D. Alexeev, G. Alkhazov, A. Alton, G. Alverson, and et al., *Combination of searches for anomalous top quark couplings with 5.4 fb^{-1} of $p\bar{p}$-collisions*, Physics Letters B **713** (July, 2012) 165–171, `arXiv:1204.2332 [hep-ex]`. 9.2.2

List of Figures

List of Tables

"*Not I, nor anyone else can travel that road for you.*
You must travel it by yourself. It is not far.
It is within reach. Perhaps you have been on it since you were born, and did not know.
Perhaps it is everywhere - on water and land."

Walt Whitman, from **Song of Myself**

Acknowledgements

At this point I would like to thank everyone who travelled this road with me, both in Göttingen/CERN or at home.
First of all, I would like to express my gratitude to Prof. Dr. Arnulf Quadt who was my supervisor during more than five years, for the opportunity to work in this young and lively institute an in a even more lively field of physics. Furthermore I would like to thank Prof. Dr. Wolfgang Wagner who agreed to be the co-referee of this thesis. I also would like to thank Kevin Kröninger, for a lot of discussions and advice, not to forget the constant encouragement (next time I just print everything in red ;)). Furthermore, I would like to thank Lisa Shabalina for all the support during our time at CERN, and also Jarka, Katha, Steffi, Johannes, Boris, Stefan and Lubka for all the ice-cream/tequila parties and football watching :)
My thanks goes also to Nuno Castro and Antonio Onofre who were always reliable teamworkers when the next conference was approaching. I also like to thank *my* :) students Chris Delitzsch, Philipp Stolte and Cora Fischer who were the best students one could wish for.

My thanks goes to everyone who helped proofreading this thesis, namely Boris, Chris, Johannes, Kevin, Philipp, Joern and Steffi. Your input and encouragement was a great help. In terms of computing needs, I would like to thank Joerg Meyer, whom I would also like to thank for fixing the cluster and giving support also at the weekends or whenever somebody needed help. My special thanks goes to Anna (for her good taste of music and the unforgettable week in Perugia ;)), Boris, who never takes me too seriously when I'm freaking out (and who is so selfless that he even sacrifices his sleep to help others), Johannes, for always keeping my spirits high when necessary and last but not least, Chris, for the unbelievable talent to be always smiling, even late at night when sitting in her office ;) .

I would also like to thank my Physics and Maths teachers in highschool for a good preparation for the university (especially my physics teacher Martin Patz). Furthermore I would like to thank my friends at home who didn't see me very often during the last years.

Finally, my biggest thanks of all goes to my parents and my sister Marion. You were always there for me when I needed you, and gave me the opportunity to do what I wanted to do without doubting or asking what it was for. I hope, at some point, I can do the same for you. My final words go to Markus, I thank you for never losing your optimism and to give me the feeling that, no matter what has happend, everything goes well in the end. Thanks so much!

Curriculum Vitae

Andrea Helen Knue

E-Mail: aknue@cern.ch

Date of birth: January 15, 1985

Place of birth: Meppen

Nationality: German

Education:

1991 – 1995	Primary School (Georgschule Altharen)
1995 – 1997	Orientierungsstufe (Martinischule Haren)
1997 – 2004	Gymnasium Haren (Abitur 2004)
2004 – May 2009	Physics student at the Georg-August-University of Göttingen
May 2009	Diploma in Physics ("Studies with the Matrix Element Method using the example of a top quark mass measurement with the ATLAS experiment")
June 2009 – March 2013	PhD student at the Georg-August University Göttingen with Prof. Dr. Arnulf Quadt

Preliminary conference results:

Moriond '11	"Measurement of the W-boson polarization in top quark decays in pp collision data at $\sqrt{s}$=7 TeV using the ATLAS detector" (ATLAS-CONF-2011-037)
Lepton/Photon '11	"Measurement of the W boson polarisation in top quark decays in 0.70 fb^{-1} of pp collisions at $\sqrt{s}$ = 7 TeV with the ATLAS detector" (ATLAS-CONF-2011-122)

Publications: "Measurement of the W boson polarization in top quark decays with the ATLAS detector" , (JHEP 1206 (2012) 088)

Göttingen, March, 2013

Hiermit versichere ich, dass ich die Dissertation mit dem Titel “Messung der W-Boson Polarisation in Top-Quark Zerfällen mit dem ATLAS-Detektor” selbständig und ohne unerlaubte Hilfe angefertigt habe.

Göttingen, den 13.02.2013

Andrea Knue